

# ACTA GEOTECHNICA SLOVENICA

2020/1  
VOL. 17

Mud-pump pressure in geothermal wells  
An extended bearing-capacity equation for shallow foundations on granular trenches in soft soil  
Observation of extensive mass movements in the Lipica II quarry with an EL beam displacement sensor  
Integration of measurement techniques in monitoring of the Laze landslide in Slovenia  
Modeling and analysis of digital surface models using high-resolution UAV images  
Experimental investigation of the influence of relative effective diameter on the ultimate shear strength of partially saturated granular soils  
Load-settlement and load-sharing behaviour of a piled raft foundation resting on layered soils  
Numerical investigation of the influence of spatial effects and supporting structures during pit excavation



### **Ustanovitelji**

### **Founders**

Univerza v Mariboru, Fakulteta za gradbeništvo, prometno inženirstvo in arhitekturo

University of Maribor, Faculty of Civil Engineering, Transportation Engineering and Architecture

Univerza v Ljubljani, Fakulteta za gradbeništvo in geodezijo  
University of Ljubljana, Faculty of Civil and Geodetic Engineering

Univerza v Ljubljani, Naravoslovnotehniška fakulteta  
University of Ljubljana, Faculty of Natural Sciences and Engineering

Slovensko geotehniško društvo  
Slovenian Geotechnical Society

Društvo za podzemne in geotehniške konstrukcije  
Society for Underground and Geotechnical Constructions

### **Izdajatelj**

### **Publisher**

Univerza v Mariboru, Fakulteta za gradbeništvo, prometno inženirstvo in arhitekturo  
Faculty of Civil Engineering, Transportation Engineering and Architecture

### **Odgovorni urednik**

### **Editor-in-Chief**

Borut Macuh University of Maribor

### **Tehnična urednica**

### **Technical Editor**

Tamara Bračko University of Maribor

### **Uredniki**

### **Co-Editors**

Jakob Likar Geoportall d.o.o.  
Janko Logar University of Ljubljana  
Primož Jelušič University of Maribor  
Stanislav Škrabl University of Maribor  
Milivoj Vulić University of Ljubljana  
Bojan Žlender University of Maribor

### **Posvetovalni uredniki**

### **Advisory Editors**

Heinz Brandl Vienna University of Technology  
Chandrakant. S. Desai University of Arizona  
Bojan Majes University of Ljubljana  
Pedro Seco e Pinto National Laboratory of Civil Eng.

### **Lektor**

### **Proof-Reader**

Paul McGuinness

### **Naklada**

### **Circulation**

220 izvodov - issues

### **Cena**

### **Price**

25 EUR/letnik - 25 EUR/vol.; (50 EUR for institutions/za institucije)

### **Tisk**

### **Print**

Tiskarna Saje d.o.o.

Revija redno izhaja dvakrat letno. Članki v reviji so recenzirani s strani priznanih mednarodnih strokovnjakov. Baze podatkov v katerih je revija indeksirana: SCIE - Science Citation Index Expanded, JCR - Journal Citation Reports / Science Edition, ICONDA - The international Construction database, GeoRef. Izid publikacije je finančno podprla Javna agencija za raziskovalno dejavnost Republike Slovenije iz naslova razpisa za sofinanciranje domačih periodičnih publikacij.

### **Uredniški odbor**

### **Editorial Board**

Marx Ferdinand Ahlinhan National University in Abomey  
Amin Barari Aalborg University  
Theodoros Hatzigogos Aristotle University of Thessaloniki  
Vojkan Jovičič IRGO-Ljubljana  
Rolf Katzenbach Technical University Darmstadt  
Nasser Khalili The University of New South Wales, Sydney  
Svetlana Melentijevic Complutense University of Madrid  
Seyed Hamed Mirmoradi Federal University of Rio de Janeiro  
Ana Petkovšek University of Ljubljana  
Borut Petkovšek Slovenian National Building and Civil Engineering Institute  
Mihael Ribičič University of Ljubljana  
César Sagasetta University of Cantabria  
Patrick Selvadurai McGill University  
Stephan Semprich University of Technology Graz  
Devendra Narain Singh Indian Institute of Technology, Bombay  
Abdul-Hamid Soubra University of Nantes  
Kiichi Suzuki Saitama University  
Antun Szavits-Nossan University of Zagreb  
Kosta Urumović Croatian geological survey  
Ivan Vaniček Czech Technical University in Prague

### **Založnik**

### **Published by**

Univerzitetna založba Univerze v Mariboru  
Slomškov trg 15, 2000 Maribor, Slovenija  
e-pošta: zalozba@um.si, http://press.um.si/, http://journals.um.si/  
University of Maribor Press  
Slomškov trg 15, 2000 Maribor, Slovenia  
e-mail: zalozba@um.si, http://press.um.si/, http://journals.um.si/

### **Naslov uredništva**

### **Address**

ACTA GEOTECHNICA SLOVENICA  
Univerza v Mariboru, Fakulteta za gradbeništvo, prometno inženirstvo in arhitekturo  
Smetanova ulica 17, 2000 Maribor, Slovenija  
Telefon / Telephone: +386 (0)2 22 94 300  
Faks / Fax: +386 (0)2 25 24 179  
E-pošta / E-mail: ags@um.si

### **Spletni naslov**

### **web Address**

http://zalozba.um.si/index.php/ags/index

The journal is published twice a year. Papers are peer reviewed by renowned international experts. Indexation data bases of the journal: SCIE - Science Citation Index Expanded, JCR - Journal Citation Reports / Science Edition, ICONDA - The international Construction database, GeoRef. The publication was financially supported by Slovenian Research Agency according to the Tender for co-financing of domestic periodicals.

<i>B. Janc in Ž. Vukelić</i> Tlak izplačne črpalke pri geotermalnih vrtinah	<i>B. Janc and Ž. Vukelić</i> Mud-pump pressure in geothermal wells	<b>2</b>
<i>J. A. Duque Felfle in drugi</i> Razširjena enačba nosilnosti temeljnih tal pod plitvimi temelji na grobozrnatih zasekih v mehkih tleh	<i>J. A. Duque Felfle et al.</i> An extended bearing-capacity equation for shallow foundations on granular trenches in soft soil	<b>12</b>
<i>D. Ignjatović Stupar in drugi</i> Opazovanje obsežnih premikov mase v kamnolomu Lipica II s senzorjem premika žarka EL	<i>D. Ignjatović Stupar et al.</i> Observation of extensive mass movements in the Lipica II quarry with an EL beam displacement sensor	<b>23</b>
<i>A. Lazar in drugi</i> Vključevanje merilnih tehnik, ki se uporabljajo za spremljanje plazu Laze v Sloveniji	<i>A. Lazar et al.</i> Integration of measurement techniques in monitoring of the Laze landslide in Slovenia	<b>33</b>
<i>A. Pal in drugi</i> Modeliranje in analiza digitalnih površinskih modelov z uporabo visoko ločljivih UAV slik	<i>A. Pal et al.</i> Modeling and analysis of digital surface models using high-resolution UAV images	<b>46</b>
<i>K. Doumi in drugi</i> Eksperimentalno raziskovanje vpliva relativnega efektivnega premera na mejno strižno trdnost delno zasičenih grobo zrnatih zemljin	<i>K. Doumi et al.</i> Experimental investigation of the influence of relative effective diameter on the ultimate shear strength of partially saturated granular soils	<b>56</b>
<i>P. Deb in S. Kumar Pal</i> Odnosa obtežba-posedek in obtežba-delitev obtežbe za temeljno ploščo na pilotih na slojevitih tleh	<i>P. Deb and S. Kumar Pal</i> Load-settlement and load-sharing behaviour of a piled raft foundation resting on layered soils	<b>71</b>
<i>P. Li in drugi</i> Numerična raziskava učinkov prostorskih vplivov in podpornih konstrukcij med izkopavanjem gradbene jame	<i>P. Li et al.</i> Numerical investigation of the influence of spatial effects and supporting structures during pit excavation	<b>87</b>
Navodila avtorjem	Instructions for authors	<b>97</b>

# MUD-PUMP PRESSURE IN GEOTHERMAL WELLS

# TLAK IZPLAČNE ČRPALKE PRI GEOTERMALNIH VRTINAH

## Blaž Janc

University of Ljubljana,  
Faculty of Natural Sciences and Engineering  
Aškerčeva c. 12, 1000 Ljubljana, Slovenia  
E-mail: blaz.janc@ntf.uni-lj.si

## Željko Vukelić

University of Ljubljana,  
Faculty of Natural Sciences and Engineering  
Aškerčeva c. 12, 1000 Ljubljana, Slovenia  
E-mail: zeljko.vukelic@ntf.uni-lj.si

DOI <https://doi.org/10.18690/actageotechslov.17.1.2-11.2020>

## Keywords

drilling hydraulics, pump pressure, drilling mud, rheological models, geothermal energy

## Ključne besede

hidravlika vrtanja, tlak črpalke, izplaka, reološki modeli, geotermalna energija

## Abstract

Rotary drilling is a mining method for the extraction and exploration of mineral resources. A significant pressure drop occurs during deep-well rotary drilling. This paper presents a procedure and a theoretical background of the working-pump-pressure determination for exploration geothermal borehole Sob-4g, located in Murska Sobota, NE Slovenia. We determined all the partial pressure drops in the mud-circulation system when drilling the final section of a 1201.15-m-deep borehole. For this, it is important to choose the correct rheological model that follows the behaviour of the drilling fluid. In the presented case, the Bingham plastic model was used. The aim of the paper's hydraulic analysis is to provide the optimal drilling parameters and therefore the maximum effects in deep-well drilling. We show that most of the drilling mud-pressure energy is consumed within the drill string and through the bit. The fluid-flow regime in the drill pipes, collars and drill bit is turbulent, while it is laminar in the annulus.

## Izvleček

Rotacijsko vrtanje je rudarska metoda za pridobivanje in raziskovanje mineralnih surovin. Med rotacijskim vrtanjem globokih vrtin prihaja do občutnega padca tlaka. V prispevku je predstavljen postopek in teoretično ozadje določanja delovnega tlaka črpalke za raziskovalno geotermalno vrtino Sob-4g, ki se nahaja v Murski Soboti, SV Slovenija. Določili smo vse delne padce tlaka v izplačnem sistemu pri vrtanju končnega odseka 1201,15 m globoke vrtine. Za to je pomembno izbrati pravilen reološki model, ki sledi obnašanju izplačnega fluida. V predstavljenem primeru je bil uporabljen Binghamov plastični model. Cilj hidravlične analize prispevka je zagotoviti optimalne parametre vrtanja in s tem največje učinke pri vrtanju globokih vrtin. Večina tlačne energije izplake se porabi znotraj drogovja in preko dleta. Režim pretoka izplačnega fluida v vrtalnem drogovju, težkem drogovju in dletu je turbulenten, medtem ko je v medprostoru laminaren.

## 1 INTRODUCTION

Deep wells are most commonly drilled for oil and gas extraction or the use of geothermal energy. One of the most important elements in the drilling process is the drilling mud. It is a fluid that performs numerous

functions, including carrying the rock fragments to the surface, providing hydrostatic pressure in the well and cooling the drill bit. The mud circulation is provided by mud pumps via a suitable working pressure and flow rate. The pump pressure provides sufficient energy for the mud circulation, while the flow rate enables the transport of the drilled cuttings to the surface.

The drilling fluid circulates in the mud system. It starts at the surface and runs downwards through the drill string and the drill bit and upwards in the annulus between the drill string and the borehole wall, back to the surface. The pressure energy from mud pump is mostly consumed in overcoming the internal friction in the drill string and for the fluid acceleration through the bit nozzles. There is a significant local reduction of the diameter in the bit nozzles, which leads to a large increase in the fluid kinetic energy and, therefore, the fluid velocity. Consequently, the bit nozzles are areas with a drastic pressure drop. Increasing the kinetic energy at the drill bit means a higher hydraulic power, which reflects in a better cutting action and a more efficient cleaning of the drilled particles beneath the bit.

Determining the working pump pressure (WPP) is an important element of the drilling hydraulics and represents an indispensable part of the deep-well design. The WPP is defined as the sum of all the partial pressure drops. Therefore, all the pressure drops in the mud circulating system have to be known. The WPP increases with an increasing drilling depth.

## 2 DRILLING PROCESS TECHNOLOGY

A borehole is drilled using a drilling rig, which is a set of machines, devices and elements that are necessary for the drilling process. The drilling process is a sequence of the following operations:

- 1) Connecting the drill pipes, drill collars and the drill bit.
- 2) Lengthening the drill pipes and lowering the drill bit into the borehole bottom.
- 3) Drilling bit action (drilling) with the simultaneous carrying of drill cuttings to the surface.
- 4) Connecting additional drill pipes due to the bit progress in depth.
- 5) Rising of the drill string from the borehole (for example, due to the wear of the drill bit).

The rock at the borehole bottom is cut using the rotation of the roller cone bit, which is attached to the end of the drill collars and affected by its load. The roller cone bit rotates together with the drill string, cutting the rock beneath it. The transport of the drilled cuttings from the borehole bottom to the surface goes via the mud fluid [1].

Three main components of the deep well drilling are:

- 1) Weight on the bit.
- 2) Bit rotation.
- 3) Circulation of the drilling fluid.

## 3 DRILLING FLUID

The mud or the drilling fluid is a liquid used in the drilling process that continuously circulates from the surface downwards through the drill pipes and bit nozzles and upwards to the surface through the annular space between the drill pipes and the borehole wall.

We can distinguish between the major and minor functions of the drilling fluids. The major functions are, in general, the removal of the drilled cuttings, the containment of the subsurface formation fluid pressures and the borehole stabilization. Minor functions, including the cooling and lubricating of the drill string and drill bit, preventing particle sedimentation at the mud-circulation stop, and reducing the weight during the drill string operations (buoyancy), aid in the formation evaluation and cleaning of the drill bit [2].

Removing the cuttings beneath the drill bit is necessary for progress in the drilling process. This is achieved by the flow of drilling fluid through the annular space between the borehole wall and the drill string. Removal of the cutting particles depends on the annular mud velocity, the mud rheological properties, the borehole deviation, the rotation of the drill string, the borehole eccentricity, the drilling rate and the size and shape of the drilled cuttings [2].

A sufficient mud density prevents the intrusion of the formation fluids into the borehole. The mud density is achieved with additives (for example, barite). Clay is added, for example, for a higher viscosity of the mud. The drilling regime is, in most cases, over-pressured, which means that the pressure gradient is greater than 9.8 kPa per meter of well depth.

## 4 MUD PUMPS

A mud pump provides enough energy for the pressure of the fluid across the circulating system. Mud-pump engines can produce around 1600 kW of power with flow rates of up to 5000 l/min and pressures of up to  $600 \cdot 10^5$  Pa. Generally, there are two types of reciprocating mud pumps: duplex and triplex.

### 4.1 Duplex pump

The principle of a double-acting, two-cylinder (duplex) pump is schematically shown in Fig. 1. As the piston moves forward (to the right-hand side in Fig. 1), it discharges fluid through the open discharge valve. At same time, the intake valve is opened, allowing fluid to enter the chamber behind the piston. There is a reversible principle as the piston returns (see Fig. 2) [3].

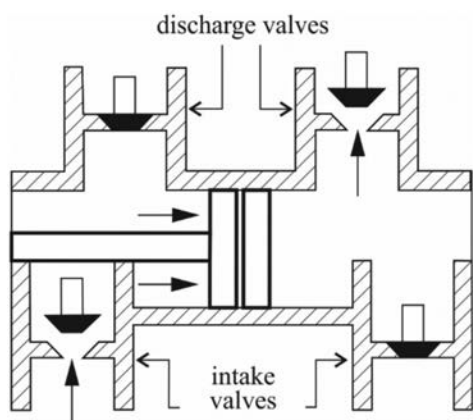


Figure 1. Duplex pump (piston moves forward).

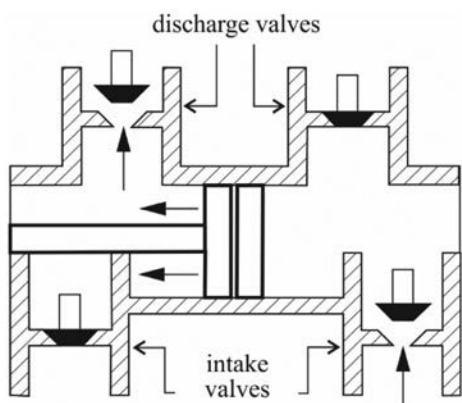


Figure 2. Duplex pump (piston moves backward).

Theoretical volume when the piston moves forward:

$$V_1 = \frac{\pi d^2 L}{4} \quad (1)$$

where  $V_1$  is the volume of the discharged fluid when the piston moves forward ( $m^3$ ),  $d$  is the inner diameter of the piston cylinder (m) and  $L$  is the piston stroke (m).

When the piston returns, the theoretical volume of the discharged fluid is:

$$V_2 = \frac{\pi(d^2 - d_r^2)L}{4} \quad (2)$$

where  $V_2$  is the volume of the discharged fluid when the piston moves backwards ( $m^3$ ) and  $d_r$  is the piston-rod diameter (m).

The total volume of discharged fluid in one crankshaft stroke is:

$$V = 2(V_1 + V_2) \eta_v = \frac{2\pi(2d^2 - d_r^2)L\eta_v}{4} \quad (3)$$

where  $\eta_v$  is the volumetric efficiency of the pump ( $/$ ).

## 4.2 Triplex pump

The principle of a single-acting, three-cylinder (triplex) pump is schematically shown in Fig. 3. With this pump the piston discharges fluid in only one direction.

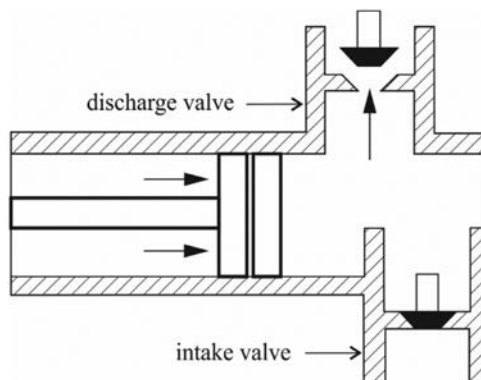


Figure 3. Triplex pump (piston moves forwards).

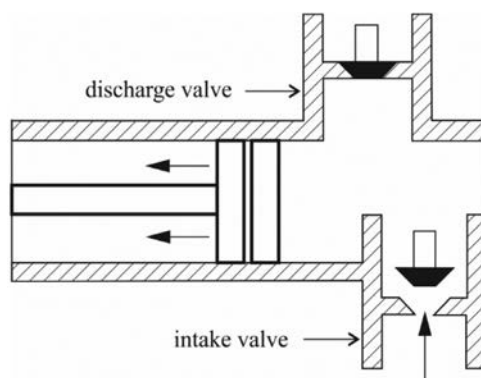


Figure 4. Triplex pump (piston moves backwards).

The total volume of discharged fluid in one crankshaft stroke is:

$$V = \frac{3\pi d^2 L \eta_v}{4} \quad (4)$$

## 5 RHEOLOGICAL MODELS

There are significant resistance forces to overcome in a mud-circulation system. Rheological models, used as an approximation for the fluid behaviour, are in general Newtonian (linear) and non-Newtonian (non-linear). These models are used to derive the pressure-drop equations.

## 5.1 Newtonian model

A Newtonian fluid is ideally viscous. It follows a linear relation between the shear stress ( $\tau$ ) and the speed of the shear deformation-shear rate ( $\dot{\gamma}$ ).

$$\tau = \mu \dot{\gamma} \quad (5)$$

where  $\tau$  is the shear stress (Pa),  $\dot{\gamma}$  is the shear rate ( $s^{-1}$ ) and  $\mu$  is the Newtonian viscosity (Pa s).

Examples of a Newtonian fluid are water, oil and gas.

The linear relationship between the shear stress and the shear rate is valid only as long as the fluid moves in layers or laminae. This is true only at relatively low rates of shear. When turbulent flow occurs, pressure drops have to be determined with empirical correlations [4].

## 5.2 Non-Newtonian models

Non-Newtonian fluids are real. They do not exhibit a direct proportionality between the shear stress and the shear rate [4]. Shear-dependent non-Newtonian fluids are pseudoplastic (shear thinning) if the apparent viscosity decreases with an increasing shear stress and dilatant (shear thickening) if the apparent viscosity increases with an increasing shear stress. Drilling fluids and cement slurries are generally thixotropic, which means that they are pseudoplastic and have a time-dependent viscosity [4].

Fluids with plastic flow behaviour (Bingham fluids) start to flow when the limit shear stress is exceeded. When the shear flow is established, fluids with plastic flow behaviour show a linear dependence of the shear stress and the shear rate. In this case the Newtonian model is valid.

The Bingham model represents a rigid matter that starts to flow as a viscous fluid when the yield strength is exceeded. After this, it behaves as a Newtonian fluid. A Bingham fluid is typical for bentonite muds. The rheological model is defined by:

$$\tau = \mu_{pl} \dot{\gamma} + \tau_0 \quad (6)$$

where  $\mu_{pl}$  is the plastic viscosity (Pa s) and  $\tau_0$  is the yield strength (Pa).

The Ostwald-de Waele model is defined as a power law:

$$\tau = K |\dot{\gamma}|^{n-1} \dot{\gamma} \quad (7)$$

where  $K$  is the flow-consistency index (Pa s) and  $n$  is the flow-behavior index ( $/$ ).

Like in the Bingham model, the equation consists of two parameters:  $K$  and  $n$ . A higher  $K$  means a higher viscosity of the fluid. The deviation of parameter  $n$  from 1 is a criterion for the fluid deviation from a Newtonian fluid. In the case when  $n=1$ , the fluid follows the Newtonian law, if  $K=\mu$ . It behaves pseudoplastically (viscosity decreases with increasing shear stress) when  $n<1$  and dilatantly (viscosity increases with increasing shear stress) when  $n>1$ . The equation is valid in the laminar-flow region.

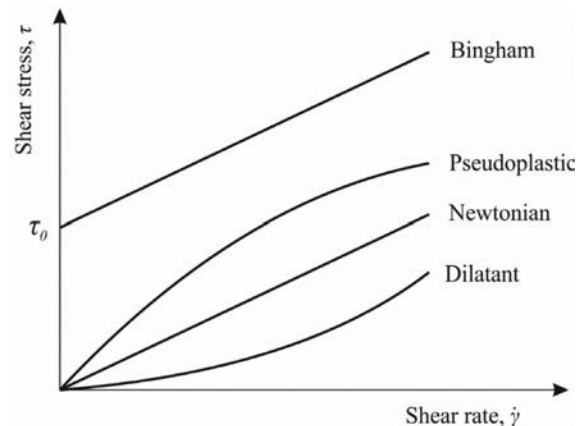


Figure 5. Rheological models.

## 6 PRESSURE DROPS

### 6.1 Generally about pressure drops

When flowing in a pipe, a fluid loses part of its energy due to the friction/resistance forces. These forces are internal friction due to the viscosity and external friction due to pipe roughness [5].

A circulating drilling mud has an initial energy represented by the pump-discharge pressure. This energy is totally lost in the mud circuit. The mud pressure is zero when it returns to the pits. In this case, the pump-discharge pressure represents the total pressure losses in the mud circuit [5].

When drilling, pressure drops occur in the following areas: surface equipment, drill pipes and drill collars, drill bit and annulus between the well bore and the drill string. Pressure drops in the drill string and annulus do not directly contribute to the drilling process, but cannot be avoided if the fluid is to be circulated around the system. Pressure drops in drill bit, on the other hand, do perform a useful function, since it helps to cut rock and clean the drilled cuttings from the face of the bit.

It is, therefore, desirable to optimize the pressure drops through the nozzles (and therefore the cleaning of the bit face) and minimize the drops in the drill string and annulus [3].

The pump pressure ( $p_p$ ) is expended by: frictional pressure losses in the surface equipment ( $p_s$ ), frictional pressure losses in the drill pipes ( $p_{dp}$ ), frictional pressure losses in the drill collars ( $p_{dc}$ ), pressure losses through the bit nozzles ( $p_b$ ), frictional pressure losses in the drill-collar annulus ( $p_{dca}$ ) and frictional pressure losses in the drill-pipe annulus ( $p_{dpa}$ ) [4].

$$p_p = \Delta p_s + \Delta p_{dp} + \Delta p_{dc} + \Delta p_b + \Delta p_{dca} + \Delta p_{dpa} \quad (8)$$

The total frictional pressure loss can be represented as  $p_f$ :

$$p_p = p_b + p_f \quad (9)$$

It is evident from the equation that the working pump pressure is consumed for the fluid acceleration in the bit nozzles and overcoming the flow resistance in drill pipes and the annulus.

Pressure drops depend on the rheological properties of the mud, the flow type (laminar or turbulent) and the geometry of the pipes and the well bore.

## 6.2 Laminar flow in the drill string and annulus

The flow type, within which the fluid flows in the drill string or annulus, depends on the Reynolds number ( $N_{Re}$ ). It is defined as (for pipe flow):

$$N_{Re_p} = \frac{\rho \bar{v} d_i}{\mu} \quad (10)$$

where  $\rho$  is the mud fluid density ( $\text{kg/m}^3$ ),  $\bar{v}$  is the fluid average velocity (m/s) and  $d_i$  is the pipe inner diameter (m).

For annular flow:

$$N_{Re_a} = \frac{\rho \bar{v} (d_b - d_o)}{\mu} \quad (11)$$

where  $d_b$  is the borehole diameter (m) and  $d_o$  is the pipe outer diameter (m).

In the case when the density and viscosity of the drilling mud are constant, the Reynolds number depends only on the pipe diameter and the mud velocity. If the flow rate is constant, the Reynolds number depends only on the pipe diameter. The value of the Reynolds number is not constant across the whole mud system, but it changes. Thus, the mud flow can be laminar at one point and turbulent at another.

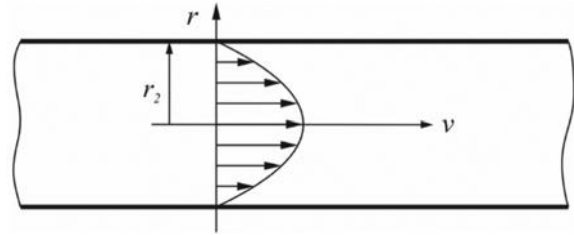


Figure 6. Mud-velocity profile for flow in a pipe ( $r_2$  is the radius of the pipe).

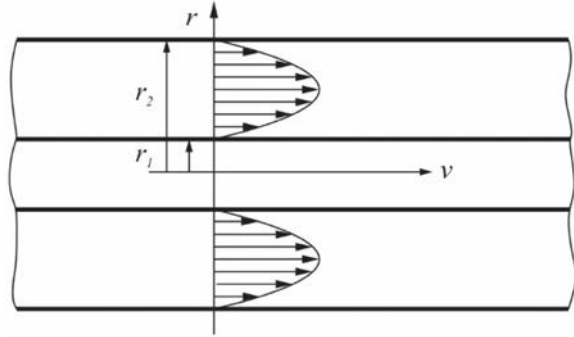


Figure 7. Mud-velocity profile for the flow in an annulus ( $r_1$  is the radius of the pipe,  $r_2$  is the radius of the borehole).

The Newtonian fluid flow is laminar if  $N_{Re}$  is less than 2100 and turbulent if  $N_{Re}$  is more than 2100. Actually, when  $N_{Re}$  values are in region 2000–4000, the flow is in a transition between laminar and turbulent flow.

Fluid flow in the drill string or annulus do not have a uniform velocity. In the case of laminar flow, the fluid velocity by the wall pipe equals zero. The velocity is the highest at the maximum distance from the pipe wall, which is in the center of the pipe.

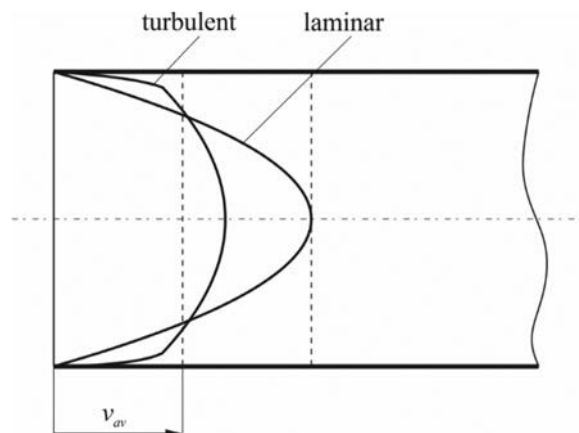


Figure 8. Laminar and turbulent velocity profiles.

Velocity profiles for laminar flow in the pipe annulus are shown in Fig. 6 and Fig. 7. Pipe flow represents the flow from the surface to the bit and annular flow represents the flow from the drill bit back to the surface.

Fig. 8 shows the velocity profile of a circular pipe (laminar and turbulent flow). The maximum velocity in the case of turbulent flow is  $v_{max,t} = (1.15 \dots 1.25)v_{av}$  and in the case of laminar flow  $v_{max,l} = 2v_{av}$ , where  $v_{av}$  represents the average velocity [6].

### 6.3 Turbulent flow in the drill string and annulus

High velocities of flow rates mean that the fluid does not flow in layers, but in a chaotic way. Turbulent flow can be divided into three regions: the laminar flow, the transition between laminar and turbulent flow and the turbulent core.

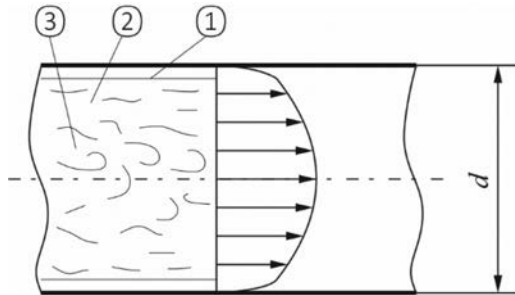


**Figure 9.** Turbulent flow in a pipe (1 thin layer of laminar flow, 2 transition layer, 3 turbulent core;  $d$  is the diameter of the pipe).

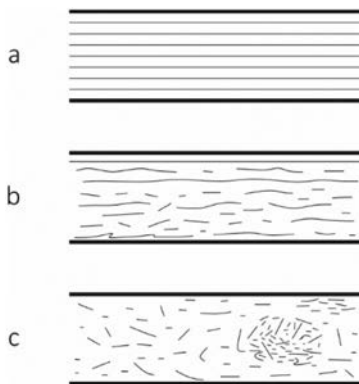


**Figure 10.** Laminar and turbulent flow patterns in a circular pipe (a - laminar flow, b - transition between laminar and turbulent flow, c - turbulent flow).

When calculating pressure drops in drill pipes and annulus, the type of fluid must be known (Newtonian, non-Newtonian). The flow type is determined with a calculation of the critical velocity, which depends on the rheological parameters of the mud.

There are some assumptions in calculating the pressure drops. These are: drill pipes are placed into the well concentric, drill pipes do not rotate, well bore is circular in shape with known diameter, mud fluid is incompressible, the flow is isothermal and the pipes are smooth. For this reason, the equations contain some experimentally determined factors.

### 6.4 Pressure drop in drill string and annulus

The equations for the pressure-drop calculation in the pipe and the annular space are given as follows, according to the Fanning equations [7].

For pipe flow:

$$\Delta p_i = \frac{2f\rho Lv^2}{d_i} \quad (12)$$

where  $\Delta p_i$  is the pipe pressure drop (Pa),  $f$  is the hydraulic friction factor ( $l$ ) and  $v$  is the flow rate (m/s).

For annular flow:

$$\Delta p_a = \frac{2f\rho Lv^2}{d_b - d_o} \quad (13)$$

where  $\Delta p_a$  is the annular pressure drop (Pa).

### 6.5 Pressure drop in bit nozzles

The purpose of bit nozzles is a better cleaning action of the drilling fluid at the bottom of the hole. Because of the small diameter of the bit nozzles, fluids reach high velocities inside the nozzle [8]. The nozzle velocity is defined as:

$$v_n = \frac{q}{A_t} \quad (14)$$

where  $v_n$  is the nozzle velocity (m/s),  $q$  is the mud flow rate ( $m^3/s$ ) and  $A_t$  is the total nozzle area ( $m^2$ ).

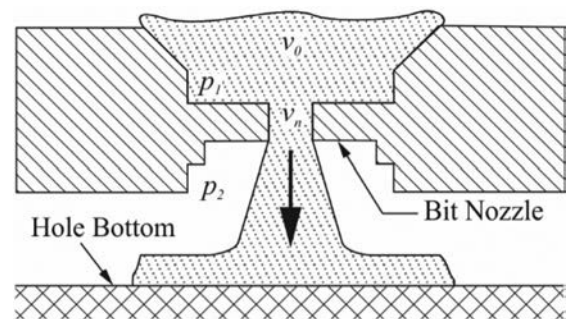


**Figure 11.** Drill bit nozzle ( $v_0$  and  $p_1$  are the mud fluid input velocity and pressure,  $v_n$  and  $p_2$  are the mud fluid output velocity and pressure).

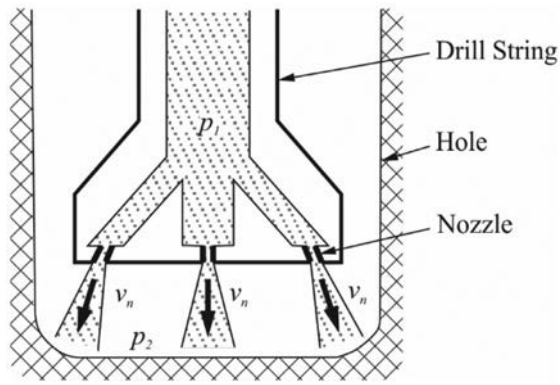


Figure 12. Drill bit with three nozzles.

Fluid flow through bit nozzles is shown in Fig. 11. The input velocity  $v_0$  is negligible compared to the output velocity  $v_n$ . Fluid acceleration occurs due to the local reduction of the diameter in the nozzles. Kinetic energy increases, while the pressure energy decreases. Consequently, a pressure drop occurs at the bit nozzles. The pressure drop is defined by [8]:

$$\Delta p_b = \frac{\rho q^2}{2C^2 A_t^2} \quad (15)$$

where  $C$  is the nozzle-discharge coefficient ( $/$ ).

## 7 EXPERIMENTAL

An exploratory geothermal borehole (EGB) Sob-4g was constructed with the aim of exploring potential geothermal aquifers for the reinjection of cooled thermo-mineral water from the Sob-3g borehole back into the production aquifers.

A reinjection system, which consist of a geothermal reinjection well and the surface reinjection unit, is a necessary part for returning the water to the production aquifer [9].

EGB Sob-4g is located in Murska Sobota close to the existing geothermal boreholes Sob-1 and Sob-2, which exploit the thermo-mineral water for district heating and balneology.

In general, geothermal energy in Slovenia is utilized for individual space heating, district heating, cooling, greenhouse heating, bathing, swimming and snow melting [10].

EGB Sob-4g is 1201.15 m deep. Drilling has been made through geological formations of Mura and Lendava. Drilling has stopped at the upper part of the Murska Sobota formation. In the first section (0–580.73 m)

bentonite drilling mud and in second section (580.73–1201.15 m) polymer drilling mud were used.

The EGB Sob-4g location belongs to one of six regional numerical models of groundwater flow in Slovenia [11].

### 7.1 Borehole construction

The borehole is constructed in two stages. The first stage consists of drilling the first section (from 0.00 m to 580.73 m) and the casing. The second stage consists of drilling the second section (from 580.73 m to 1201.15 m).

Table 1. Drilled intervals.

Section	Drilled interval (m)	Bit diameter (mm)
1	0.00–580.73	444.50
2	580.73–1201.15	311.20

Table 2. Casing intervals.

Section	Casing interval (m)	Casing diameter (mm)
1	0.00–578.25	339.70
2	530.30–1201.00	177.80

Table 3. Drilling equipment for second stage drilling.

	Drilling Equipment	Length (m)
drill bit	311.15 mm HUGES, IADC	0.30
	135 GTX-G3; nozzles 3×10.32 mm	
1. stabilizer	Ø 311.15 mm	1.21
drill collar	Ø 165.1 mm	8.47
2. stabilizer	Ø 311.15 mm	1.49
drill collar	Ø 165.1 mm	8.90
3. stabilizer	Ø 311.15 mm	1.39
drill collar	Ø 165.1 mm	78.98
transition pipe	101.6 mm IF (male) × 101.6 mm IF (female)	0.28
drill pipe	Ø 127.00 mm, 29 kg/m, 114.3 mm IF	524.49
transition pipe	114.3 mm IF (male) × 101.6 mm FH (female)	0.61
drill pipe	Ø 101.60 mm, 22.6 kg/m, 101.6 mm FH	568.83
kelly	hexagonal; thread 88.9 mm IF (male)	8.2

All the pressure drops during drilling at the final depth (1201.15 m) are determined. At the final depth the maxi-

mum pressure drop that the mud pump has to overcome is expected.

In Table 3 the drilling equipment in the borehole is listed. Individual tools are described from the borehole bottom to the top. It means that the drill bit is located at the borehole bottom, followed by sections of stabilizers and drill collars, a transition pipe, drill pipes and a kelly at the borehole surface.

**Table 4.** Calculation input data – borehole construction.

Section	Length (m)	Hole/Casing diameter (m)	Drill String type	Drill String – outer diameter (m)	Drill String – inner diameter (m)
1	525	0.318	drill pipe	0.127	0.109
2	53	0.318	drill pipe	0.102	0.085
3	516	0.311	drill pipe	0.102	0.085
4	97	0.311	drill collar	0.165	0.076

Table 4 represents the input data for calculation of the pressure drops. The borehole is divided into four sections. The first three sections are equipped with drill pipes and the fourth section with drill collars.

**Table 5.** Calculation input data – mud properties.

$\rho$ (kg/m <sup>3</sup> )	1150
$\tau_0$ (Pa)	13
$\mu_{pl}$ (10 <sup>-3</sup> Pa s)	22
$q$ (m <sup>3</sup> /s)	0.0183

For the working pump pressure determination, all the partial pressure drops have to be calculated.

The pressure drop in the surface equipment is estimated to be  $3 \cdot 10^5$  Pa (from Drilling Data Handbook).

The calculation of all the other pressure drops is made relating to the calculation input data, shown in Table 4 and Table 5. Equations for the Bingham rheological model are used.

## 8 RESULTS

The pressure drop in the drill string (drill pipes and drill collars) is  $18.741 \cdot 10^5$  Pa, in the annular space  $3.239 \cdot 10^5$  Pa, in the drill bit  $38.427 \cdot 10^5$  Pa and in the surface equipment  $3 \cdot 10^5$  Pa. The total pressure drop is  $63.4 \cdot 10^5$  Pa. The mud pump has to provide a minimum of  $63.4 \cdot 10^5$  kPa of pressure at a flow rate of  $0.0183$  m<sup>3</sup>/s (1100 l/min).

Fig. 13 shows the dependency of the pressure drop versus the well bore depth and the type of equipment.

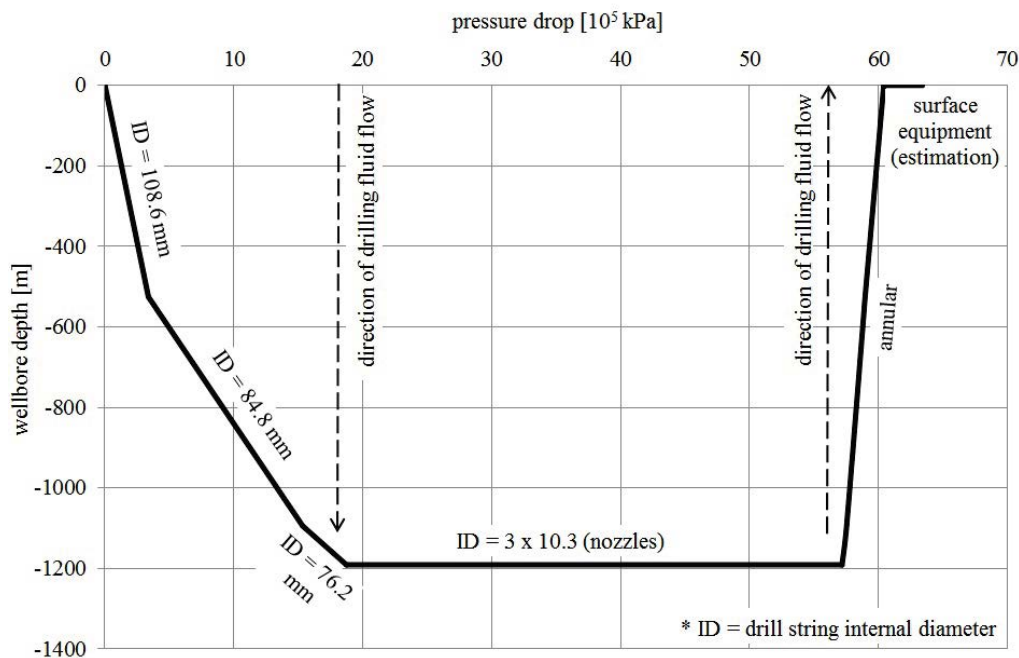


**Figure 13.** Pressure drop versus well bore depth. The direction of the drilling fluid flow follows the black line from the left- to the right-hand side of the diagram.

**Table 6.** Pressure drop in drill pipes and drill collars (mud fluid moves in the downwards direction).

Section	Fluid velocity (m/s)	Critical velocity (m/s)	Fluid flow type	Pressure drop ( $10^5$ Pa)
1	1.978	1.913	turbulent	3.371
2	3.242	1.971	turbulent	1.114
3	3.242	1.971	turbulent	10.844
4	4.019	2.002	turbulent	3.413

**Table 7.** Pressure drop in annular space (mud fluid moves in upwards direction).

Section	Fluid velocity (m/s)	Critical velocity (m/s)	Fluid flow type	Pressure drop ( $10^5$ Pa)
1	0.270	1.686	laminar	1.444
2	0.253	1.670	laminar	0.128
3	0.270	1.676	laminar	1.307
4	0.336	1.731	laminar	0.360

**Table 8.** Pressure drop at drill bit (mud fluid moves in downwards direction).

Nozzle number	Nozzle diameter (mm)	Fluid velocity (m/s)	Pressure drop ( $10^5$ Pa)
1	10.32		
2	10.32	73.113	38.427
3	10.32		

The fluid actual and critical velocities in the drill string are shown in Table 6. It is evident that in all four sections of the borehole, the fluid flow type is turbulent because the actual velocity exceeds the critical velocity. In contrast, actual fluid velocities in the annular space are significantly lower than the critical velocities. Consequently, the fluid flow type is laminar, as shown in Table 7.

The maximum pressure drop occurs in the drill pipes and the drill-bit nozzles. In the shown experimental case, the pressure drop in the drill bit equals 61 % and the pressure drop in the drill pipes equals 29 % of all the pressure drops. Other pressure drops arise in the surface equipment and the annular space. They are negligible.

Fluid-flow type through the drill pipes (drill string and drill collars) and the drill bit nozzles is turbulent. The fluid flow type in the annular space is laminar. Fluid velocities in the drill pipes are in range 1 m/s to 5 m/s, depending on the inner diameter of the drill pipe. The drill bit nozzle output velocity exceeds 70 m/s. The drill

bit pressure drop (61 % of all the pressure drops) is in range of hydraulics optimization and therefore suitable.

## 9 CONCLUSIONS

In this article, deep drilling hydraulics and pressure drops have been studied in order to determine the working pressure of a mud pump. Based on the governing equations of Bingham non-Newtonian fluid flow, a numerical method has been used to calculate all the pressure drops while drilling the final section of the exploratory geothermal borehole Sob-4g, located in Murska Sobota, NE Slovenia.

The results of the numerical analysis shows where the areas of maximum pressure drops in the deep well drilling are to be expected.

The majority of the pressure drop occurs in the drill bit nozzles and the drill pipes. The fluid flow is turbulent in both of these regions. The pressure drops in the annular space and the surface equipment is minimal. They are negligible in comparison with the pressure drops in the pipes and the drill bit.

The contribution of this article can be placed in the wider context of geothermal energy usage development. With the use of the described model for determining the pressure drops in a deep geothermal borehole, it is shown how we can predict the hydraulic state within the borehole during the process of drilling.

## REFERENCES

- [1] Hossain, M. E., Al-Majend, A. A. 2015. Fundamentals of Sustainable Drilling Engineering. Scrivener, Beverly, MA.
- [2] Azar, J. J., Samuel, G. R. 2007. Drilling Engineering. PenWell Corporation, Tulsa, Oklahoma.
- [3] Ford, J. (2005). Drilling Engineering. Heriot Watt University, Department of Petroleum Engineering, Edinburgh.
- [4] Bourgoyne, A. T. J., Millheim, K. T., Chenevert, M. E., Young, F. S. J. 1991. Applied Drilling Engineering. Society of Petroleum Engineering, Richardson.
- [5] Gabolde, G., Nguyen, J. P. 1999. Drilling data handbook. Technip, Paris.
- [6] Stropnik, J. 1999. Hidromehanika. Tehniška založba Slovenije, Ljubljana.
- [7] Ma, D., Li, G., Huang, Z., Niu, J., Hou, C., Liu, M., Li, J. 2012. A model of calculating the circulating pressure loss in coiled tubing ultra-short radius radial drilling. Petroleum exploration and develop-

- ment 39(4), 528-533.
- [8] Boyun, G., Gefei, L. 2011. Applied Drilling Circulation Systems. Gulf Professional Publishing, Houston, Texas.
  - [9] Vukelić, Ž., Kraljič, M., Dervarič, E. 2013. Lendava – the first geothermal city in Slovenia. 5<sup>th</sup> Balkan Mining Congress Proceedings, Ohrid, pp. 422-430.
  - [10] Rajver, D., Rman, N., Lapanje, A. 2016. The state of exploitation of geothermal energy and some interesting achievements in geothermal research and development in the world. *Geologija* 59(1), 99-114.
  - [11] Souvent, P., Vižintin, G., Celarc, S., Čenčur Curk, B. 2014. An expert system as a support to the decision making process for groundwater management of alluvial groundwater bodies in Slovenia. *Geologija* 57(2), 245-252.

# AN EXTENDED BEARING-CAPACITY EQUATION FOR SHALLOW FOUNDATIONS ON GRANULAR TRENCHES IN SOFT SOIL

# RAZŠIRJENA ENAČBA NOSILNOSTI TEMELJNIH TAL POD PLITVIMI TEMELJI NA GROBOZRNATIH ZASEKIH V MEHKIH TLEH

**Jose Alejandro Duque Felfle** (corresponding author)

University del Norte,  
Department of Civil and Environmental Engineering  
Km.5 Vía Puerto, Barranquilla, Colombia  
E-mail: jfelfle@uninorte.edu.co

**Carlos José Lascarro Estrada**

University del Norte,  
Department of Civil and Environmental Engineering  
Km.5 Vía Puerto, Barranquilla, Colombia  
E-mail: cjascarro@uninorte.edu.co

**Melany Gil Rueda**

University del Norte,  
Department of Civil and Environmental Engineering  
Km.5 Vía Puerto, Barranquilla, Colombia  
E-mail: gmelany@uninorte.edu.co

**Oscar Fernando García Guardo**

University del Norte,  
Department of Civil and Environmental Engineering  
Km.5 Vía Puerto, Barranquilla, Colombia  
E-mail: oguard@uninorte.edu.co

**William Mario Fuentes Lacouture**

University del Norte,  
Department of Civil and Environmental Engineering  
Km.5 Vía Puerto, Barranquilla, Colombia  
E-mail: fuentesw@uninorte.edu.co

**DOI** <https://doi.org/10.18690/actageotechslov.17.1.12-22.2020>

## Keywords

granular trenches, bearing capacity, Extended Drucker-Prager model, footings

## Ključne besede

grobozrnati zrnati zaseki, nosilnost, Drucker-Pragerjev razširjeni model, temeljenje

## Abstract

*In this article a method to estimate the bearing capacity of a shallow foundation on a granular trench in soft soil is proposed. The method is based on the interpolation of two equations: the first describing the bearing capacity of the shallow foundation on a homogeneous soft soil, and the second, on an infinitely wide layer of compacted granular fill above the soft soil. The proposed relationship was calibrated using finite-element (FE) simulations. A constitutive model for the soil, accounting for a pressure-dependent elasticity and an extended Drucker-Prager yield criterion, was considered. An analysis of the results showed that the proposed relationship gives more accurate estimations of the bearing capacity than those delivered by the conventional average-parameters method. The comparison was conducted for different dimensions of the granular trench. Finally, the relationship was used to predict the bearing capacity of a physical model test.*

## Izvleček

*V članku je predlagana metoda za oceno nosilnosti temeljnih tal pod plitvemu temeljem na grobozrnatem zaseku v mehkih tleh. Metoda temelji na interpolaciji dveh enačb: prva opisuje nosilnost temeljnih tal pod plitvim temeljem na homogeni mehki zemljini, druga pa na neskončno širokem sloju zgoščenega zrnatega nasipa ležečega na mehki zemljini. Predlagani odnos je bil umerjen s simulacijami z uporabo metode končnih elementov. Uporabljen je bil konstitutivni model tal, ki upošteva elastičnost kot funkcijo tlačnih napetosti in razširjeni Drucker-Pragerjev kriterij tečenja. Analiza rezultatov je pokazala, da predlagani odnos daje natančnejše ocene nosilnosti od tistih, ki jih daje običajna metoda povprečnih parametrov. Primerjava je bila izvedena za različne dimenzije grobozrnatega zaseka. Na koncu je bil odnos uporabljen za napovedovanje nosilnosti fizičnega modela preizkusa.*

## 1 INTRODUCTION

---

An estimation of the bearing capacity is important for the design of shallow foundations. The first bearing capacity model was proposed by [1], and has been subjected to further enhancements in [2, 3, 4] and others. These methods consider a slip surface geometry developed for homogeneous soils, e.g., [1, 5, 6], which limits their application in layered soil profiles. This is disappointing, as in geotechnical engineering it is common to work with shallow foundations on stratified soils.

In addition, many soft soils do not guarantee the required bearing capacity to withstand the design loads. Some methods to improve the mechanical characteristics of such soils have been proposed, such as soil-cement mixing [7], soil-lime mixing [8], gravel and stone columns [9, 10, 11, 12, 13], granular trenches [14, 15, 16, 17, 18, 19] among many others. Numerical investigations of these alternatives have also been reported [20, 21, 22, 23]. In particular, granular trenches is one of the most used methods due to its low cost, the availability of the granular fills and the simplicity of its construction. This is undoubtedly one of the most employed methods in regions where the required technology for other alternatives is not available.

A granular trench in a soft soil consists of a bed of competent material beneath the footing that improves the bearing capacity of the system. Engineers often employ compacted fill materials, classified as SW-SP, SW-SC, SP and SC according to the USCS, or as A-1 and A-2 according to the AASHTO. The geometry of the trench, i.e., its thickness and width, are carefully designed in order to obtain the required bearing capacity. This is not a simple task, as conventional methods for estimating the bearing capacity assume a homogeneous soil. As an alternative, engineers can compute the “average (geomechanical) parameters” to be used in conventional methods for bearing capacity, following the recommendations of some authors [24]. However, this method is debatable, since the slip-surface geometry should depend on the granular trench dimensions as well. Moreover, sophisticated methods for estimating the bearing capacity considering the geometry of the granular trench have been proposed by other authors, [17, 19, 25, 26, 27]. These methods are also limited by some assumptions, such as equal unit weights for both materials, saturation conditions, among others. It seems that further research is still required to provide methods for estimating the bearing capacity of the shallow foundations supported on granular trenches in soft soils.

In this work a simple relationship to estimate the bearing capacity of a foundation supported on a granular trench

is proposed. For this purpose a set of finite-element models of a strip foundation was constructed. A constitutive model for soils, considering a pressure-dependent elasticity and an extended Drucker-Prager criterion, was considered. Different geometries of the granular trench were simulated, and the results were carefully analyzed. Consequently, a bearing-capacity relationship is proposed based on the interpolation between the bearing capacity of a foundation on a homogeneous soft soil (without a granular trench), and the one on an infinitely wide granular trench above the soft soil. The relationship gives accurate estimations compared to those of conventional methods with average parameters. Additionally, the results of a physical test reported by [28] are compared with the estimations of the proposed relationship. Finally, some conclusions are drawn.

The notation of the article is as follows: scalar quantities are denoted with italic fonts (e.g.,  $a$ ,  $b$ ), vectors with bold italic fonts (e.g.,  $\mathbf{a}$ ,  $\mathbf{b}$ ), second rank-tensors with bold fonts (e.g.,  $\mathbf{A}$ ,  $\boldsymbol{\sigma}$ ), and fourth-rank tensors with special fonts (e.g.,  $\mathbf{E}$ ,  $\mathbf{L}$ ). Tensors represented with the indicial notation are denoted with italic symbols and their respective lower indices (e.g.,  $A_{ij}$ ,  $\sigma_{ij}$ ). Multiplication by two dummy indices, also known as double contraction, is denoted with a colon “:” (e.g.  $\mathbf{A}:\mathbf{B} = A_{ij}B_{ij}$ ). When the symbol is omitted, it is understood to be a dyadic product (e.g.,  $\mathbf{AB} = A_{ij}B_{kl}$ ). The mean stress is defined as  $p = 1/3\sigma_{ii}$  and the deviator stress as  $q = \sqrt{3/2} \|\boldsymbol{\sigma}^{dev}\|$ , where  $\boldsymbol{\sigma}^{dev} = \boldsymbol{\sigma} - 1/3p\mathbf{1}$  is the deviator stress tensor, and  $\mathbf{1}$  is the Kronecker delta tensor.

## 2 BRIEF DESCRIPTION OF THE FINITE-ELEMENT (FE) MODELS

---

In this section a brief description of the finite-element (FE) models is given. The models simulate a strip footing on a granular trench surrounded by a soft soil. For the sake of generality, a soft soil is here considered as either a very loose sand or a normally consolidated clay, both of which are cohesionless  $c = 0$ . Different geometries of the granular trench were considered to construct the FE models. Figure 1 presents an illustrative scheme of the problem to solve. The width of the footing is fixed at  $B = 2$  m and the embedment depth at  $D_f = 1$  m. The commercial software ABAQUS Standard V6.16 [29] was employed to build and solve the problem. The mechanical behavior of the soil was simulated through an elastoplastic model, with a pressure-dependent elastic stiffness and a yield surface according to an extended Drucker Prager criterion that accounts for the Lode’s angle dependence. In the following sections the Boundary Value Problem is described, and the obtained results are discussed.

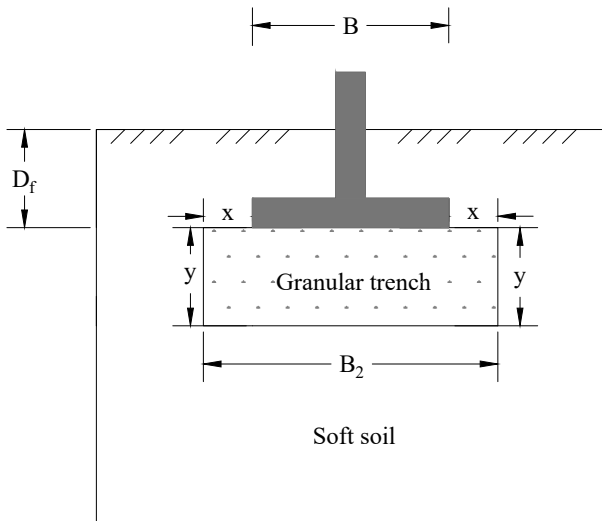


**Figure 1.** Sketch of the problem to solve. Values of  $B = 2$  m and  $D_f = 1$  m are fixed. Different values of  $B_2$  and  $y$  are considered.

### 2.1 Geometry, mesh and boundary conditions

The numerical model assumed plane-strain conditions and considered dry soil under a static analysis. Therefore, its solution is based on the linear momentum equation neglecting the inertial terms, see Equation (1):

$$\frac{\partial}{\partial x} (\sigma_{ij}) + \rho g_i = 0 \quad (1)$$

where  $\sigma_{ij}$  is the effective stress,  $\rho$  is the mass density and  $g_i$  is the gravity vector. Figure 2 presents the geometry and mesh of the Boundary Value Problem (BVP). Advantage was taken of the symmetry, and only one-half of the problem was simulated. The geometry was 20 m high and 30 m wide. Previous analyses showed that these dimensions avoid a boundary-dependent solution to the problem. The mesh was refined in the vicinity of the footing to achieve mesh convergence, see Figure 2. Horizontal displacements were restrained at the lateral boundaries, while vertical and horizontal displacements were restrained at the bottom boundary, see Figure 3. In order to simulate different geometries of the granular trench, some mesh partitions were introduced, as shown in Figure 3. This allowed the finite elements to be grouped according to their materials, as shown in Figure 4. In total, three materials were simulated, i.e., the concrete of the footing, the granular trench, and the soft soil, see Figure 4. The concrete was simulated with a linear elastic model, while the soil was simulated with the extended Drucker-Prager model.

### 2.2 Initial conditions and steps of analysis

Initial geostatic stresses were defined assuming oedometric conditions. The initial vertical stresses  $\sigma_v$  were

computed by considering the densities of the materials, see Table 1. A lateral earth coefficient  $K_0$  was calculated for each material to determine the horizontal stresses  $\sigma_h = K_0 \sigma_v$ . The relationship proposed by Jaky  $K_0 = 1 - \sin \varphi'$  was used for this purpose, where  $\varphi'$  is the friction angle presented in Table 1. Considering this initial state, a geostatic step was taken to solve Equation (1). The generated displacements were reset to zero before proceeding with the loading of the footing, which was executed during the next step of the analysis. The footing load was introduced as a vertical displacement at the top boundary of the footing. The load was considered as a displacement boundary condition and not as an external load, to avoid numerical problems related to instability issues, i.e., a loss of controllability in the constitutive model [30]. The displacement was gradually increased until reaching failure. During this process, the vertical reaction force on the top of the footing was measured. For this work, the maximum vertical reaction force

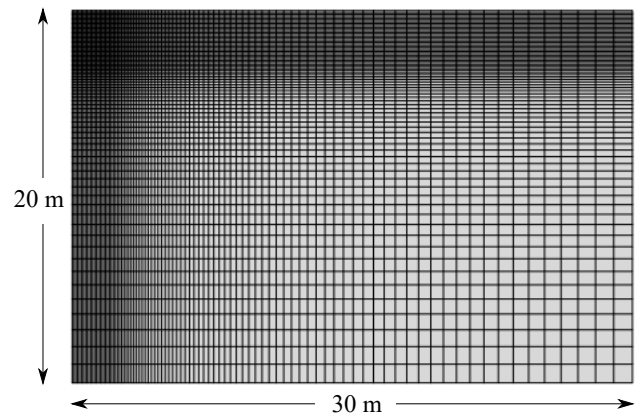


**Figure 2.** Geometry of the Boundary Value Problem (BVP).

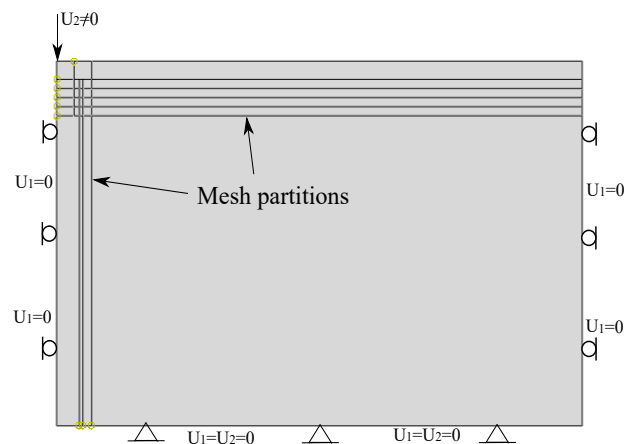


**Figure 3.** Boundary conditions and internal mesh partitions.

divided by the width of the footing is understood as the ultimate bearing capacity  $q_u$ . This method is similar to those recommended by professional software packages for geotechnical numerical modeling [31, 32].

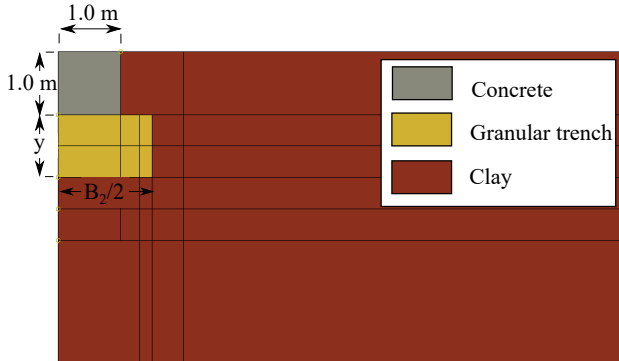


Figure 4. Geometry of the materials.

### 2.3 Description of the elastoplastic model for the soils

An elastoplastic constitutive model was used to simulate the mechanical behavior of the granular fill material and the soft soil. The constitutive model aims to describe the behavior of the effective stresses. The general equation of the constitutive model is presented in Equation (2):

$$\dot{\sigma} = E: (\dot{\epsilon} - \dot{\epsilon}^p) \quad (2)$$

where  $\dot{\sigma}$  is the stress rate,  $\dot{\epsilon}$  is the strain rate,  $\dot{\epsilon}^p$  is the plastic strain rate and  $E$  is the elastic stiffness (fourth-rank) tensor. For the elastic stiffness, modified Cam-Clay relationships were adopted. The elastic stiffness is isotropic and was computed using the relationship  $E = K\mathbf{1}\mathbf{1} + 2G(\mathbf{I} - \mathbf{1}\mathbf{1})$ , where  $\mathbf{1}$  corresponds to the Kronecker delta tensor,  $\mathbf{I}$  is the fourth-order tensor for symmetric tensors,  $K$  is the bulk modulus, see Equation (3), and  $G$

is the shear modulus, see Equation (4). Accordingly, the latter factors read [33]:

$$K = \frac{(1 + e_o)}{\kappa} p' \quad (3)$$

$$G = \frac{3(1 - 2\nu)}{2(1 + \nu)} K \quad (4)$$

where  $\nu$  is the Poisson ratio,  $\kappa$  is the swelling index, both considered as material parameters,  $p'$  is the mean effective stress and  $e_o$  is the initial void ratio. The plastic strain rate  $\dot{\epsilon}^p$  is computed by considering an extended Drucker-Prager yield surface function  $F$ , Equation (5), defined as:

$$F = t - p \tan \beta - d = 0 \quad (5)$$

where  $t$  is a transformed deviator stress that accounts for the Lodes angle  $\theta$  dependence, defined in the sequel, and  $\beta$  and  $d$  correspond to the modified friction angle and the modified cohesion defined in the space of  $t$  vs.  $p$ , respectively, see Equations (6) and (7). The parameters  $\beta$  and  $d$  are related to the classic Mohr-coulomb parameters  $\varphi$  and  $c$ , the latter are defined in the shear stress  $\tau$  vs. normal stress  $\sigma$  space, through the relationships [33]:

$$\tan \beta = \frac{3\sqrt{3} \tan \varphi}{\sqrt{(9 + 12 \tan^2 \varphi)}} \quad (6)$$

$$d = \frac{3\sqrt{c}}{\sqrt{(9 + 12 \tan^2 \varphi)}} \quad (7)$$

The transformed deviator stress  $t$  is defined in Equation (8) [29, 34]:

$$t = \frac{1}{2} q \left( 1 + \frac{1}{K} - \left( 1 - \frac{1}{K} \right) \left( \frac{r}{q} \right)^3 \right) \quad (8)$$

where  $r$  is the third stress invariant,  $q$  is the deviator stress and  $K = M_e / M_c$  corresponds to the ratio between the slope of the yield surface for the triaxial extension  $M_e$  and the triaxial compression  $M_c$ , see Figure 5.

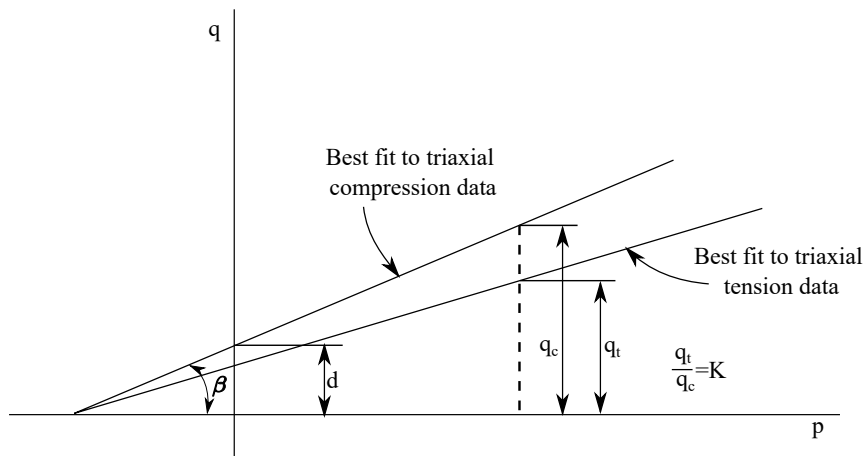


Figure 5. Extended Drucker Prager yield surface in the  $q$  vs.  $p$  space for triaxial compression and extension. Source: [29].

Having the yield surface defined, the plastic strain rate  $\dot{\epsilon}^p = \lambda \mathbf{m}$  is computed with the consistency parameter  $\dot{\lambda}$  and considering an associated flow rule  $\mathbf{m} = dF/d\boldsymbol{\sigma}$ . Assuming a perfectly plastic material, no hardening should be experienced by the yield surface. Details of the deductions and other properties of classic and advanced elastoplastic models can be found in [29, 33, 35, 36, 37].

The model requires the calibration of four parameters that are commonly used in geotechnical practice, i.e., the swelling index  $\kappa$ , the Poisson ratio  $\nu$ , the friction angle  $\varphi$  and the cohesion  $c$ . While the first pair of parameters defines the elastic stiffness, the second controls the failure conditions. Their values were selected according to reported typical ranges [24, 38, 39] and considering some experimental results of these types of materials [40]. Table 1 presents the values of the adopted parameters for the simulations under the consideration of the aforementioned statements. Note that in this work the parameters controlling the failure conditions correspond to the effective friction angle  $\varphi'$  and the effective cohesion  $c'$ . The results of the numerical model are explained in the next subsection.

**Table 1.** Material parameters of the constitutive models.

Description		Unit	Value
<b>Concrete (linear elastic model)</b>			
Elastic model			
$E$	Young's modulus	[MPa]	20000
$\nu$	Poisson's ratio	[-]	0.24
$\rho$	Mass density	[kg/m <sup>3</sup> ]	2400
<b>Granular fill (extended Drucker-Prager model)</b>			
Elastic stiffness (pressure dependent)			
$\kappa$	Swelling index	[-]	0.003
$\nu$	Poisson's ratio	[-]	0.3
Plasticity			
$\varphi'$	Friction angle	[°]	35
$c'$	Cohesion	[kPa]	0
Additional parameter			
$\rho$	Mass Density	[kg/m <sup>3</sup> ]	2000
<b>Soft soil (extended Drucker-Prager model)</b>			
Elastic stiffness (pressure dependent)			
$\kappa$	Swelling index	[-]	0.02
$\nu$	Poisson's ratio	[-]	0.3
Plasticity			
$\varphi'$	Friction angle	[°]	20
$c'$	Cohesion	[kPa]	0
Additional parameter			
$\rho$	Mass Density	[kg/m <sup>3</sup> ]	1700

## 2.4 Results of the numerical model

In total, 16 numerical models were built, each one with a different geometry of the granular trench. Combinations of different widths  $B_2 = \{0, 2, 2.6, 3, 4, \infty\}$ , depths  $y = \{0, 1, 1.5, 2\}$  and outer widths of the granular trench beyond the footing  $X = (B_2 - B)/2$  were considered, see Figure 1. Table 2 presents the resulting bearing capacity  $q_u$  of the simulations.

**Table 2.** Results of the numerical models with finite elements.

$B[m]$	$y[m]$	$B_2[m]$	$X[m]$	$q_u[kPa]$
2	0.0	(homogenous case)		320
2	1.0	2.0	0.0	420
2	1.0	2.6	0.3	440
2	1.0	3.0	0.5	444
2	1.0	4.0	1.0	446
2	1.0	$\infty$	14.0	520
2	1.5	2.0	0.0	470
2	1.5	2.6	0.3	500
2	1.5	3.0	0.5	506
2	1.5	4.0	1.0	510
2	1.5	$\infty$	14.0	620
2	2.0	2.0	0.0	500
2	2.0	2.6	0.3	540
2	2.0	3.0	0.5	560
2	2.0	4.0	1.0	584
2	2.0	$\infty$	14.0	760

## 3 CALIBRATION OF THE EQUATION FOR BEARING CAPACITY

In this section a new relationship to estimate the bearing capacity  $q_u$  of shallow foundations on granular trenches in soft soils is proposed. The proposed relationship makes use of the following variables:

- $q_{u1}$ : Bearing capacity of the footing on a homogeneous soft soil, see Figure 6(a). This case does not consider the existence of a granular trench.
- $q_{u2}$ : Bearing capacity of the footing on an infinitely wide granular trench with thickness  $y$ , see Figure 6(b), above the soft soil.

The proposed relationship is based on the following function:

$$q_u = f \cdot q_{u1} \quad (9)$$

where  $f$  is an interpolation function that is proposed to meet the following requirements: for the case of a homogenous soil (Figure 6(a)), function  $f$  renders  $f = 1$ . For an infinitely wide granular fill (Figure 6(b)), function  $f$  gives  $f = \alpha$ , where  $\alpha$  is defined as:

$$\alpha = \frac{q_{u2}}{q_{u1}} \quad (10)$$

For intermediate cases, function  $f$  delivers a value within the range  $1 < f < \alpha$ , see Equation (11). A suitable interpolation function able to match the aforementioned requirements is:

$$f = 1 + (1 - e^{-c_1 \frac{B_2}{B}})(\alpha - 1) \quad (11)$$

where  $c_1$  is an interpolation parameter. Notice that the ratio  $B_2/B$  is used as the interpolation variable. In the following lines, the proposed relationship (Equation (9)–(11)) is statistically adjusted to the results of the FE simulations.

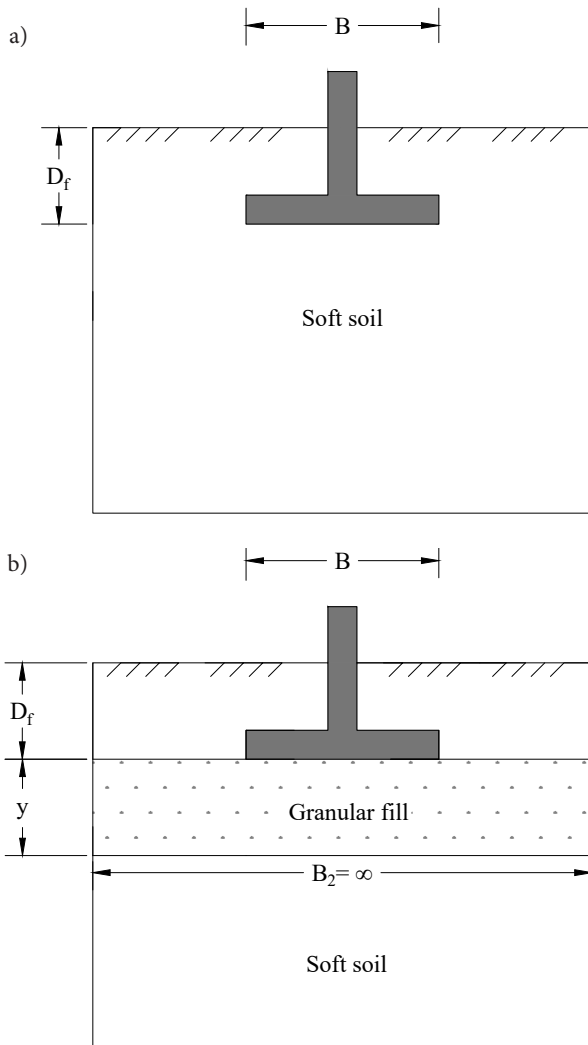


Figure 6. a) Geometry for the determination of  $q_{u1}$   
 b) Geometry for the determination of  $q_{u2}$ .

The results of the FE simulations are compiled in Table 2. For the case of a homogenous soil, the bearing capacity gives  $q_{u1} = 320$  kPa. For the case of an infinitely wide granular fill ( $B_2 = \infty$ ), the bearing capacity  $q_u = q_{u2}$  is found for each particular thickness  $y = \{1 \text{ m}, 1.5 \text{ m}, 2 \text{ m}\}$ , see Figure 6(b). For other values of  $B_2$ , intermediate values of  $q_{u1} < q_u < q_{u2}$  are obtained. The task is to find a parameter  $c_1$  that provides the best fit to the simulation results. To achieve this, the sum of the squared residuals is minimized as follows: for each data point, the residual value  $e_i$  is computed as shown in Equation (12).

$$e_i = q_{ui-proposed} - q_{ui-FEM} \quad (12)$$

where  $q_{ui-proposed}$  is the estimated bearing capacity according to the proposed relationship, and  $q_{ui-FEM}$  is the one resulting from the numerical model. The sum of the squared residuals is computed as  $S = \sum e_i^2$ . The selected parameter  $c_1$  is the one that gives the minimum value for  $S$ . Using this methodology, a different value of  $c_1$  was adjusted for each thickness  $y$  and a “general” value of  $c_1$  was obtained for all the simulations. The results are presented in Table 3. According to this set of data, the “general” value is  $c_1 = 0.552$ . Replacing the value of  $c_1$  in Equation (11), Equation (13) is recommended as the interpolation function:

$$f = 1 + (1 - e^{-0.552 \frac{B_2}{B}})(\alpha - 1) \quad (13)$$

Note that the proposed equation has been statistically adjusted. According to the results, the values for the coefficient of determination  $R^2$  are always greater than  $R^2 > 0.93$  when adjusting the function  $f$  to each particular thickness  $y$ . When the function  $f$  is adjusted for all the simulation results ( $c_1 = 0.552$ ), the values of  $R^2$  are greater than  $R^2 > 0.88$ . Table 3 provides the specific values of  $c_1$  and  $R^2$  for the evaluated cases.

Table 3. Values of the parameter  $c_1$  and the corresponding  $R^2$ .

		$y = 1 \text{ m}$	$y = 1.5 \text{ m}$	$y = 2 \text{ m}$
Adjusted to each thickness $y$	$c_1$	0.626	0.628	0.508
	$R^2$	0.99	0.93	0.93
Adjusted for all simulations	$c_1$	0.552	0.552	0.552
	$R^2$	0.97	0.88	0.88

The proposed relationship and the simulation results are plotted in Figures 7 to 10. As shown, a value of approximately  $q_u \approx q_{u2}$  is obtained for  $B_2/B > 6$ . This conclusion holds in all cases, independently of its thickness  $y$ . The bearing capacities  $q_u$ , estimated using the interpolation constant  $c_1 = 0.552$ , are shown in Figures 9 and 10. The results show a satisfactory agreement, with some small discrepancies.

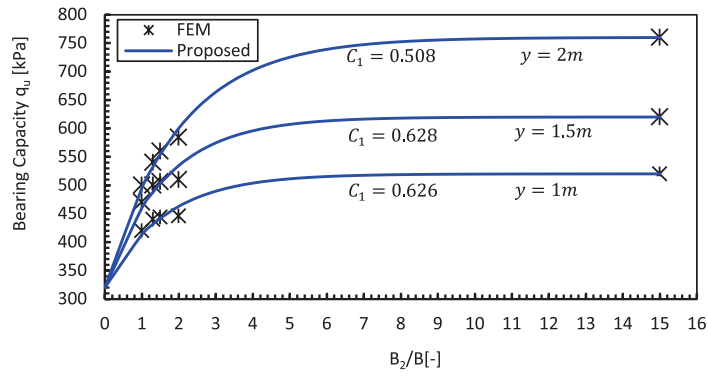


Figure 7. Numerical models and proposed relationship. Adjustment with different  $c_1$  for each thickness  $y$ .

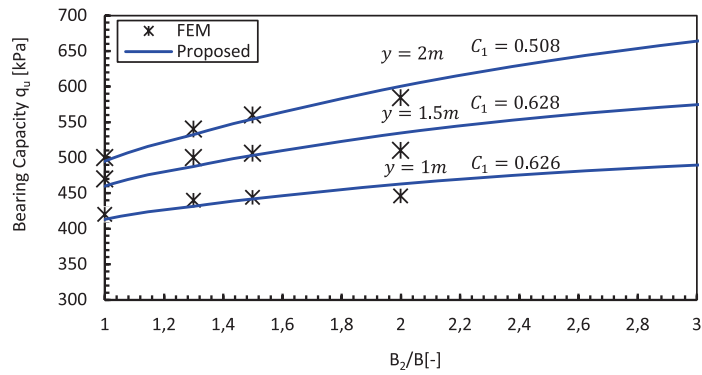


Figure 8. Numerical models and proposed relationship. Adjustment with different  $c_1$  for each thickness  $y$ .

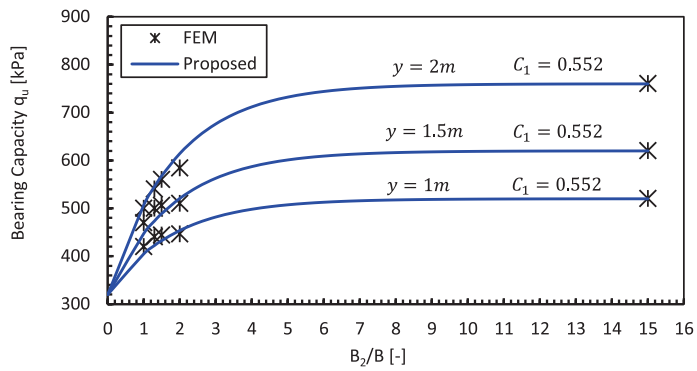


Figure 9. Numerical models and proposed relationship. Adjustment with  $c_1 = 0.552$  for all cases.

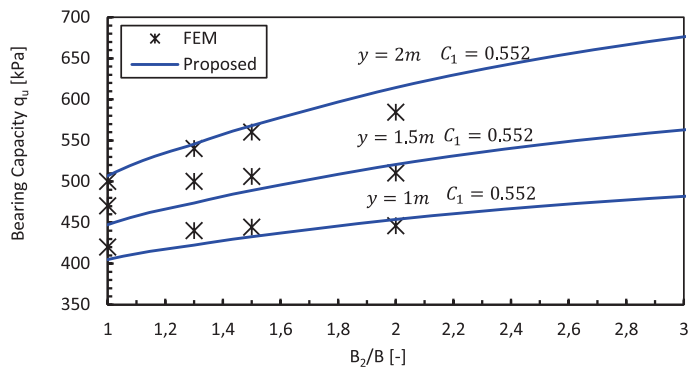
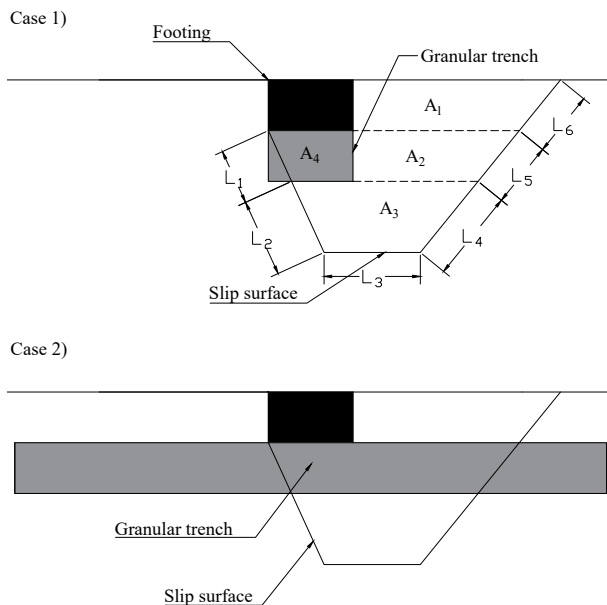


Figure 10. Numerical models and proposed relationship. Adjustment with  $c_1 = 0.552$  for all cases.

#### 4 COMPARISON OF THE PROPOSED RELATIONSHIP WITH THE AVERAGE-PARAMETERS METHOD (APM)

This section presents a comparison between the performance of the proposed relationship and the conventional average parameters method (APMs). The latter has been widely used by engineers, and is offered by various geotechnical software packages, e.g., [41]. According to this method, a stratified soil profile is analyzed as a homogeneous profile with “average (geomechanical) parameters”, which allows the direct computation of the bearing capacity with conventional methods. The calculation of the average parameters requires the definition of a slip surface. A schematic example of such a surface is shown in Figure 11 for two cases: the first case considers a granular fill of the same width as the footing  $B = B_2$ , and the second case considers a much wider granular fill. The average friction angle  $\varphi$ , the average cohesion  $c$  and the average unit weight  $\gamma$  are computed as shown in Equations (14), (15) and (16), respectively, for case 1 and in Equations (17), (18) and (19), respectively, for case 2.



**Figure 11.** Sketch of a slip surface through a soft soil with granular trenches of different widths. A slip surface with constant geometry is assumed.

For case 1 (see Figure 11):

$$\varphi = \frac{\varphi_1(L_1) + \varphi_2(L_2 + L_3 + L_4 + L_5 + L_6)}{\sum_{i=1}^n L_i} \quad (14)$$

$$c = \frac{c_1(L_1) + c_2(L_2 + L_3 + L_4 + L_5 + L_6)}{\sum_{i=1}^n L_i} \quad (15)$$

$$\gamma = \frac{\gamma_1 A_4 + \gamma_2(A_1 + A_2 + A_3)}{\sum_{i=1}^n A_i} \quad (16)$$

For case 2 (see Figure 11):

$$\varphi = \frac{\varphi_1(L_1 + L_5) + \varphi_2(L_2 + L_3 + L_4 + L_6)}{\sum_{i=1}^n L_i} \quad (17)$$

$$c = \frac{c_1(L_1 + L_5) + c_2(L_2 + L_3 + L_4 + L_6)}{\sum_{i=1}^n L_i} \quad (18)$$

$$\gamma = \frac{\gamma_1(A_4 + A_2) + \gamma_2(A_1 + A_3)}{\sum_{i=1}^n A_i} \quad (19)$$

where  $\varphi_1$ ,  $c_1$  and  $\gamma_1$  are the parameters of the granular trench and  $\varphi_2$ ,  $c_2$  and  $\gamma_2$  are the parameters of the soft soil.

Now, the comparison between the proposed relationship and the average-parameters method is performed. For this purpose, the same problem shown in Figure 1 is considered. The bearing capacities of the foundation supported by granular trenches with different geometries are estimated with the proposed relationship and the average parameter method. In particular, the resulting values for  $q_{u1}$  and  $q_{u2}$  for a granular fill layer with thickness  $y = \{1, 1.5, 2\}$  are given in Table 4. The bearing capacities estimated with each method are plotted in Figure 12 and show a large discrepancy between them, especially in the range  $1 < B_2/B < 4$ . In this range the proposed relationship approaches asymptotically a value of  $q_u \approx q_{u2}$ , while the average parameter method delivers a constant lower value. The resulting behavior of the average-parameter method can be explained as follows: within the range of  $B_2/B \leq 1$ , the behavior is similar to case 1 in Figure 11, in which the average parameters result from the intersection of the slip surface with the granular fill at its left boundary and the soft soil. For higher values of  $B_2 > B$ , the portion of the slip surface intersecting the granular fill remains constant, and therefore no increase in the average parameters is experienced. Finally, when the granular fill is sufficiently wide, the slip surface intersects it at its right boundary, as depicted in case 2 in Figure 11. In reality, the shape of the slip surface depends on the geometry of the granular trench, and therefore the results given by the average-parameters method are unrealistic. Hence, special care must be taken when considering this method for design purposes.

**Table 4.** Bearing capacities  $q_u$  for different thickness  $y$ .

$y$ [m]	$q_{u1}$ [kPa]	$q_{u2}$ [kPa]	$\alpha = q_{u2} / q_{u1}$ [-]
1.0	211.70	345.65	1.63
1.5	211.70	426.34	2.01
2.0	211.70	533.80	2.52

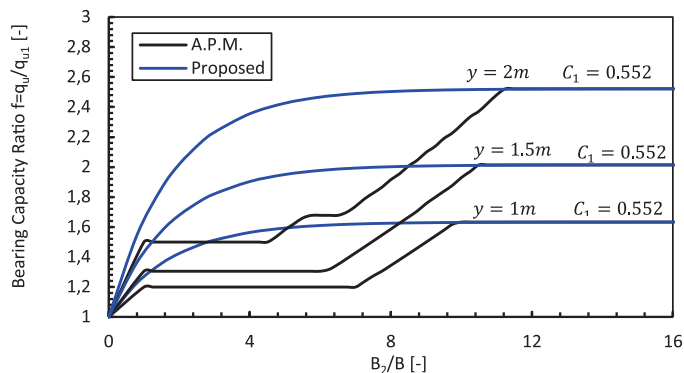


Figure 12. Estimation of the bearing capacity according to the proposed relationship and average-parameter method (APM).

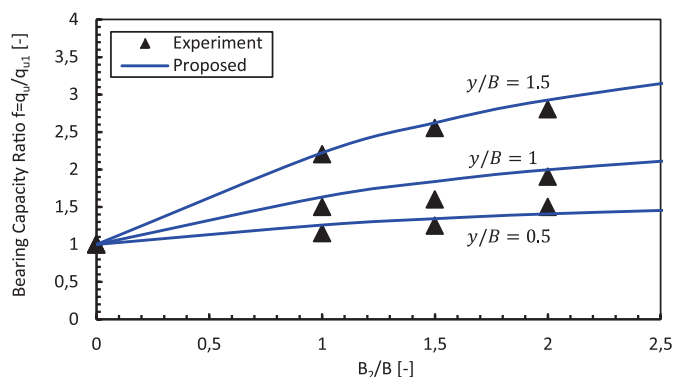


Figure 13. Proposed relationship compared to results reported by [28] for a scaled foundation test.

## 5 COMPARISON WITH A SCALED FOUNDATION TEST

The performance of the proposed relationship is now evaluated on a scaled foundation test reported by [28]. The reported values of  $q_{u1}$  and  $q_{u2}$  by [28] were used in Equation (13). The trend of  $f = q_u/q_{u1}$  is analyzed for different trench geometries. In the mentioned work, a ring-type foundation with an outer diameter of 200 mm and an inner diameter of 76.2 mm was placed and loaded on a soft soil reinforced with a granular trench. Details of the test set up can be found in [28]. The results of the proposed relationship and the scaled test are shown in Figure 13, in which three different ratios of  $y/B = \{0.5, 1, 1.5\}$  are included. The results show that the proposed relationship provides accurate estimations, although the shallow foundation geometry is very different than those analyzed in the previous sections of this study.

## 6 FINAL REMARKS AND LIMITATIONS

In the present study a method to estimate the bearing capacity of footings on soft soils improved with granular trenches was proposed. The proposed relationship interpolates between two bearing capacities, the one of a footing on a homogeneous soft soil  $q_{u1}$ , see Figure 6(a), and the one of a soft soil improved with an infinitely wide granular trench  $q_{u2}$ , see Figure 6(b). The function was calibrated to match a set of numerical analyses with finite elements, where a constitutive model able to reproduce the monotonic behavior of soils was used. The results indicated that the proposed relationship fits the numerical results. A comparison of the proposed relationship with the conventional average-parameter method evidenced the weak performance of the latter method. An inspection on the average-parameter method suggested that it delivers an underestimation of the bearing capacity within the range  $1 < B_2/B < 4$  because it is based on a slip-surface geometry for homogeneous soil. Subsequently, the proposed relationship was evaluated on a scaled-foundation test [28] with a different geometry than the one used to calibrate the equation. Only the

trend of  $f = q_u/q_{u1}$  was evaluated and showed satisfactory results. At the moment, additional research is being carried to validate the applicability of this relationship on a wider range of problems, such as trenches with larger thickness, different shallow foundation geometries and different types of soft soils.

## Acknowledgment

The authors appreciate the financial support given by COLCIENCIAS for the project with code 1215748-59323 from the convocation 748-2016.

## REFERENCES

- [1] Terzaghi, K. 1943. *Theoretical Soil Mechanics*, 6<sup>th</sup> edition, New York: John Wiley & Sons.
- [2] Hansen, B. 1961. A general formula for bearing capacity. *The Danish geotechnical institute* 11(1), 38-46.
- [3] Meyerhof, G. 1963. Some recent research of the bearing capacity of foundations. *Canadian Geotechnical Journal* 1(1), 16-26. DOI: <https://doi.org/10.1139/t63-003>
- [4] Vesic, A. Analysis of ultimate loads of shallow foundations. *Journal of the Soil Mechanics and Foundations Division* 99(1), 45-73.
- [5] Prandtl, L. 1920. Über die Härte plastischer Körper. *Nachrichten von der Gesellschaft der Wissenschaften zu Göttingen* 13(1), 74-85.
- [6] Reissner, H. 1926. Zum Erddruckproblem. *Proceedings of the 1<sup>st</sup> International Congress for Applied Mechanics*, Delft, pp. 295-311.
- [7] Farouk, A., Shahien, M. 2013. Ground improvement using soil-cement columns: Experimental investigation. *Alexandria Engineering Journal* 52(4), 733-740. DOI: <https://doi.org/10.1016/j.aej.2013.08.009>
- [8] Broms, B. 1991. *Stabilization of Soil with Lime Columns*. *Foundation Engineering Handbook*, New York, Van Nostrand Reinhold, pp. 833-855.
- [9] Andreou, P., Frikha, W., Frank, R., Canou, J., Papadopoulos, V., Dupla, J. 2008. Experimental study on sand and gravel columns in clay. *Journal of Ground Improvement* 161(4), 189-198. DOI: <https://doi.org/10.1680/grim.2008.161.4.189>
- [10] Fattah, M., Zabar, B., Hassan, H. 2016. Experimental Analysis of Embankment on Ordinary and Encased Stone Columns. *International Journal of Geomechanics* 16(4). DOI: [https://doi.org/10.1061/\(ASCE\)GM.1943-5622.0000579](https://doi.org/10.1061/(ASCE)GM.1943-5622.0000579)
- [11] Fattah, M., Zabar, B., Hassan, H. 2015. Soil arching analysis in embankments on soft clays reinforced by stone columns. *Structural Engineering and Mechanics* 56(4), 507-534. DOI: <https://doi.org/10.12989/sem.2015.56.4.507>
- [12] Fattah, M., Shlash, K., Al-Waily, M. 2013. Experimental evaluation of stress concentration ratio of model stone columns strengthened by additives. *International Journal of Physical Modelling in Geotechnics* 13(3), 79-98. DOI: <https://doi.org/10.1680/ijpmsg.12.00006>
- [13] Fattah, M., Shlash, K., Al-Waily, M. 2011. Stress Concentration Ratio of Model Stone Columns in Soft Clays. *Geotechnical Testing Journal* 34(1), 50-60. DOI: <https://doi.org/10.1520/GTJ103060>
- [14] Meyerhof, G. 1974. Ultimate Bearing Capacity of Footings on Sand Layer Overlying Clay. *Canadian Geotechnical Journal* 11(2), 223-229. DOI: <https://doi.org/10.1139/t74-018>
- [15] Hanna, A., Meyerhof, G. 1980. Design charts for ultimate bearing capacity of foundations on sand overlying soft clay. *Canadian Geotechnical Journal* 17(2), 300-303. DOI: <https://doi.org/10.1139/t80-030>
- [16] Hamed, J., Das, B., Echelberger, W. 1986. Bearing capacity of a strip foundation on granular trench in soft clay. *Civil Engineering for Practicing and Design Engineers* 5(5), 359-376.
- [17] Venkata, S., Kurapati, R., Madhav, M. 2016. Kinematics and bearing capacity of strip footing on RFB over compressible ground stabilized with granular trench. *Japanese Geotechnical Society* 2(37), 2115-2120. DOI: <https://doi.org/10.3208/jgssp.IND-14>
- [18] Bhattacharya, P., Kumar, J. 2017. Bearing capacity of foundations on soft clays with granular column and trench. *Soils and Foundations* 57(3), 488-495. DOI: <https://doi.org/10.1016/j.sandf.2017.05.013>
- [19] Noorzard, A., Badakhshan, E. 2017. Investigations on pullout behavior of geogrid-granular trench using CANAsand constitutive model. *Journal of Rock Mechanics and Geotechnical Engineering* 9(4), 726-740. DOI: <https://doi.org/10.1016/j.jrmge.2017.03.013>
- [20] Unnikrishnan, N., Johnson, A., Rajan, S. 2010. Response of Strip Footings Supported on Granular Trench. *Indian Geotechnical Conference GEOTrendz*, pp. 525-528.
- [21] Unnikrishnan, N., Rajan, S. 2012. Bearing capacity of strip footings on geosynthetic encapsulated granular trenches. *Proceedings of International Conference on Ground Improvement and Ground Control*, pp. 977-983.
- [22] Fattah, M., Baghdadi, W., Omar, M., Shanebleh,

- A. 2013. Analysis of strip footings resting on reinforced granular trench by the finite element method. *International Journal of Geotechnical Engineering* 4(4), 471-482. DOI: <https://doi.org/10.3328/IJGE.2010.04.04.471-482>
- [23] Abhishek, S., Rajyalakshmi, K., Madhav, M. 2014. Bearing capacity of strip footing on reinforced foundation bed over soft ground with granular trench. *Indian Geotechnical Journal* 45(3), 304-317. DOI: <https://doi.org/10.1007/s40098-014-0138-y>
- [24] Bowles, J. 2001. *Foundation Analysis and Design*, 5<sup>th</sup> edition, McGraw-Hill.
- [25] Madhav, M., Vitkar, P. 1978. Strip footing on weak clay stabilized with a granular trench or pile. *Canadian Geotechnical Journal* 15(4), 605-609. DOI: <https://doi.org/10.1139/t78-066>
- [26] Das, B., Puri, V. 1989. Bearing capacity of shallow foundations on granular trench in weak clay. *Proceedings of the 3<sup>rd</sup> international symposium held at Niagara Falls, Canada*, pp. 8-11.
- [27] Fattah, M., Al-Waily, M. 2015. Bearing Capacity of Foundations Resting on a Trench of Local Reclaimed Asphalt Pavement Material. *Global Journal of Engineering Science and Research Management* 2(12), 90-105.
- [28] Shalaby, S. 2017. Bearing Capacity of Ring Footing on Stabilized Clay with Sand Trench- Stone Pile Combination. *International Journal of Scientific Engineering and Applied Science* 3(5), 218-226.
- [29] Dassault Systèmes. 2016. *Simulia Abaqus Theory manual* 6.14.
- [30] Niemunis, A. 2003. *Extended hypoplastic models for soils*. Dissertation for habilitation, Karlsruhe Institute for Technology (KIT), Germany.
- [31] Plaxis, 2017. *Plaxis Manuals. CONNECT Edition V20*.
- [32] Roddeman, D. 2017. *Tochnog professional user's manual*.
- [33] Helwany, S. 2007. *Applied Soil Mechanics whit ABAQUS applications*, 1st edition, John Wiley & sons, Inc.
- [34] Fattah, M., Abbas, S., Karim, H. 2012. A Model for Coupled Dynamic Elastic-Plastic Analysis of Soils. *Journal of GeoEngineering* 7(3), 43-50. DOI: [10.6310/jog.2012.7\(3\).2](https://doi.org/10.6310/jog.2012.7(3).2)
- [35] Simo, J., Hughes, T. 1998. *Computational Inelasticity*, 1<sup>st</sup> edition, New York: Interdisciplinary Applied Mathematics.
- [36] Fuentes, W., Tafili, M., Triantafyllidis, T. 2018. An ISA-plasticity-based model for viscous and non-viscous clays. *Acta Geotechnica* 13(2), 367-386. DOI: <https://doi.org/10.1007/s11440-017-0548-y>
- [37] Fuentes, W., Tafili, M., Triantafyllidis, T. 2015. Constitutive Model for Clays Under the ISA Framework, in *Holistic Simulation of Geotechnical Installation Processes*, Springer International Publishing, pp. 115-129.
- [38] Das, B., Sobhan, K. 2013. *Principles of geotechnical engineering*, 8<sup>th</sup> edition, Cengage Learning.
- [39] Fuentes, W., Duque, J., Lascarro, C., Gil, M. 2019. Study of the Bearing Capacity of Closely Spaced Square Foundations on Granular Soils. *Geotechnical and Geological Engineering* 37(3), 1401-1410.
- [40] Fuentes, W., Duque, J., Lascarro, C. 2018. Constitutive simulation of a Kaolin with vertical and horizontal sedimentation axes. *DYNA* 85(207), 227-235. DOI: <http://dx.doi.org/10.15446/dyna.v85n207.69197>
- [41] Spread-Footing, 2017. *GEO5, Fine Civil Engineering Software*.

# OBSERVATION OF EXTENSIVE MASS MOVEMENTS IN THE LIPICA II QUARRY WITH AN EL BEAM DISPLACEMENT SENSOR

# OPAZOVANJE OBSEŽNIH PREMIOV MASE V KAMNOLOMU LIPICA II S SENZORJEM PREMIOVA ŽARKA EL

**Danijela Ignjatović Stupar**  
International Space University  
67400 Illkirch-Graffenstaden, France  
E-mail: danijela.stupar@isunet.edu

**Andrej Kos**  
Marmor Sežana d.d  
6210 Sežana, Slovenia  
E-mail: kos@marmorsezana.com

**Milivoj Vulić**  
University of Ljubljana,  
Faculty of Natural Sciences and Engineering  
Aškerčeva cesta 12, 1000 Ljubljana, Slovenia  
E-mail: milivoj.vulic@guest.arnes.si

**DOI** <https://doi.org/10.18690/actageotechslov.17.1.23-32.2020>

## Keywords

natural stone quarry, stability assessment, high safety pillar, rock mass, EL Beam, ARIMA

## Ključne besede

kamnolom iz naravnega kamna, ocena stabilnosti, visok varnostni steber, kamnita masa, EL žarek, ARIMA

## Abstract

*It is not only that humans are playing with the environment, giving the quarry a bad external image, nature also returns a blow into the internal mass movements by decreasing the safety parameters of the room-and-pillar excavation. This paper presents the analytical methods used to observe the individual parameters in the context of monitoring the safety pillars and the deformation of the discontinuities in the underground excavation in the Lipica II natural stone mine. To monitor movements and deformations, the EL-beam gauges are installed on the surface of the safety pillars. The observations used in this case study are represented by two vertical EL-beam displacement measurements, acting as one year-long time series. Using ARMA modelling, we analysed the differences between the measured and predicted values of EL-beam displacements. The obtained predictions of the displacements, their negligible effect on the measurements themselves, and the absence of any trends in the calculated differences, proves the feasibility of the applied prediction model.*

*A longer observation period would allow predictions of possible seasonal characteristics of the time series, while the development of the automatic responding monitoring system, triggered by the warning events, will improve the reporting system for the sudden changes in the smoothness of the predicted values.*

## Izveček

*Ne samo, da se ljudje igrajo z okoljem, ki daje kamnolomu slabo zunanjo podobo, narava tudi vrača udarec v gibanja notranjih mas z zmanjšanjem varnostnih parametrov izkopavanja prostora in stebrov. V prispevku so predstavljene analitične metode za opazovanje posameznih parametrov v okviru spremljanja varnostnih stebrov in deformacije diskontinuitet v podzemnem izkopu v rudniku naravnega kamna Lipica II. Za spremljanje premikov in deformacij so merilniki žarkov EL nameščeni na površini varnostnih stebrov. Opazovalnici, uporabljeni v tej študiji primera, predstavljata dve navpični meritvi premika snopa EL, ki delujeta kot enoletno časovno vrsto. S pomočjo ARMA modeliranja so bile analizirane razlike med izmerjenimi in predvidenimi vrednostmi premikov El-snopa. Pridobljene napovedi premikov, njihov zanemarljiv učinek na same meritve in odsotnost trendov izračunanih razlik dokazujejo izvedljivost uporabljenega modela napovedovanja.*

*Daljše obdobje opazovanja bi omogočilo napovedi možnih sezonskih značilnosti časovne serije, medtem ko bo razvoj sistema samodejnega odzivanja za spremljanje, ki ga sprožijo opozorilni dogodki, izboljšal sistem poročanja za nenadne spremembe v gladkosti predvidenih vrednosti.*

# 1 INTRODUCTION

Progressive paleogeographic differentiation, which started in the Santonian and later in the Campanian, has already strongly influenced the sedimentary environments of the Adriatic-Dinaric region. This phenomenon was later followed into the Maastrichtian and Paleogene platform. The subaerial transition of this part of the platform induced palaeokarstification of the limestone sedimentation of the Lipica formation, with the deposition of the carbonates in the Karst region (Fig. 1). In this way, the new magasequence in the formation of the Liburnia and "alveolidic-nummulitic limestone" was begun [1, 2].



Figure 2. Lipica II quarry.

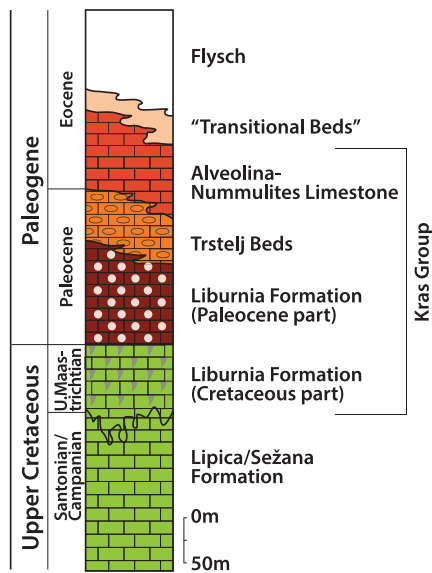


Figure 1. Geological Upper Cretaceous Eocene succession in the Kras (Karst) [2].

Because of its massive structure and uniform texture, this limestone is economically the most important part of carbonate rocks of the classic Karst area. The topography of the Karst region is extremely shallow and skeletal; therefore, the natural recuperation in the case of excavation of the natural stone in the quarries is extremely difficult to control.

The Lipica II quarry (Fig. 2) is one of the successful examples of quarries of natural stone in Slovenia [3]. It represents a progressive spontaneous pollute, although it is made completely of bare rocks. Due to slow leavening, the quarry is still visible as an environmental sore. Nevertheless, it turned out that with the exploitation plan itself, the relief of the affected land can be regulated in an acceptable form.

The company Marmor Sežana d.d. has been excavating "Lipica Unito" natural stone from the Lipica II quarry since 1986 [4]. Extraction is performed by the room-and-pillar mining method, which is adapted directly on the site (Fig.3). The so-called "room-and-pillar" is a special

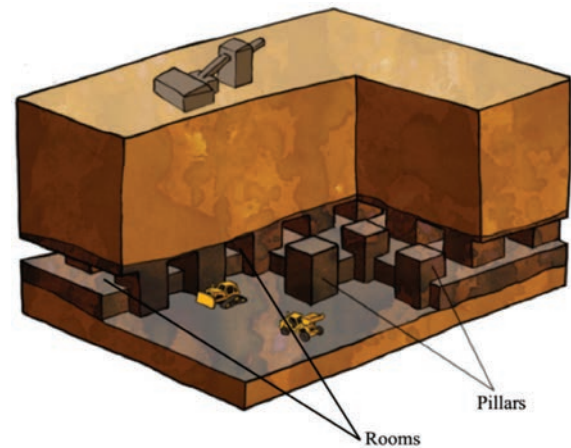


Figure 3. The rooms and pillars mining methodology at Lipica II (top) and room-and-pillar method layout (bottom) [5].

method of mining, where the stone is excavated across a horizontal plane, thus creating horizontal networks between the rooms. In this system rooms/galleries represent the “ore” part, while the pillars are unrestrained materials left out to support the overload of the rooms/galleries’ roof. The advantage of the pillars is that their presence reduces the risk of potential subsidence.

Subsidence is one of the main occurrences above underground mining. It has huge impact on the environmental surroundings [6]. Regarding a more natural impact from, but also vice-versa on, the quarry itself, the tree roots can grow deeper through rock cracks and make dissolution on the karst features. This study was used in a limestone quarry in northern Mexico [7].

Other research was dedicated to air pollution near the quarry. The results showed that the concentration of suspended particulate matter (SPM) emissions are  $360 \mu\text{g}\cdot\text{m}^{-3}$  in the work zone, which is less than  $130 \mu\text{g}\cdot\text{m}^{-3}$  beyond the site boundary [8]. Taking this impact into consideration, it is recommended to design a green belt around the quarry to decrease the influence on the air quality.

Due to those consequences, before any mine site is opened, jointly with the mine excavation planning, the rehabilitation program of the quarry has to be involved in the mine planning system. This procedure has already been successfully applied in nine limestone quarries. The rehabilitation covers six programs, split into three categories, such as planning, operational, and plan-do-check-act management [9]. The suggested procedure, which was already used in several quarries, could be a good analytical proposal for an environmental recovery solution for Sežana’s quarries.

## 2 MATERIALS AND METHODS

### 2.1 Materials

The room-and-pillar method layout has to be mapped carefully before the excavation starts. The calculation which determines the important elements of this type of underground mining is a very complex procedure. Geological and geotechnical analyses of a future mining site are introduced through environmental observations. Their results provide an appropriate landmark of the exact methodology that has to be applied in the choice of the mining methodology. The results also define the parameters of the type of tools, machines, and technology which will be used in the excavation. According to the obtained results, the shape and size of the pillars, likewise their position in the mine, are consolidated.

From the mechanical point of view, the excavation procedure for mining natural stone traditionally uses a combined drilling-and-cutting method with the diamond wire and chain cutting machine that is introduced in Fig. 4.



Figure 4. Diamond wire and chain cutting machine.

Prior to the onset of the underground mining, numerical modelling and a calculation of the stability of the predicted underground spaces was performed using the Finite-Difference Method (FLAC<sup>2D</sup>). The FLAC<sup>2D</sup> model assesses the overall stability of the planned openings and acquires a sensitivity analysis of the input parameters, such as the mechanical characteristics of the rock, including its primary stress, likewise the dimensions and the shape of the mine rooms [3]. The results obtained using these calculations ultimately form the basic design elements of the underground mining site (the rooms and the pillars) and a crucial overview of the selection of a mining method for the long-term extraction of natural stone blocks. Prior to the high safety pillars (HSP) plan making and designing an introduction to determine the largest span of the rooms has to be calculated. This represents the distance between the HSPs and depends on the geomechanical

rock's properties, the geological properties of the site (primary tectonics properties), and the loaf ceiling, which was overloaded by the arch. Increasing the span, the stability of the ceiling decreases. For that reason it is extremely important to determine the width and the height dimensions of the open spaces (the rooms) and, obviously, the high pillars safety [10, 11].

One of the faster and more visual methods is based on using a terrestrial handhold scanner. Terrestrial Laser Scanning (TLS) makes it possible to collect dense point clouds, representing a visual interpretation of the underground mine rooms and the pillars together. To complete the geolocalization of the observed point cloud, a set of reference points is accurately established on the walls. The first step of the photointerpretation of the geometric characteristics of the mine is cleaning from the unnecessary features (e.g., working equipment, vehicles, cables, etc.). From this mesh, the subsequent 3D topographic maps and orthorectified models are conducted [12].

As already mentioned above, the dimensions of the rooms depend on the geological condition and the mining technology being applied. For instance, in case of Lipica II, the heights of the mining levels range between 4 m and 6 m. Kortnik in [13] provided a numerical analysis based on the geo-mechanical properties of the compact limestone and came up with a model where galleries-rooms with different widths (13 m, 15 m or 20 m) are stable up to a width-to-height ratio of  $r = 0.28$ . He also estimated that the portal portion of the pillar (the periductular cross section to the surface levels) has to be greater than 13 m.

Named “unwedge”, it is yet another block analysis mainly conducted during the excavation. It is focused on the underground block stability structures, followed indirectly by follow-up monitoring of the relative

deformations of the discontinuities (stone cracks). A study of a micro fracture network of open cracks could help to better understand the tectonic constraints and to distinguish the origins of the fractures (mechanic or tectonic) [14].

Kortnik in [13], in addition to an analytical calculation and numerical modelling, also provided in-situ data of the stress state and strain measurements of the Lipica II safety pillars. He monitored the behaviour of “safety pillars and rooms” ceilings for a period of 2 years (from 2010 to 2012). The case studies considered the safety pillars SP02 and SP04. The in-situ control measurements were used for monitoring the main stress in a single vertical plane (for the safety pillar SP02), likewise the observation of the temperature. These changes were monitored with a 2D VW stress meter (Model 4350 Vibrating Wire), (Fig. 5).



Figure 5. Biaxial stress meters (VW) [15].

The vertical strains (lateral displacement) were measured with vertical EL beam sensors. The horizontal EL beam sensors monitor the horizontal movement to determine the displacement of the open dikes (Fig. 6).

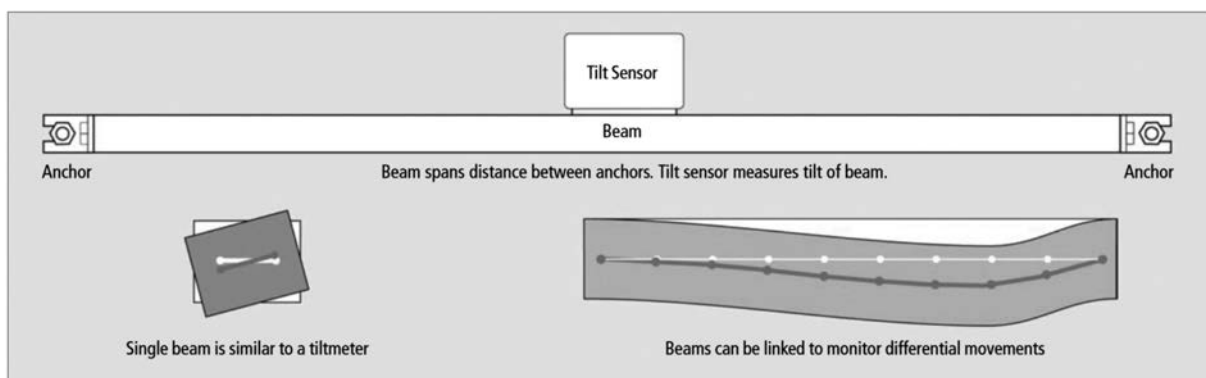


Figure 6. beam sensor [16].



Figure 7. Different types of pillar discontinuities.

In addition, a dike-displacement meter was used as a third option to manually measure the displacements between at least three screws installed along a crack (Fig. 7).

Comparing the numerical model with the in-situ measurements for SP02, Kortnik found congruent results between them.

## 2.2 Methods

To ensure the stability of the underground galleries, self-supporting stones named high safety pillars are established directly during the stone excavation. Unfortunately, those pillars are exposed to natural extensive mass movements, and for that reason they intersect with many discontinuities. Depending on the types of cracks (Fig. 8), the deformation characteristics and the strength of the rock, the reinforcement requirements are defined. For their definition it is necessary to continuously monitor the safety pillars and, in that way, to detect failures on time, which will allow the mining engineers to react properly with the protection of miners and equipment equally.

There are other techniques that were used for geo-mechanical applications.

One of the experiments was conducted in a quarry in southern Switzerland using 3-axis ground-penetrating radar (georadar) to monitor a quarry's floor [18]. It has

been concluded through collected results that the estimation of the quality of the rock can be easily made by using georadar in the observation of excavated or yet to be cut stone. This method could also be used to predict future possible room and pillars cracks and to avoid a possible quarry collapse.

At the Lipica II quarry, the procedure of deformation monitoring has already been applied for many years. There are two established types of monitoring pillar wedges stability:

- using a screw open fissures displacement meter in combination with a glass fissures displacement seal (Fig. 7), and
- monitoring using electronic level (EL) beam gauges.

The latter is focused on voltage conditions in high security pillars, observed by bi-axial stress-meters (vibrating wire sensor). To monitor the movements and deformations, EL-beam gauges are installed on the surface of the safety pillars. The EL beam looks like a bar strain gauge tilt sensor, metal rod, 1.5 to 6 m long, and horizontal/vertical gauges.

Observations from our case study are organized in two time series for two vertical EL-beam displacement measurements. The time series represent a set of measurements or other statistics distributed at regular

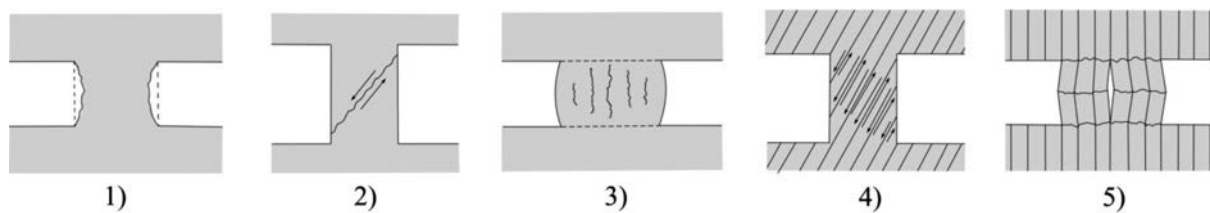


Figure 8. Different types of pillars discontinuities, remodelled from [17].

time intervals. One of the goals of time-series analysis is to make forecasts, i.e., to predict the future values of the tested statistics. The time series contain one or more of the following characteristics: trends, seasonal effects, cycles, and residuals.

To decompose the time series into the mentioned elements, we can use autoregressive (AR) or moving average (MA) processes, or a combination of the two. The AR process of order  $p$  is given by the equation:

$$X_t = \sum_{r=1}^p \beta_r X_{t-r} + \varepsilon_t \quad (1)$$

with:

- $\beta_r$  ( $r=1,p$ ) – a set of constants,
- $\varepsilon_t$  – a random variable.

The definition of the MA process of order  $q$  is:

$$X_t = \sum_{s=0}^q \xi_s \varepsilon_{t-s} \quad (2)$$

where  $\xi_s$  ( $s=0,q$ ) is a set of constants and  $\{\varepsilon_s\}$  is a series of uncorrelated random variables.

Combining models (1) and (2), the ARMA( $p,q$ ) process is obtained:

$$X_t - \sum_{r=1}^p \beta_r X_{t-r} + \varepsilon_t = \sum_{s=0}^q \xi_s \varepsilon_{t-s} \quad (3)$$

Model (3) applies for stationary processes. If the process is not a stationary one we integrate the original process by calculating the differences of  $d$  order, obtaining an autoregressive integrated process ARIMA ( $p,d,q$ ). In order to discover the order of the AR and MA processes, as well as a possible order of differentiating, autocorrelation function (ACF) and partial autocorrelation function (PACF) are used in this case study.

### 3 RESULTS

#### 3.1 Assumptions and starting conditions

The safety pillar, VS3 from Lipica II, has been monitored since 2010 (Fig. 9). In [13], the results of the observed open discontinuities of VS3 were discussed. The oversight was taken part for a period from October 2010 to June 2012. From a technical point of view, the EL beam gauge has been used as an optimal tool for high-safety-pillar stability monitoring. The EL beam gauge is easy to control in the case of technical failure. Its yearly control in a metrological laboratory is of great importance. Like other measuring equipment, its features and characteristics such as accuracy could vary in the changed environmental conditions [19]. In the case of vibrating-wire

stress meters that were used in parallel, the correction or replacement is impossible due to the definitive fixation in a borehole with concrete.



(a)



(b)



Figure 9. Safety Pillar VS3 (a) and Vertical EL beam gauge (b).

It was observed that the temperature has a huge impact on the metal rod of the EL beam gauge. That is why the temperature dataset, around the column, was collected during this monitoring of pillar VS3 where the 2-m-long datalogger was installed.

### 3.2 Measurements and results

The available dataset comprises the measured displacements with two vertically placed EL-beams in the form of time series, covering the period April 2018 to April 2019. The measurements were performed on an hourly basis. The temperature measurements were also triggered for each measuring epoch in order to monitor the changes in the environmental conditions that could have an impact on the calculation of the trend lines for the displacements of the EL beams.

The EL-beam measurements for both beams are transformed to mm and put in Fig. 10. There are a few discrepancies in the dataset with the longest between 20-12-2018 and 14-1-2019.

It can be concluded from Fig. 10 that the measurements of the two EL-beams ( $e_1$  and  $e_2$ , respectively) are highly correlated. That is also numerically confirmed by the calculated correlation coefficient of 0.99. The same

consideration applies to the dependency between the measurements and the temperature, having the correlation coefficients  $r_{e_1,T} = r_{e_2,T} = 0.99$ .

In order to test the changes in the EL-beam lengths due to temperature we introduced a correction thermal expansion term. The applied EL-beams are made of aluminium with a thermal expansion factor of 23.6 ppm/°C. After correcting the measurements for the influence of the ambient temperature, the corrected time series  $e_1'$  and  $e_2'$  were obtained. After the application of the correction for temperature, the EL-beam measurements were still closely correlated with the temperature ( $r=0.99$ ), meaning that the ambient temperature did not affect the instrumental characteristics. However, displacements do change in time due to changes in the temperature.

An analysis of the displacements was performed using ARMA modelling. To discover the order of the model, i.e., to find if there is a periodic behaviour of the time series, a test on autocorrelation was performed. To accomplish that we calculated the autocorrelation function (ACF). Since the ACF is only valid for stationary processes, and our dataset is not due to its variable standard deviation, we calculated the first-order differences for the whole dataset. The graphical result is depicted in Fig. 11.

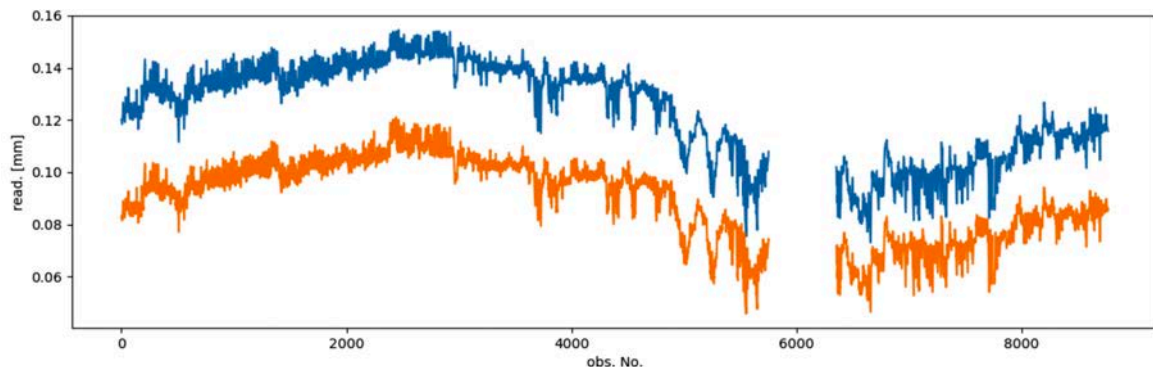


Figure 10. Measurements obtained from EL-beams 1 and 2.

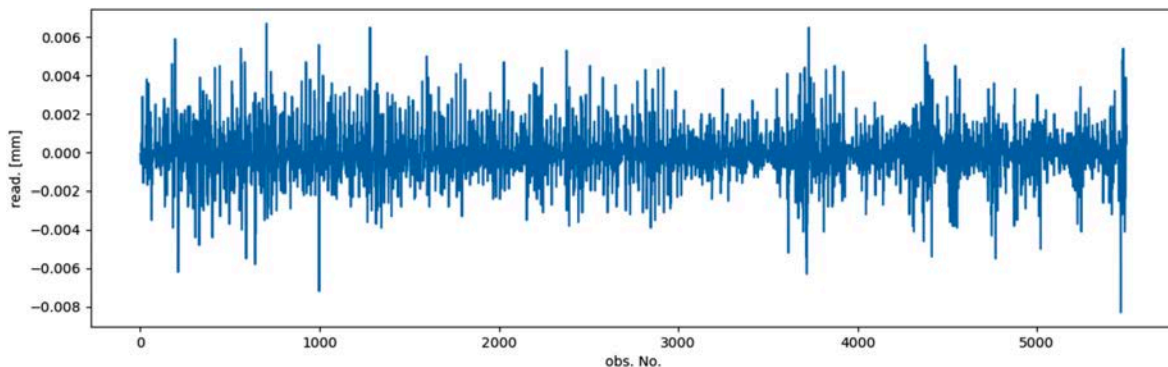


Figure 11. 1<sup>st</sup>-order differences for EL-beam 1 time series.

Due to the discrepancies in the observation material, the rest of the analysis was performed for the period 24/5/2018 to 20/12/2018, containing the continuous observations. Also, due to the high correlation of El-beam 1 and El-beam 2, an ARMA prediction is performed with El-beam 1 only. In the case of the different behaviour of time series 1 and 2, the analysis of trends would be made with both El-beams, because the reason for such behaviour could be related to an uneven displacement of the pillars. The same stands for temperature measurements. The temperature was measured each hour. The high correlation between the temperature

and the El-beam displacements means that hourly changes in the readings on El-beams are only due to the daily changes in temperature. Therefore, temperature measurements are still needed, in order to monitor the El-beam measurements and calculate the corrections for the temperature expansion.

The ACF graph is showed in Fig. 12. The shape of the graph and the observed periodic patterns in the form of a large spike at the first lag and more significant spikes with amplitudes of alternating sign at the further lags indicate that the dataset contains an autoregressive term

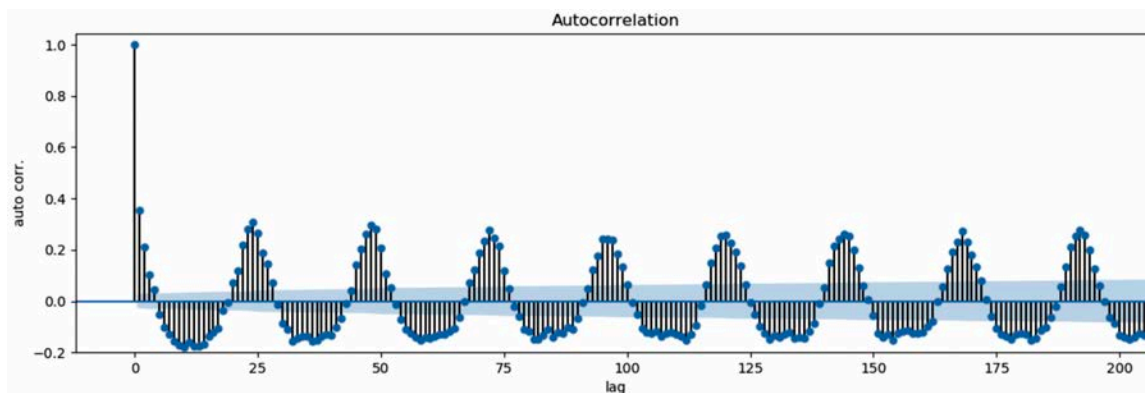


Figure 12. ACF plot for 1<sup>st</sup>-order differenced El-beam 1 time series.

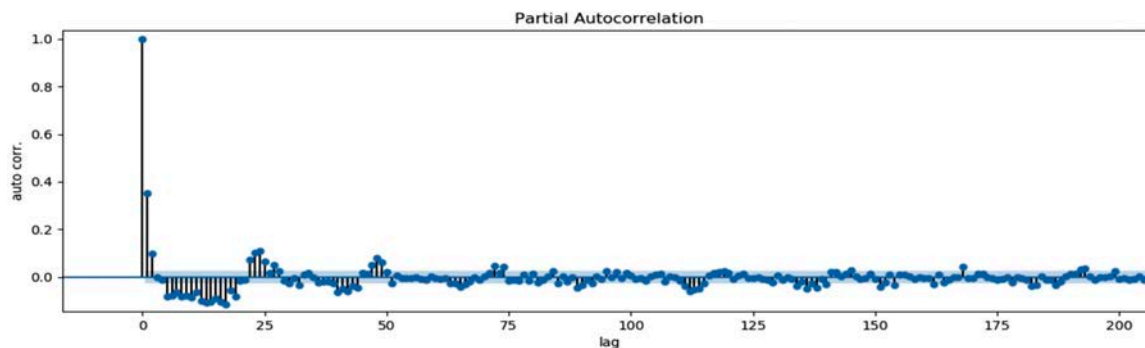


Figure 13. PACF plot for 1<sup>st</sup>-order differenced El-beam 1 time series.

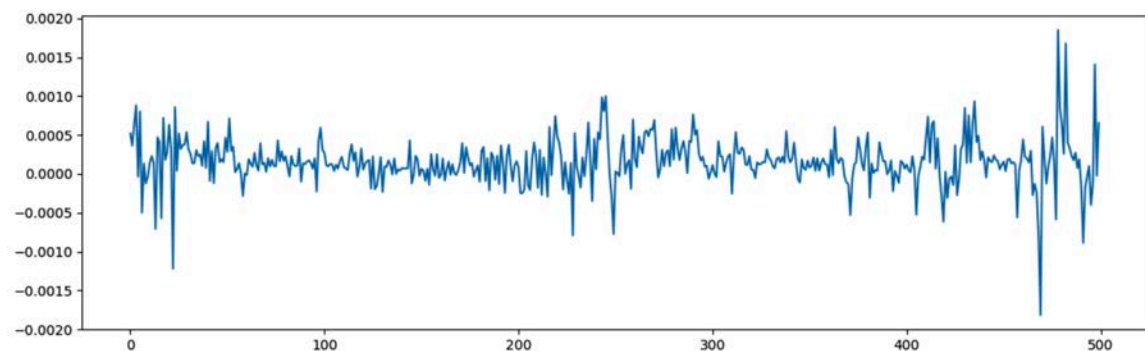


Figure 14. Differences between the 500 last predicted and original El-beam 1 readings.

of higher order. Due to the large dataset, only the first 200 lags are given in Fig. 3–4. The same pattern repeats for the rest of the dataset.

Determination of the order for the autoregressive term is made by calculating the partial autocorrelative function (PACF). The graphical representation of the result is presented in Fig. 13. Again, only the first 200 lags are shown because of the quantity of the processed data.

The obtained PACF results and the significant correlation only at the first lag with other correlations falling within the interval  $(-0.2; +0.2)$  suggests that the order of the AR coefficient is 1.

Analysing the ACF and PACF function graphs we performed the prediction with the ARMA(1,1) model. A test of the model congruence was made on the last 500 readings within the EL-beam 1 dataset. A graphical representation of the differences is given in Fig. 14.

## 4 DISCUSSION

---

The graph in Fig. 14 represents the result of our study case. We used the whole available continual dataset as an input for our prediction model. Analysing the differences between the measured and predicted values given in Fig. 14, it can be concluded that all the predictions fall into the interval  $-0.002$  to  $0.002$ . Their values are  $1/10^{\text{th}}$  of the measured values, which is negligible compared to the measurements themselves. In addition, there are no trends in the calculated differences. Therefore, the chosen model for the predictions is correctly chosen and applied [20, 21].

This model will be utilized in a sense to monitor, on daily basis, the values obtained using the ARMA prediction. The trend of predicted values should be smooth and within the proposed limits. The signal for some unusual events would be a sharp change in the trendline. In that case, certain actions should be taken. The whole process could be improved by automatically triggering alarms if the predicted values exceed certain given limits.

The applied dataset comprised a period of less than 1 year. From Fig. 10 it looks like a seasonal trend would occur. A longer time span of the observations should be included in the data processing to confirm this.

## 5 CONCLUSIONS

---

The observations used in this research consist of the measured displacements on two vertically placed

El-Beams. Besides the linear discrepancies, the ambient temperatures were measured. Preliminary data processing showed, as expected, a significant correlation between both El-beams' measurements, as well as the temperatures correlated with the linear displacements, which was needed to investigate in more detail. The results of this analysis stage suggested there was no influence of the temperature on the El-beams, but rather on the stone itself.

In order to deal with possible dangerous situations that can occur in the case of the rapid displacements of rock blocks, we have developed a prediction model based on a time series of linear displacement measurements. The analysis of the observation material, its periodic characteristics and distribution over the time scale, showed that the ARMA(1.1) model describes the stochastic process the best. It resulted from the ACF and PACF plots created from the El-beam measurements.

In order to test the congruence of the calculated model, the predictions were made for 500 epochs, where real measured values already exist. The predictions showed a high level of congruence with the testing values, reflected in the calculated differences falling between  $-0.002$  and  $0.002$ , which is insignificant compared to the measurement accuracy of the El-beam. This result, therefore, proves the feasibility of the applied prediction model.

A longer observation period would also make possible the testing seasonal characteristics of the time series. Further work on this specific issue will include developing the automatic responding monitoring system, which would be triggered by warning events when the model reports sudden changes in the smoothness of the predicted values.

## Acknowledgments

This research was supported by the Slovenian Ministry of Education Science and Sport, Faculty of Natural Sciences and Engineering, and research program P2 0268 financed by the Slovenian Research Agency. We would like to express our gratitude to Marmor Sežana d.d., who provided data. We would also like to thank the anonymous reviewers and members of the editorial team for their comments.

## REFERENCES

---

- [1] Jurkovšek, B., Biolchi, S., Furlani, S., et al 2016. Geology of the Classical Karst Region. *J Maps* 12,

- 352–362. <https://doi.org/10.1080/17445647.2016.1215941>
- [2] Otoničar, B. 2000. Upper Cretaceous to Paleogene forbulge unconformity associated with foreland basin evolution (Kras, Matarsko Podolje and Istria; SW Slovenia and NW Croatia). *Acta Carsologica* 36, 101–120. <https://doi.org/10.3986/ac.v36i1.213>
- [3] Kortnik, J. 2009. Underground natural stone excavation technics in Slovenia Tehnike podzemnega pridobivanja naravnega kamna v Sloveniji.
- [4] Marmor Sežana Lipica II. <http://www.marmorsezana.com/en/quarry/lipica-ii-quarry/>. Accessed 19 Apr 2019.
- [5] Natural Sciences. <http://www.mstworkbooks.co.za/natural-sciences/gr9/gr9-eb-03.html>. Accessed 19 Apr 2019.
- [6] Lee, F.T., Abel, J.F. 1983. Subsidence from Underground Mining: Environmental Analysis and Planning Considerations. GEOLOGICAL SURVEY CIRCULAR 876. <https://doi.org/10.3133/cir876>
- [7] Estrada-Medina, H., Graham, R.C., Allen, M.F., et al. 2013. The importance of limestone bedrock and dissolution karst features on tree root distribution in northern Yucatán, México. *Plant Soil* 362, 37–50. <https://doi.org/10.1007/s11104-012-1175-x>
- [8] Chaulya, S.K., Chakraborty, M.K., Singh, R.S. 2001. Air Pollution Modelling for a Proposed Limestone Quarry. *Water Air Soil Pollut* 126, 171–191. <https://doi.org/10.1023/A:1005279819145>
- [9] Neri, A.C., Sánchez, L.E. 2010. A procedure to evaluate environmental rehabilitation in limestone quarries. *J Environ Manage* 91, 2225–2237. <https://doi.org/10.1016/J.JENVMAN.2010.06.005>
- [10] Kortnik, J. 2009. Optimisation of the high safety pillars for the underground excavation of natural stone blocks. *Acta Geotech Slov* 1, 34–48.
- [11] Bogert, H., Jung, S.J., Lim, H.W. 1997. Room and pillar stope design in highly fractured area. *Int J Rock Mech Min Sci*. 34 (3,4), 145.e1-145.e14. [https://doi.org/10.1016/S1365-1609\(97\)00155-X](https://doi.org/10.1016/S1365-1609(97)00155-X)
- [12] Lollino, G., Manconi, A., Guzzetti, F., et al. 2015. Engineering Geology for Society and Territory- Volume 5 Urban Geology, Sustainable Planning and Landscape Exploitation. [https://doi.org/10.1007/978-3-319-09048-1\\_71](https://doi.org/10.1007/978-3-319-09048-1_71)
- [13] Kortnik, J. 2015. Stability assessment of the high safety pillars in Slovenian natural stone mines. *Arch Min Sci*. 60, 403–417. <https://doi.org/10.1515/amsc-2015-0027>
- [14] Fronteau, A., Lejeune, G., Sosson, O., et al. 2010. Influence of geomorphological constraints and exploitation techniques on stone quarry spatial organisation. Example of Lutetian underground quarries in Rheims. Laon Soissons areas Eng Geol 115, 268–275. <https://doi.org/10.1016/j.enggeo.2010.05.004>
- [15] Biaxial Stressmeters | GEOKON, INCORPORATED. <https://www.geokon.com/4350>. Accessed 20 Apr 2019.
- [16] EL Beam Sensor - DGSI - Durham Geo - Tiltmeters - Geotechnical Instrumentation. <https://durhamgeo.com/product/el-beam-sensor/>. Accessed 20 Apr 2019.
- [17] Brandy, B.H.G., Brown, E.T. 2004. Rock mechanics for underground mining. Springer Science, pp 372–380.
- [18] Grasmueck, M. 1996. 3-D ground-penetrating radar applied to fracture imaging in gneiss. *GEOPHYSICS* 61, 1050–1064.
- [19] Gučević, J., Delčev, S., Ogrizović, V. 2011. Determining Temperature Dependence of Collimation Error of Digital Level Leica DNA 03. In: FIG Working Week 2011, Bridging the Gap between Cultures, Marrakech, Morocco, 18-22 May 2011. FIG, Marrakech, Morocco, p 1.12.
- [20] Kaluderović, D., Koren, E., Vižintin, G. 2018. Application of analytic element method in hydrogeology. *Mater Geoenvironment* 65, 35–44. <https://doi.org/10.1515/rmzmag-2018-0002>
- [21] Vižintin, G., Ravbar, N., Janež, J., et al. 2018. Integration of models of various types of aquifers for water quality management in the transboundary area of the Soča/Isonzo river basin (Slovenia/Italy). *Sci Total Environ* 619–620, 1214–1225. <https://doi.org/10.1016/j.scitotenv.2017.11.017>

# INTEGRATION OF THE MEASUREMENT TECHNIQUES USED FOR MONITORING THE LAZE LANDSLIDE IN SLOVENIA

# VKLJUČEVANJE MERILNIH TEHNIK, KI SE UPORABLJAJO ZA SPREMLJANJE PLAZU LAZE V SLOVENIJI

## Aleš Lazar

Geoservis, d.o.o.  
Litijska cesta 45, 1000 Ljubljana, Slovenia  
E-mail: ales.lazar@geoservis.si

## Tomaž Beguš

Geotrias, d.o.o.  
Dimičeva ulica 14, 1000 Ljubljana, Slovenia  
E-mail: t.begus@gmail.com

## Milivoj Vulić

University of Ljubljana,  
Faculty of Natural Sciences and Engineering  
Aškerčeva cesta 12, 1000 Ljubljana, Slovenia  
E-mail: milivoj.vulic@guest.arnes.si

DOI <https://doi.org/10.18690/actageotechslov.17.1.33-45.2020>

## Keywords

monitoring, landslide, movement and deformational analysis, geotechnology, environmental protection

## Ključne besede

monitoring, plaz, analiza premikov in deformacij, geotehnologija, varstvo okolja

## Abstract

*The slow movement of the terrain in the area of the village Laze in the municipality Gorenja vas-Poljane accelerated significantly after heavy rainfall in early 2014. Research was conducted to determine the volume of the landslide, the depth of the sliding plane and the displacement dynamics. During a study of the creep sliding dynamics we found the old orthophoto plans and a comparison of the cyclic aerial imagery very useful. The article describes the monitoring system that has been established and describes innovative procedures for using existing spatial data for a better interpretation of the movement dynamics. These comparative analyses of the absolute or relative shifts are useful for land-use planners and for risk analysis as a part of an environmental policy.*

## Izvleček

*Počasno premikanje terena na območju vasi Laze v občini Gorenja vas-Poljane se je močno pospešilo po intenzivnih padavinah v začetku leta 2014. Raziskave so bile izvedene za določitev prostornine plazu, globine drseče ravnine in dinamike premika. Med študijo dinamike drsenja lezenja smo ugotovili stare ortofoto načrte in primerjavo cikličnih letalskih posnetkov za zelo koristne. Članek opisuje vzpostavljen sistem spremljanja in opisuje inovativne postopke za uporabo obstoječih prostorskih podatkov za boljšo interpretacijo dinamike gibanja. Te primerjalne analize absolutnih ali relativnih premikov so uporabne za načrtovalce rabe zemljišč in za analizo tveganja kot del okoljske politike.*

## 1 INTRODUCTION

The landslide body is composed of rock, debris or soil. A slip occurs within the mass of this composition or at the contact with the ground [1]. One third of the Slovenian territory is defined by a high to a very high probability

of landslides [2]. Landslides endanger people, housing and infrastructure [3,4,5]. In 2015, 7273 landslides were recorded on the Slovenian territory [6]. Smaller landslides, depressions and rockfalls are the most common [2,7,8,9].

A natural risk analysis is an essential part of any preventive action and a cornerstone of spatial planning assessments, programs and policies [10,11,12,13]. The first condition for successful prevention is to recognize and understand the properties of the slope's mass movements and the local factors that cause them [14]. The properties of these processes can be determined by establishing a monitoring system to perform periodic and systematic observations and obtain data on changes in time and space [15,16,17,18]. For this purpose, the results of the different measurement methods for observation are used [9,19,20,21,22,23,24,25].

### 1.1 The area of research

The Laze landslide represents a morphological form between the valley below the ridge of Blegoš in the north and the Kopačnica valley in the south, and generally falls at an angle of 10°. It winds in an S shape down the terrain (shown in Figure 1). The length of the morphological form is 3 km, its width is 0.4 km, and it narrows

towards the valley so that at the bottom it is approx. 70 m wide. The area of the Laze landslide is estimated to be 105.5 ha. Traces of the movement of the terrain are visible throughout the area, either as a morphologically pronounced crease of the terrain or as an extremely thick cover or an active land movement. Considering the extremely active land movement within the area of the Laze landslide, we distinguish two parts:

- The **upper landslide** in the Slug valley is a mud stream 600 m long, 130 m wide and is characterized by scattered trees and clearly visible movement of the terrain. Sliding has been active for a long time (at least 20 years). The size of the area was estimated to be 4.8 ha and is several meters thick,
- The **landslide in Laze village** is 550 m long and 250 m wide and is characterized by marked cracks that extend in the direction of the slope, especially at the edges of the movement. They occurred in January and February 2014 as a result of intense rainfall [26]. The size of the area was estimated to be 10.5 ha and is several meters thick.

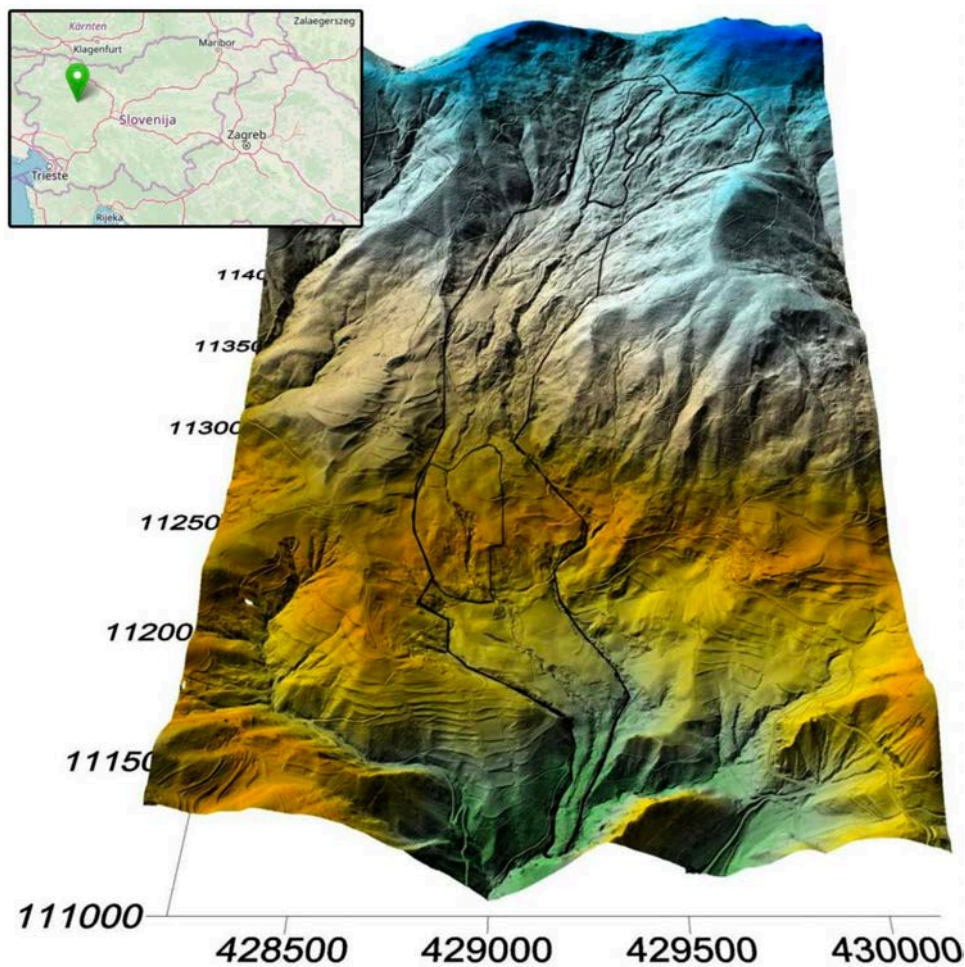


Figure 1. 3D view of the Laze landslide with two of the most active parts. Looking north.

The area of Blegoš, including the examined area, represents a complex tectonic contact between the outer and inner Dinarides, which manifests itself in the form of vertical breaks or fracture zones and thrusts (Figure 2). The thrusts occur in the northern part of the map (upper landslide) and break in the area of the village Laze. Tectonic elements certainly influence the sliding in terms of creating preferential waterways, water barriers and directed clay lots within rock packages.

Generally speaking, the entire area consists of Ladinian and Carnian rock - Pseudo-zilian beds. These are dark-gray graywacke, aleurolites and clay slate, tuff, tuffite, rhyolite and in some places dark gray limestone. These rocks are characterized by rapid weathering and high subjection to sliding, especially when in contact with water. At the end of the landslide the dolomite and rarely limestone of the Norian and Rhaetic ages appear in

layers and belts. These layers represent a kind of barrier to the landslide material.

## 2 MATERIALS AND METHODS

Measurement networks and individual groups of monitoring parameters were focused on finding the volume of the landslide, the sliding dynamics, the depth of the landslide, determining the groundwater depth, and finding options to reduce the movement by lowering the groundwater levels. With these measures the image of the landslide was made and based on these appropriate measures were prescribed. Depending on the nature of the measurements, we divide them into monitoring networks. A graphical representation of the position of the networks is shown in Figure 3. Analytical shading of the digital terrain model is used for the background of the map [27].

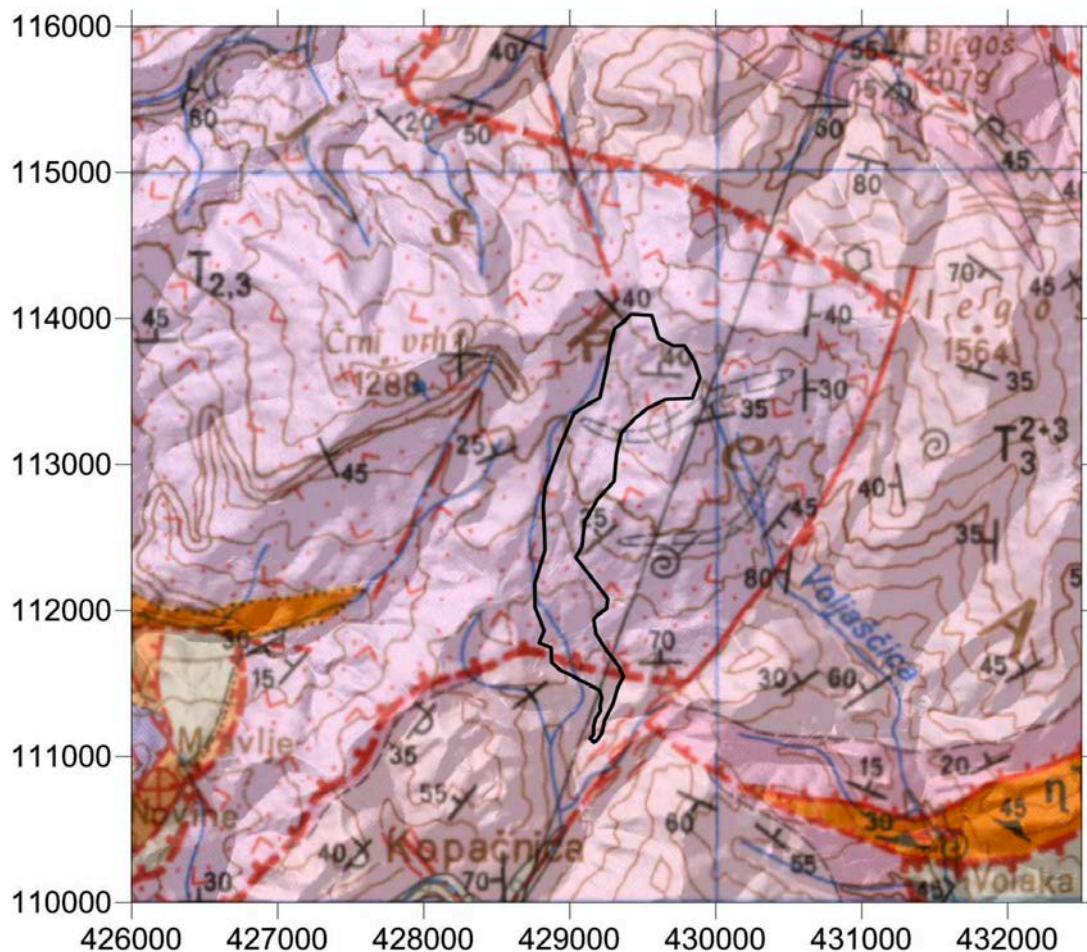


**Figure 2.** Position of the Laze landslide in the Basic geological map, sheet Kranj: The majority of the area consists of Pseudo Ziljan beds.

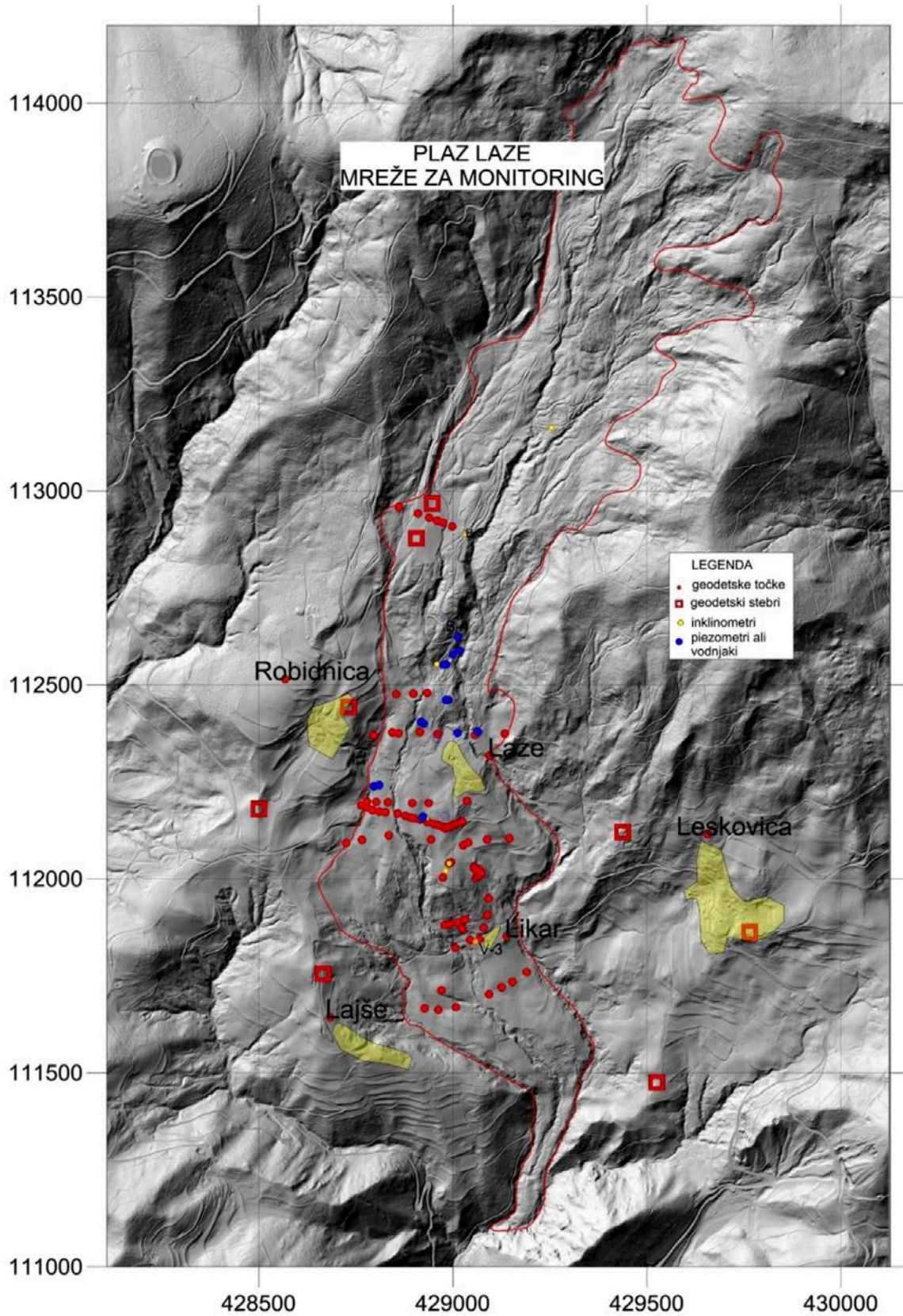


Figure 3. A system of Laze landslide monitoring networks.



**Figure 4.** Landslide in the Slug Valley. Laze in the background. Looking south.

## 2.1 Overview of the landslide area and the use of an unmanned aerial vehicle

The landslide was first thoroughly examined by visual inspection, especially the area where the morphological features indicated possible sliding. This information was supplemented with occasional flights using unmanned aircraft (Figure 4). These data were initially used to determine the extent of the sliding area; the main morphological characteristics to determine the dynamics of the sliding.

## 2.2 Inclination boreholes

In the Laze landslide area, eight boreholes were drilled between 2014 and 2016 to determine and monitor the depth of the sliding surface. Six boreholes were drilled to determine the depth of the sliding surface. An additional two boreholes were made to control the movement above the structure (house/homestead). Geomechanical laboratory tests were carried out on samples from some of the boreholes.

## 2.3 Wells for monitoring the water level and the pumping water

Boreholes for monitoring the groundwater levels and the pumping water that supplies the landslide were drilled

in 2015 and 2016. Large boreholes (nominal 300 mm) called **wells** (marked VOD) were equipped with filters, and boreholes of smaller diameter called **piezometers** (code Pz) were drilled for monitoring the water level.

In 2015, three pairs of wells were drilled: wells for groundwater extraction (300 mm in diameter and 34 m in length) and adjacent wells, piezometers, smaller in diameter (100 mm) and about the same length. The groundwater levels were then determined in these wells. In two of the three wells, the soil is so impermeable that it is not possible to pump water. One of these three wells is suitable for intensive water pumping and the other two are for inclination measurements. The groundwater levels are systematically monitored in these wells. One of the wells along the side of the road has a groundwater level meter installed and in the event of a sudden rise an alarm is sounded.

## 2.4 Surveying and LIDAR terrain recording

Prior to conducting the research, LIDAR was recorded for the entire area where the sliding occurred.

The first movement-monitoring network was set up in 2015. At that time, 37 measurement points were set. The layout of the measuring points followed the most evident shifts in the lower landslide area and around the houses.



**Figure 5.** On the left, a measuring column on stable ground, in the background Leskovica, where a measuring prism is placed on the bell tower. Right, polygon point in the ground under a protective cover.

In 2016, the movement-monitoring network was systematized and extended to the entire area of the Laze landslide. The system is based on seven cross-sections on the landslide, which determine those parts of the landslide that are moving faster. There are 95 measuring points. The network is based on eight fixed geodetic points outside the landslide area, the position of which is determined by precise GNSS observation. The fixed points are the starting points for each observation. The obtained data are millimeter precision. The heights are absolute.

## 2.5 Measurement stations

Displacement sensors were initially set on the lateral portions of the landslide to monitor the movements in real time. In the event of major sudden movements, an alarm is triggered and the appropriate municipal emergency department is notified. The results did not show a clearly pronounced movement that could be registered. Therefore, a landslide displacement-measurement system was set up at the landslide, which is then transmitted to



**Figure 6.** On the left, searching for a movement detector location through a clearly pronounced lateral crack. Right, measuring station to monitor the movement in the borehole. Station MS1.

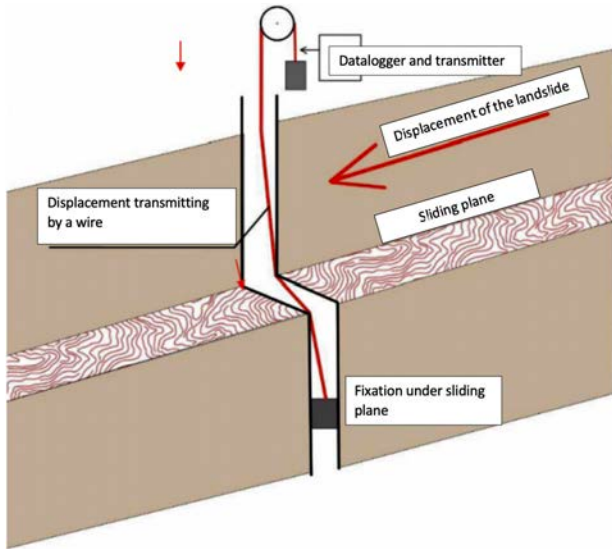


**Figure 7.** Schematic representation of a measurement at the measuring stations [28].

surface recorders with a system that enables immediate reporting to the appropriate services. Inclination boreholes are used in which an anchor is fixed under the sliding surface. The registers record the movements.

On the cracks in the apartment house of the Likar homestead, a measuring instrument is installed to measure the movements of the cracks. This part also has a rain station.

## 2.6 Review of old aerial photographs

Since 1985 Slovenia has been regularly aerial recording in the envisaged three-year cycles (Cyclical Aerial Survey - CAS). In 2003, part of the territory was first recorded in color. Since 1994, aerial photographs of Slovenia and their enlargements have been made publicly available. Aerial imagery is basically the source for making orthophoto plans [29].

As part of the analysis of landslide movement in the past, we have reviewed older and newer orthophoto plans. We performed a comparative analysis between them to determine the dynamics of the movements in different periods.

## 3. PROCEDURES AND RESULTS

### 3.1 Landslide area inspection and unmanned aerial vehicle inspections

The morphological forms that indicated sliding did not change in the post-2014 period to an extent to determine the dynamics. The most obvious are the shifts on

the local municipal road, where the two lateral sections of the landslide are clearly showing shear cracks.

### 3.2 Results of the inclination measurements

Inclinations in individual boreholes were measured for the first time a few weeks after installation, as there was a fear that measurements could no longer be possible due to the displacements.

In three boreholes (I-1, I-2 and I-3; manufactured in 2014), a shift in boreholes was evident shortly after the installation. The boreholes I-1 and I-2 were already considerably displaced in 2015. For this reason, further measurements were no longer possible.

From the inclination measurements, the sliding surface of the Laze landslide was clearly determined. Movement dynamics can also be seen from the measurements. Impenetrable boreholes were used to continuously monitor the landslide movements.

**Table 1.** Results of the inclination measurements.

borehole	Feature - sliding surface at depth
I-1/2014	Sliding surface at depth 24–25 m
I-2/2014	Sliding surface at depth 31–32 m
I-3/2014	Sliding surface at depth 20 m and minor displacement at depth 6–7 m
I-4/2015	Sliding surface at depth 22–26 m
I-5/2015	Sliding surface position not clear, possibly at depth 56 m
I-6/2015	Sliding surface at depth 31 m
I-7/2016	Displacement at depth 25–26 m
I-8/2016	Displacement at depth 23–24 m

### 3.3 Results for monitoring the water level and pumping water

A water pumping test was performed at each well. In most boreholes, a probe was installed to automatically register the levels.

Samples for chemical analysis of the water were taken from some boreholes. The boreholes contain sodium calcium hydrocarbonate sulphate water and sodium calcium hydrocarbonate water.

In most boreholes, the groundwater level does not, or very poorly, fluctuate. Bores indicating a higher amplitude of oscillation are likely to be in the more fractured area (inclinometers).

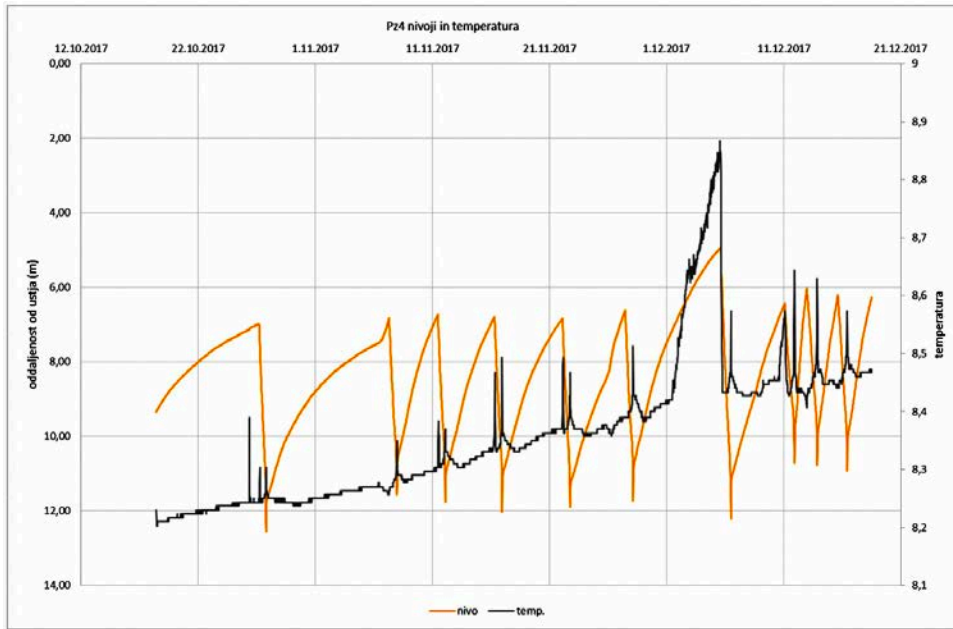


Figure 8. Influence of pumping water in well 4/16 on the level in the Pz4 piezometer.

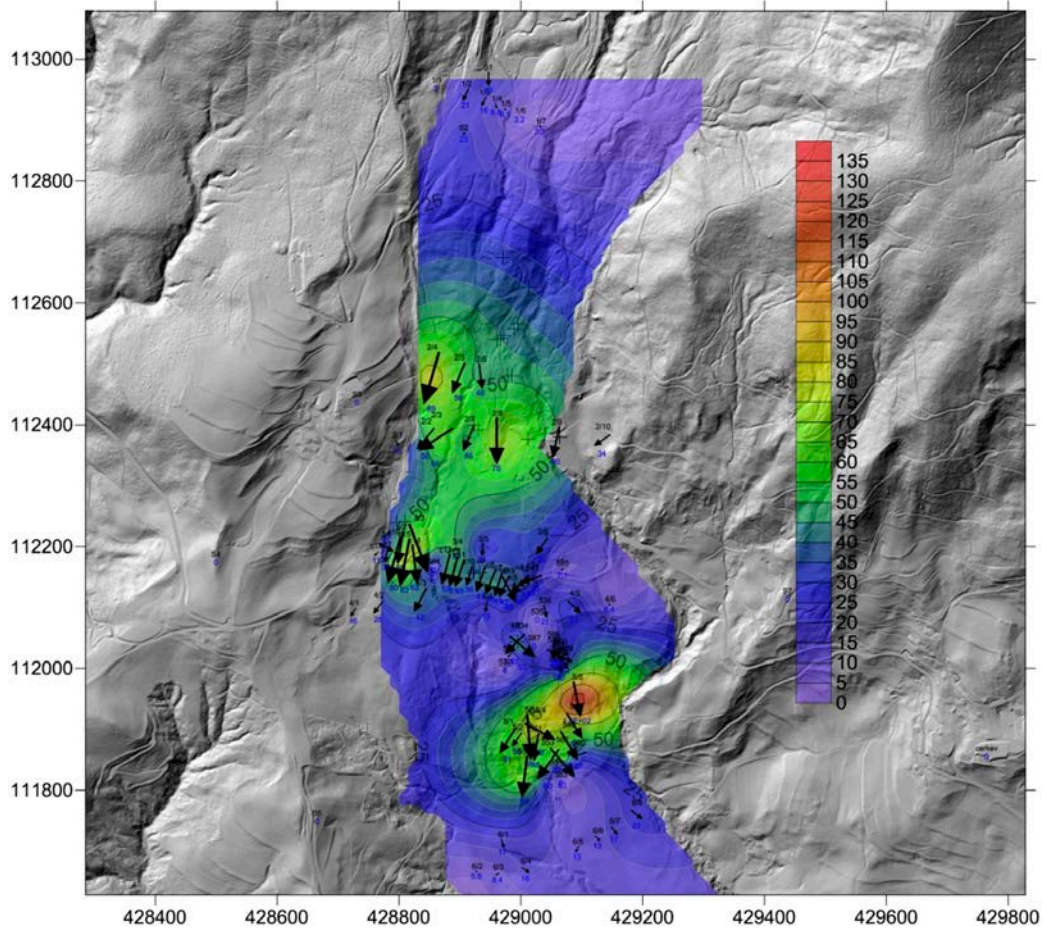


Figure 9. Isolines of the annual displacements of the Laze landslide.

The effect of the pumping water in Platoon 4/16 on the level in Pz4 is clearly visible.

### 3.4 Tracking movements and ground settlement

The results of two cyclical LIDAR recordings of the Laze landslide were available: from 2014 and 2015. Due to the short periods in between the two recordings, the movements could not be determined. It is also difficult to determine the translational movements of the landslide from the LIDAR recording if no markers are present in the field.

A review of the results of the measurements between 2015 and 2017 showed displacements throughout the measured area. They average 8 cm/year. We made isolines of the annual displacements (Figure 9).

### 3.5 Past displacements

We examined the spatially placed orthophoto plans of the Laze landslide area. The geometric resolution (pixel size on the ground) was not precise enough for our purposes. With the occurrence of coloured orthophotos, the usefulness of these products for the purposes of landslide monitoring has increased.

We performed a comparative analysis between the orthophotos from 2005 and 2014. We identified the same elements on both orthophotos. The older type of orthophotos do not have our own observation points, so we monitored objects and their position in space. As the most reliable object in nature, we recognized the power line in combination with its visible shadow. Although the power lines on the orthophotos are projected differently, their contact with the earth is well defined by the



**Figure 10.** The left image shows a 2004 photo where the position of the power line pole on the ground (arrow) is clearly visible. The right image shows a 2014 photo of the same pole marked with a cross. The displacement is obvious and is 2.1 m.



**Figure 11.** Graphical display of the displacements between 2005 and 2014.

**Table 2.** Displacements on the Laze landslide between 2005 and 2014.

ID	Difference 2005 - 2014				
	dX (m)	dY (m)	dH (m)	movement dXY (m)	3D movement (m)
1	-0.037	-2.555	-0.291	2.56	2.57
2	-0.223	-1.502	0.004	1.52	1.52
3	0.027	-1.980	-0.349	1.98	2.01
4	-0.265	-2.249	-0.211	2.26	2.27
5	-0.172	-1.993	-0.189	2.00	2.01
6	0.000	-2.289	0.064	2.29	2.29
7	-0.049	-2.070	-1.258	2.07	2.42
8	0.062	-2.129	-0.249	2.13	2.14
9	0.062	-2.006	-0.418	2.01	2.05
10	-0.031	-1.267	0.211	1.27	1.28
11	0.062	-1.081	0.086	1.08	1.09
12	0.683	-1.850	-0.239	1.97	1.99
13	0.543	-1.772	-0.663	1.85	1.97
14	0.544	-1.983	-0.157	2.06	2.06
15	0.477	-1.981	-0.069	2.04	2.04
16	-0.200	-2.049	-0.482	2.06	2.11
17	-0.085	-2.088	-0.201	2.09	2.10
18	0.321	-0.921	-1.389	0.98	1.70
19	0.361	-1.482	-0.300	1.53	1.55
20	0.961	-1.235	-0.449	1.56	1.63
21	0.894	-2.179	0.052	2.35	2.36
22	-0.077	-0.384	-0.189	0.39	0.43
23	0.038	-0.133	-0.018	0.14	0.14
24	1.484	0.816	-0.018	1.69	1.69
25	0.742	-0.742	-0.251	1.05	1.08
26	0.646	-0.246	-0.004	0.69	0.69
27	0.039	-2.208	-0.360	2.21	2.24
28	0.237	-2.287	-0.231	2.30	2.31
29	-0.039	-2.405	-0.014	2.41	2.41
30	0.000	-2.366	0.317	2.37	2.39
31	0.237	-1.735	-0.144	1.75	1.76
32	-0.315	-2.484	-0.296	2.50	2.52
33	-0.473	-2.168	-0.022	2.22	2.22
34	-0.710	-1.853	-0.309	1.98	2.01
35	0.777	-0.915	-0.457	1.20	1.28
36	0.056	-0.224	-0.007	0.23	0.23
37	0.067	0.000	-0.007	0.07	0.07
38	0.000	-0.103	-0.006	0.10	0.10
39	-0.310	-0.155	-0.092	0.35	0.36
40	0.000	-0.144	-0.023	0.14	0.15
41	0.648	0.576	-0.023	0.87	0.87
42	0.000	-0.230	-0.092	0.23	0.25
43	-0.134	-0.269	-0.095	0.30	0.31
44	0.000	-0.134	-0.044	0.13	0.14
45	-0.044	-0.311	-0.048	0.31	0.32
46	0.622	-0.266	-0.198	0.68	0.70
47	-0.526	0.364	0.031	0.64	0.64
48	0.690	-1.610	-0.852	1.75	1.95
49	0.236	-1.892	-0.219	1.91	1.92
50	0.047	-2.081	-0.279	2.08	2.10
51	-0.636	-1.765	-0.164	1.88	1.88
			Max displacement:	2.56	2.57
			Average displacements:	1.46	1.50

onset of the shadow (example in Figure 10). The elevation data is related to the digital terrain model that was generated when creating the orthophotos.

During a period of 9 years (between 2005 and 2014) the landslide in the village Laze has moved approximately 1.5 to a maximum of 2.5 meters. The graphical representation of the movements during this period is illustrated in Figure 11, where the average displacement is emphasized (the graphical basis is DOF 2014).

## 4 DISCUSSION

Landslide monitoring is performed by physical inspections of the landslide, measurements and study of the obtained parameters. With physical inspection of the landslide, possible changes are determined. The study of the data obtained determines the extent of the displacements and the dynamics of the sliding.

A very rough projection of the volume of stored water in the landslide may be as follows. The water supply surroundings of the village Laze measure  $1.045 \text{ km}^2$ , a thickness of 30 m and a porosity of 5 %. The conclusion is that  $1,568,358 \text{ m}^3$  ( $1,045,572 \text{ m}^2 \times 30 \text{ m} \times 0.05$ ) of water can be stored in the landslide. If this water seizes  $\frac{1}{2}$  of the total landslide volume, we expect the volume of water to be  $784,179 \text{ m}^3$ .

Rainfall at the Leskovica rain station is 1742 mm/year. Subtracting evaporation (500 mm/year) from this quantity and the drainage coefficient at 0.3 gives the following values:  $Q = 1,045,572 \text{ m}^2 \times 1242 \text{ l/m}^2 \times 0.7 = 909,020 \text{ m}^3$  of stored water annually. By pumping, at least 10 % of this water could be removed.

The entire unstable region of Laze is subject to sliding, which is activated at different time periods. Different areas move as different episodes, and the movement covers the entire area. During the 2014–2016 survey phase, it was determined that the sliding plane was at least 20–30 m below the surface of village Laze, and that it slides approximately a decimetre per year. The largest displacement occurred in January 2014, before the measures to reduce the speed of the sliding had been taken. Between 2005 and 2014, the average displacement was 1.5 m.

Because of its constant movement, the dynamics of sliding was detected on the older orthophoto plan from 2005. In identifying the same objects on orthophotos from different periods, we used an innovative method where we determined the ground point of power-line poles. Vertical objects at the junction with their shadow define the point on the ground. On condition that it is sunny.

In Slovenia, a cyclic aerial survey is carried out approximately every 3 years. This permanently creates an orthophoto and digital terrain model for the whole territory of Slovenia. The survey shows that by comparing well-defined points on orthophotos from different periods, the dynamics of the movement of natural objects can be monitored. With new insights into determining landslide dynamics, we can model predictions of landslide movement. By analysing the stability of the slopes, the risk of landslides can be determined.

## 5 CONCLUSIONS

The Laze landslide is classified as a slow-moving landslide (summarized by [30,31,32]). Water is the main generator of the sliding. By pumping water from the wells, the water flow in the sliding area is reduced. Since 2014, when these measures were taken, the landslide in the observed area slides about 8 cm per year. Prior to the measures, its speed was estimated to be 16 cm per year, and therefore twice as fast.

Changes in time and space can also be determined for the period prior to the establishment of the systematic monitoring of the landslide if spatial data such as a cyclic aerial survey were periodically obtained in the area. In Slovenia, this system is well regulated, which is why we have a great potential for establishing a high-quality landslide-forecasting model. This would reduce the risk of natural disasters as part of environmental policy.

## Acknowledgment

This research was supported by the Slovenian Ministry of Education Science and Sport, Faculty of Natural Sciences and Engineering, and research program P2-0268 financed by the Slovenian Research Agency. We would like to thank the companies Geotrias d.o.o., which provided us with access to the collected data. We would also like to thank the municipality of Gorenja vas - Poljane for their engagement with the issues of the Laze landslide. We would also like to thank the anonymous reviewers and members of the editorial team for their comments.

## REFERENCES

- [1] Ribičič, M. 2002. Zemeljski plazovi, usadi in podori. V: Ušeničnik, B. (ur.). Nesreče in varstvo pred njimi. Ljubljana, Ministrstvo za obrambo: pp. 260–266.
- [2] Komac, M., Fajfar, D., Ravnik, D., Ribičič, M. 2007. Slovenian National Landslide DataBase – A prom-

- ising approach to slope mass movement prevention plan. *Geologija* 50 (2), 393–402. doi:10.5474/geologija.2007.02
- [3] Bavec, M., Budkovič, T., Komac, M. 2005. Geohazard – geološko pogojena nevarnost zaradi procesov pobočnega premikanja. Primer občine Bovec. *Geologija* 48 (2), 303–310. doi:10.5474/geologija.2005.025
- [4] Vižintin, G., Stevanovič, L., Vukelič, Ž. 2008. Development of environmental criteria for estimation of land development using GIS. *RMZ-materials and geoenvironment* 55 (2), 237–258.
- [5] Devkota, K. C., Regmi, A. D., Pourghasemi, H. R., Yoshida, K., Pradhan, B., Ryu, I. C., Dhital, M. R., Althuwaynee, O. F. 2013. Landslide susceptibility mapping using certainty factor, index of entropy and logistic regression models in GIS and their comparison at Mugling–Narayanghat road section in Nepal Himalaya. *Natural Hazards* 65, 135–165. doi: 10.1007/s11069-012-0347-6
- [6] Jemec Auflič, M., Kumelj, Š., Prkič, N., Šinigoj, J. 2015. Zbiranje podatkov o zemeljskih plazovih in zanesljivost napovedovanja njihovega proženja. *Ujma* 29, 363–370.
- [7] Logar, J., Fifer Bizjak, K., Kočevar, M., Mikoš, M., Ribičič, M., Majes, B. 2005. History and present state of the Slano Blato landslide. *Natural Hazards and Earth System Sciences* 5, 447–457. doi:10.5194/nhess-5-447-2005
- [8] Jemec, M., Komac, M. 2013. Rainfall patterns for shallow landsliding in perialpine Slovenia. *Natural Hazards* 67 (3), 1011–1023. doi:10.1007/s11069-011-9882-9
- [9] Peternel, T. 2017. Dinamika pobočnih masnih premikov na območju Potoške planine z uporabo rezultatov daljinskih in terestričnih geodetskih opazovanj ter in-situ meritev. PhD thesis. Univerza v Ljubljani, Naravoslovnotehniška fakulteta: 183 f.
- [10] Agliardi, F., Crosta, G., Zanchi, A. 2001. Structural constraints on deep-seated slope deformation kinematics. *Engineering Geology* 59 (1–2), 83–102. doi:10.1016/S0013-7952(00)00066-1
- [11] Vanut, J., Leroueil, S. 2002. Analysis of Post-Failure Slope Movements within the Framework of Hazard and Risk Analysis. *Natural Hazards* 26 (1), 83–109. doi:10.1023/A:1015224914845
- [12] Đurović, B., Ribičič, M., Mikoš, M. 2005. RHDM postopek analize potencialne ogroženosti zaradi odlomne nevarnosti. *Geologija* 48 (1), 33–51. doi:10.5474/geologija.2005.005
- [13] Capitani, M., Ribolini, A., Bini, M. 2014. The slope aspect: A predisposing factor for landsliding? *Comptes Rendus Geoscience* 345 (11–12), 427–438. doi:10.1016/j.crte.2013.11.002
- [14] Guzzetti, F., Cardinali, M., Reichenbach, P., Cipolla, F., Sebastiani, C., Galli, M., Salvati, P. 2004. Landslides triggered by the 23 November 2000 rainfall event in the Imperia Province, Western Liguria, Italy. *Engineering Geology* 73 (3–4), 229–245. doi:10.1016/j.enggeo.2004.01.006
- [15] Meisina, C., Zucca, F., Fossati, D., Ceriani, M., Allievi, J. 2006. Ground deformations monitoring by using the Permanent Scatterers Technique: the example of the Oltrepo Pavese (Lombardia, Italy). *Engineering Geology* 88 (3–4), 240–259. doi:10.1016/j.enggeo.2006.09.010
- [16] Dewitte, O., Jasselette, J. C., Cornet, Y., Van Den Eeckhaut, M., Collignon, A., Poesen, J., Demoulin, A. 2008. Tracking landslide displacements by multi-temporal DTMs: A combined aerial stereo-photogrammetric and LIDAR approach in western Belgium. *Engineering Geology* 99 (1–2), 11–22. doi:10.1016/j.enggeo.2008.02.006
- [17] Guzzetti, F., Cesare Mondini, A.C., Cardinali, M., Fiorucci, F., Santangelo, M., Chang, K.T. 2012. Landslide inventory maps: New tools for an old problem. *Earth-Science Reviews* 112 (1–2), 42–66. doi:10.1016/j.earscirev.2012.02.001
- [18] Herrera, G., Gutiérrez, F., García-Davalillo, J.C., Guerrero, J., Notti, D., Galve, J.P., Fernández-Merodo, J.A., Cooksley, G. 2013. Multi-sensor advanced DInSAR monitoring of very slow landslides: The Tena Valley case study (Central Spanish Pyrenees). *Remote Sensing of Environment* 128, 31–43. doi:10.1016/j.rse.2012.09.020
- [19] Ribičič, M., Komac, M., Mikoš, M., Fajfar, D., Ravnik, D., Gvozdanovič, T., Komel, P., Miklavčič, L., Fras, M. 2005. Novelacija in nadgradnja informacijskega sistema o zemeljskih plazovih in vključitev v bazo GIS\_UJME. Ciljni raziskovalni projekt: Konkurenčnost Slovenije 2001–2006. Ljubljana, Univerza v Ljubljani, Fakulteta za gradbeništvo in geodezijo: 16 f.
- [20] Michoud, C., Abellan, A., Derron MH, Jaboyedoff, M. 2012. Review of techniques for landslide detection, fast characterization, rapid mapping and long-term monitoring. *SafeLand deliverable 4.1 (7<sup>th</sup> Framework Programme)*. Lausanne, Université de Lausanne (UNIL), Institut de Géomatique et d'Analyse du Risque: 401 f.
- [21] Niethammer, U., James, M.R., Rothmund, S., Travelletti, J., Joswig, M. 2012. UAV-based remote sensing of the Super-Sauze landslide: Evaluation and results. *Engineering Geology* 128, 2–11. doi:10.1016/j.enggeo.2011.03.012
- [22] Turner, D., Lucieer, A., Watson, C. 2012. An Automated Technique for Generating Georectified Mosaics from Ultra-High Resolution Unmanned

- Aerial Vehicle (UAV) Imagery, Based on Structure from Motion (SfM) Point Clouds. *Remote Sensing* 4 (5), 1392–1410. doi:10.3390/rs4051392
- [23] Stumpf, A., Malet, J.P., Kerle, N., Niethammer, U., and Rothmund, S. 2013. Image-based mapping of surface fissures for the investigation of landslide dynamics. *Geomorphology* 186, 12–27. doi:10.1016/j.geomorph.2012.12.010
- [24] Scaioni, M., Longoni, L., Melillo, V., Papini, M. 2014. Remote Sensing for Landslide Investigations: An Overview of Recent Achievements and Perspectives. *Remote Sensing* 6 (10), 9600–9652. doi:10.3390/rs6109600
- [25] Peternel, T., Kumelj, Š., Oštir, K., Komac, M. 2017. Monitoring the Potoška planina landslide (NW Slovenia) using UAV photogrammetry and tachymetric measurements. *Landslides* 14 (1), 395 – 406. doi: 10.1007/s10346-016-0759-6
- [26] Public information of Slovenia, ARSO, National Meteorology Service. 2018. <http://meteo.arso.gov.si> (Acquired 18.11.2018).
- [27] Vižintin, G. 2015. Using raster GIS for slope stability analysis. *Geonauka* 3 (1). doi: 10.14438/gn.2015.05
- [28] Kirschke, D. 1977. Superficial and Underground Investigations at Sliding Rock Slopes in Greece. International Symposium on Field Measurements in Rock Mechanics - Zurich, April 4-6, 1977, pp 775 - 788.
- [29] Kosmatin Fras, M. 2004. Vpliv kakovosti vhodnih podatkov na kakovost ortofota = Influence of input data quality on the quality of orthophoto. *Geodetski vestnik* 48 (2), 167–178.
- [30] Cruden, D. M., Varnes, D. J. 1996. Landslide types and processes. V: Turner A.K. (ur.), Schuster R.L. (ur.). *Landslide Types and Processes. Landslide investigation and mitigation. Special Report.* US National Research Council. Transportation Research Board, National Academy of Sciences. Washington: DC., pp. 36-75.
- [31] Fell, R. 2000. Landslide risk management concepts and guidelines. Australian Geomechanics Society, Sub-committee on landslide risk management, 69.
- [32] Hungr, O., Leroueil, S., Picarelli, L. 2014. The Varnes classification of landslide types, an update. *Landslides* 11 (2), 167–194. doi:10.1007/s10346-013-0436-y

# MODELING AND ANALYSIS OF DIGITAL SURFACE MODELS USING HIGH-RESOLUTION UAV IMAGES

# MODELIRANJE IN ANALIZA DIGITALNIH POVRŠINSKIH MODELOV Z UPORABO VISOKO LOČLJIVIH UAV SLIK

## Andrej Pal

University of Ljubljana,  
Faculty of Natural Sciences and Engineering,  
Department of Geotechnology, Mining and  
Environment  
Aškerčeva 12, 1000 Ljubljana, Slovenia  
E-mail: andrej.pal@ogr.ntf.uni-lj.si

## Mirko Borisov

University of Novi Sad,  
Faculty of Technical Sciences  
Trg Dositeja Obradovića 6, 21000 Novi Sad,  
Republic of Serbia  
E-mail: mborisov@uns.ac.rs

## Milivoj Vulić

University of Ljubljana,  
Faculty of Natural Sciences and Engineering,  
Department of Geotechnology, Mining and  
Environment  
Aškerčeva cesta 12, 1000 Ljubljana, Slovenia  
E-mail: milivoj.vulic@guest.arnes.si

DOI <https://doi.org/10.18690/actageotechslov.17.1.46-55.2020>

## Keywords

digital photogrammetry, UAV, GNSS measurements, point cloud, DSM

## Ključne besede

digitalna fotogrametrija, meritve UAV, meritve GNSS, oblak točk, DSM

## Abstract

*Unmanned aerial vehicles (UAVs) are increasingly used for geodata collection and topographic mapping. The use of UAVs in photogrammetric surveying provides an effective way to obtain orthophotographs and digital surface models (DSMs). Detailed investigations can be carried out in inaccessible parts of the observed area, such as steep slopes, muddy and silty terrain, locations with high risk, etc. There are various software packages for the processing of UAV photogrammetric-based data. In this study, 618 high-resolution images of an open-pit excavation were obtained with an Anafi Parrot-type UAV from a height of approximately 30 m. The ground control points were established with customized markers and fast static GNSS measurements. The high-resolution images were processed using two software tools: Agisoft Metashape Professional and Pix4Dmapper Pro. From the produced high-density 3D point clouds, DSMs, orthomosaics and digital elevation models (DEMs) were developed. The quality of the UAV-produced digital models was assessed by a comparison with terrestrial measurements, where the focus was on water areas that cause noise on the model surface.*

## Izvleček

*Brezpilotna letalska vozila (UAV) se vedno pogosteje uporabljajo za zbiranje geodetskih podatkov in topografsko kartografijo. Uporaba UAV-jev pri fotogrametričnem raziskovanju zagotavlja učinkovit način za pridobivanje ortofotografij in digitalnih površinskih modelov (DSM). Podrobne preiskave se lahko izvajajo na nedostopnih delih opazovanega območja, kot so strma pobočja, blatni in močvirni teren, lokacije z visokim tveganjem itd. Obstajajo različni programski paketi za obdelavo podatkov na podlagi fotogrametričnih podatkov UAV. V tej raziskavi je bilo z UAV tipom Anafi Parrot z višine približno 30 m pridobljenih 618 posnetkov visoke ločljivosti izkopa odprte gradbene jame. Vzpostavljene so bile talne kontrolne točke s prilagojenimi označevalci in hitrimi statičnimi meritvami GNSS. Slike z visoko ločljivostjo so bile obdelane z uporabo dveh programskih orodij: Agisoft Metashape Professional in Pix4Dmapper Pro. Iz proizvedenih 3D točkovnih oblakov visoke gostote smo razvili modele DSM, otomozaike in digitalne višinske modele (DEM). Kakovost digitalnih modelov, ki jih proizvajajo UAV, je bila ocenjena s primerjavo z zemeljskimi meritvami, kjer je bil poudarek na vodnih območjih, ki povzročajo hrup na površini modela.*

## 1 INTRODUCTION

---

Aerial imagery has long been used in geodesy and cartography to obtain an overhead view of terrain, infrastructure, and to situate sites within the visual and physical landscape. This was accomplished by placing cameras on the hull of aircraft or other utility vehicles with extendable platforms [1, 2]. In the past decade, technological advances have allowed air-bound surveying techniques to be re-established in practical terms and are nowadays extensively applied in the process of digital 3D terrain modeling [3-16]. In a variety of engineering disciplines, affordable and flexible unmanned aerial vehicles (UAVs) are being used to obtain high-resolution remote-sensing data of larger (observational) areas on the Earth's surface. An UAV-based photogrammetry technique allows multi-temporal, multi-spectral imagery in a fast, cost-effective and simple way [3, 4]. Therefore, many researchers explored these recent developments in numerous studies, such as: monitoring terrain deformations [5-7], surveying construction projects [8, 9], characterization of geological features within mining areas [10], abandoned-mine risk assessment [11, 12], highly accurate 3D modeling of mining excavation sites [13-15] or of cultural heritage [16], precise farming [3], etc. These applications require high-resolution, geospatial information and very high accuracy. The accuracy of the produced orthophoto and digital terrain model (DTM) mostly depends on the obtained raw images and the photogrammetric processing methods, such as Structure from Motion (SfM) [17-19].

SfM uses mathematics and digital pattern recognition to calculate the distance/direction of the motion between multiple overlapping images and to triangulate the surface points for geometry reconstruction. It is different to traditional photogrammetric methods because SfM generates positions in an arbitrary coordinate system and requires a georeferencing strategy [17]. Georeferencing can be done directly by using UAV onboard sensors to calculate the camera coordinates at the exact moment of the measurement (photograph acquirement), or indirectly by establishing recognizable ground control points (GCPs), the coordinates of which are known [18]. When using GCPs, an accuracy issue arises in relation to the distribution and the number of points. Even though there are no general GCP positioning rules, Harwin and Lucieer [19] showed that the biggest impact of GCP distribution is in areas with significant relief features. According to their findings, the GCPs should be evenly spread throughout the observation area so that the individual points are spaced at a distance of 1/5 to 1/10 of the UAV flight height,

while on steeper parts of the terrain the distance is reduced. Coordinates of GCPs can be obtained by using Global Navigation Satellite System (GNSS) surveying techniques, allowing an average GCP accuracy at the cm level [20]. In critical areas of the terrain, where the GNSS measurements cannot be carried out, GCPs can be determined using a terrestrial laser scanner (TLS). Additionally, the improved accuracy of the obtained coordinates (at the mm level) from the combination of photogrammetry and TLS contributes to the quality of the generated orthophotos and 3D models, as reported by Tong et al. [15]. The application of SfM, georeferencing, 3D point cloud and digital surface model (DSM) development can all be done with various software packages. Aicardi et al. [16] focused on free and commercial photogrammetric software solutions and based on a verification with LiDAR data, they confirmed that Agisoft Photoscan Professional and Pix4D are best suited to conventional applications, as well as producing good results.

The main purpose of this study was the modeling and analysis of digital surface models (DSMs). Using high-resolution images acquired from photogrammetric UAV surveying, and two software packages, digital models of the observation area were produced. The visual confirmation of the DSMs was done with the obtained images, while for the quantitative assessment, terrestrial measurements were carried out. By comparing UAV and terrestrial-based digital models, the verification was performed on critical areas (water bodies) and along transversal profiles.

## 2 METHOD AND TECHNOLOGY OF THE STUDY

---

### 2.1 Case-study area

The observational, case-study area is located in the eastern part of the Autonomous Province of Vojvodina, in the north Republic of Serbia. Namely, it is the Central Banat District, the cadastral municipality of Novi Bečej, on the eastern border of the construction zone near the city area called "Garajevac" (Fig. 1).

There is not much vegetation in the observed area, so the surface of the soil is clayey with smaller areas of low vegetation or grass, which was very convenient from the viewpoint of the UAV photogrammetry application. The observational area was divided into three smaller areas of interest, as shown in Fig. 2, which were numbered and named on the basis of their characteristics: 1. main excavation pit; 2. the tailings pond and 3. northeastern excavation pit.

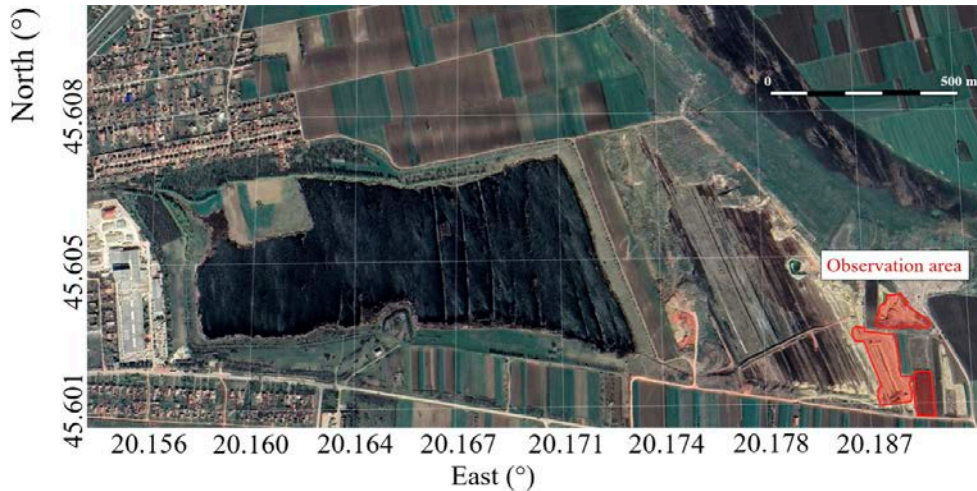


**Figure 1.** Location of the observational area on the in the construction zone near the city Novi Bečej, Autonomous Province of Vojvodina in the north Republic of Serbia.



**Figure 2.** Three smaller areas of interest within the observational area.

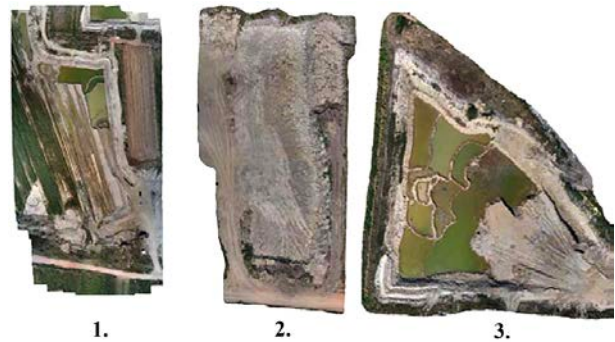


**Figure 3.** Terrain characteristics of each of the smaller observational areas.

The division of the area into three locations was made primarily because of the limitations dictated by the instrument's performance (UAV) and the hardware requirements for processing and analyzing data. Furthermore, the area division was executed due to the terrain configuration and the characteristics within each individual location (Fig. 3).

1. Main excavation pit - land is covered with clay and low occasional vegetation on the perimeter. Several larger water surfaces cover the area. From the shape of the excavation a saw-tooth-like profile of the terrain remains in some locations.
2. The tailings – land is covered with clay, soil and fine dust. Due to the excavation procedures, the surface is

approximately flat with abrupt changes as it approaches the perimeter dirt roads.

3. Northeast excavation pit – land is covered with clay and the vegetation is low and sparse alongside the perimeter. On the west side there is a field of sunflowers and on the north side there is a waste landfill. The excavation formed a land ramp that goes down to the lowest parts of the excavation pit, while the edges of the land are very sharp. Several larger water surfaces are also spread out in this area.

Also, for this area, periodic surveying of the terrain was conducted in order to monitor changes on the excavation pit's surface, mainly for the purpose of determining the volume of excavated clay and the estimation of raw-material reserves for future excavations. The observational area was suitable for low UAV flights and 3D models due to its flat topography. The highest point of the observational area was 80 m (above sea level), while the lowest part was 69 m.

## 2.2 UAV and camera

The four-rotor quadcopter UAV, type Anafi Parrot and equipped with a Camera Locations, which was used for this project, is shown in Fig. 4. A three-axis gimbal made it possible to take pictures from different angles and directions. Manual or autonomous navigation was managed with a Parrot Skycontroller 3 flight controller.



**Figure 4.** Unmanned aerial vehicle (UAV) Anafi Parrot.

The 24 megapixel camera equipped with a rolling shutter was adjusted to take one image every 2 seconds, resulting in a database of more than 618 images with a resolution of 4608×3456.

Both oblique and vertical photographs were taken in the observational area. The image calibration was 100 % (618/618 images calibrated). The flight was carried out at a height of 30 m above the average height of the terrain.

## 2.3 Ground control points and check points

In order to determine the spatial location of the 9 GCPs, a fast static GNSS survey was conducted. Each GCP was observed for 20 minutes in fast static GNSS mode, using three Trimble R10 GNSS instruments [21]. This allowed us to obtain valid horizontal coordinates with an accuracy of 3 mm + 0.5 ppm. The RMS precision in a horizontal and 5 mm + 0.5 ppm RMS precision in a vertical position in fast static surveying. For the block adjustment, georeferenced orthophotos and the DSM development, a total of 23 GCPs were used. Absolute accuracy was tested with 26 checkpoints (CPs) that were established in the observational area (Fig. 5). Red-and-white painted metal plates were used as the GCPs and CPs (Fig. 5 and 6).

Leica Geo Office (LGO 2.0) software was used to process the GNSS signals and obtain precise coordinates for the observed points.



**Figure 5.** Layout of ground control points (GCPs) within the observational area. Type of marker (red-and-white plate) is presented in the top-right corner.



**Figure 6.** Positioning marker for GCP or CP.

The coordinates of the check points were calculated by taking the average of the two observations of 5 epochs with a recording interval of 1 second. The coordinates of the 26 CPs are presented in Table 1 (next page).

Problems with the image block absolute positioning within the chosen coordinate frame as well as problems with the deformation effects of the camera's systematic errors, can be solved with an appropriate distribution of the GCP [22]. As a result of the fast static adjustment, the horizontal was 0.01 m and the vertical accuracy was 0.03 m.

**Table 1.** The coordinates ( $x,y,z$ ) of 26 check points (CPs).

ID	$x$ (m)	$y$ (m)	$z$ (m)
o1	7436695.67	5051084.59	77.23
k1	7436695.12	5051084.29	77.22
k2	7436643.42	5051058.71	77.15
o2	7436644.09	5051059.11	77.13
o3	7436632.47	5051137.34	70.11
k3	7436632.75	5051136.59	70.11
o4	7436627.22	5051183.44	70.09
k4	7436627.57	5051182.29	70.09
o5	7436585.07	5051225.70	70.06
k5	7436585.67	5051225.63	70.06
k6	7436620.58	5051219.71	70.61
o7	7436666.29	5051160.47	76.96
o8	7436658.72	5051245.78	76.87
o10	7436658.53	5051267.17	79.07
o11	7436694.74	5051276.42	76.09
o12	7436728.15	5051278.95	76.03
o13	7436677.70	5051301.45	71.68
o14	7436702.28	5051322.14	72.73
o15	7436660.59	5051362.67	75.18
o16	7436634.71	5051384.64	75.27
o17	7436705.42	5051127.03	77.19
o18	7436745.88	5051129.90	77.99
o19	7436735.82	5051040.62	78.22
k7	7436707.93	5051056.45	77.54
k10	7436721.70	5051088.89	76.90
k11	7436701.06	5051099.65	77.21

## 2.4 Flight control

The flight control equipment included an UAV controller in the form of a mobile phone on which a drone-movement-management application and a flight-mission-planning application were installed. Specifically, in our case the Pix4D Capture application was used. The flight control station was established at one of the highest points in the observational area. The flight lasted for approximately 10 minutes. During the flight the mobile phone enabled simultaneous verification of the obtained images. To provide a desired location resolution of 0.02 m or less, the flight height was planned to be approximately 30 m and the overlap rates were 80 % overlapping and 70 % sidelap covering. According to the calculations performed in Pix4D and Agisoft the GSD (Ground Sample Distance) of the data is approximately 0.80 cm and 0.82 cm respectively.

## 3 PROCESSING OF DATA

Pix4Dmapper Pro [23] and Agisoft Metashape Professional [24] were used in the photogrammetric process chains to produce orthophoto and DSM in ITRF (International Terrestrial Reference Frame) datum.

The collected data are images of the observed clayey terrain within an open pit. Initially, all the images were uploaded, then a visual inspection of those that were located on the perimeter was performed, and by recognizing the details of each image, those that covered any terrain beyond our area of interest were removed. The relevant images were imported into both software packages. With Pix4Dmapper the Initial Processing tool was applied, while with Agisoft Metashape we applied the Align Photos tool. In both cases it was possible to set the image size in which the similarity points were searched. After starting the matching process, a cloud of reference tie-points is formed. The latter is not the final targeted point cloud for surface modeling, but it serves to identify two or more images and improve the fit between them. Following the matching process, the next step is to optimize the shots by referencing the coordinates of the GCPs. A list is loaded into the program coordinates, which were previously derived from the GNSS controllers in CSV format.

The image-matching process generated a cloud made up of matching points, which is a preliminary point cloud with a less-frequent density, and from the camera positions and the calculated-depths information, the generation of a high-density point cloud. The generated point clouds with a given level of detail to ‘medium’, in terms of application and quality, are acceptable for further analyses. A dense point cloud was generated for every observation area, as shown in Fig. 7.

The created terrain models in the form of point clouds, such as the results show, result in huge amounts of data [25]. More specifically, the data of such a structure are reflected in a huge number of points, each with its own spatial position and possibly an attached RGB color code, determined by the snapshot from which the data originates. It is this massive quantity of data that is gaining importance in the modern approach to 3D modeling of real objects [26]. From a geodesy point of view, this kind of data structure should be considered as raw data, which, while very faithfully representing reality, also provides a large number of manipulation options for targeted use.

The software packages enable the transformation of models in the point-cloud structure into a series of others, where each derived model can then be exported to a multitude of data formats. In the domain of digital

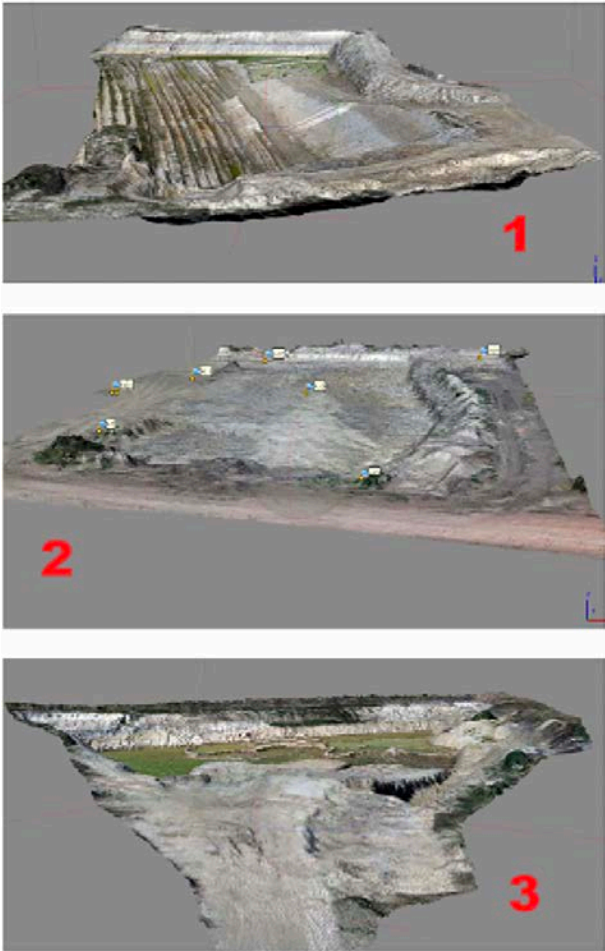


Figure 7. High density 3D point cloud for each observational area.

terrain models, one standard way of interpretation is the DSM structure. The acquisition of UAV data by a diameter system made it possible to obtain a point cloud that displays, in addition to the surface area, the objects on it. The spatial resolution of the digital model is directly related to the level of detail that created the dense cloud point, so the transformation comes down to a choice of projection planes, boundaries, and interpolation modes. For all three projection areas of interest, the chosen map

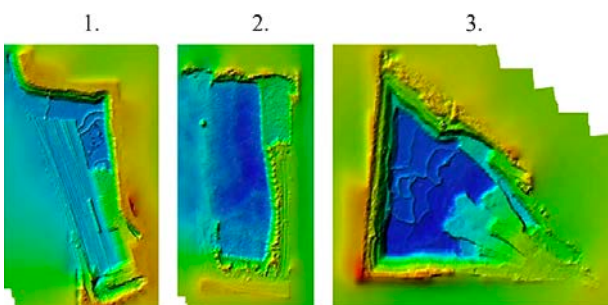


Figure 8. Digital elevation model (DEM) for each observational area.

projections were used, i.e., UTM Zone 34N, geodetic system ETRS89 (Fig. 8).

Twenty-six CPs were used for georeferencing. The coordinates of the dense point cloud were obtained from the photogrammetric process and were referred to as UTM Zone 34N (ETRS89) and the elevation set at Mean Sea Level (MSL) by using the EGM08 geoid model. The coordinates of the 26 CPs, measured by RTK control (Real Time Kinematics GNSS) observations, were compared with the coordinate values obtained from both software programs (Agisoft and Pix4D). A number of overlapping images were computed for each orthomosaic pixel (Fig. 9).

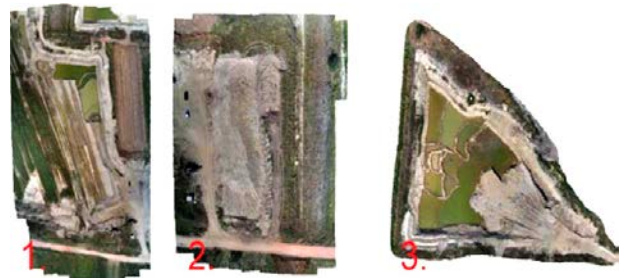


Figure 9. Orthomosaic for each observational area.

Running the procedure opens up a dialog to adjust the projection, which is same as with DEM, reconstructed model source (DEM, MESH) and defining pixel sizes whose standard value is identical to the pixel size for the original photographs. According to the desired usage, the resolution can be optimized with the hardware. The export formats for a model structured this way are: \*.TIFF, \*.JPEG, \*.PNG, \*.KMZ, World Wind Tiles (\*.Zip) and many more.

## 4 RESULTS AND DISCUSSION

The orthophoto and DSM were produced from high-resolution UAV images using Agisoft Metashape Professional and Pix4Dmapper Pro software. Aerial images were taken at heights between 30 and 35 m with 80 % overlapping and 70 % sidelap covering, and were scaled by precisely coordinated locations using static GNSS observations.

Visual inspection is one of the basic controls of the produced DSM. Given the extensiveness and size of the data that was obtained with the UAV photogrammetric techniques, the produced 3D models were very realistic (Fig. 10). Any texture irregularities or model deviations could be easily identified.

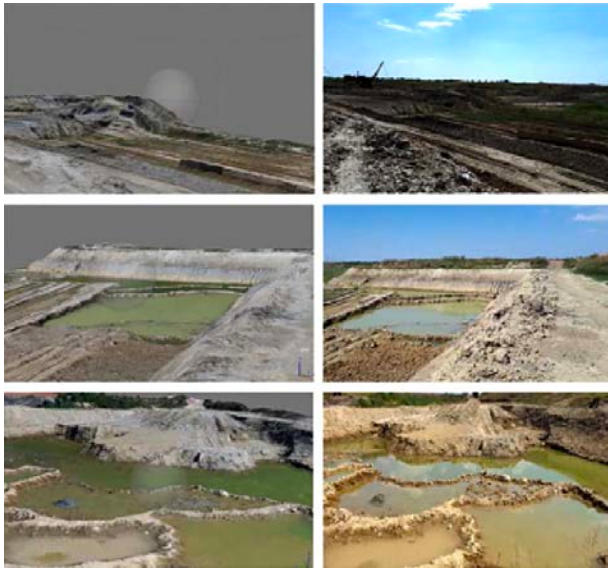


**Figure 10.** Digital surface models (DSMs) and their corresponding ortomosaics.

It is clear that the formed digital model is very true to the picture of the realistic terrain. The identified problematic situations were surfaces covered with water bodies and denser vegetation. Given that two areas were largely underwater and the bottom was not visible, a large noise was observed in the point cloud. This negative phenomenon slightly improves when generating the 3D model, but in some places there were unrealistic peaks of the model.

The method of analysis presented, comparing the formed terrain model with the images and the perception of reality, is based solely on the subjective experiences by the person conducting the inspection. Intro-

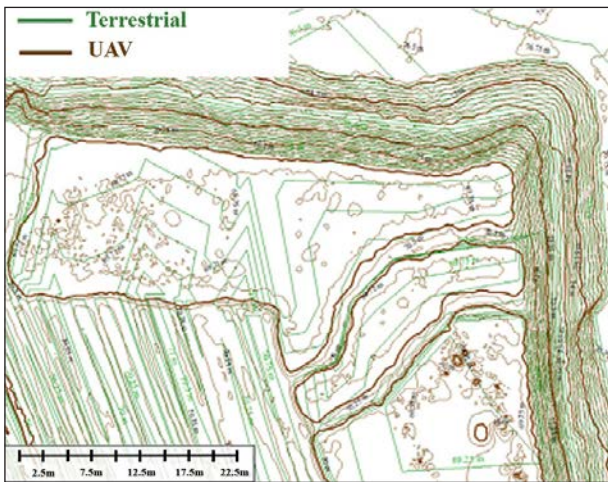


**Figure 11.** Digital surface model (DSM) based on isolines.

ducing symbology and numerics, even in the context of visual inspection can greatly facilitate and reduce the subjective influence in the analysis process. One of ways of representing a DSM is using isolines based on data from terrestrial and UAV surveying (Fig. 11).

The point "water\_Marker" (Fig. 12) was measured on the model immediately adjacent to the land boundary where the noise is less, and it increases moving towards the center of the water surface. Given that the points on the water surface should be the same, this was checked with points reading at different positions on the water surface.

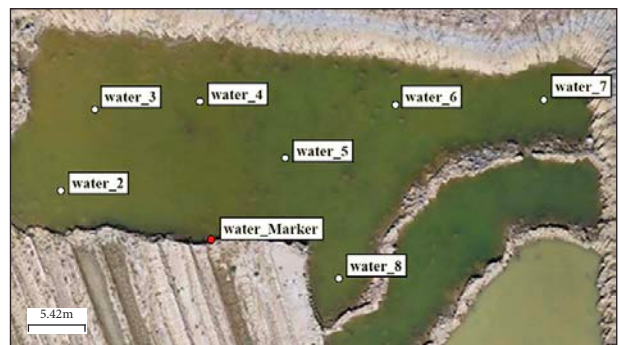


**Figure 12.** Height of points on the surface of the water.

By comparing the marked points on the water surface of the UAV model and the altitude representations of the terrain on the terrestrial model, when there was no water on the ground, a match can be observed (Fig. 13).

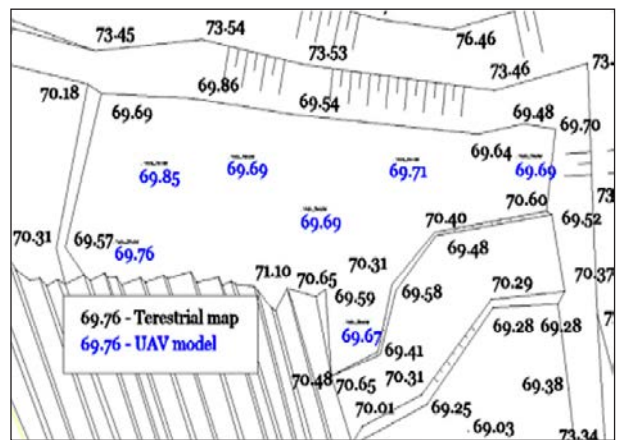


**Figure 13.** Comparing the marked points.

Comparing the elevation points that are more significant to study in the context of using a DSM, it is noticeable that the biggest deviation is at the same point, which is located at the very perimeter of the area, while at other points the deviations are above the expected accuracy.

Therefore, we can assume that the formed digital model is of satisfactory quality (Table 2).

**Table 2.** Control points on the water surface.

ID	Elevation GNSS (m)	Elevation UAV DSM (m)	$\Delta H$ (m)
water_2	69.92	69.76	0.16
water_3	69.92	69.85	0.07
water_4	69.92	69.69	0.23
water_5	69.92	69.69	0.23
water_6	69.92	69.71	0.21
water_7	69.92	69.69	0.23
water_8	69.92	69.67	0.25

For the purpose of a comparative analysis of the UAV digital model with the model and maps, based on terrestrial measurements, the surface points were vectorized and shown in Fig. 14.



**Figure 14.** Vectorization of the 3D terrain model.

These points are of most interest because they are the spatial positions for terrestrial determination. So, the idea was to vectorize the points on the UAV terrain model in the immediate vicinity of the terrestrial points. By selecting the vectorization option, the points on the model are selected, where it is again the best view for vectorization via orthomosaics for realism. In addition to vectorization of the points, it is possible to do the same with lines and polygons, but this geometric format was selected according to the comparative analysis described.

The model of location 3 (the northeast excavation pit) contains a total of 70 vectorized points. Their height differences between the terrestrial and the UAV DEM measurements are given in Table 3.

**Table 3.** Heights from GNSS measurements (I), heights from DEM UAV (II), surface type (III) and height differences (IV).

ID	I	II	III	IV
1	69.66	69.18	Water	48
2	69.68	69.14	Water	54
3	69.65	69.47	Water	18
4	70.05	69.83	Water	21
5	70.20	70.17	Clay	3
6	70.04	70.13	Water	-9
7	70.08	69.91	Water	17
8	70.13	69.66	Water	47
9	70.11	69.78	Water	33
10	70.11	69.66	Water	45
11	69.61	69.26	Water	35
12	69.70	69.48	Water	22
13	69.59	69.06	Water	53
14	69.59	69.07	Water	52
15	71.12	71.13	Clay	-1
16	71.39	71.33	Clay	6
17	71.61	71.41	Clay	20
18	72.19	72.02	Clay	17
19	74.88	74.97	Clay	-10
20	76.04	76.07	Clay	-4
21	74.82	74.86	Clay	-5
22	76.02	76.03	Clay	-1
23	76.15	76.18	Clay	-3
24	76.11	76.10	Clay	1
25	72.60	72.55	Clay	6
26	74.18	74.17	Clay	1
27	72.84	72.74	Clay	11
28	73.66	73.68	Clay	-3
29	75.36	75.37	Clay	-1
30	72.22	72.13	Clay	9
31	72.45	72.28	Clay	17
32	71.87	71.77	Clay	10
33	71.89	71.81	Clay	8
34	72.53	72.56	Clay	-3
35	72.22	72.09	Clay	13
36	75.83	75.83	Clay	0
37	75.94	75.95	Clay	-1
38	75.94	75.94	Clay	0
39	75.96	75.79	Clay	17
40	75.25	74.94	*LV	30
41	75.26	75.09	Clay	18
42	75.01	74.93	Clay	8
43	74.86	74.62	Clay	24
44	74.85	74.65	Clay	20
45	74.60	74.58	Clay	2
46	75.04	74.97	Clay	7
47	71.79	71.69	Clay	10
48	71.83	71.75	Clay	8
49	73.48	73.48	Clay	0
50	75.35	74.88	*LV	47
51	74.86	74.97	Clay	-11
52	74.98	74.92	Clay	6
53	75.37	75.38	Clay	-1
54	75.30	75.27	Clay	3
55	74.83	74.93	Clay	-10
56	71.80	71.57	Clay	23
57	70.06	69.81	Clay	25
58	70.43	70.26	Clay	17
59	72.40	72.58	Clay	-19
60	72.43	72.45	Clay	-2
61	72.73	72.66	Clay	7
62	72.43	72.40	Clay	3
63	72.49	72.34	Clay	15
64	75.22	75.19	Clay	2
65	75.62	75.56	Clay	6
66	77.44	77.22	*LV	22
67	72.99	72.95	Clay	3
68	75.91	75.93	Clay	-2
69	75.34	75.36	Clay	-2
70	76.23	76.24	Clay	-1

I – elevation GNSS (m); II – elevation DEM (m); III – surface type; IV – height difference (cm); \*LV – low vegetation.

In addition, quantitative analyses were considered for the terrestrial and UAV DEM results by profiles. Namely, the terrain profiles in the same area were extracted from the different DEMs and then compared. A comparison of the terrestrial and UAV-based DEM is shown in Fig. 15.

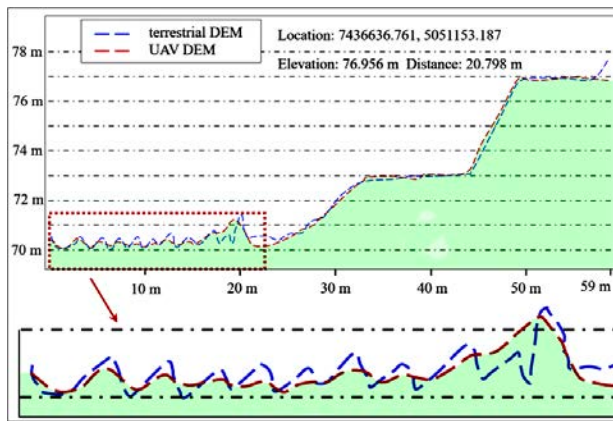


Figure 15. Comparison of terrestrial and UAV-based DEM.

The two DEMs are considered as a good approximation. Some differences occur on the water area and sharp crossings of the terrain. Special attention was given to areas covered with water bodies, because there is the greatest noise on the model. The noise is smaller immediately adjacent to the land boundary and it grows, moving towards the center of the water surface.

## 5 CONCLUSIONS

This study was carried out to obtain high-quality DSMs with an accuracy and precision at the centimeter level. Agisoft Metashape Professional and Pix4Dmapper Pro were used to process the UAV-based photogrammetric high-resolution images, where both software packages produced satisfactory GSD values. At the 26 GCP locations, which were determined by the GNSS measures, the GSD value was calculated as 0.5 cm/pixel with the Agisoft software, while the Pix4D software calculated it as 0.42 cm/pixel. In the resulting 3D point clouds, large noise was observed at the surfaces that were covered with water bodies and denser vegetation. This negative phenomenon slightly improves when generating the digital model, but in some places unrealistic model peaks remain. Nevertheless, when comparing the terrestrial and UAV-based DEM, a good match is shown in areas where no water bodies are present.

UAV-based photogrammetry has clear advantages over piloted aircraft, satellites and traditional surveying

methods, particularly because of the low cost, operational flexibility, better spatial and temporal resolution, and because it requires less time than other techniques for data acquisition. Such approaches can be efficiently applied in situations where classic photogrammetric surveying is not possible.

## Acknowledgments

This study was conducted with the support of the research program P2-0268 and the Slovenian Research Agency. The authors are grateful to the anonymous reviewers and members of the editorial team for their comments.

## REFERENCES

- [1] Burnside, C.D. 1985. The future prospects of data acquisition by photographic and other airborne systems for large scale mapping. *The Photogrammetric Record* 11(65), 495-506. DOI: 10.1111/j.1477-9730.1985.tb00519.x
- [2] Hsieh, Y.C., Perlant, F., McKeown, D.M. 2015. Recovering 3D information from complex aerial imagery. in *Proceedings - International Conference on Pattern Recognition*.
- [3] Candiago, S., et al. 2015. Evaluating multispectral images and vegetation indices for precision farming applications from UAV images. *Remote Sensing* 7(4), 4026-4047. DOI: 10.3390/rs70404026
- [4] Turner, D., Lucieir, A., Wallace, L. 2014. Direct georeferencing of ultrahigh-resolution UAV imagery. *IEEE Transactions on Geoscience and Remote Sensing* 52(5), 2738-2745. DOI: 10.1109/TGRS.2013.2265295
- [5] Gupta, S.K., Shukla, D.P. 2018. Application of drone for landslide mapping, dimension estimation and its 3D reconstruction. *Journal of the Indian Society of Remote Sensing* 46(6), 903-914. DOI: 10.1007/s12524-017-0727-1
- [6] van der Sluijs, J., et al. 2018. Permafrost terrain dynamics and infrastructure impacts revealed by UAV photogrammetry and thermal imaging. *Remote Sensing* 10(11). DOI: 10.3390/rs10111734.
- [7] Niethammer, U., et al. 2011. Open source image-processing tools for low-cost UAV-based landslide investigations. in *International Archives of the Photogrammetry, Remote Sensing and Spatial Information Sciences - ISPRS Archives*.
- [8] Ham, Y., et al. 2016. Visual monitoring of civil infrastructure systems via camera-equipped Unmanned Aerial Vehicles (UAVs): a review of

- related works. *Visualization in Engineering* 4(1). DOI: 10.1186/s40327-015-0029-z
- [9] Siebert, S., Teizer, J. 2014. Mobile 3D mapping for surveying earthwork projects using an Unmanned Aerial Vehicle (UAV) system. *Automation in Construction* 41, 1-14. DOI: 10.1016/j.autcon.2014.01.004
- [10] Chen, J., et al. 2015. Open-pit mining geomorphic feature characterisation. *International Journal of Applied Earth Observation and Geoinformation* 42, 76-86. DOI: 10.1016/j.jag.2015.05.001
- [11] Suh, J., Choi, Y. 2017. Mapping hazardous mining-induced sinkhole subsidence using unmanned aerial vehicle (drone) photogrammetry. *Environmental Earth Sciences* 76(4). DOI: 10.1007/s12665-017-6458-3
- [12] Cara, S., Fiori, M., Matzuzzi, C. 2013. Assessment of landscape by photogrammetry proximity uav survey technique: A case study of an abandoned mine site in the Furtei area (Sardinia-Italy). in 23rd International Mining Congress and Exhibition of Turkey, IMCET 2013.
- [13] Kršák, B., et al. 2016. Use of low-cost UAV photogrammetry to analyze the accuracy of a digital elevation model in a case study. *Measurement: Journal of the International Measurement Confederation* 91, 276-287. DOI: 10.1016/j.measurement.2016.05.028
- [14] Shahbazi, M., et al. 2015. UAV-based point cloud generation for open-pit mine modelling. in *International Archives of the Photogrammetry, Remote Sensing and Spatial Information Sciences - ISPRS Archives*. DOI: 10.5194/isprsarchives-XL-1-W4-313-2015
- [15] Tong, X., et al. 2015. Integration of UAV-based photogrammetry and terrestrial laser scanning for the three-dimensional mapping and monitoring of open-pit mine areas. *Remote Sensing* 7(6), 6635-6662. DOI: 10.3390/rs70606635
- [16] Aicardi, I., et al. 2016. UAV photogrammetry with oblique images: First analysis on data acquisition and processing. in *International Archives of the Photogrammetry, Remote Sensing and Spatial Information Sciences - ISPRS Archives*. DOI: 10.5194/isprsarchives-XLI-B1-835-2016
- [17] Westoby, M.J., et al. 2012. 'Structure-from-Motion' photogrammetry: A low-cost, effective tool for geoscience applications. *Geomorphology* 179, 300-314. DOI: 10.1016/j.geomorph.2012.08.021
- [18] Sanz-Ablanedo, E., et al. 2018. Accuracy of Unmanned Aerial Vehicle (UAV) and SfM photogrammetry survey as a function of the number and location of ground control points used. *Remote Sensing* 10(10). DOI: 10.3390/rs10101606
- [19] Harwin, S., Lucieer, A. 2012. Assessing the accuracy of georeferenced point clouds produced via multi-view stereopsis from Unmanned Aerial Vehicle (UAV) imagery. *Remote Sensing* 4(6), 1573-1599. DOI: 10.3390/rs4061573.
- [20] Mancini, F., et al. 2013. Using unmanned aerial vehicles (UAV) for high-resolution reconstruction of topography: The structure from motion approach on coastal environments. *Remote Sensing* 5(12), 6880-6898. DOI: 10.3390/rs5126880
- [21] Trimble R10. Available online: <https://www.trimble.com/survey/trimble-r10.aspx> (accessed on 14/02/2020).
- [22] Gerke, M., Przybilla H.J. 2016. Accuracy analysis of photogrammetric UAV image blocks: Influence of onboard RTK-GNSS and cross flight patterns. *Photogrammetrie, Fernerkundung, Geoinformation* 2016(1), 17-30. DOI: 10.1127/pfg/2016/0284
- [23] Pix4D. Available online: <https://support.pix4d.com/hc/en-us/sections/360003718992-Manual> (accessed on 14/02/2020).
- [24] Agisoft. Available online: [https://www.agisoft.com/pdf/photoscan-pro\\_1\\_4\\_en.pdf](https://www.agisoft.com/pdf/photoscan-pro_1_4_en.pdf) (accessed on 14/02/2020).
- [25] Zhou, Q. 2017. Digital Elevation Model and Digital Surface Model. *The International Encyclopedia of Geography*, John Wiley & Sons, Inc. 2017, pp 17. <https://doi.org/10.1002/9781118786352.wbieg0768>
- [26] Wilson, J.P., Gallant, J.C. 2000. *Terrain Analysis: Principles and Applications*. John Wiley & Sons, Inc. 2000.

# EXPERIMENTAL INVESTIGATION OF THE INFLUENCE OF RELATIVE EFFECTIVE DIAMETER ON THE ULTIMATE SHEAR STRENGTH OF PARTIALLY SATURATED GRANULAR SOILS

# EKSPERIMENTALNO RAZISKOVANJE VPLIVA RELATIVNEGA EFEKTIVNEGA PREMERA NA MEJNO STRIŽNO TRDNOST DELNO ZASIČENIH GROBO ZRNATIH ZEMLJIN

**Khayreddine Doumi** (*corresponding author*)  
University of Chlef,  
Laboratory of Material Sciences & Environment  
Algeria  
E-mail: doumikhayreddine@gmail.com

**Mostefa Belkhatir**  
University of Chlef,  
Laboratory of Material Sciences  
& Environment  
Algeria

**Abdellah Cherif Taiba**  
University of Chlef,  
Laboratory of Material Sciences  
& Environment  
Algeria

**Youcef Mahmoudi**  
University of Chlef,  
Laboratory of Material Sciences & Environment  
Algeria  
E-mail: doumikhayreddine@gmail.com

**Wiebke Baille**  
Ruhr-Universität Bochum,  
Laboratory of Foundation Engineering  
Bochum, Germany

DOI <https://doi.org/10.18690/actageotechslov.17.1.56-70.2020>

## Keywords

Skempton's parameter, Relative effective diameter, Wet deposition, steady state, sandy soils, triaxial test

## Ključne besede

Skemptonovi parametri, relativni efektivni premer, vlažni sediment, stabilno stanje, peščene zemljine, triosni preizkus

## Abstract

*This experimental investigation describes fundamental research to explore the influence of relative effective diameter on the mechanical behavior, in terms of ultimate shear strength, of partially saturated granular sandy soils. In this context, a series of laboratory triaxial experiments were performed on two groups of sandy soils with three maximum diameters and two different effective diameters under consideration. The sandy-soil samples were reconstituted in the laboratory using the wet deposition method at an initial loose relative density, tested under different Skempton pore-pressure parameters and subjected to a constant confining pressure. The obtained data indicate that the Skempton pore-pressure parameter could be correlated with the ultimate shear strength of the tested materials for medium and higher Skempton pore-pressure parameters and become more significant for lower Skempton*

## Izvleček

*Predstavljena eksperimentalna preiskava opisuje temeljne raziskave za raziskovanje vpliva relativnega učinkovitega premera na mehansko obnašanje delno zasičenih zrnatih peščenih tal. V tem okviru je bila izvedena vrsta laboratorijskih triosnih preizkusov na dveh skupinah peščenih zemljin s tremi maksimalnimi premeri in dvema različnima efektivnima premeroma. Preizkušanci peščene zemljine so bili obnovljeni v laboratoriju po metodi mokrega usedanja pri začetnem rahlem gostotnem stanju, preizkušeni pri različnih parametrih Skemptonovega porenega tlaka in obteženi s stalnim bočnim tlakom. Pridobljeni podatki kažejo, da bi lahko bil parameter Skemptonovega porenega tlaka koreliran z mejno strižno trdnostjo preizkušenih materialov za srednje in višje parametre Skemptonovega porenega tlaka in postal pomembnejši za nižje parametre Skemptonovega*

pore-pressure parameters in the case of a higher effective diameter. Moreover, the obtained test results demonstrate clearly that the maximum diameter is a suitable parameter for an assessment of the monotonic undrained shear strength (known as the static liquefaction resistance) and the brittleness index of the wet deposited samples. In addition, the introduced new parameter named as the relative effective diameter appears as an appropriate factor for predicting the partially saturated ultimate shear strength, the brittleness index and the mobilized ultimate internal friction angle of the two groups of sandy soils.

novega pornega tlaka v primeru višjega učinkovitega premer. Poleg tega dobljeni rezultati preizkusov jasno kažejo, da je maksimalni premer primeren parameter za oceno monotone nedrenirane strižne trdnosti (znane kot statični odpor proti utekočinjanju) in indeksa krhkosti mokro sedimentiranih vzorcev. Poleg tega se predstavljeni nov parameter, imenovan relativni efektivni premer, zdi primeren faktor za napovedovanje mejne strižne trdnosti delno zasičenih zemljin, indeksa krhkosti in mobilizirane mejnega kota notranjega trenja dveh obravnavanih peščenih zemljin.

## Abbreviations

$a, b, c$	= Equation's coefficients
$A_i, B_i, C_i$	= Sandy-soil samples
$B$	= Skempton's pore-pressure parameter
$C_u$	= Coefficient of uniformity
$C_c$	= Coefficient of curvature
$D$	= Diameter of sample
$D_{max}$	= Maximum diameter
$D_{min}$	= Minimum diameter
$D_{10}$	= Effective grain size
$D_{50}$	= Mean grain size
$D_r$	= Initial relative density
$e_i$	= Initial void ratio
$e_{max}, e_{min}$	= Extreme void ratios

$F_c$	= Fines content
$G_s$	= Specific gravity
$H$	= Height of the sample
$H/D$	= Height-to-diameter ratio of the sample
$I_B$	= Brittleness index
$P'_c$	= Initial confining pressure
$q$	= Deviator stress
$q_{peak}$	= Undrained peak shear strength
$q_{ss}$	= Steady-state shear strength
$q_u$	= Ultimate shear strength
$R^2$	= Coefficient of determination
$RED$	= Relative effective diameter
$USCS$	= Unified Soil Classification System
$\omega$	= Water content
$\varphi_u$	= Mobilized ultimate internal friction angle

## 1 INTRODUCTION

The liquefaction of granular sandy soils is one of the most interesting, complex and controversial topics in the geotechnical earthquake engineering field. This phenomenon is characterized by a decrease in the undrained shear strength of saturated sandy soils due to a rapid buildup of the excess pore-water pressure within a short time under monotonic and cyclic loading [1, 2 and 3]. Several investigations into this phenomenon were initiated after the two earthquakes that occurred in Nigita and Alaska in 1964. Many investigations were reported in the published literature regarding the influence of some factors on the liquefaction phenomenon of sandy soils, such as sample preparation, sample size, grain size and shape, grading characteristics, confining pressure, stress history, pre-shearing and loading conditions [3, 4, 5, 6, 7, 8, 9, 10, 11, 12, 13, 14, 15, 16, 17 and 18]. However, the impacts of other variables such as the degree of saturation, particle size and shape, etc. are incomplete and require further investigations.

Moreover, the influence of the degree of saturation has been subjected to extensive research in the published

literature. Indeed, many researchers have indicated that the liquefaction resistance of sandy soils is strongly affected by the degree of saturation which is expressed in terms of Skempton's pore-pressure parameter ( $B$ ) [19, 20, 21, 22, 23, 24, 25 and 26]. Several laboratory tests have shown that the undrained shear strength of sandy soils increased when the degree of saturation decreased [4, 26, 27, 28 and 29]. In [26] the authors found that the liquefaction resistance increased with a decrease in  $B$  value, although it was near zero. Indeed, they showed that with a Skempton's coefficient  $B \geq 80\%$ , it was good enough to apply three cycles to obtain the sample liquefaction; however, eight cycles were needed to reach soil liquefaction of the samples having a coefficient  $B$  close to 50%. Reference [10] indicated that an increase in Skempton's pore-pressure coefficient  $B$  reduced the soil dilatancy and consequently amplified the phase of contractancy. The authors of [30] reported that an increase of Skempton's coefficient ( $B$ ) from 89% to 95% induced a decrease of the initial stiffness of sandy soil and its shear strength and consequently an increase of the contractancy phase leading to a significant increase in the excess pore-water pressure of the tested granular sandy soils. Moreover, they indicated that for lower

loading amplitudes ( $CSR \leq 0.40$ ) for the undrained cyclic tests, the number of cycles required to cause liquefaction increased appreciably with the decrease of the Skempton's coefficient ( $B$ ) of Chlef sandy soils.

On other hand, the influence of particle size distribution is an important subject when assessing the undrained shear strength (liquefaction resistance) response of soils [3, 5, 6, 7, 8, 15, 31, 32, 33, 34, 35 and 36]. In addition, [5] reported that the undrained shear strength of Chlef sand could be correlated with the mean grain size and coefficient ( $D_{50}$  and  $C_u$ ). Reference [6] indicated that the grain size distribution in terms of effective diameter ( $D_{10}$ ), mean grain size ( $D_{50}$ ), coefficient of uniformity ( $C_u$ ), effective size ratio ( $ESR$ ), mean grain size ratio ( $MGRS$ ) and coefficient of uniformity ratio ( $C_{UR}$ ) had significant influences on the excess pore-water pressure of silty sand soils. The authors of [34] showed that for samples with the same relative density, the undrained shear strength and the phase transformation deviatoric stress gradually decreases with the increase of the coefficient of uniformity  $C_u$ . The authors of [37] observed that the liquefaction resistance of clean sand decreases with a decrease of  $D_{50sand}$  and  $C_{usand}$  with the same relative density for the loose samples; however, the undrained shear strength of silty sand soils decreases with an increase of the coefficient of uniformity ( $C_u$ ). In [7 and 8] it was reported that the gradation and particle shape have a significant influence on the undrained shear strength (liquefaction resistance) of two silty sand soils. Moreover, their test results confirm the existence of simple correlations between the liquefaction resistance and the different grading characteristics ( $D_{10}$ ,  $D_{30}$ ,  $D_{50}$ ,  $D_{60}$ ,  $C_u$ ,  $D_{10R}$ ,  $D_{50R}$  and  $C_{UR}$ ) of the tested soils. The authors of [8] suggested that the instability stress and steady-state ratios can be correlated to the grading characteristics ( $D_{10}$ ,  $D_{30}$ ,  $D_{50}$ ,  $D_{60}$ ,  $C_u$ ,  $D_{10R}$ ,  $D_{50R}$  and  $C_{UR}$ ). Indeed, they decrease in a logarithmic and a linear manner with the decrease of grain size ( $D_{10}$ ,  $D_{30}$ ,  $D_{50}$  and  $D_{60}$ ) and an increase of fines content, respectively. However, they decrease logarithmically with an increase of the coefficient of uniformity for the different graded sand-silt mixtures. It was reported in [3] that the grain size distribution in terms of extreme diameters (maximum diameter " $D_{max}$ " and minimum diameter " $D_{min}$ ") and the mean grain size ( $D_{50}$ ) had appropriate effects on the liquefaction resistance of the wet deposited sandy samples reconstituted in the laboratory with an initial relative density ( $D_r=25\%$ ). However, in the published literature, previous studies have not reported the influence of the grain-size distribution on the shear strength of partially saturated sandy soils under consideration.

For this purpose the present study is undertaken to evaluate the influences of a newly proposed grain size distri-

bution named the relative effective diameter ( $RED=D_{10}/D_{max}$ ) on the ultimate shear strength of two groups of granular sandy soils named  $A_1$ ,  $B_1$  and  $C_1$  with the maximum diameter ranging from  $1\text{ mm} \leq D_{max} \leq 4\text{ mm}$  and a constant effective diameter  $D_{10}=0.25\text{ mm}$  for group 1,  $A_2$ ,  $B_2$  and  $C_2$  with a maximum diameter ranging from  $1\text{ mm} \leq D_{max} \leq 4\text{ mm}$  and the same effective diameter  $D_{10}=0.08\text{ mm}$  for group 2. Wet deposition is the most popular laboratory method to prepare loose sandy-soil samples and it consists of placing sand layers of specified thickness into a mold and tamping each layer with a flat tamper [12]. Therefore, it is selected as a suitable sample depositional technique for the present experimental program. All the samples were reconstituted using the wet-deposition method ( $\omega=5\%$ ) at an initial relative density ( $D_r=25\%$ ), tested under three Skempton pore-pressure values ( $B=20\%$ ,  $50\%$  and  $90\%$ ) and subjected to a constant confining pressure ( $P'_c=100\text{ kPa}$ ).

## 2 EXPERIMENTAL PROGRAM

### 2.1 Index properties of tested soils

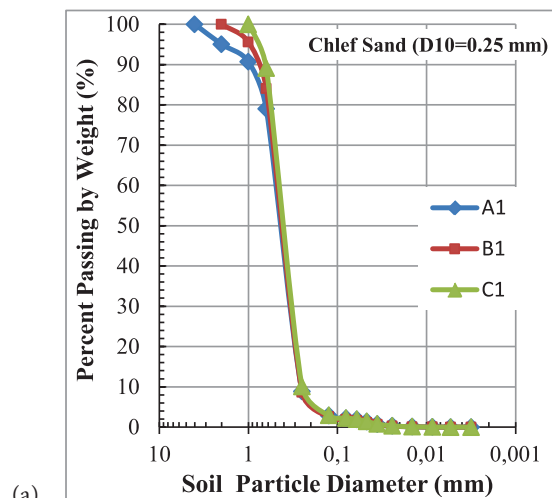
For this investigation the granular sandy-soil samples were obtained from liquefied soil deposit areas along the Chlef River where liquefaction cases were recorded during the 1980 El Asnam earthquake. The samples were collected from the banks of the Chlef River and were used in the preliminary tests as well as in the triaxial tests presented in this laboratory research work. The tested materials were classified according to the Unified Soil Classification System (*USCS*) as poorly graded sandy soils. The index properties of the sandy soils used in this study are summarized in Table 1. Their grain size distribution curves are shown in Figure 1. The tested samples were prepared according to their maximum diameter ( $D_{max}$ ) and effective grain size ( $D_{10}$ ), subdivided into two groups, as indicated in Table 1. The values of the extreme void ratios ( $e_{max}$  and  $e_{min}$ ) of the sandy-soil samples were determined according to standards [38 and 39] for this experimental research.

### 2.2 Sample preparation and test procedure

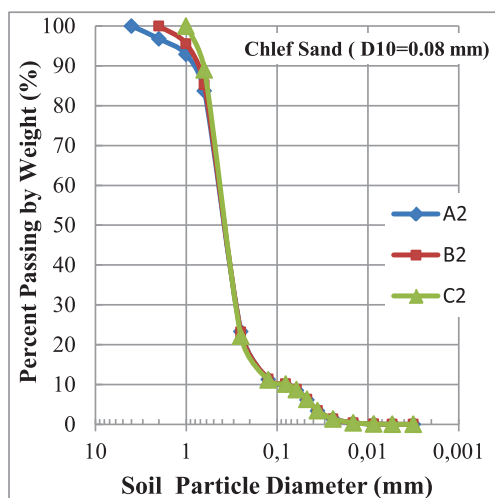
Numerous reconstitution methods have been reported in published literature reviews for the deposition of granular sandy soils, such as wet deposition, dry funnel pluviation, water sedimentation, etc. [2, 5, 7, 8 and 40]. In addition, several researches have clearly shown the impacts of sample-reconstitution techniques on the undrained shear response of granular sandy soils and they have claimed that the wet-deposition method approximates closely to the in-situ fabric of fluvial sandy

**Table 1.** Index properties of tested materials

	Sample	$G_s$	$D_{max}$ (mm)	$D_{min}$ (mm)	$D_{10}$ (mm)	$C_u$	$C_c$	$e_{max}$	$e_{min}$
Group 1	$A_1$	2.674	4	0.0016	0.25	2.080	1.053	0.840	0.635
	$B_1$	2.675	2	0.0016	0.25	1.960	1.058	0.880	0.664
	$C_1$	2.675	1	0.0016	0.25	1.920	0.963	0.889	0.666
Group 2	$A_2$	2.683	4	0.0016	0.08	5.750	2.446	0.772	0.527
	$B_2$	2.684	2	0.0016	0.08	5.875	2.237	0.804	0.552
	$C_2$	2.679	1	0.0016	0.08	5.625	2.336	0.817	0.555



(a)



(b)

**Figure 1.** Grain size distribution curves of tested materials. (a) Group 1 ( $D_{10}=0.25$  mm), (b) Group 2 ( $D_{10}=0.08$  mm).

soils [12, 13, 18 and 41]. In this study all the tested sandy-soil samples were prepared by the wet-deposition method with a constant water content ( $\omega=5\%$ ) and then placed in a cylindrical mold with a diameter of  $D=100$  mm and a height of  $H=200$  mm “ $H/D=2$ ” in

successive layers with a constant thickness of 20 mm for each layer (10 layers). A constant number of strokes were applied with a flat tamper to obtain a homogeneous and isotropic soil fabric. Then, the samples were placed in the classic monotonic triaxial compression. After that, the sandy-soil samples were purged by passing carbon dioxide ( $\text{CO}_2$ ) for different times (15 min for  $B=20\%$ , 25 min for  $B=50\%$  and 35 min for  $B=90\%$ ). In addition, the samples were also saturated with de-aerated and demineralized water. In this experimental investigation, a back pressure of 200 kPa was applied for all the performed tests and the sandy-soil samples were subjected to a constant effective stress of  $P'_c=100$  kPa. All the undrained monotonic triaxial tests were carried out at a constant strain rate of 0.225 mm per minute, which was slow enough to allow the pore-pressure change to equalize throughout the sample with the pore pressure measured at the base of the sample.

### 2.3 Relationship between the void ratio index and the relative effective diameter

For the purpose of evaluating the relationship between the extreme void ratio index in terms of maximum void ratio ( $e_{max}$ ) and minimum void ratio ( $e_{min}$ ) with the proposed grain size ratio named as the relative effective diameter ( $RED=D_{10}/D_{max}$ ) for the two groups of sandy soils named as  $A_1$ ,  $B_1$  and  $C_1$  with the maximum diameter  $1 \text{ mm} \leq D_{max} \leq 4 \text{ mm}$  and effective diameter  $D_{10}=0.25$  mm for group 1 and  $A_2$ ,  $B_2$  and  $C_2$  with the maximum diameter  $1 \text{ mm} \leq D_{max} \leq 4 \text{ mm}$  and the effective diameter  $D_{10}=0.08$  mm for group 2 under study. It is clear from Figure 2 that the extreme void ratios ( $e_{max}$  and  $e_{min}$ ) display a logarithmic relationship with the relative effective diameter ( $R^2=0.99$ ) for all the tested materials under consideration. Indeed, the maximum and minimum void ratios ( $e_{max}$  and  $e_{min}$ ) increase with the increase of the relative effective diameter of the selected sandy soils for the two values of the effective diameter ( $D_{10}=0.25$  mm and  $D_{10}=0.08$  mm) and the maximum diameter range ( $1 \text{ mm} \leq D_{max} \leq 4 \text{ mm}$ ).

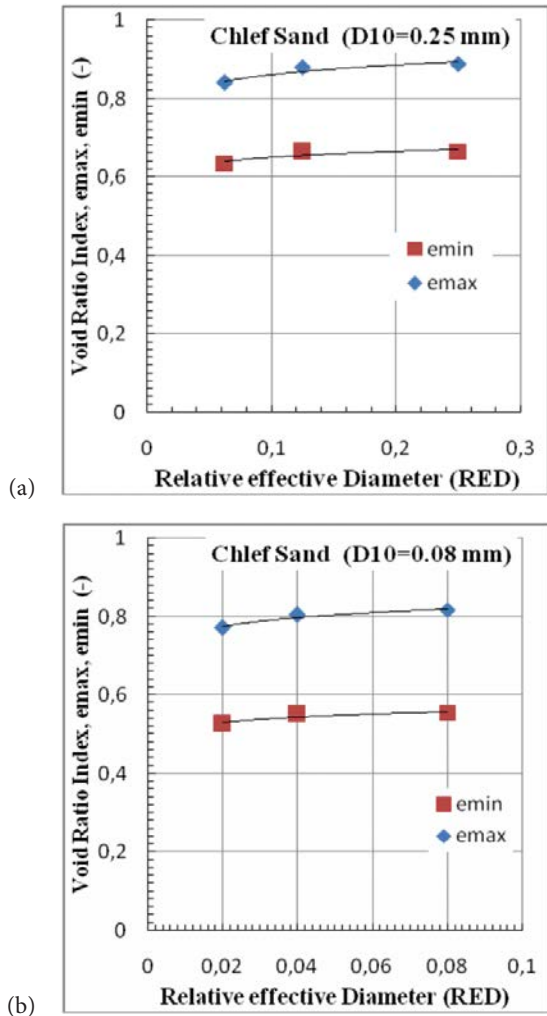


Figure 2. Extreme voids ratios index versus relative effective diameter. (a) Group 1 ( $D_{10}=0.25$  mm), (b) Group 2 ( $D_{10}=0.08$  mm).

### 3 RESULTS AND DISCUSSION

The result of the undrained monotonic compression triaxial tests performed on two groups and each group reconstituted of three sandy-soil samples named as  $A_1$ ,  $B_1$  and  $C_1$  with the same effective diameter ( $D_{10}=0.25$  mm) and three values of the maximum diameter of  $D_{max}=4$  mm for  $A_1$ ,  $D_{max}=2$  mm for  $B_1$  and  $D_{max}=1$  mm for  $C_1$  for group 1 and three sandy soils termed as  $A_2$ ,  $B_2$  and  $C_2$  reconstituted with an effective diameter of  $D_{10}=0.08$  mm with three different maximum diameter values ( $D_{max}=4$  mm, 2 mm and 1 mm), respectively, for group 2. All the samples were reconstituted with an initial relative density of  $D_r=25\%$  and subjected to three different values of Skempton's pore-pressure parameter ( $B=20\%$ ,  $50\%$  and  $90\%$ ) and a constant confining pressure of  $P'_c=100$  kPa.

#### 3.1 Undrained monotonic triaxial compression test results

##### 3.1.1 Group 1 ( $A_1$ , $B_1$ and $C_1$ with $D_{10}=0.25$ mm)

Figures 3,4 and 5 illustrate the undrained monotonic triaxial compression tests performed on three laboratory-reconstituted sandy-soil samples named  $A_1$ ,  $B_1$  and  $C_1$  with the same effective diameter ( $D_{10}=0.25$  mm). It can be observed from these figures that completed and limited static liquefaction cases were recorded for the different tested samples under different Skempton pore-pressure parameters ( $B$ ) with a clear impact of the maximum diameter  $D_{max}$  on the undrained shear strength (static liquefaction resistance) response. Moreover, it is clear that the undrained shear strength (liquefaction resistance) of the samples  $A_1$ ,  $B_1$  and  $C_1$  increases with the decrease of

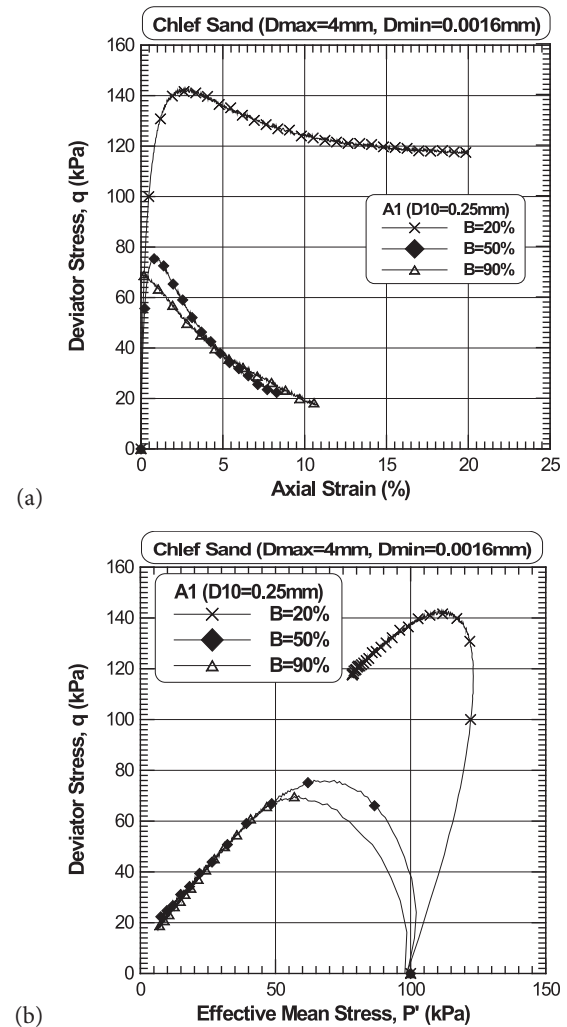
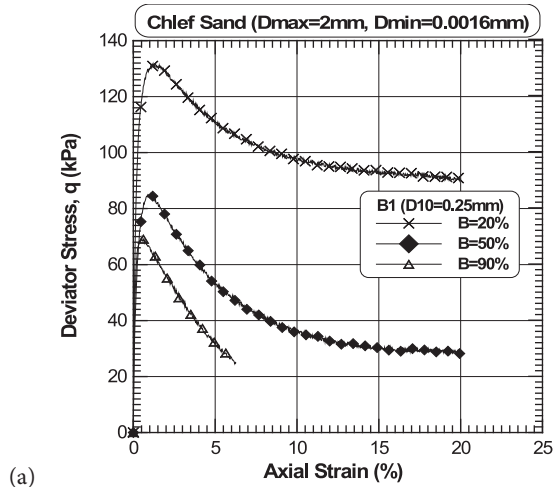
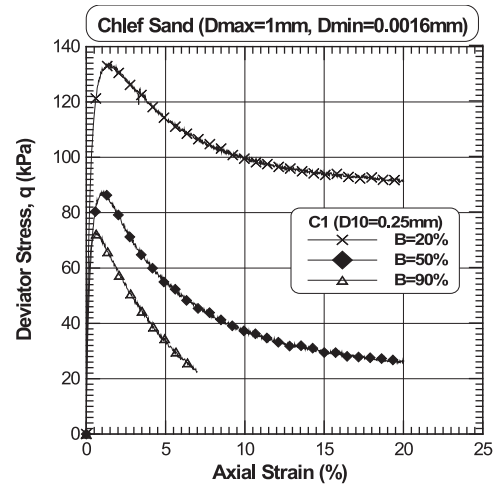


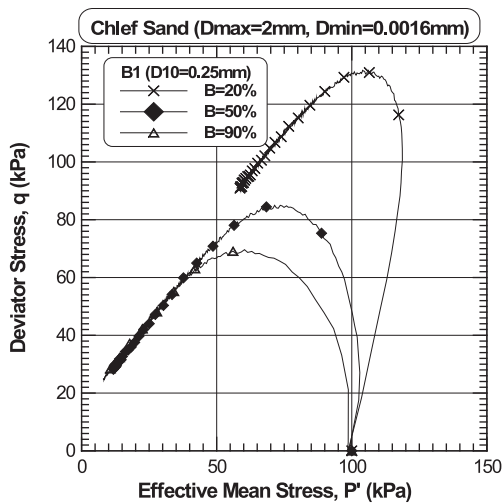
Figure 3. Undrained monotonic behavior of Chlef sandy soils ( $A_1$ ) ( $D_{max}=4$  mm,  $D_{min}=0.0016$  mm,  $D_{10}=0.25$  mm,  $D_r=25\%$ ,  $P'_c=100$  kPa). (a) Deviator stress versus axial strain. (b) Deviator stress versus Effective mean Stress.



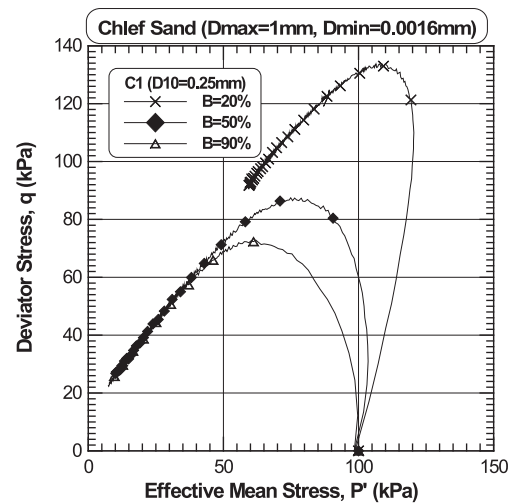
(a)



(a)



(b)



(b)

**Figure 4.** Undrained monotonic behavior of Chlef sandy soils ( $B_1$ ) ( $D_{max}=2$  mm,  $D_{min}=0.0016$  mm,  $D_{10}=0.25$  mm,  $D_r=25$  %,  $P'_c=100$  kPa). (a) Deviator stress versus axial strain. (b) Deviator stress versus Effective mean Stress.

**Figure 5.** Undrained monotonic behavior of Chlef sandy soils ( $C_1$ ) ( $D_{max}=1$  mm,  $D_{min}=0.0016$  mm,  $D_{10}=0.25$  mm,  $D_r=25$  %,  $P'_c=100$  kPa). (a) Deviator stress versus axial strain. (b) Deviator stress versus Effective mean Stress.

**Table 2.** Summary of undrained monotonic triaxial tests for group 1.

Characteristics of materials	$A_1$			$B_1$			$C_1$		
	20	50	90	20	50	90	20	50	90
$B$ (%)	20	50	90	20	50	90	20	50	90
$q_u$ (kPa)	117.85	21.83	17.67	90.54	28.68	24.86	91.40	26.43	22.50
$RED$ (-)	0.0625	0.0625	0.0625	0.125	0.125	0.125	0.25	0.25	0.25
$\varphi_u$ (°)	34.48	57.62	57.71	35.18	49.16	58.29	35.10	52.99	57.73
$I_B$ (-)	0.17	0.71	0.75	0.31	0.66	0.64	0.32	0.70	0.69
Soil response	All the samples exhibit flow behavior								

Skempton's pore-pressure parameter in the range 50–90 % and becomes more obvious at a lower Skempton's pore-pressure parameter  $B=20$  %. In addition, the obtained data indicate that the percentage of increasing in the shear

strength is 0.09 %, 22 % and 20 % for the range of Skempton's pore-pressure parameter ( $B=50-90$  %) and becomes very significant (87 %, 55 % and 53 %) in the range of Skempton's pore-pressure parameter ( $B=20-50$  %) for the

tested sandy-soil samples  $A_1$ ,  $B_1$  and  $C_1$  respectively. This sandy-soils trend can be attributed to the increase in the particle interlocking between the coarse grains of sandy soils due to the decrease of Skempton's pore-pressure parameter inducing a contractive character of the tested samples. Therefore, the higher peak undrained shear strength correspondsto the higher maximum diameter ( $D_{max}=4$  mm) and the lower Skempton's pore-pressure parameter ( $B=20\%$ ). In contrast, the inverse tendency is observed for the higher Skempton's pore-pressure parameters ( $B=50\%$  and  $B=90\%$ ) where they exhibit the lower peak undrained shear strength with the increasing of the maximum diameter from  $D_{max}=1$  mm to  $D_{max}=4$  mm for the tested materials. In addition, all the samples  $A_1$ ,  $B_1$  and  $C_1$  indicate that the ultimate shear strength is reached within 10–20 % axial strain (Figures 3a, 4a and 5a). Our findings are in good agreement with the observations of

[4, 10 and 24]. The stress path in the ( $p'$ ,  $q$ ) plane clearly shows the role of the Skempton's pore-pressure parameter and the maximum diameter ( $B$  and  $D_{max}$ ) in the decrease of the average effective stress and the maximum deviatoric stress (Figures 3b, 4b and 5b). A summary of the undrained monotonic triaxial tests results for group 1 are summarized in Table 2.

### 3.1.2 Group 2 ( $A_2$ , $B_2$ and $C_2$ with $D_{10}=0.08$ mm)

Figures 6, 7 and 8 show the undrained-shear-strength response of three granular sandy soils termed as  $A_2$ ,  $B_2$  and  $C_2$ , reconstituted with an effective diameter of  $D_{10}=0.08$  mm. The test results demonstrate clearly that the completed and limited static liquefaction cases were recorded for the different tested samples under different values of the Skempton's pore-pressure parameter ( $B=20\%$ ,  $50\%$  and  $90\%$ ) with a clear impact of

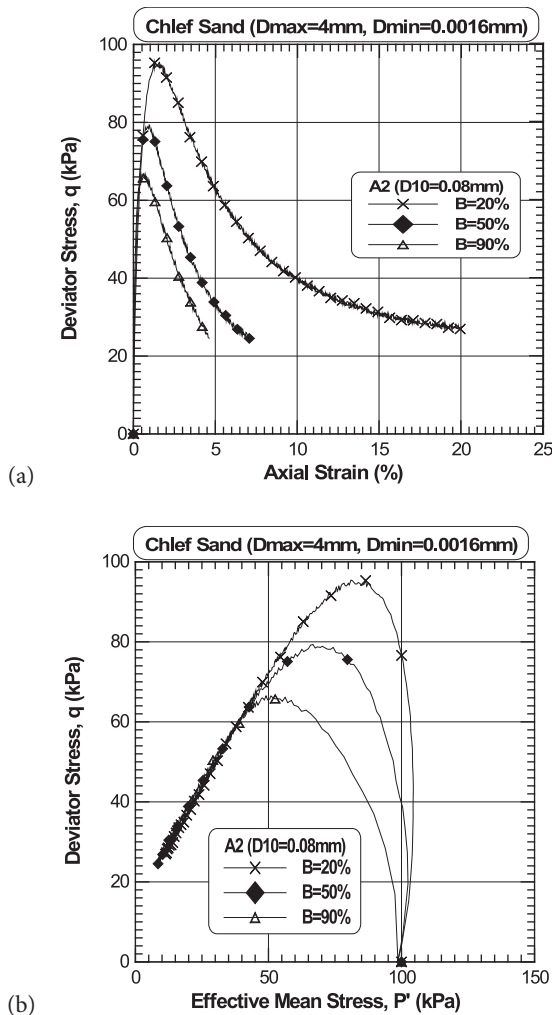


**Figure 6.** Undrained monotonic behavior of Chlef sandy soils ( $A_2$ ) ( $D_{max}=4$  mm,  $D_{min}=0.0016$  mm,  $D_{10}=0.08$  mm,  $D_r=25\%$ ,  $P'_c=100$  kPa). (a) Deviator stress versus axial strain. (b) Deviator stress versus Effective mean Stress.

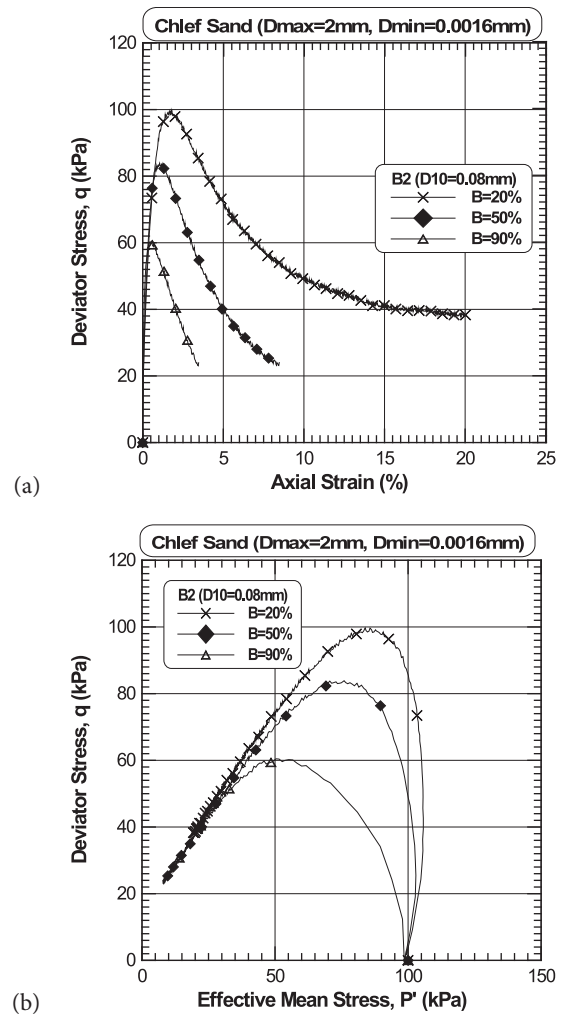


**Figure 7.** Undrained monotonic behavior of Chlef sandy soils ( $B_2$ ) ( $D_{max}=2$  mm,  $D_{min}=0.0016$  mm,  $D_{10}=0.08$  mm,  $D_r=25\%$ ,  $P'_c=100$  kPa). (a) Deviator stress versus axial strain. (b) Deviator stress versus Effective mean Stress.

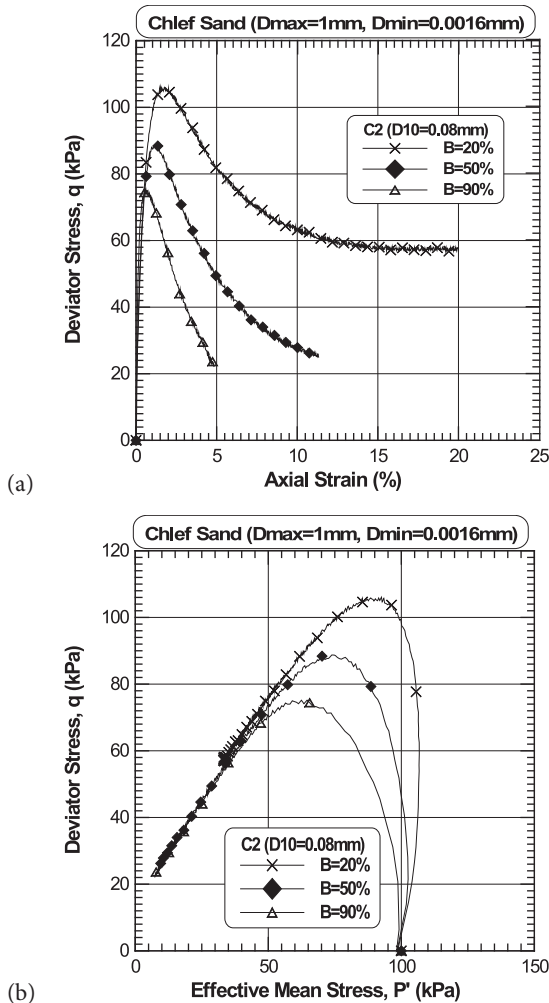


**Figure 8.** Undrained monotonic behavior of Chlef sandy soils ( $C_2$ ) ( $D_{max}=1\text{ mm}$ ,  $D_{min}=0.0016\text{ mm}$ ,  $D_{10}=0.08\text{ mm}$ ,  $D_r=25\%$ ,  $P'_c=100\text{ kPa}$ ). (a) Deviator stress versus axial strain. (b) Deviator stress versus Effective mean Stress.

the maximum diameter  $D_{max}$  on the undrained shear strength behavior.

Moreover, the undrained shear strength of the samples  $A_2$ ,  $B_2$  and  $C_2$  decreases with the increase of the

Skempton's pore-pressure parameter. In addition, for the lower Skempton's pore-pressure parameter ( $B=20\%$ ), the higher maximum diameter ( $D_{max}=4\text{mm}$ ) exhibits the lower peak undrained shear strength. The inverse tendency is observed for the higher values of the Skempton's pore-pressure parameter ( $B=50\%$  and  $B=90\%$ ). Therefore, the obtained data indicate that the ultimate shear strength is reached within 4–20 % axial strain for all the sandy-soil samples  $A_2$ ,  $B_2$  and  $C_2$ , see Figures 6a, 7a and 8a, respectively. The obtained results are in good agreement with the results of [4, 10 and 24]. The stress path in the ( $p'$ ,  $q$ ) plane shows clearly the role of the Skempton's pore-pressure parameter ( $B$ ) and the maximum diameter ( $D_{max}$ ) in decreasing the average effective stress and the maximum deviatoric stress (Figures 6b, 7b and 8b). A summary of the undrained monotonic triaxial tests results for group 2 are summarized in Table 3.

### 3.2 Effect of Skempton's pore pressure on the undrained ultimate shear strength

Figure 9 summarizes the effect of Skempton's pore-pressure parameter ( $B=20\%$ ,  $B=50\%$  and  $B=90\%$ ) on the undrained ultimate shear strength of six sandy-soil samples ( $A_1$ ,  $B_1$ ,  $C_1$ ,  $A_2$ ,  $B_2$  and  $C_2$ ). It is clear from Figure 9 that the decrease of the Skempton's pore-pressure parameter leads to a remarkable increase of the undrained ultimate shear strength and becomes more significant for the lower Skempton's pore-water pressure ( $B=20\%$ ) of the tested sandy-soil samples. The obtained data indicate that the sandy-soil samples with the higher maximum diameter ( $D_{max}=4\text{ mm}$ ) and the lower Skempton's pore-pressure parameter ( $B=20\%$ ) exhibit a higher undrained ultimate shear strength compared to that induced by higher Skempton's pore-pressure parameters ( $B=50\%$  and  $90\%$ ) for the tested samples of group 1.

In contrast, the inverse tendency was observed in the case of group 2, where the sandy-soil samples with the higher maximum diameter ( $D_{max}=4\text{ mm}$ ) exhibited a lower undrained ultimate shear strength for the same Skempton's pore-pressure parameter ( $B=20\%$ )

**Table 3.** Summary of undrained monotonic triaxial tests for group 2.

Characteristics of materials	$A_2$			$B_2$			$C_2$		
$B$ (%)	20	50	90	20	50	90	20	50	90
$q_u$ (kPa)	27.57	24.46	24.58	38.33	24.02	23.95	56.92	25.97	23.67
$RED$ (-)	0.02	0.02	0.02	0.04	0.04	0.04	0.08	0.08	0.08
$\phi_u$ ( $^\circ$ )	49.65	58.58	57.71	42.78	57.69	57.72	37.99	57.44	57.57
$I_B$ (-)	0.71	0.69	0.63	0.62	0.71	0.63	0.46	0.71	0.69
Soil response	All the samples exhibit flow behavior								

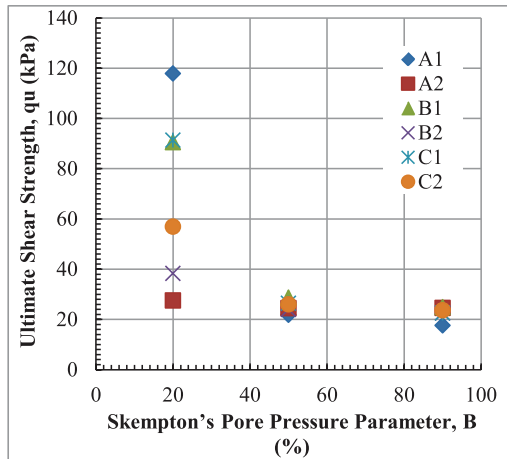
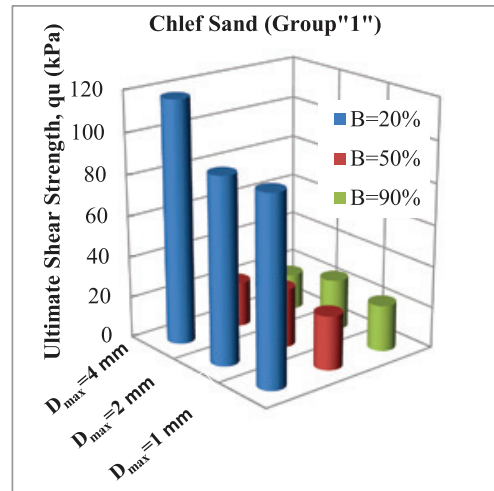


Figure 9. Ultimate shear strength versus Skempton's pore-pressure parameter of the sandy soils ( $D_r=25\%$ ,  $P'_c=100$  kPa).

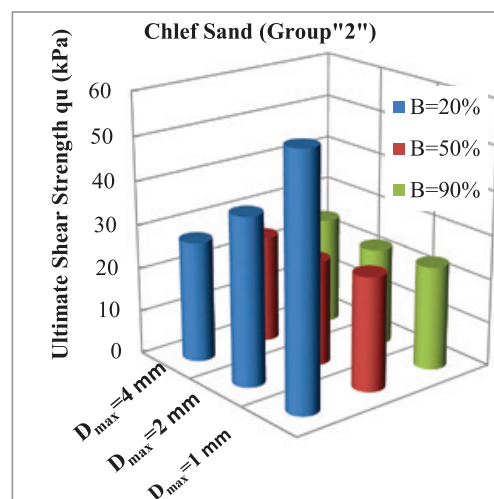
compared to the higher Skempton's pore-pressure parameters ( $B=50\%$  and  $90\%$ ). In addition, the ultimate shear strength of the sandy-soil samples of group 1 is more significant than that of group 2. This behavior indicates that the increasing in the effective diameter leads to a significant increase in the undrained ultimate shear strength of the tested sandy soils under consideration. Moreover, the sandy-soil samples of group 2 with an effective diameter  $D_{10}=0.08$  mm demonstrate clearly that the presence of the low plastic fines between the coarse grains of  $A_2$ ,  $B_2$  and  $C_2$  makes the sandy soils more compressible, leading to a reduction of the interparticle forces and consequently to a decrease in the undrained ultimate shear strength of the used materials.

### 3.3 Effect of the maximum diameter on the undrained ultimate shear strength

The influence of maximum diameter ( $D_{max}$ ) on the undrained ultimate shear strength ( $q_u$ ) of the two groups of sandy soils is illustrated in Figure (10). It is clear from the bar chart that the maximum diameter ( $D_{max}$ ) exhibits a significant influence on the undrained ultimate shear strength of the tested materials. Indeed, the undrained ultimate shear strength increases with the increase of the maximum diameter for the lower value of the Skempton's pore pressure ( $B=20\%$ ) in the case of the group 1 samples, while the inverse tendency was observed for the sandy-soil samples of group 2, where the undrained ultimate shear strength decreases with the increase of the maximum diameter for the same Skempton's coefficient ( $B=20\%$ ). The observed tendency can be attributed to the combined effects of the maximum and effective diameters with ( $B=20\%$ ) in the increasing and decreasing of the interparticle forces between the coarse grains for group 1 ( $D_{10}=0.25$  mm, the small amount of



(a)



(b)

Figure 10. Ultimate shear strength versus maximum diameter of sandy soils. ( $D_r=25\%$ ,  $P'_c=100$  kPa).

(a) Group 1 ( $D_{10}=0.25$  mm). (b) Group 2 ( $D_{10}=0.08$  mm).

low plastic fines  $F_c \leq 3\%$ ) and group 2 ( $D_{10}=0.08$  mm), the presence of low plastic fines  $F_c=10\%$  leading to a decrease of the interlocking of the coarse particles and consequently to a significant decrease in the undrained shear strength. In contrast, quite similar observations were recorded for the ultimate shear strength in the case of the intermediate and higher Skempton's coefficients ( $B=50\%$  and  $90\%$ ) for all the tested sandy-soil samples.

### 3.4 Effect of the relative effective diameter on the undrained ultimate shear strength

The effect of the relative effective diameter ( $RED=D_{10}/D_{max}$ ) on the undrained ultimate shear strength ( $q_u$ ) of the two groups of sandy soils is shown in Figure (11). The obtained data from the current study indicate that the relative effective diameter ( $RED$ ) could be correlated

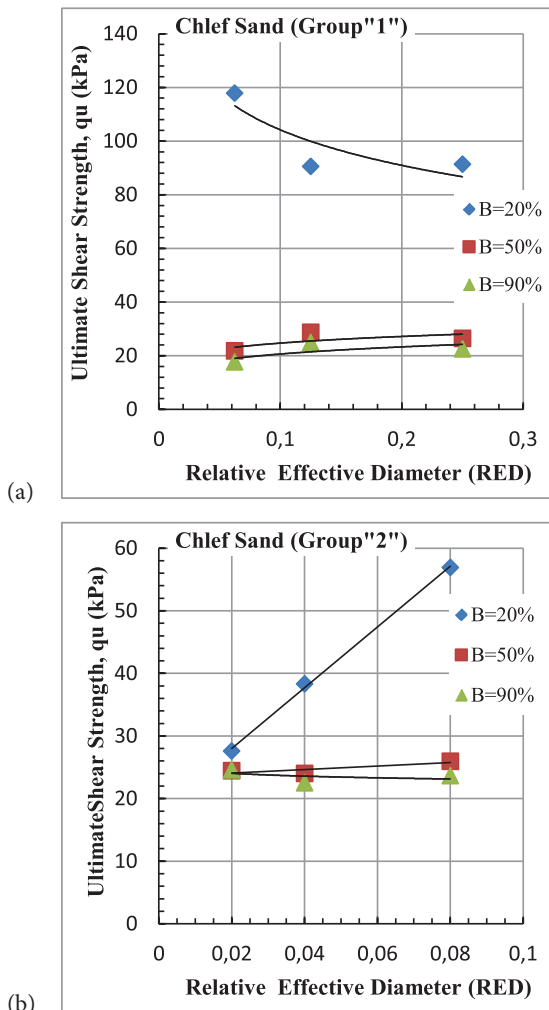


**Figure 11.** Undrained ultimate shear strength versus relative effective diameter ( $D_r=25\%$ ,  $P'_c=100$  kPa). (a) Group 1 ( $D_{10}=0.25$  mm). (b) Group 2 ( $D_{10}=0.08$  mm).

with the undrained ultimate shear strength of the tested sandy soils for the tested Skempton’s pore-pressure parameter ( $B=20\%$ ,  $50\%$  and  $90\%$ ) values under study.

In addition, it is clear from Figure 11a that the undrained ultimate shear strength decreases with an increase of the relative effective diameter for the lower Skempton’s pore-pressure parameter ( $B=20\%$ ) for the samples of group 1. However, the inverse tendency is observed for the intermediate and higher Skempton’s pore-pressure parameter ( $B=50\%$  and  $90\%$ ) for the same group, where the ultimate shear strength increases with the increase of the relative effective diameter (RED). For group 2, the tested sandy-soil samples exhibit the opposite trend for all the considered Skempton’s pore pressures ( $B=20\%$ ,  $50\%$  and  $90\%$ ) (Figure 11b). On the other hand, it can be seen from these plots that the variation of the undrained

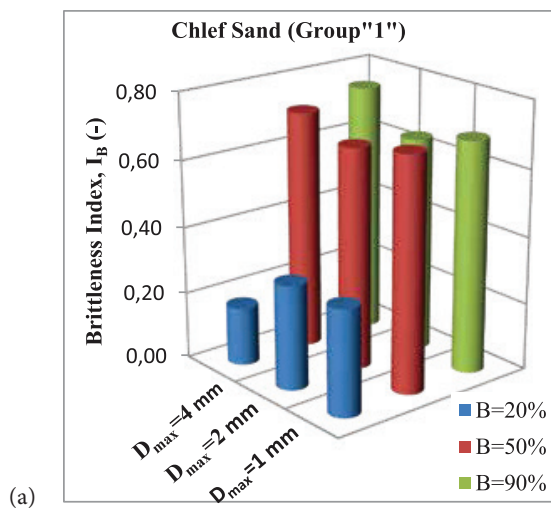
ultimate shear strength ( $q_u$ ) with the relative effective diameter (RED) of the tested sandy soils for the lower Skempton’s pore-pressure parameter ( $B=20\%$ ) is highly affected rather than that of the intermediate and higher Skempton’s pore-pressure parameter ( $B=50\%$  and  $B=90\%$ ) for both groups under consideration. These tendencies confirm that the decrease in the Skempton’s pore-pressure parameter induces a significant increase of the interparticle forces between the coarse and fine grains, inducing a clear increase of the undrained ultimate shear strength of the tested materials under study. However, the relative effective diameter (RED) has an effect on the resistance liquefaction. The results of the ultimate shear strength are summarized in Tables 2 and 3, respectively, for group 1 and group 2.

### 3.5 Effect of the maximum diameter and Skempton’s pore-pressure parameter on the brittleness index of the sandy soils

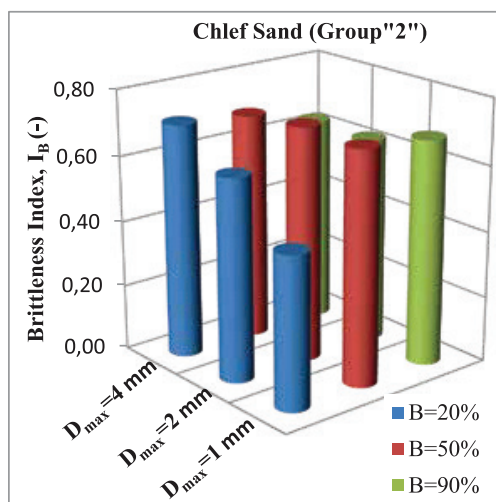
To quantify the amount of strain softening during undrained loading, [42] proposed a new parameter to identify this behavior named the brittleness index ( $I_B$ ), which is defined as:

$$I_B = \frac{q_{Peak} - q_{ss}}{q_{Peak}} \quad (1)$$

where  $q_{peak}$  is the peak shear strength (instability point in the plane of the stress path) and  $q_{ss}$  is the steady-state shear strength. In which  $I_B$  ranges  $0 \leq I_B \leq 1$ . If  $I_B=1$ , the soil exhibits a very brittle response associated with lower steady-state shear strength (complete liquefaction). In contrast, if  $I_B=0$ , the soil occurs in a non-brittle or strain-hardening response (non-flow). Based on these findings, Figure 12 presents the impacts of the maximum diameter and Skempton’s pore-pressure parameter on the brittleness index ( $I_B$ ) of the two types of sandy soils. In general, the obtained data indicate that the brittleness index ( $I_B$ ) affects significantly the mechanical behavior of the tested sandy soils, considering the effects of the maximum diameter ( $D_{max}$ ) and the Skempton’s pore-pressure parameter ( $B$ ). Indeed, it is clear from the bar chart (Figure 12a) that the increase of maximum diameter leads to a remarkable decreasing of the brittleness index for the lower Skempton’s pore-pressure parameter ( $B=20\%$ ) of the tested materials. The inverse tendency was observed for the sandy soils of group 2 considering the same Skempton’s pore-pressure parameter ( $B=20\%$ ) (Figure 12b). This variation is more significantly affected for group 2, compared to group 1. However, similar brittleness index ( $I_B$ ) values were obtained for intermediate and higher Skempton’s coefficients ( $B=50\%$  and  $90\%$ ) for all the tested sandy-soil samples. The results are summarized in Tables 2 and 3 for group 1 and group 2, respectively.

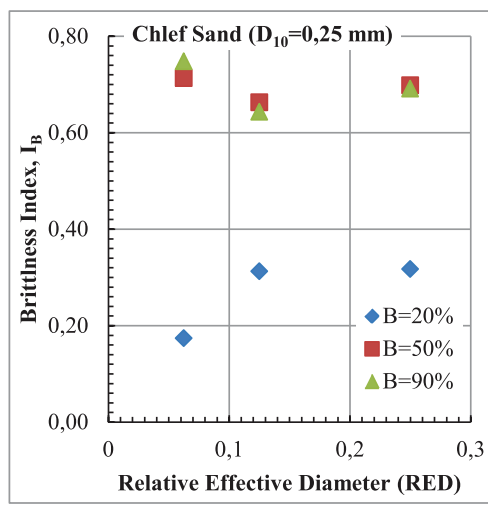


(a)

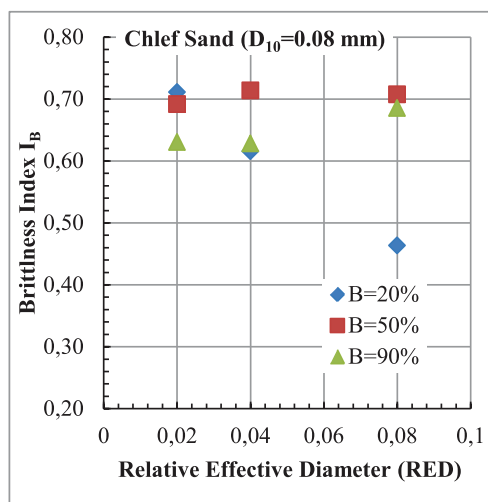


(b)

**Figure 12.** Brittleness index versus maximum diameter of sandy soils ( $D_r=25 \%$ ,  $P'_c=100 \text{ kPa}$ ). (a) Group 1 ( $D_{10}=0.25 \text{ mm}$ ). (b) Group 2 ( $D_{10}=0.08 \text{ mm}$ ).



(a)



(b)

**Figure 13.** Brittleness index versus relative effective diameter of sandy soils ( $D_r=25 \%$ ,  $P'_c=100 \text{ kPa}$ ). (a) Group 1 ( $D_{10}=0.25 \text{ mm}$ ). (b) Group 2 ( $D_{10}=0.08 \text{ mm}$ ).

### 3.6 Relationship between the brittleness index and the relative effective diameter

The relationship between the brittleness index ( $I_B$ ) and the relative effective diameter ( $RED$ ) of six sandy-soil samples ( $A_1, B_1$  and  $C_1$  for group 1 and  $A_2, B_2$  and  $C_2$  for group 2) is discussed in this section. The test results show that the brittleness index could be correlated with the relative effective diameter of the tested materials for all the parameters under consideration. In addition, it is clear from Figure 13a that the brittleness index ( $I_B$ ) increases with an increase of the relative effective diameter ( $RED$ ) for the lower Skempton's pore-pressure parameter ( $B=20 \%$ ) of the tested sandy-soil samples of

group 1. However, the inverse tendency was observed for the intermediate and higher Skempton's pore-pressure parameter ( $B=50 \%$  and  $90 \%$ ), where the brittleness index ( $I_B$ ) decreases with the increase of the relative effective diameter ( $RED$ ) of the tested materials ( $A_1, B_1$  and  $C_1$ ) under study. Moreover, it is clear from Figure 13b that the brittleness index decreases with an increase of the relative effective diameter ( $RED$ ) of the tested materials under a lower Skempton's pore-pressure parameter ( $B=20 \%$ ). In contrast, the inverse tendency was shown for two other Skempton pore-pressures parameters ( $B=50 \%$  and  $90 \%$ ), where the brittleness index increases with an increase of the relative effective diameter for the sandy-soil samples ( $A_2, B_2$  and  $C_2$ ).

### 3.7 Relationship between Skempton's pore-pressure parameter and the mobilized ultimate internal friction angle of sandy soils

The correlation between the Skempton's pore-pressure parameter ( $B$ ) and the mobilized ultimate internal friction angle ( $\phi_u$ ) for the two groups is presented in Figure (14). The obtained data indicate that the Skempton's pore-pressure parameter could be correlated with the mobilized ultimate internal friction angle of the tested materials. Indeed, the mobilized ultimate internal friction angle increases in a good polynomial manner ( $R^2=0.83$ ) with an increase of the Skempton's pore-pressure parameter from  $B=20\%$  to  $B=90\%$  of the  $A_1, B_1$  and  $C_1$  for group 1 and  $A_2, B_2$  and  $C_2$  for group 2. Moreover, it is clear from Figure 14 that the higher Skempton's pore-pressure parameter ( $B=90\%$ ) indicates a similar undrained mobilized ultimate internal friction angle for all the used materials compared to the lower Skempton's pore-pressure parameter ( $B=20\%$  and  $50\%$ ), where the tendency shows a higher range between the values of the mobilized ultimate internal friction angle of the tested materials under study. This trend confirms that the Skempton's pore-pressure parameter has a significant influence on the undrained shear strength and consequently on the undrained mobilized ultimate internal friction angle of the sandy soils, where it has a remarkable effect on increasing the interparticle forces between the coarse and fine grains, leading to an important increase in the mobilized ultimate internal friction angle of the tested sandy soils.

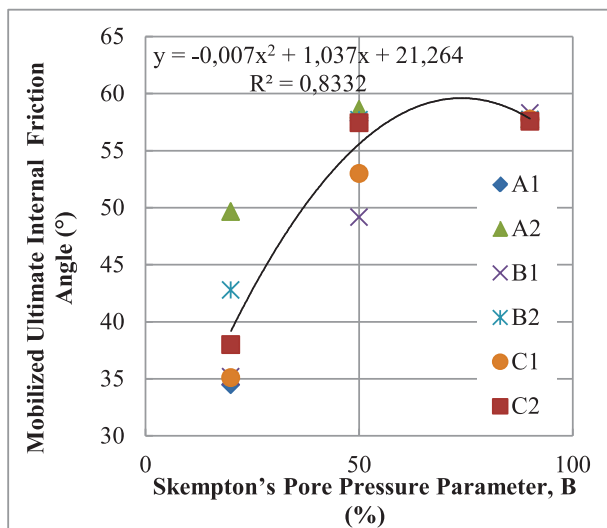


Figure 14. Mobilized ultimate internal friction angle versus Skempton's pore-pressure parameter of sandy soils ( $D_r=25\%$ ,  $P'_c=100$  kPa).

### 3.8 Relationship between the mobilized ultimate internal friction angle and the relative effective diameter of the sandy soils

The variation of the mobilized ultimate internal friction angle ( $\phi_u$ ) and the relative effective diameter ( $RED$ ) of the two groups of sandy-soil samples is presented in Figure 15. The obtained data indicate that the relative

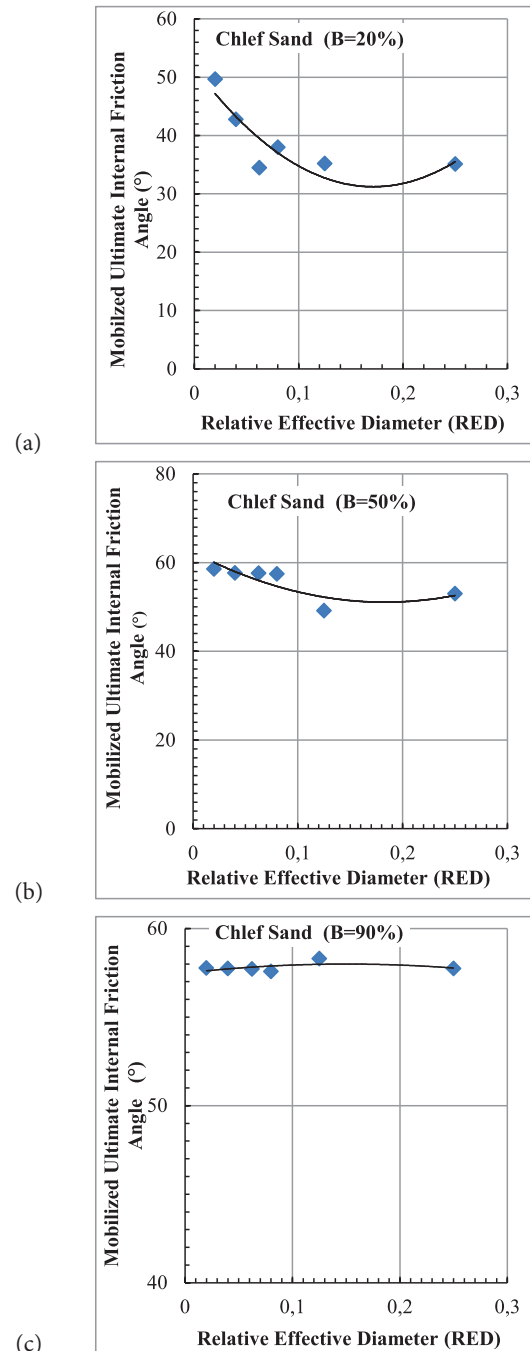


Figure 15. Mobilized ultimate internal friction angle versus relative effective diameter of sandy-soil samples ( $D_r=25\%$ ,  $P'_c=100$  kPa). (a)  $B=20\%$ , (b)  $B=50\%$ , (c)  $B=90\%$ .

effective diameter ( $RED$ ) could be correlated with the mobilized ultimate internal friction angle ( $\varphi_u$ ) for the materials under study. Indeed, the mobilized ultimate internal friction angle decreases in a polynomial manner with an increase of the relative effective diameter for the lower and intermediate Skempton's pore-pressure parameters ( $B=20\%$  and  $50\%$ ). However, the influence of the relative effective diameter on the mobilized ultimate internal friction angle is insignificant for the higher Skempton's pore-pressure parameter ( $B=90\%$ ). The obtained sandy-soils tendency confirms that the decrement of the Skempton's pore-pressure parameter plays a major role in increasing the mobilized ultimate internal friction angle-relative effective diameter response leading to a significant increase in the interparticle forces between the coarse grains of the tested sandy soils under consideration.

## 4 CONCLUSION

This laboratory research work is based on a series of undrained compression tests using static triaxial apparatus for the purpose of evaluating the effects of the relative effective diameter ( $RED=D_{10}/D_{max}$ ) on the mechanical behavior of partially saturated sandy soils. The tested samples were subdivided into two groups:  $A_1, B_1, C_1$  and  $A_2, B_2, C_2$ . They were reconstituted with the wet-deposition method ( $\omega=5\%$ ) at an initial relative density ( $D_r=25\%$ ), examined under three different Skempton's pore-pressure parameter values ( $B=20\%$ ,  $50\%$  and  $90\%$ ) and subjected to a constant confining pressure ( $P'_c=100$  kPa). The main conclusions of this study are summarized below:

1. The obtained test results show that the Skempton's pore-water-pressure parameter has a significant influence on the undrained-shear-strength response of the wet-deposited sandy-soil samples. Indeed, the ultimate shear strength increases with the decrease of the Skempton's pore-pressure parameter from the higher value ( $B=90\%$ ) to the lower value ( $B=20\%$ ), and it becomes more significant for the effective diameter ( $D_{10}=0.25$  mm). Completed and limited static liquefaction response cases were observed for all the tested partially saturated sandy-soil samples, as illustrated in Figures 3b, 4b, 5b, 6b, 7b and 8b.
2. The test results demonstrate clearly that the maximum diameter could be correlated with the ultimate shear strength and the brittleness index of the used materials. Indeed, the increase of the maximum diameter leads to an increase of the ultimate shear

strength and a decrease of the brittleness index of the samples of group 1 ( $A_1, B_1$  and  $C_1$ ) for ( $B=20\%$ ) and the inverse tendency was observed for group 2, where the ultimate shear strength decreases and the brittleness index increases with an increase of the maximum diameter for the same Skempton's coefficient ( $B=20\%$ ). In contrast, similar observations were made for the ultimate shear strength in the case of medium and higher Skempton's coefficients ( $B=50\%$  and  $90\%$ ) for all the tested sandy-soil samples, as shown in Figure (12 and 13).

3. The obtained findings confirm that the relative effective diameter ( $RED$ ) has a significant influence on the mechanical behavior of sandy soils in terms of the ultimate shear strength ( $q_u$ ). The increase of the relative effective diameter leads to a decrease of the ultimate shear strength for the lower Skempton's pore-pressure parameter ( $B=20\%$ ) of the tested sandy-soil samples of group 1 and increase it for the intermediate ( $B=50\%$ ) and higher ( $B=90\%$ ) Skempton's pore-pressure parameter for the same group and consequently to an increase of the undrained shear strength (liquefaction resistance). Moreover, the inverse trend was observed in the case of group 2 for all the tested Skempton's pore-pressure-parameter values ( $B=20\%$ ,  $50\%$  and  $90\%$ ), as illustrated in Figures 10 and 11.
4. Finally, the relative effective diameter ( $RED$ ) could be correlated with the brittleness index ( $I_B$ ) and the mobilized ultimate internal friction angle ( $\varphi_u$ ) of the two groups and control effectively the undrained shear strength of the sandy soils tested under three Skempton's pore-pressure-parameter values ( $B=20\%$ ,  $50\%$  and  $90\%$ ) at an initial relative density ( $D_r=25\%$ ) and subjected to a constant confining pressure ( $P'_c=100$  kPa), as presented in Figure (15).

## Acknowledgments

The authors are grateful to Professor Tom Schanz for putting at the disposal of the research teams all the necessary laboratory equipment to achieve the objective of this research project. The writers acknowledge the technician Michael Skubisch, who effectively contributed to the achievement of this experimental program.

## REFERENCES

- [1] Kramer, S. L. 1996. *Geotechnical Earthquake Engineering* Prentice Hall. New York.
- [2] Belkhatir, M., Arab, A., Della, N., Schanz, T. 2012. Experimental study of undrained shear strength of silty sand: effect of fines and gradation. *Geotech GeolEng* 30(5), 1103–1118. DOI: [org/10.1007/s10706-012-9526-1](https://doi.org/10.1007/s10706-012-9526-1)
- [3] Hazout, L., Zitouni, Z. E. A., Belkhatir, M., Schanz, T. 2017. Evaluation of Static Liquefaction Characteristics of Saturated Loose Sand Through the Mean Grain Size and Extreme Grain Sizes. *Geotechnical and Geological Engineering*, pp 1-27. DOI: [org/10.1007/s10706-017-0230-z](https://doi.org/10.1007/s10706-017-0230-z)
- [4] Arab, A., Shahrour, I., Lancelot, L. 2011. A laboratory study of liquefaction of partially saturated sand. *J IberGeol* 37(1), 29–36. DOI: [10.5209/rev\\_jige.2011.v37.n1.2](https://doi.org/10.5209/rev_jige.2011.v37.n1.2)
- [5] Belkhatir, M., Arab, A., Missoum, H., Della, N., Schanz, T. 2011. Laboratory study on the liquefaction resistance of sand–silt mixtures: effect of grading characteristics. *Granular Matter* 13, 599–609. DOI: [org/10.1007/s10035-011-0269-0](https://doi.org/10.1007/s10035-011-0269-0)
- [6] Belkhatir, M., Schanz, T., Arab, A., Della, N., Kadri, A. 2014. Insight into the effects of gradation on the pore pressure generation of sand–silt mixtures. *Geotech Test J* 37(5), 922–931. DOI: [org/10.1520/gtj20130051](https://doi.org/10.1520/gtj20130051)
- [7] Cherif Taiba, A., Belkhatir, M., Kadri, A., Mahmoudi, Y., Schanz, T. 2016. Insight into the effect of granulometric characteristics on the static liquefaction susceptibility of silty sand soils. *Geotechnical and Geological Engineering* 34(1) 367–382. DOI: [org/10.1007/s10706-015-9951-z](https://doi.org/10.1007/s10706-015-9951-z)
- [8] Cherif Taiba, A., Mahmoudi, Y., Belkhatir, M., Kadri, A., Schanz, T. 2017a. Experimental characterization of the undrained instability and steady state of silty sand soils under monotonic loading conditions. *International Journal of Geotechnical Engineering*, pp 1-17. DOI: [org/10.1080/19386362.2017.1302643](https://doi.org/10.1080/19386362.2017.1302643)
- [9] Cherif Taiba, A. 2017b. Etude en laboratoire de la susceptibilité à liquéfaction des sables limoneux: Influence de la taille et forme des grains (Doctoral dissertation, KADRI Abdelkader, BELKHATIR Mostefa).
- [10] Della, N., Arab, A., Belkhatir, M. 2011. Static liquefaction of sandy soil: an experimental investigation into the effects of saturation and initial state. *Acta Mech* 218(1–2), 175–186. DOI: [org/10.1007/s00707-010-0410-x](https://doi.org/10.1007/s00707-010-0410-x)
- [11] Lade, P. V., Yamamuro, J. A. 1997. Effects of non plastic fines on static liquefaction of sands. *Canadian Geotechnical Journal* 34(6), 918–928. DOI: [org/10.1139/t97-052](https://doi.org/10.1139/t97-052)
- [12] Mahmoudi, Y., Cherif Taiba, A., Belkhatir, M., Schanz, T. 2016. Experimental investigation on undrained shear behavior of over consolidated sand–silt mixtures: effect of sample reconstitution. *Geotech Test J* 39(3):515–523. DOI: [10.1520/GTJ20140183](https://doi.org/10.1520/GTJ20140183)
- [13] Mahmoudi, Y., Cherif Taiba, A., Belkhatir, M., Arab, A., Schanz, T. 2016. Laboratory study on undrained shear behavior of over consolidated sand–silt mixtures: effect of the fines content and stress state. *International Journal of Geotechnical Engineering*, pp 1-15. DOI: [10.1080/19386362.2016.1252140](https://doi.org/10.1080/19386362.2016.1252140)
- [14] Xenaki, V.C., Athanasopoulos, G.A. 2003. Liquefaction resistance of sand-silt mixtures: an experimental investigation of the effect of fines. *Soil DynEarthqEng* 23(3), 183–194. DOI: [org/10.1016/S0267-7261\(02\)00210-5](https://doi.org/10.1016/S0267-7261(02)00210-5)
- [15] Yilmaz, Y., MollaMahmutoglu, M., Ozaydin, V., Kayabali, K. 2008. Experimental investigation of effect of grading characteristics on the liquefaction resistance of various graded sands. *EngGeol J* 100, 91–100. DOI: [org/10.1016/j.enggeo.2007.12.002](https://doi.org/10.1016/j.enggeo.2007.12.002)
- [16] Cherif Taiba, A., Mahmoudi, Y., Belkhatir, M., and Schanz, T. 2018. Experimental Investigation into the Influence of Roundness and Sphericity on the Undrained Shear Response of Silty Sand Soils. *Geotechnical Testing Journal*. DOI: [10.1520/GTJ20170118](https://doi.org/10.1520/GTJ20170118)
- [17] Cherif Taiba, A., Mahmoudi, Y., Hazout, L., Belkhatir, M., Baille, W. 2019. Evaluation of hydraulic conductivity through particle shape and packing density characteristics of sand-silt mixtures. *Marine Georesources & Geotechnology*. DOI: [10.1080/1064119X.2018.1539891](https://doi.org/10.1080/1064119X.2018.1539891)
- [18] Mahmoudi, Y., Cherif Taiba, A., Hazout, L., Wiebke, B., Belkhatir, M. 2018. Influence of Soil Fabrics and Stress State on the Undrained Instability of Overconsolidated Binary Granular Assemblies. *StudiaGeotechnica et Mechanica*.40(2), 96–116. DOI: [org/10.2478/sgem-2018-0011](https://doi.org/10.2478/sgem-2018-0011)
- [19] Atigh, E., Byrne, P.M. 2004. Liquefaction flow of submarine slopes under partially undrained conditions: an effective stress approach. *Can Geotech J* 41, 154–165. DOI: [org/10.1139/t03-079](https://doi.org/10.1139/t03-079)
- [20] Chaney, R. C. 1978. Saturation effects on the cyclic strength of sands. In *From Volume I of Earthquake Engineering and Soil Dynamics--Proceedings of the ASCE Geotechnical Engineering Division Specialty Conference, June 19-21, 1978, Pasadena, California*. Sponsored by Geotechnical Engineering Division of ASCE in cooperation with: (No.

- Proceeding).
- [21] Kokusho, T. 2000. Correlation of pore pressure B-value with p-wave velocity and Poisson's ratio imperfectly saturated sand or gravel. *Soils Found* 40(4), 95–102. DOI:org/10.3208/sandf.40.4\_95
- [22] Mathiroban, S., Grozic, J. 2004. A model to predict the undrained behaviour of loose gassy sand. In: *Proceedings of 57th Geotechnical conference, session 6G*, 16–22. DOI:org/10.11575/PRISM/22820
- [23] Pietruszczak, S., Pande, G., Oulapour, M. 2003. A hypothesis for mitigation of risk of liquefaction. *Geotechnique* 53(9), 833–838. DOI:org/10.1680/geot.2003.53.9.833
- [24] Sherif, A.M., Tsuchiya, C., Isibashi, I. 1977. Saturation effects on initial soil liquefaction. *J. Geotech. Eng. Div.* 103(8), 914–917.
- [25] Yang, J., Sato, T. 2001. Analytical study of saturation effects on seismic vertical amplification of a soil layer. *Geotechnique* 51(2), 161–165. DOI:org/10.1680/geot.2001.51.2.161
- [26] Yoshimi, Y., Tanaka, K., Tokimatsu, K. 1989. Liquefaction resistance of a partially saturated sand. *Soils and foundations*, 29(3), 157–162. DOI:org/10.3208/sandf1972.29.3\_157
- [27] Ishihara, K., Tsuchiya, H., Huang, Y., Kamada, K. 2001. Recent studies on liquefaction resistance of sand effect of saturation. In: *Proceedings of 4th conference, recent advances in geotechnical earth engineering, Keynote Lecture*.
- [28] Ishihara, K., Tsukamoto, Y., Kamada, K. 2004. Undrained behavior of near-saturated sand in cyclic and monotonic loading. In: *Proceedings of conference, cyclic behavior of soils and liquefaction phenomena*, pp 27–39.
- [29] Martin, G.R., Finn W.D.L., Seed H.D. 1978. Effects of system compliance on liquefaction tests, *Journal of the Geotechnical Engineering Division* 104 (4), 463–479.
- [30] Arab, A., Belkhatir, M., & Sadek, M. 2016. Saturation Effect on Behaviour of Sandy Soil Under Monotonic and Cyclic Loading: A Laboratory Investigation. *Geotechnical and Geological Engineering*, 34(1), 347–358. DOI:org/10.1007/s10706-015-9949-6
- [31] Finn, W.D.L., Bransby, P.L., Pickering, D.J. 1970. Effect of strain history on liquefaction of sand. *J Soil Mech Found ASCE* 96(SM6), 1917–1934.
- [32] Ishihara, K., Tatsuoka, F., Yasuda, S. 1975. Undrained deformation and liquefaction of sand under cyclic stresses. *Soils Found* 15(1), 29–44. DOI:org/10.3208/sandf1972.15.29
- [33] Lee, K.L., Fitton, J.A. 1968. Factors affecting the cyclic strength of soil. *Vibration effects on earthquakes on soils and foundations*. ASTM STP 450, 71–95.
- [34] Liu, Y.J., Li, G., Zhen, Y.Y., Dano, C., Hicher, P.Y., Xiao, H.X., Wang, J.H. 2014. Influence of grading on the undrained behavior of granular materials. *Symposium about: recent advances in the mechanics of granular and porous media at the European solid mechanics conference in Graz, Austria*. DOI:org/10.1016/j.crme.2013.11.001
- [35] Miura, S., Toki, S., Tatsuoka, F. 1994. Cyclic undrained triaxial behavior of sand by a cooperative test program in Japan. In: Ebelhar RJ, Drenvich VP, Kutter BL (eds) *Dynamic geotechnical testing II*, ASTM STP 1213, 246–260. DOI: 10.1520/STP13217S
- [36] Seed, H. B., Peacock, W. H. 1971. Test procedures for measuring soil liquefaction characteristics. *Journal of Soil Mechanics & Foundations Div.*
- [37] Monkul, M. M., Etminan, E., Şenol, A. 2016. Influence of coefficient of uniformity and base sand gradation on static liquefaction of loose sands with silt. *Soil Dynamics and Earthquake Engineering*, 89, 185–197. DOI:org/10.1016/j.soildyn.2016.08.001
- [38] ASTM D 4253-00, 2002. Standard test method for maximum index density and unit weight of soils using a vibratory table. *Annual Book of ASTM Standards*. American Society for Testing and Materials, West Conshohocken, PA, pp. 1–14, www.astm.org.
- [39] ASTM D 4254-00, 2002. Standard test method for minimum index density and unit weight of soils and calculation of relative density. *Annual Book of ASTM Standards*. American Society for Testing and Materials, West Conshohocken, PA, pp. 1–9, www.astm.org.
- [40] Vaid, Y.P., Sivathayalan, S., Stedman, D. 1999. Influence of specimen reconstituting method on the undrained response of sand. *Geotech. Test J* 22(3), 187–195. DOI:org/10.1520/GTJ11110J
- [41] Sze, H.Y., Yang, J. 2014. Failure modes of sand in undrained cyclic loading: impact of sample preparation. *Geotech GeoenvironEng* 140, 152–169. DOI:org/10.1061/(ASCE)GT.1943-5606.0000971
- [42] Bishop, A. W. 1967. Progressive failure: with special reference to mechanism causing it. *Proceedings of the geotechnical conference, Oslo 2*, 142–150.

# LOAD-SETTLEMENT AND LOAD-SHARING BEHAVIOUR OF A PILED RAFT FOUNDATION RESTING ON LAYERED SOILS

# ODNOSA OBTEŽBA-POSEDEK IN OBTEŽBA-DELITEV OBTEŽBE ZA TEMELJNO PLOŠČO NA PILOTIH NA SLOJEVITIH TLEH

**Plaban Deb** (*corresponding author*)  
National Institute of Technology Agartala,  
Civil engineering department  
799046 Tripura, India  
E-mail: plaban930@gmail.com

**Sujit Kumar Pal**  
National Institute of Technology Agartala,  
Civil engineering department  
799046 Tripura, India  
E-mail: skpal1963@gmail.com

DOI <https://doi.org/10.18690/actageotechslov.17.1.71-86.2020>

## Keywords

piled raft, load-settlement behaviour, load-sharing behaviour, load-improvement ratio, numerical analysis

## Ključne besede

temeljna plošča na pilotih, odnos obremenitev-posedanje, odnos obtežba-delitev obtežbe, razmerje obtežba-izboljšanje, numerična analiza

## Abstract

*To understand the load-settlement and load-sharing behaviour of a piled raft foundation resting on different layered soils, small-scale laboratory model tests were conducted. The investigational programme includes a prototype model test on an unpiled raft, braced by a single pile,  $2 \times 2$  and  $3 \times 3$  pile groups. 3D numerical analyses were also implemented to ensure the experimental model's verification and to explore the settlement criterion of the piled raft foundation. The influences of the number of piles, the diameter of the piles and the raft sizes on the ultimate failure load, the load-improvement ratio and the percentage load carried by the raft at different settlement levels and different types of settlements that influence the foundation design criteria are illustrated. The relative contributions of these different design variables were also found using statistical analyses. The test results show the efficacy of using piles as settlement reducers with the raft. From the studies it is clear that as the number of piles below the raft increases from 1 to 9, the load-improvement ratio increases by 20% to 69%, whereas the load shared by the raft decreases with the addition of piles below the raft. From the numerical analyses it was found that the normalized differential settlement of the rafts can be optimized by introducing a number of piles in the central area of the raft.*

## Izvleček

*Za lažje razumevanje odnosov obtežba-posedek in porazdelitve obremenitve na temeljni plošči na pilotih, ki leži na različnih slojevitih zemljinah, so bili izvedeni laboratorijski preizkusi v zmanjšanem merilu. Raziskovalni program vključuje preizkus prototipnih modelov temeljne plošče, in temeljnih plošč podprtih z enim pilotom, ter skupinama pilotov  $2 \times 2$  in  $3 \times 3$ . Za preverjanje eksperimentalnega modela in preučitev kriterija posedanja temeljne plošče na pilotih so bile izvedene 3D numerične analize. Razloženi so vplivi števila pilotov, premera pilotov in velikosti pilotov na mejno porušno obtežbo, razmerje obtežba-izboljšanje in delež obtežbe, ki jo nosi temeljna plošča pri različnih nivojih posedanja ter različnih tipov posedanja, ki vplivajo na kriterije zasnove temeljev. Relativni prispevki teh različnih projektnih spremenljivk so bili ugotovljeni tudi s pomočjo statističnih analiz. Rezultati preizkusov kažejo na učinkovitost uporabe pilotov za zmanjšanje posevkov temeljnih plošč. Iz študij je razvidno, da se s povečanjem števila pilotov pod temeljno ploščo z 1 na 9 razmerje obtežba-izboljšanje poveča za 20 % do 69 %, medtem ko se obtežba, ki jo prevzame temeljna plošča, zmanjša z dodajanjem pilotov pod temeljno ploščo. Iz numeričnih analiz je bilo ugotovljeno, da je mogoče normalizirani diferencialni posedek temeljne plošče optimizirati z uvedbo števila pilotov v osrednjem območju temeljne plošče.*

## 1 INTRODUCTION

---

The growing need for high-rise structures and the scarcity of the available land area are forcing us to have concerns about a weaker soil base to use for foundation purposes. This is compelling us to have various alternative foundation techniques in various soil types. These foundation systems transfer the superstructure's load safely into the firm soil, confirming the overall strength and serviceability. Piled raft foundations are generally used when the isolated footing covers more than 70 % of the area under a superstructure. These are being used in several countries to sustain different kinds of superstructures, like buildings, bridges or industrial plants in various types of subsoil. Using these foundation systems, differential settlement can be reduced to a great extent as the piles improve the load-carrying capability of the raft. In the piled-raft foundation technique, the raft is directly contacted with the subsoil and hence there is a greater number of load exerts on the raft, thereby making the method very tedious, which also leads to an over-design of the foundation. Although considering the settlement reduction, a piled raft is a commonly used foundation technique in today's world. The idea of using a pile as a settlement reducer was suggested by Burland et al. [1]. Using this concept, an approach has been specified by some researchers, considering piles as settlement reducers (Randolph [2], Burland [3], de Sanctis et al. [4], Fioravante et al. [5]). The fundamental concept of this foundation approach is to minimize the number of piles by allowing a certain limited number of piles that are enough to reduce the settlement to an acceptable level by transmitting the load from the superstructure through the raft. This methodology permits the piled raft foundation's design to be enhanced and the number of piles under a raft to be substantially reduced. However, a comparatively small number of piles in a piled raft can lead to complications like high bending moments and hence there is a tendency of the raft to offer cracking, and a large amount of axial stress originates in the pile heads (Wong et al. [6]). If the structural load is assumed to be relatively consistently distributed over the whole area of the raft, the unpiled raft tends to deflect in the center. If piles are added underneath the central portion of the raft and are loaded nearly to their probable critical capacity, they will reduce the central settlement and this will help in minimizing the differential settlement. In an orthodox piled raft foundation having a large number of piles, the piles are usually expected to take all the loads after the mobilization of pile, and the raft starts taking the loads up to its structural capacity.

For the effective design of a raft with settlement-reducing piles, the capacity of the piles is anticipated to be 80 % mobilized under the external load (Clancy and Randolph

[7]). The nature of a piled raft along with the self-supporting pile group and unpiled raft foundations were compared by Cooke [8], who employed some prototypical tests on the piled raft foundation. It was observed that the spacing between the piles and the quantity of piles under the raft were the focal object for understanding the load-sharing response. It was also seen that the central settlement of the raft foundation was larger than those at the edges of the raft. According to Horikoshi and Randolph [9] and Reul and Randolph [10] the strategic placement of the piles under the centre of the raft can effectively decrease any differential settlement under uniform loading conditions. The effects of a variation in the pile and raft geometry to determine the piled raft's stiffness were studied with a centrifuge test on the piled raft system (Conte and Mandolini [11]). To explore the effect of the pile installation and the pile-raft interaction, Lee and Chung [12] performed an experimental test on a piled raft foundation system in a sandy soil. The load-carrying capacity and the load-sharing behaviour of the foundation can be changed depending on the specific settlement level. Bajad and Sahu [13] accomplished a 1-g model test to study the influence of the pile's dimensions and the number of piles on the settlement behaviour and the load-sharing response with different raft thicknesses using various pile configurations such as 4, 9 and 16 piles. To study the effect of the pile's dimension and the pile's arrangement Kumar and Kumar [14] performed a 1-g model test on a piled raft foundation in sandy soil at different relative densities. Based on this experimental model test data, Kumar and Kumar [15] developed an ANN model on Matlab to predict the settlement behaviour of a piled raft foundation.

In today's groundwork context, as stated earlier, deep foundations are now being furnished in every soil type, regardless of the profile of the soil and its strength criterion. However, it was found from a review of the literature that only very limited research has been accomplished on the behaviour of a piled raft on different layered soils. Every researcher has restricted their investigations to a single-layer system, whereas most of the soil profiles generally consist of multiple layers. Hence, in this paper, the load-settlement response and the load-sharing behaviour are explored through a prototype laboratory model test as well as through a finite-element analysis on various piled raft foundation systems resting on multiple layered soils.

## 2 LOAD-SHARING BEHAVIOUR OF A PILED RAFT

---

The load-settlement relationship for a piled raft can be decomposed into the raft and the piles. From Fig. 1 it is obvious that the proportions of the load withstood by

the raft and the piles vary as a function of the settlement. The load-sharing behaviour can be described using the load-sharing ratio  $\alpha_{pr}$  that represents the ratio of the load carried by the piles to the total load imposed on the piled raft, as follows:

$$\alpha_{pr} = \frac{Q_p}{Q_{pr}} = \frac{Q_p}{Q_r + Q_p} = 1 - \frac{Q_r}{Q_{pr}} \quad (1)$$

where,  $Q_{pr}$  = load executed on a piled raft; and  $Q_r$  and  $Q_p$  = loads supported by the raft and the piles, respectively. The values of  $\alpha_{pr}$  were investigated experimentally using centrifuge tests (Horikoshi and Randolph [16], Giretti [17]). Horikoshi and Randolph [16] conducted centrifuge tests and presented the values of  $\alpha_{pr}$  for flexible foundations with different numbers of piles. It was observed that  $\alpha_{pr}$  decreases with an increasing load level and increases with the number of piles. Giretti [17] and Comodromos [18] have also presented a similar variation of  $\alpha_{pr}$  decreasing with an increasing settlement. Several acceptable settlements are specified and used in the design of a foundation. For an improved piled raft design, the variation of  $\alpha_{pr}$  with the settlement needs to be identified and considered appropriately. The non-linear behaviour of the load responses in a piled raft foundation also needs to be included as it has an effect on the values of  $\alpha_{pr}$  for a given settlement. Since the most current definitions and propositions of  $\alpha_{pr}$  are addressed in terms of the stiffness and the geometry of a foundation, the research is much needed to idealize the settlement-reliant, non-linear variation of  $\alpha_{pr}$ .

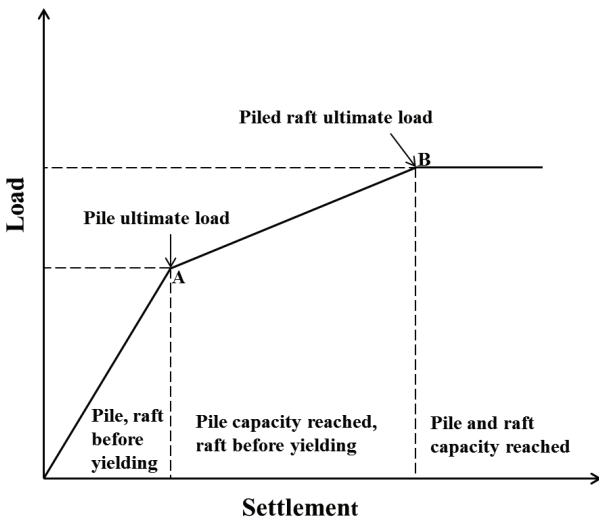


Figure 1. Simplified contact piled raft load-settlement curve.

### 3 EXPERIMENTAL PROGRAMME

A number of laboratory tests were accomplished on the models of the unpiled raft and the central piled raft with two different sizes of raft and different diameters

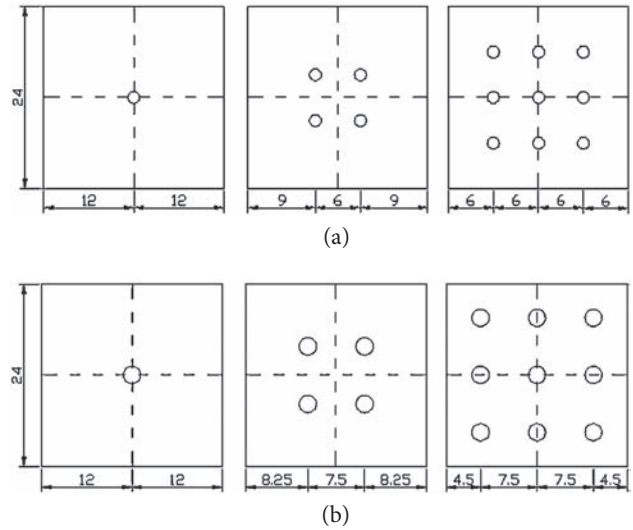


Figure 2. Pile configurations (a) for a pile diameter of 20 mm and (b) for a pile diameter of 25 mm (all dimensions are in cm).

Table 1. Model test programme.

Foundation type	Test denotation	Dia. of pile (mm)	s/d
Unpiled Raft	R-240	-	-
	R-180	-	-
Raft + 1 central pile	PRF-1-240-25	25	-
	PRF-1-240-20	20	-
	PRF-1-180-25	25	-
	PRF-1-180-20	20	-
Raft + 4 central pile	PRF-4-240-25	25	3
	PRF-4-240-20	20	3
	PRF-4-180-25	25	3
	PRF-4-180-20	20	3
Raft + 9 central pile	PRF-9-240-25	25	3
	PRF-9-240-20	20	3
	PRF-9-180-25	25	3
	PRF-9-180-20	20	3

R - Raft, PRF - Piled raft foundation, s/d - Spacing to diameter ratio

of the piles. The programme of the laboratory model tests on the unpiled raft and the piled-raft foundations are presented in Table 1. The pile configurations for the model raft's dimension of 240 mm are shown in Fig. 2. Similar pile configurations and spacings were also used for the raft's dimension of 180 mm. The dimensions of the model pile and the raft were chosen to ensure that no stress is concentrated at the periphery of the tank.

### 3.1 Subsoil materials

In the present study, three types of subsoil materials were used, i.e., silty-clay soil, silty-sand soil and sandy soil. The engineering and physical properties of the soil samples were evaluated using laboratory tests as per the standard techniques as recommended by the ASTM codes. The summary of the index and engineering characteristics of the subsoil materials is shown in Table 2 and the particle size distribution curves for all the soil samples are shown in Fig. 3.

**Table 2.** Engineering characteristics of subsoil materials.

Properties	Silty-clay soil	Silty-sand soil	Sandy soil
Grain size:			
Sand (%)	4.5	58.5	97.3
Silt (%)	43.23	35.7	2.7
Clay (%)	52.27	5.8	-
Specific gravity, $G$	2.71	2.65	2.6
Maximum Dry Density, $MDD$ ( $kN/m^3$ )	17.05	17.41	15.35
Optimum Moisture Content, $OMC$ (%)	23.5	16.2	13.6
Liquid Limit, $LL$ (%)	45.2	26.32	NP
Plastic Limit, $PL$ (%)	23.78	17.12	NP
Cohesion, $c$ ( $kN/m^2$ )	21.22	16.4	Cohesionless
Angle of internal friction, $\phi$ (degree)	20.54	27.4	31.2

NP = non-plastic

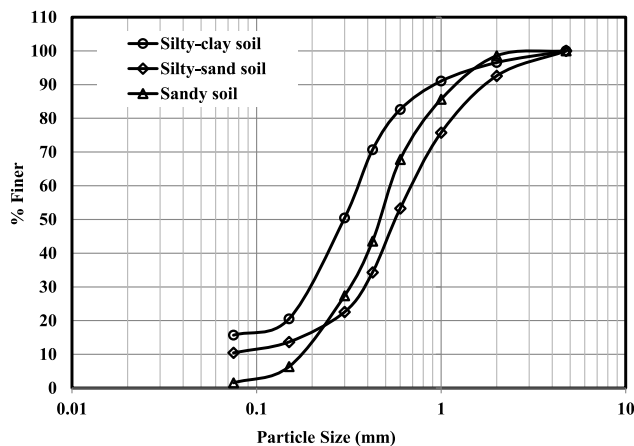


**Figure 3.** Particle size distribution curve.

### 3.2 Model raft and pile materials

The model raft was made of steel plates having a square cross-section with dimensions of 180 mm × 180 mm × 10 mm and 240 mm × 240 mm × 10 mm, and having a

smooth surface. The plate had screwed holes from the bottom surface to fix the different groups of circular piles. The outer surface of each pile top (up to 10 mm) was screw threaded to ensure a rigid connection between the pile and the raft. The arrangements of the piles and the raft are shown in Fig.4. A notch was then created in the centre of the raft to support the calibrated proving ring. In choosing the material for the model piles, aluminium was found to be more convenient than steel due to its light weight. Two sizes of pile diameter, i.e., 25 mm and 20 mm outer diameter, with 250-mm-long pipes were used as the model pile. The model piles under the rafts were smooth, hollow and circular, closed-ended, non-displacement piles. The spacings between the piles for the group pile were kept at three times the diameter of the pile. A scaling factor of 1/60 was used to select the model dimension, similar to Park and Lee [19]. The configuration for the pile groups selected in the study were a single pile, a 2 × 2 pile group and a 3 × 3 pile group.



**Figure 4.** Arrangement of piles and raft.

## 4 EXPERIMENTAL SET-UP AND TEST PROCEDURE

### 4.1 Testing tank and test set-up

The testing tank was made up of 12 mm thick translucent Perspex sheet and 10 mm thick steel plates. It had a square cross-section with a base dimension of 70 cm ×

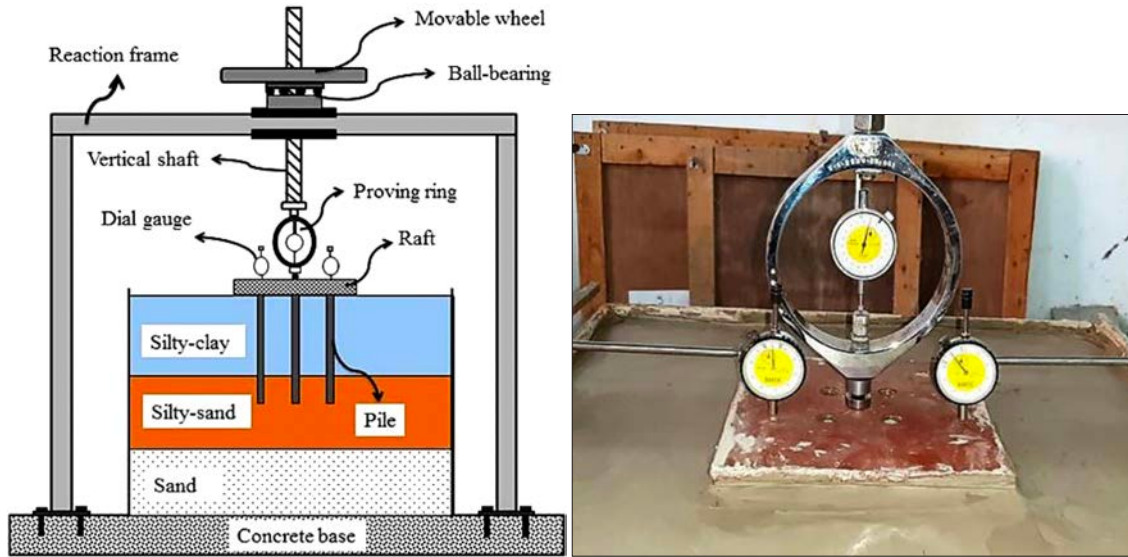


Figure 5. Experimental test set-up.

70 cm and having a height of 60 cm. Horizontal stiffeners were attached to two sides of the tank, where the translucent Perspex sheet was present, with nuts and bolts to avoid any bulging of the tank throughout the preparation of the soil bed and during the loading process. It is obvious that the dimensions of the test tank are large enough to overcome the scaling effects and the boundary conditions on the piled raft. The vertical load test set-up used for the piled raft is shown in Fig. 5, consisting of a soil tank, a piled raft, a screw-gear wheel, loading frames, a proving ring and two dial gauges. A movable wheel based on screw-gear mechanism was used to apply the vertical load. A vertical shaft made of steel acted as a screw jack that worked on the principle of nut and screw motion, and a manually operated movable wheel was used to control the vertical movement of the shaft. The application of the load through the shaft and wheel was controlled by the action of a ball-bearing system. The whole arrangements of the test set-up were rested on the horizontal beam of a loading frame, attached with the vertical frames, and the frames were bolted to the concrete base for better stability of the test set-up. A proving ring having capacity of 25 kN with 0.01 kN accuracy was mounted over the steel plate's center notch via a ball bearing for measuring the vertical load and two dial gauges on each side with 0.01 mm sensitivity were used to measure the vertical deformations.

#### 4.2 Soil bed preparation and model pile installation

The depth of the soil bed was maintained at more than two times the embedded length of the pile (i.e., 54 cm) to ensure a minor effect of the rigid base response of

the piles (Horikoshi and Randolph [20]). The top 6 cm thickness of the soil tank was kept free to avoid any overflow of the soil during the whole compaction process. The test was performed on three-layered soil, keeping an equal depth (i.e., 18 cm) for each layer. The top layer of the soil bed consisted of silty-clay soil; the second layer consisted of silty-sand soil; and sandy soil was kept in the bottom layer. For all the tests the bottom layer soil, i.e., the sandy soil, was used, having a relative density of 70%. To achieve a uniform density over the soil bed, the 'sand-raining technique' was used. The relative density of the sandy soil is dependent on the height of the free fall of the sand particles and, therefore, a relationship between the relative density and the height of the free fall was obtained, and is presented in Fig. 6. The height of the free fall of the sand particles corresponding to a relative density of 70% was found to be 270 mm.

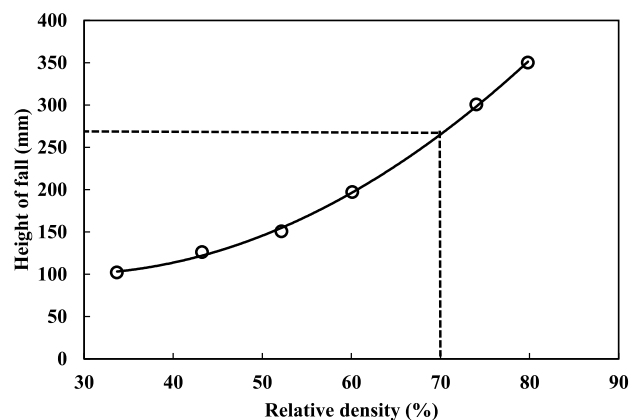


Figure 6. Calibration of height of free fall vs. relative density.

For the middle layer, i.e., for the silty-sand soil, it was placed with a bulk density ( $\gamma$ ) of 20.23 kN/m<sup>3</sup> at a water content ( $w$ ) of 16.2 %. For achieving the required bulk density, the silty-sand layer was divided into three sub layers of 6 cm each. The dry weight of the silty-sand soil was calculated and mixed with water (at  $w = 16.2$  %), and then filled uniformly in the respective layers. A steel plate hammer (with a light compaction energy) was used to compact the silty-sand for each layer. The achieved density was checked by accumulating samples in several containers of known volume kept at several locations of each layer of the silty-sand soil during the soil filling. For all the tests the achieved density was found to vary by only  $\pm 2$  %, which was insignificant.

The top-soil layer, i.e., the silty-clay soil layer, was prepared with an undrained shear strength for a given consistency. A series of UCS tests were performed on a silty-clay soil sample at different water contents to obtain the undrained shear strength at a given consistency. For all the tests, the water content of the silty-clay soil was maintained at around 34 %. The undrained shear strength and the bulk density corresponding to a 34 % water content was 10 kPa and 18.76 kN/m<sup>3</sup>, respectively.

The arrangement of the installation of pile was started from the inner pile, then the corner pile, and finally the edge piles. In the first stage, the soil was poured up to the tip of the pile and then the pile was employed on the centre line alignment. These arrangements helped in the equal distribution of the load over the whole raft. After that, the sub-soil was again packed up to the necessary height. At the time of this filling process the pile was kept vertical and any inclination of the piles was detected cautiously by a level. This process of pile fabrication was assumed to optimize the stress conditions around the piles that were cast in-situ. After the completion of one test, all the piles and the soil from the tank were removed and a similar method was repeated for the subsequent tests. Prior to the test, the soil was permitted to set at room temperature for about 24–30 hours to confirm the uniform circulation of the moisture content. The vertical settlements were recorded at the end of each load increment. The rate of loading was 0.1 kN/min. For each test, the loading was continued until the settlement of the foundation reached about 25 mm (El-Garhy et al. [21]).

## 5 FINITE-ELEMENT ANALYSIS OF THE MODEL PILED RAFT

The numerical analysis of the piled raft foundation presented in this paper was carried out with the 3D finite-element software package ABAQUS. The dimen-

sions of the elements of the numerical model were kept as similar as possible to the experimental model. However, to counteract the complexity of the numerical simulation, the circular pile was replaced by square piles having the same shaft circumference (Reul [22], Sinha and Hanna [23]). An isotropic elastic Hooke's model was used to verify the elements of the pile and the raft. To account for the non-linear behaviour, elastic-perfectly-plastic stress-strain relationships were selected to establish the soil mass, considering the total stress on the model because of the undrained behaviour of the soil mass in the numerical model (Rose et al. [24], Alshenawy et al. [25]). To account for the settlement behaviour of the piled raft, elastic solutions were chosen in most of the studies (Poulos [26], Lee [27], Teh and Wong [28]). These elastic solutions are mostly based on 'Mindlin's analytical point load solution' within an infinite elastic half space. Here, the soil yielding is not considered at the pile-soil interface. However, it was also observed that the elastic solutions overestimated the settlement for the piled raft foundation (Lee et al. [29]). The Mohr-Coulomb failure criterion was selected to relate the material behaviour with the parameters described in Table 3. The loading was simulated into three steps: the geostatic step was used to generate the initial conditions where the geostatic stress field (equal to the gravitational acceleration of 10 m/s<sup>2</sup>) was applied to the soil mass, prior to the installation of the pile; to keep the model in equilibrium, self-weight was introduced in the whole model in the second step and finally the loading was applied to the top of the raft in the third step. The pore change in the model was not required to be accounted for, as the loading was applied relatively quickly (Rose et al. [24]).

All the elements in the model were selected as 8-noded hexahedron brick elements (C3D8R) with a reduced integration so as to lower the Gaussian integral points that would allow the FEA solver to reduce the computational time with a minimal reduction in accuracy. Different mesh densities were utilized in this model, seeded with different aspect ratios so as to minimize the computational efforts. Thicker meshes lead to a more

**Table 3.** Properties introduced in the modelling.

Soil Layers	Modulus of Elasticity (kPa)	Poisson's ratio	Density (kN/m <sup>3</sup> )
Silty-clay soil	$6 \times 10^3$	0.5	18.76
Silty-sand soil	$30 \times 10^3$	0.35	20.23
Sandy soil	$25 \times 10^3$	0.38	14.25 <sup>a</sup>
Pile	$69 \times 10^6$	0.28	27
Raft	$12 \times 10^7$	0.3	78.7

a = density corresponding to relative density of 70%

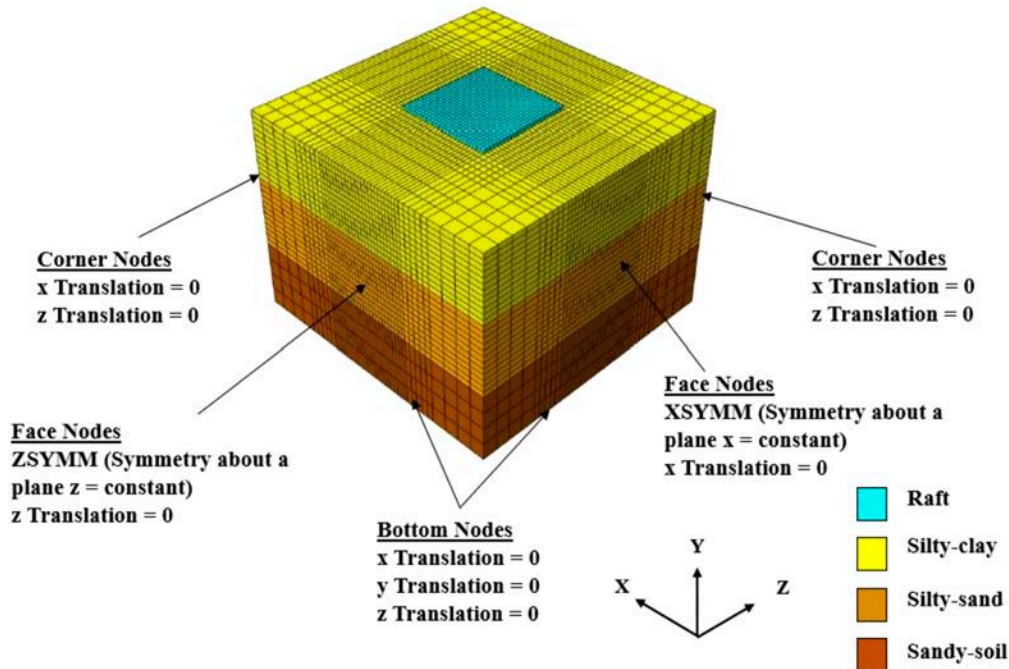


Figure 7. Mesh and boundary of 3D FE model.

accurate analysis, but it may slow the running process. Therefore, a high concentration of meshes was generated in the vicinity of the pile-soil interface and the thinner meshes were applied in the regions of less importance. The meshing pattern and boundary conditions are described in Fig. 7.

### 5.1 Soil-structure interaction

The interaction between the soil and the related structure plays an important role in simulating the actual loading conditions, and hence it becomes one of the major issues in identifying the accurate soil-structure interaction. When the compressive load is applied only on the piled raft, the pile conveys the shear stresses along their lateral surfaces, but when the piles come into contact with the soil surface, a frictional surface is developed according to the modified Coulomb friction theory. In this paper the Coulomb friction model was used to mimic the soil-pile interface, which related the maximum allowable shear stress (friction) across an interface to the contact pressure between the contacting bodies. An interface frictional coefficient and a limiting shear displacement of 5 mm were used to engender the elasto-plastic slip analysis. The contact surface between the pile and the raft was selected as being perfectly rigid, which means there was no relative motion between the nodes of the pile and the raft. The raft-soil interface was considered as a smooth surface.

### 5.2 Validation of the numerical model

The vital phase of constructing a model using any numerical software is to make it compatible with the reference model in order to ensure that the numerical model is acting as expected. To confirm that the simulated model created in ABAQUS is capable of representing the actual behaviour of the laboratory model test, it is required to run various trials in numerical analyses. The model test outcomes from the actual laboratory investigations can be correlated with those of the results obtained from the replicated tests in the software and thus it can be confirmed whether the numerical model resembles to the actual situation in a realistic way or not. Thus, a series of numerical model tests were carried out for the raft and the piled raft system. The numerical model represents a copy of the experimental set-up with the same model configurations, while the loading conditions are also simulated with the experimental circumstances. Fig. 8 shows a comparison between the laboratory tests and the numerical model. As exemplified in the presented figure, no peak load is detected in the results i.e., with an increasing of the pile settlement, the vertical load increases. It is obvious that the numerical analysis provides acceptable remarks and can be utilized to predict the piled raft's behaviour. It is also observed that the numerical analysis (model scale) is in a close agreement with the results from the experimental tests.

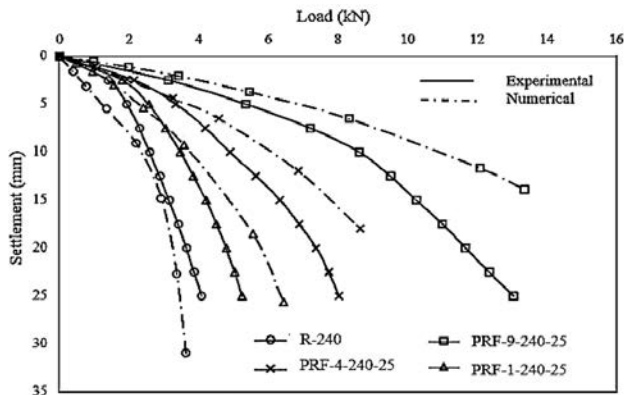


Figure 8. Comparison of experimental and numerical results.

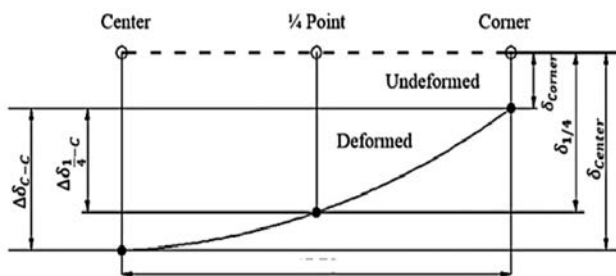


Figure 9. Reference settlement.

### 5.3 Settlement behaviour

From the numerical model, the settlement was acquired at three different positions, i.e., the central point on the raft, the corner point on the raft and the point at a distance of one-quarter from the corner. From these vertical settlement values, the average settlement ( $\delta_{avg}$ ), the differential settlement ( $\delta_{c-c}$ ) and the reference settlement ( $\delta_{ref}$ ) were calculated by Eqs. (2) to (4) (Reul and Randolph [10]),

$$\delta_{avg} = (2\delta_{Center} + \delta_{Corner})/3 \quad (2)$$

where,  $\delta_{avg}$  = average settlement,  $\delta_{Center}$  = Settlement at the raft centre and  $\delta_{Corner}$  = the settlement at the raft corner. The differential settlement and the reference settlement are generally considered as the most crucial ones, because these might be the reason for increasing the internal stress inside any superstructure, which ultimately possesses a negative impact by reducing the service life of the superstructure on which the piled raft foundation is provided. The minimal differential settlement criterion can be achieved by providing the pile group only in the central portion of any flexible raft (Prakoso and Kulhawy [30]). Fig. 9 demonstrates the schematic representation of the differential settlement and the reference settlement. The differential settlement and the reference settlement were calculated using Eqs. (3) and (4), respectively (Prakoso and Kulhawy [30]).

$$\delta_{c-c} = \delta_{Center} - \delta_{Corner} \quad (3)$$

$$\delta_{ref} = (\delta_{Center} + 2\delta_{1/4} + 2\delta_{Corner})/5 \quad (4)$$

where,  $\delta_{c-c}$  = differential settlement,  $\delta_{ref}$  = reference settlement,  $\delta_{Center}$  = Settlement at the raft centre,  $\delta_{Corner}$  = Settlement at the raft corner and  $\delta_{1/4}$  = settlement at a point at a distance of one-quarter from the corner.

## 6 RESULTS AND DISCUSSION

The experimental results obtained from the laboratory tests and the outcomes obtained from the numerical simulations are analysed and discussed in this section. For the experimental data acquisition, each test was repeated twice and the average value of the two trials was selected as the final test result. In most cases the measured values for the two trials differed by less than 1 % and in some cases, the result differed by 2–3 %. If the difference in the results was found to be more than 5 %, the test data were discarded and the test was repeated.

### 6.1 Effect of the size of the unpiled raft and the number of piles on the load-settlement curve

The experimental load-settlement curves for the unpiled raft and the piled raft are illustrated in Figs. 10–12. The load-settlement curves for all the tests indicate that the curves do not show any peak behaviour, i.e., with an increase in the settlement value, the load-carrying capability increases. From Fig. 10 it is clear that the load-carrying capability of the unpiled raft can be boosted by increasing the raft size. This phenomenon can be ascribed to the fact that the increased raft size aids in increasing the relative raft stiffness, which helps in sustaining more load. From the test outcomes it can be seen that the capability of the raft of size 240 mm × 240 mm at a settlement of 25 mm is 12.7 % more than the capacity of the raft of size 180 mm × 180 mm. From Figs. 11 and 12 it can be seen for all the cases that the load capacity of the piled raft rises as the amount of pile increases below the raft. It can also be detected that with an improvement in the number of piles below the raft, the yield load level of the piled raft system is also increased. Usually, an increased number of piles can be effective in enhancing the stiffness of any piled raft and hence the capability of piled raft is also increased. A similar trend was found by El-Garhy et al. [21]. From Figs. 11 and 12 it can also be concluded that with an increase of the pile diameter below the rafts, the load-carrying capacity is also increased. This increase might be due to the increase of the surface area and the stiffness of piled raft system as the diameter of the settlement-reducing pile increases.

From Fig. 13 it is seen that the piled raft behaviour shows three separate stages when subjected to an external load. In the first stage, the load-settlement relationship is found to be linear, because both the pile and the raft are elastic. In the second stage, once the load increases, the load-settlement relationship converts to more curvilinear, because the settlement rises little more than the first stage. This stage can be called the critical stage of the pile. During the final stage, the load-settlement criterion changes to linear again, although the settlement increases relatively faster, but the load does not increase substantially. In Fig. 13, during stage I, the OA is linear since the load-settlement relationship for the pile and raft are elastic. During stage II, AB is nonlinear because the pile reaches its full capacity. During stage III, BC becomes a straight line because the settlement increases quickly, but load taken by the pile does not increase substantially. This agrees with the observation of Patil et al. [31].

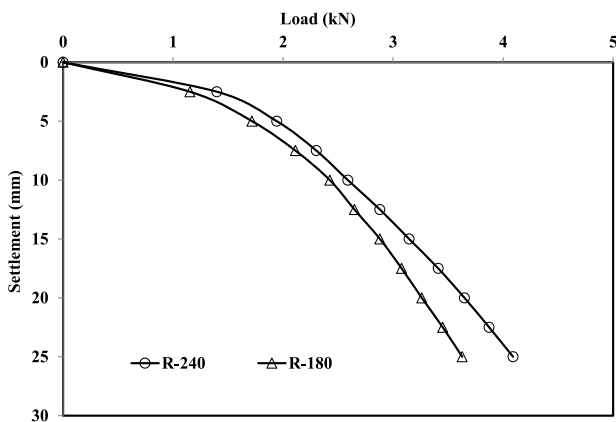


Figure 10. Load-settlement curves for the unpiled raft.

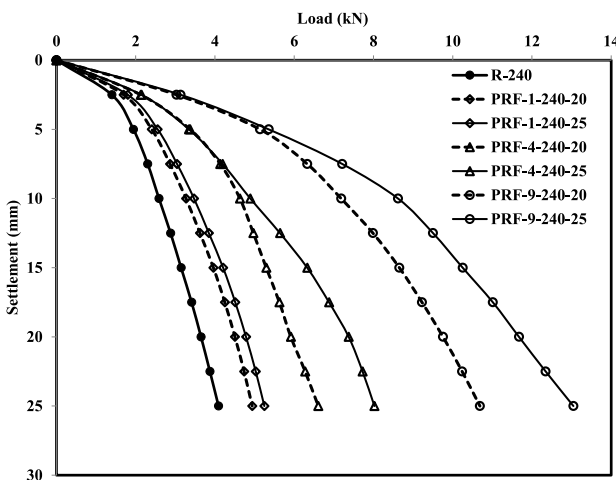


Figure 11. Load-settlement curves of the raft and the central piled raft.

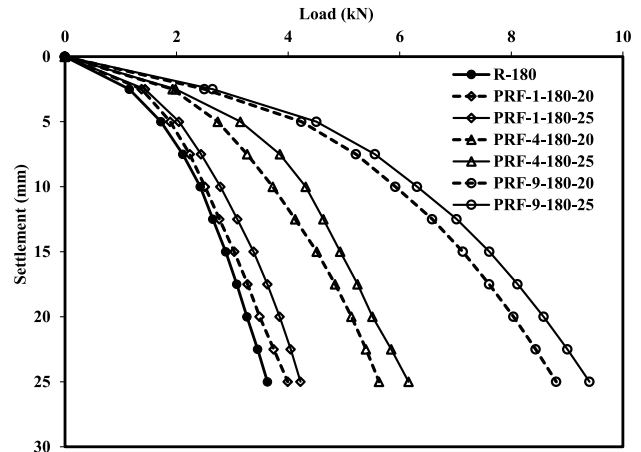


Figure 12. Load-settlement curves of the raft and the central piled raft.

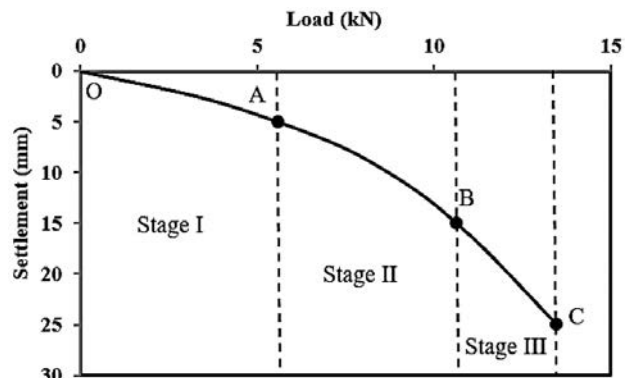


Figure 13. Load-settlement curve for PRF-9-240-25.

## 6.2 Effect of the number of piles on the ultimate failure load

For the present study, the ultimate failure load is determined by the tangent intersection method (Ismael [32]). In this methodology a tangent from the initial point and another tangent at the point where the curved part of the load-settlement curve changes to a steep straight line has

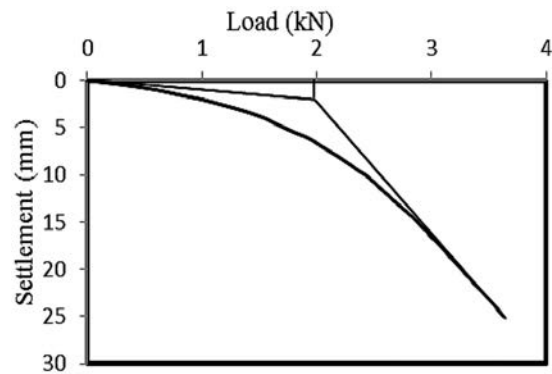


Figure 14. Evaluation of the ultimate failure piled raft load for R-240.

been drawn and their intersecting point gives the value of the ultimate failure load. The evaluation procedure for the ultimate failure load is shown in Fig. 14. The variation of the ultimate failure load with the number of piles is shown in Fig. 15. From the relation between the ultimate failure loads vs. the number of piles, it can also be anticipated that the noted ultimate failure load increases with an increase in the number of piles in a piled raft.

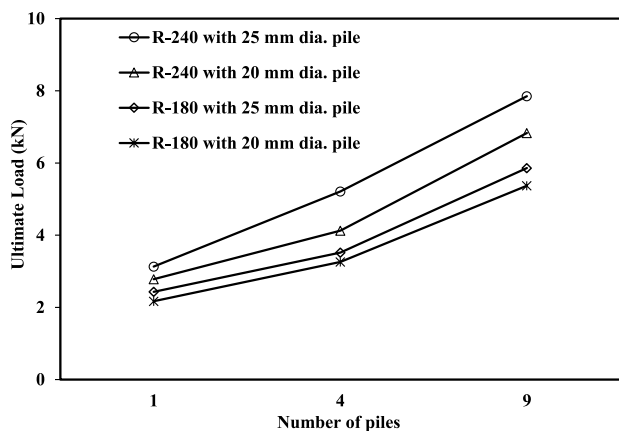


Figure 15. Ultimate load vs. number of piles curves of central piled raft.

### 6.3 Effect of number of piles on the load-improvement ratio (LIR) at different settlement levels

The enrichment of the external load-carrying capability of the raft at 10 mm and 25 mm settlements is defined as the load-improvement ratio (LIR). It is expressed as a fraction of the load conveyed by the piled raft to the unpiled raft at settlements of 25 mm and 10 mm. Figs. 16 and 17 demonstrate the changes in the LIR with the number of piles at 25 mm and 10 mm settlements for pile diameters of 25 mm and 20 mm, respectively. From the figures it can be seen that for the same raft sizes, as the number of piles under the raft and the pile diameter increases, the LIR also shows an increment. This is due to the fact that more load might be taken by the piles as the number of piles increases. For example, at a settlement of 25 mm, for a raft size of 240 mm × 240 mm, installing 9 piles having a 25 mm diameter increases the load taken by the raft by 69 %, while installing one pile with the same diameter increases the raft load by 20 %, as compared to the unpiled raft. From Figs. 16 and 17 it can be seen for all the cases that the LIR for a 10 mm settlement is little more than that of the LIR at a 25 mm settlement. A similar kind of variation of the LIR has been reported by El-Garhy et al. [21]. This clarifies the method of load sharing among the raft and the piles, i.e., at the start of the loading on the piled raft, the piles carry a major portion of the load, and with the increase of the

settlement, the load is transferred to the raft. It means that, at the early stage of loading, the pile carries more load than the raft. This can be attributed to the pile-soil-raft interaction and enhancing more overburden pressure over the neighbouring soil, inducing a more effective stress and shear resistance. In addition, the piles can also be regarded as reinforcement elements that escalate the shear resistance of the supporting soil, due to which the load-improvement ratio decreases as the settlement level increases.

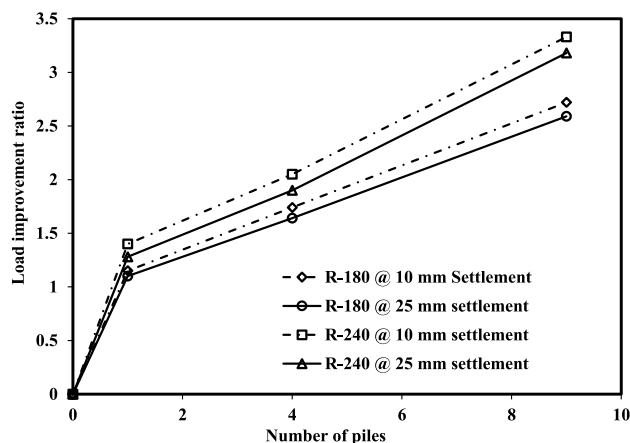


Figure 16. Variation of the load-improvement ratio with the number of piles at 10 mm and 25 mm settlements for a 25 mm diameter pile.

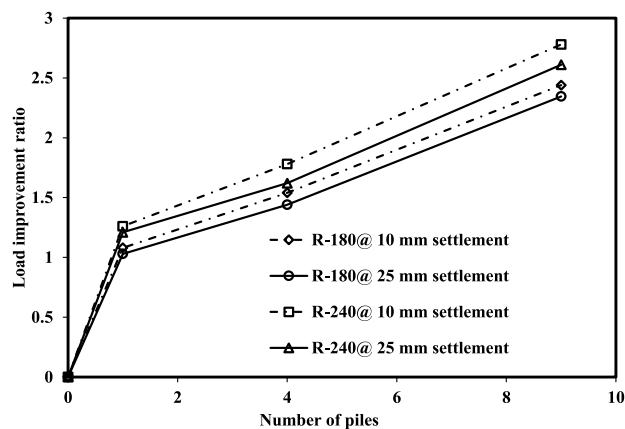


Figure 17. Variation of the load-improvement ratio with the number of piles at 10 mm and 25 mm settlements for a 20 mm diameter pile.

### 6.4 Load sharing between the raft and the pile

Poulos [33] stated that the proportion of the load shared by the raft can be expressed as the inverse of the load-improvement ratio (LIR). Fig. 18 displays the variation of the proportions of the loads carried by the raft with the number of piles for the raft models of 240 mm × 240 mm and 180 mm × 180 mm at settlements of 10 mm

and 25 mm. The figure illustrates that the proportion of the load carried by raft continues to reduce as the number of piles in a piled raft starts increasing. This is because of the additional resistance offered by the piles by the increase in the pile bearing and the pile skin friction, for a larger number of piles. It can also be observed that the percentage of the total load that is gained by the raft decreases as the diameter of the pile beneath the raft increases. This may be due to the increase of the stiffness and the surface area the of the piled raft system as the diameter of the settlement-reducing pile increases.

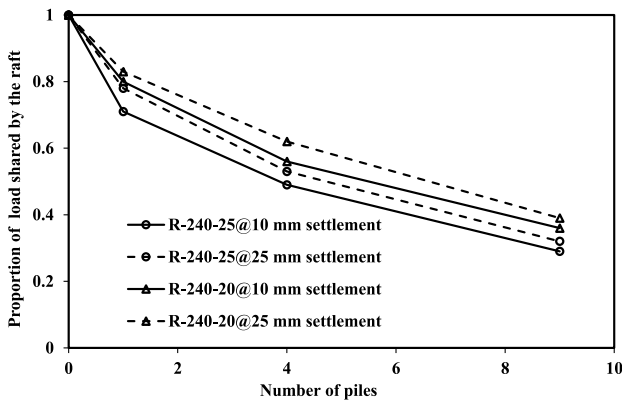


Figure 18. Proportion of the load carried by the raft vs. the number of piles.

### 6.5 Normalized average settlement

The average settlement for a piled raft foundation having different pile and raft configurations is obtained from Eq. (5) and the normalized average settlement is then obtained from the ratio of the average settlement of the piled raft to the unpiled raft, i.e., the normalized average settlement,  $\delta_r = \delta_{avg}$  of the piled raft/ $\delta_{avg}$  of the unpiled raft. The variation of the normalized average settlement corresponding to the raft’s central load is plotted in Fig. 19. It is clear from the figure that the increased number of piles increase the capacity of the piled raft and the normalized average settlement gradually decreases. The reason behind this phenomenon is that more piles would carry more load, as compared to the single pile, which would assist in lowering the settlement. From the figure it is also seen that the raft’s size and the pile’s size also affect the load-carrying capacity and the normalized average settlement of the piled raft. The larger size of the pile and raft showed a minimum value of the average settlement. The  $3 \times 3$  pile group having a pile diameter of 25 mm provides the maximum load sustainability compared to the other configurations and it possesses the least value of the normalized average settlement.

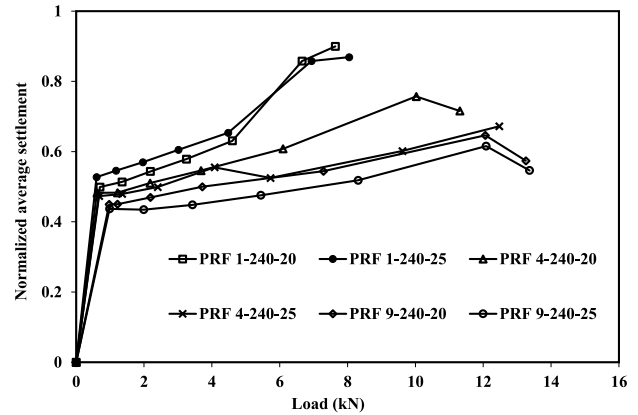


Figure 19. Normalized average settlement vs. raft central load.

### 6.6 Normalized differential settlement

The relationship between the piled raft and the raft’s differential displacement or normalized differential settlement ( $\delta_n$ ) and the factor of safety (FS) is mapped in Fig. 20. The factor of safety for a raft or piled raft ensures the capacity of the external load without failure. The overall FS can be obtained from the formula used by Prakoso and Kulhawy [30] and it is labelled as,

$$\text{Factor of safety} = (Q_g + Q_r)/Q \quad (5)$$

where,  $Q_g$  = pile group compression capacity,  $Q_r$  = raft compression capacity, and  $Q$  = applied load. From Fig. 20 it is clear that with the increase of FS in the piled raft system, the normalized differential settlement gradually decreases. A similar trend was also found by Prakoso and Kulhawy [30]. Among the different relationships, an exponential relationship showed a better goodness of fit with a co-relation factor of  $R^2 = 0.79$ , which indicates that the normalized differential settlement has a substantial effect to ensure the level of safety for any superstructure. It can also be observed from the relationship that, although the normalized differential settlement takes an imperative role,

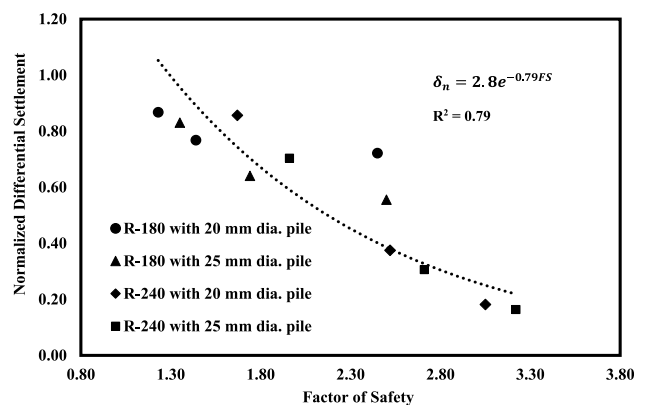


Figure 20. Normalized differential settlement vs. factor of safety.

there are certain other factors that also need to be considered for verifying the factor of safety for any structure.

### 6.7 Reference settlement

The reference settlement generally represents the nominal average displacement in the piled raft considering its settlement at the centre point, corner point and the one-quarter point from the corner. The reference settlement for the different piled raft configuration is obtained using Eq. (4). Fig. 21 shows the relationship between the load-sharing ratio ( $\alpha_{pr}$ ) and the reference settlement.  $\alpha_{pr}$  is obtained for all the configurations using Eq. (1), as conferred in the preceding context. From the figure it is understood that the load-sharing ratio has a significant effect on the reference settlement for the piled raft foundation. An increase in the load-sharing ratio certifies the stiffness of any foundation, consequently moderating the settlement. This non-linear response of  $\alpha_{pr}$  along with the reference settlement can be incorporated for the optimized design of the piled-raft foundation.

The reference settlement is then normalized to that of the corresponding raft reference settlement, and

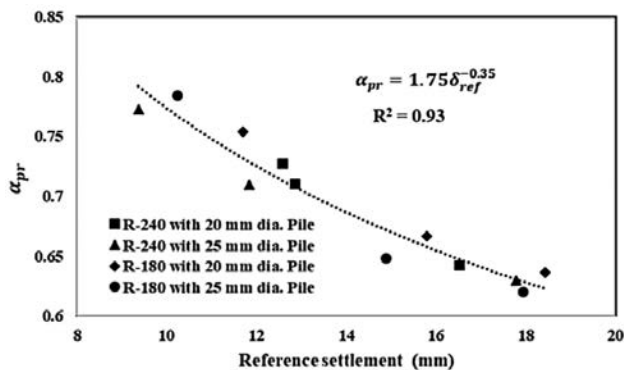


Figure 21. Load-sharing ratio ( $\alpha_{pr}$ ) vs. reference settlement.

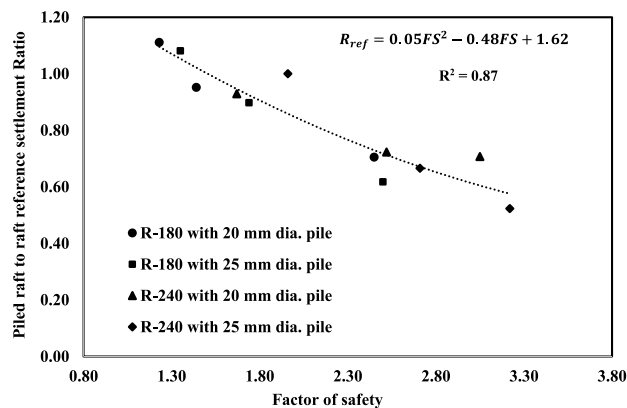


Figure 22. Piled raft to raft reference settlement ratio ( $R_{ref}$ ) vs. factor of safety.

the piled raft-to-raft reference settlement ratio ( $R_{ref}$ ) is evaluated ( $R_{ref} = \delta_{ref}$  for piled raft/ $\delta_{ref}$  for the corresponding raft).  $R_{ref}$  shows a non-linear decrease with the factor of safety, as observed in Fig. 22. A second-order polynomial relation between  $R_{ref}$  and FS shows a better goodness of fit, having  $R^2 = 0.87$ , which ensures the influence of  $R_{ref}$  on the factor of safety and consequently, on the serviceability of any structure.

### 6.8 Contribution of design variables to the reference settlement

The effect of different foundation elements (i.e., number of piles, size of pile and raft, etc.) on the reference settlement of the piled raft is identified using a statistical analysis. The analysis of variance (ANOVA) was performed to identify the contribution of different independent variables to the reference settlement. The diameter of the pile, the width of the raft and the number of piles beneath the raft are considered as the independent variables and the reference settlement is taken as the dependent variable. The influence of each design variable is acquired by taking the sum of the squares of each variable, divided by the total sum of the squares. It can be seen from Table 4 that the number of piles under the raft makes the maximum contribution to the reference settlement. It is worth mentioning that the number of piles beneath the raft helps to improve the load-sustaining capability of the foundation and hence it has a remarkable effect on reducing the settlement level. The contribution of the number of piles is 50.29 %, which is the maximum contribution among all the variables, followed by the size of the raft and the cross-sectional area of the pile.

Table 4. Relative contribution of the design variables to the reference settlement.

Variables	Degree of freedom (DF)	Sum of square (SS)	% Contribution	P-value	Remarks
Diameter of pile	1.00	2.83	9.15	0.019	Significant
Number of piles	2.00	15.56	50.29	0.013	Significant
Raft size	1.00	7.45	24.08	0.009	Significant
Error	7.00	5.10	16.48	0.017	Significant
Total		30.94	100.00		

### 6.9 Settlement in the horizontal direction

The settlement of the piled raft in the radial direction is obtained for all the configurations and presented in Fig. 23. The settlement is taken on both sides from the center of the raft and it is clear that the settlement gradu-

ally decreases over the horizontal length, showing the maximum amount of settlement in the central portion. A similar trend was obtained by Rabiei [34], and this is also quite obvious for the piled raft foundation, as the displacement at the corner point of the raft is always somewhat less than that of the raft center. Fig. 23(a) presents the radial settlement of different pile configurations having a raft width of 180 mm and Fig. 23(b) is the same for the raft width of 240 mm.

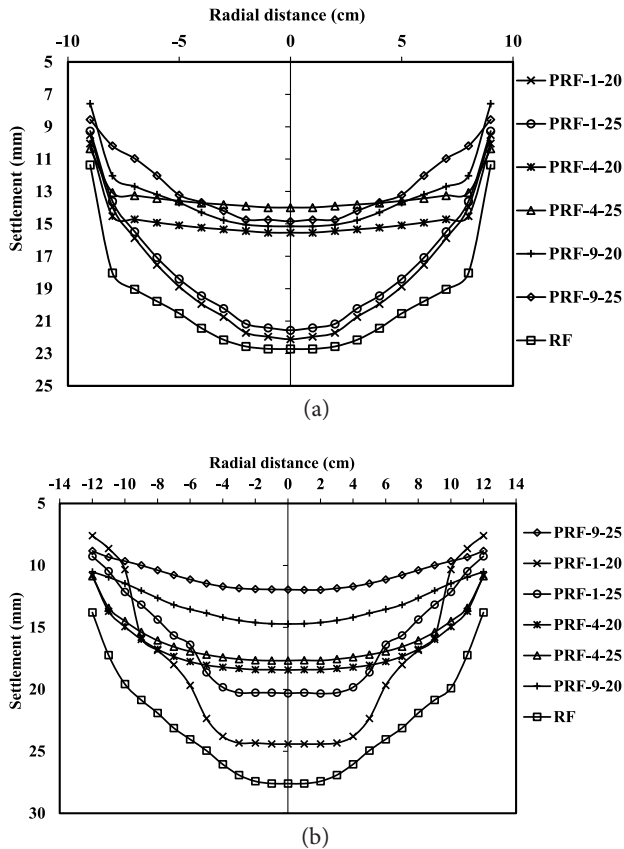


Figure 23. Radial distance of raft vs. settlement, (a) for raft size of 180 mm, (b) for raft size of 240 mm.

### 6.10 Maximum bending moment

The maximum positive bending moment at the raft top for different pile configuration is plotted in Fig. 24. Selvadurai [35] proposed one elastic solution to compute the maximum bending moment on the raft. However, that case included only the ideal condition of a single concentrated load over a semi-infinite elastic raft. Another realistic approach was developed by Fraser and Wardle [36], where the multi-layered soil system was converted to an equivalent soil layer. In this paper the maximum bending moment criterion is estimated using the equations suggested by Polous [33]. From the figure

it is seen that the piled raft configuration with nine piles has the maximum bending moment, which means that this configuration can sustain more moment developed due to the external load. It can also be detected from the relation that the increase in raft size helps to withstand more bending moment. This may be because the occurrence of a large amount of pile beneath the raft offered more stiffness to the system, which helped in sustaining more bending moment compared to other configurations having a smaller number of piles.

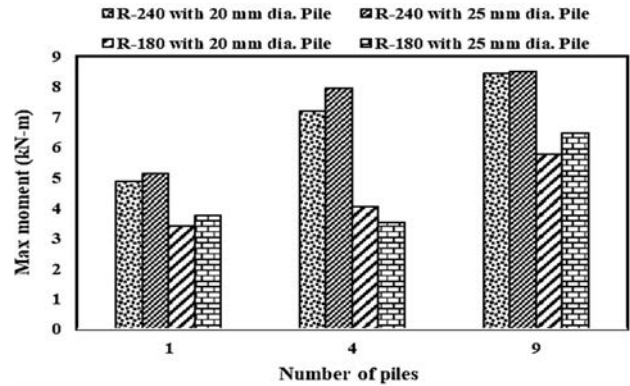


Figure 24. Maximum positive bending moment at the raft top for different pile configurations.

### 6.11 Effect of settlement behaviour on the subsoil material

The piled raft is generally intended to reduce the sub-soil settlement and to avoid any unwanted failure by transferring the load to the hard stratum. Transmitting the loads from the top surface to any hard stratum helps in reducing the settlement of the top layer. Three different types of soils are used in this study and the effect of the piled raft foundation and the unpiled raft foundation on the settlement behaviour of the subsoil conditions are shown in Fig. 25. Vertical settlement along the subsoil depth is taken at different positions on both sides from the centre (up to the raft width from both sides) and then the average is taken to obtain the mean settlement. The settlement of the 3 × 3 pile group with raft dimension of 180 mm × 180 mm is compared with the unpiled raft of the same dimensions and it is seen from the figure that the inclusion of piles along with the raft helped in transferring the load from the top layer to the bearing layer; thereby, reducing the settlement on the top layer. In this case, the maximum vertical settlement of the subsoil with the unpiled raft is almost 1.7 times that of the subsoil of the piled-raft foundation. In Fig. 25 point A shows the interface of the top and the middle layer. The settlement for both cases gradually decreases along with the vertical depth, but the settlement for the piled-

raft foundation is slightly higher than that of the unpiled raft foundation beyond point A. This can be attributed to the fact that the pile is resting on that transition zone, and as it transmits the vertical load on its tip, the subsoil exists there, experiences a sudden sensation, which causes an escalation in the settlement. However, the difference in the value of the settlement in the transition zone is very small. This ensures the efficacy of the piled raft foundation for different layered soils.

The settlement of sub-soil with the 3 × 3 pile-group configuration having a raft dimension of 240 mm × 240 mm piled raft foundation along the radial direction is presented in Fig. 26. A similar trend is observed for all the other configurations, and therefore, the others are not discussed here. The radial distance is taken on both the sides from the centre for each layer. The mean value of the radial settlement is obtained by taking different divisions in each layer. The figure reveals that the settlement gradually decreases along the horizontal distance finally diminished to zero. In this case, the settlement propagates up to 30 cm from centre, where the length of

the modelled soil system was 35 cm. For every case the settlement of each layer decreased to almost zero within the specified limit, i.e., in no cases does the settlement extend beyond 35 cm, which confirms the precision of the experimental and numerical model.

## 7 CONCLUSIONS

This paper presented the experimental results of load tests on model rafts with the settlement-reducing piles embedded in layered soils to investigate the load-settlement behaviour and load sharing between the piles and the raft. The numerical analysis is also made to account for different types of settlement criterion and to assess the effect of the settlement-reducing pile on the serviceability of the foundation. The effect of the piled raft foundation on the sub-soil condition is also investigated through finite-element modelling.

From the results of the experimental and numerical investigations on the behaviour of the unpiled raft and the piled raft in layered soils under axially loaded modelled circular piles, the following conclusions can be drawn:

1. The addition of piles under the central area of the raft increases the load-bearing capacity of the piled raft resting on layered soils. As the number of piles increases, the load-carrying capacity of the rafts with settlement-reducing piles has been increased up to 20 % to 69 % as compared to the unpiled raft. It can also be concluded from the results that the increase in the pile diameter below the rafts increases the load-carrying capacity.
2. In layered soils, as the number of settlement-reducing piles increases, the load improvement ratio (LIR) increases at 10 mm and 25 mm settlements. However, the value of LIR at the 10 mm settlement is greater than that of at the 25 mm settlement, i.e., at the beginning of the loading, central piles carry the major portion of the load and with the increase of settlement level, the load is gradually transferred to the raft.
3. In the case of multi-layer soil, as the number of piles beneath the raft increases, the percentage of the load shared by the raft decreases for a given raft size and increases as the diameter of the pile decreases.
4. From the numerical analysis, it is understood that the normalized average settlement and normalized differential settlement of the rafts can be optimized

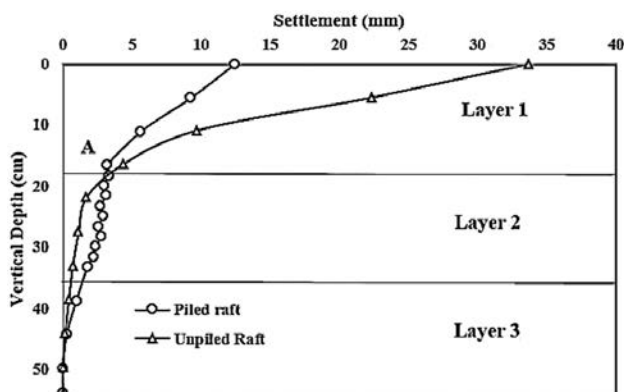


Figure 25. Vertical settlement along the sub-soil depth.

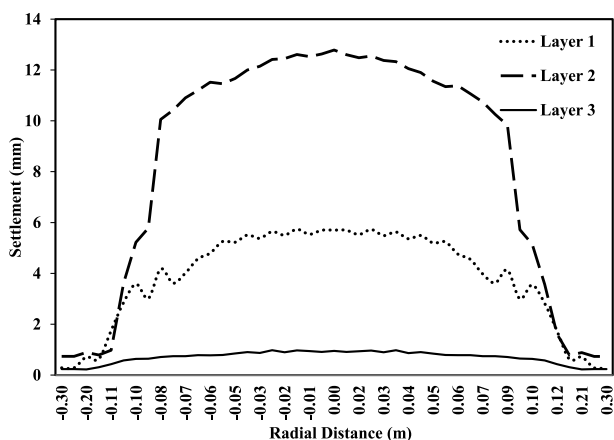


Figure 26. Radial distance of sub-soil vs. settlement (For PRF-9-240-25).

by introducing a number of piles at the center of the raft.

5. The statistical analysis carried out by the ANOVA test showed that the number of piles beneath the raft possessed the highest contribution among different design variables in the reference settlement, followed by the size of the raft and the diameter of the pile.
6. The settlement of the piled raft and the unpiled raft resting in layered soils indicates a non-linear decrease along the radial direction of the raft showing the maximum settlement at the centre of the raft.
7. Inclusion of a pile under the raft helps in transferring the load from the top layer to the underlying layers, thereby reducing the top-layer settlement. If the pile is resting in any transition zone of two layers, the settlement of the lower layer might be slightly higher than that of the unpiled raft, but the top-layer settlement for a piled raft is much lower than the unpiled one.
8. The increasing number of piles in a group and an increasing raft size may assist in reducing the reference settlement of the foundation, thereby increasing the factor of safety of the system. The factor of safety of the piled raft foundation exponentially varies with the normalized differential settlement and a 2<sup>nd</sup>-order polynomial relationship with the piled raft to raft reference settlement ratio ( $R_{ref}$ ) of the system.
9. From the overall analysis using both the experimental and numerical investigations, it is concluded that the use of a piled raft foundation can be an effective solution for foundations constructed in layered soils.

## REFERENCES

- [1] Burland, J.B., Brooms, B.B., de Mello, V.F.B. 1977. Behavior of foundations and structures. Proc. 9 ICSMFE, Tokyo 2, pp 495-546.
- [2] Randolph, M.F. 1994. Design methods for pile groups. In: Proc. 13<sup>th</sup> Intl. Conf. on Soil Mechanics and Foundation Engineering, pp. 61–82.
- [3] Burland, J.B. 1995. Piles as settlement reducers. In: The 8<sup>th</sup> Italian Conference on Soil Mechanics.
- [4] de Sanctis, L.D., Mandolini, A., Russo, G., Viggiani, C. 2002. Some remarks on the optimum design of piled rafts. In: Deep Foundations 2002: An International Perspective on Theory, Design, Construction and Performance, Orlando, ASCE, pp. 405–25.
- [5] Fioravante, V., Giretti, D., Jamiolkowski, M. 2008. Physical modeling of raft on settlement reducing piles. In: From Research to Practice in Geotechnical Engineering. Reston, pp. 206–39 [http://dx.doi.org/10.1061/40962\(325\)2](http://dx.doi.org/10.1061/40962(325)2)
- [6] Wong, I.H., Chang, M.F., Cao, X.D. 2000. Raft foundations with disconnected settlement reducing piles, Design application of raft foundations and ground slabs. Chap. 17, Thomas Telford, London, pp 469–486.
- [7] Clancy, P., Randolph, M.F. 1993. An Approximate Analysis Procedure for Piled Raft Foundations. Int. J. Numer. Anal. Methods Geomech. 17(12), 849-869. <https://doi.org/10.1002/nag.1610171203>
- [8] Cooke, R.W. 1986. Piled raft foundations on stiff clays. Contribution to design philosophy, Geotechnique 35(2), 169–203. <https://doi.org/10.1680/geot.1986.36.2.169>
- [9] Horikoshi, K., Randolph, M.F. 1996. Centrifuge modelling of piled raft foundation on clay, Geotechnique 46(4), 741–752. <https://doi.org/10.1680/geot.1996.46.4.741>
- [10] Reul, O., Randolph, M.F. 2004. Design strategies for piled rafts subjected to nonuniform vertical loading. J. Geotech. Geoenviron. Eng. ASCE 130(1), 1–13. [https://doi.org/10.1061/\(ASCE\)1090-0241\(2004\)130:1\(1\)](https://doi.org/10.1061/(ASCE)1090-0241(2004)130:1(1))
- [11] Conte, G., Mandolini, A., Randolph, M.F. 2003. Centrifuge modeling to investigate the performance of piled rafts. In: Van Impe WF (ed) Proceedings of the 4<sup>th</sup> international geotechnical seminar on deep foundations on bored and auger piles. Millpress, Rotterdam, pp. 359–366.
- [12] Lee, S.H., Chung, C.K. 2005. An experimental study of the interaction of vertically loaded pile groups in sand. Can. Geotech. J. 42, 1485–1493. <https://doi.org/10.1139/t05-068>
- [13] Bajad, S.P., Sahu, R.B. 2008. An experimental study on the behavior of vertically loaded piled raft on soft clay. In: The 12<sup>th</sup> international conference of international association for computer methods and advances in geomechanics (IACMAG), pp 84–90.
- [14] Kumar, V., Kumar, A. 2018. An experimental study to analyse the behaviour of piled-raft foundation model under the application of vertical load. Innov. Infrastruct. Solut. 3(35), 1-7. <https://doi.org/10.1007/s41062-018-0141-8>
- [15] Kumar, V., Kumar, A. 2018. Predicting the settlement in raft and piled-raft foundations using neural models. Int. J. Adv. Struct. Geotech. Eng. 6(4), 134-43. <http://doi.org/10.5281/zenodo.1288017>
- [16] Horikoshi, K., Randolph, M.F. 1998. A contribution to optimum design of piled rafts, Geotechnique 48(1), 1–10. <https://doi.org/10.1680/geot.1998.48.1.1>

- nique 48(3), 301-317. <https://doi.org/10.1680/geot.1998.48.3.301>
- [17] Giretti, D. 2010. Modelling of piled raft foundations in sand. (Doctoral dissertation, Università degli Studi di Ferrara).
- [18] Comodromos, E.M. 2004. Response evaluation of axially loaded fixed head pile groups using 3D nonlinear analysis. *Soils Found.* 44(2), 31-39. [https://doi.org/10.3208/sandf.44.2\\_31](https://doi.org/10.3208/sandf.44.2_31)
- [19] Park, D., Lee, J. 2014. Comparative analysis of various interaction effects for piled rafts in sands using centrifuge tests. *J. Geotech. Geoenviron. Eng. ASCE* 141(1), 04014082. [https://doi.org/10.1061/\(ASCE\)GT.1943-5606.0001183](https://doi.org/10.1061/(ASCE)GT.1943-5606.0001183)
- [20] Horikoshi, K., Randolph, M.F. 1999. Estimation of overall settlement of piled rafts. *Soils Found.* 39(2), 59-68. [https://doi.org/10.3208/sandf.39.2\\_59](https://doi.org/10.3208/sandf.39.2_59)
- [21] El-Garhy, B., Galil, A.A., Youssef, A.F., Raia, M.A. 2013. Behavior of raft on settlement reducing piles: Experimental model study. *J. Rock Mech. Geotech. Eng.* 5(5), 389-399. <https://doi.org/10.1016/j.jrmge.2013.07.005>
- [22] Reul, O. 2004. Numerical study of the bearing behavior of piled rafts. *Int. J. Geomech. ASCE* 4(2), 59-68. [https://doi.org/10.1061/\(ASCE\)1532-3641\(2004\)4:2\(59\)](https://doi.org/10.1061/(ASCE)1532-3641(2004)4:2(59))
- [23] Sinha, A., Hanna, A.M. 2016. 3D numerical model for piled raft foundation. *Int. J. Geomech. ASCE* 17(2), 04016055. [https://doi.org/10.1061/\(ASCE\)GM.1943-5622.0000674](https://doi.org/10.1061/(ASCE)GM.1943-5622.0000674)
- [24] Rose, A.V., Taylor, R.N., El Naggar, M.H. 2013. Numerical modelling of perimeter pile groups in clay. *Can. Geotech. J.* 50(3), 250-258. <https://doi.org/10.1139/cgj-2012-0194>
- [52] Alshenawy, A.O., Alrefeai, T.O., Alsanabani, N.M. 2016. Analysis of piled raft coefficient and load-settlement on sandy soil. *Arab. J. Geosci.* 9(6), 475. <https://doi.org/10.1007/s12517-016-2494-7>
- [26] Poulos, H. G., Davis, E.H. 1980. Pile foundation analysis and design.
- [27] Lee, I.K. 1993. Analysis and performance of raft and raft-pile systems. Proceedings: Third International Conference on Case Histories in Geotechnical Engineering, St. Louis, Missouri, June 1-4, SOA 4.
- [28] Teh, C.I., Wong, K.S. 1995. Analysis of downdrag on pile groups. *Geotechnique* 45(2), 191-207. <https://doi.org/10.1680/geot.1995.45.2.191>
- [29] Lee, C.J., Bolton, M.D., Al-Tabbaa, A. 2002. Numerical modelling of group effects on the distribution of dragloads in pile foundations. *Geotechnique* 52(5), 325-335. <https://doi.org/10.1680/geot.2002.52.5.325>
- [30] Prakoso, W.A., Kulhawy, F.H. 2001. Contribution to piled raft foundation design. *J. Geotech. Geoenviron. Eng. ASCE* 127(1), 17-24. [https://doi.org/10.1061/\(ASCE\)1090-0241\(2001\)127:1\(17\)](https://doi.org/10.1061/(ASCE)1090-0241(2001)127:1(17))
- [31] Patil, J.D., Vasanvala, S.A., Solanki, C.H. 2016. An experimental study on behaviour of piled raft foundation. *Indian Geotech. J.* 46(1), 16-24. <https://doi.org/10.1007/s40098-015-0145-7>.
- [32] Ismael, N.F. 2001. Axial load tests on bored piles and pile groups in cemented sands. *J. Geotech. Geoenviron. Eng. ASCE* 127(9), 766-773. [https://doi.org/10.1061/\(ASCE\)1090-0241\(2001\)127:9\(766\)](https://doi.org/10.1061/(ASCE)1090-0241(2001)127:9(766))
- [33] Poulos, H.G. 2001. Piled raft foundations: design and applications. *Geotechnique* 51(2), 95-114. <https://doi.org/10.1680/geot.2001.51.2.95>
- [34] Rabiei, M. 2009. Parametric study for piled raft foundations. *EJGE* 14, 1-11.
- [35] Selvadurai, A.P.S. 1979. The interaction between a uniformly loaded circular plate and isotropic elastic half-space: a variational approach. *J. Struct. Mech.* 7(3), 231-246. <https://doi.org/10.1080/03601217908905320>
- [36] Fraser, R. A., Wardle, L. J. 1978. Discussion: Numerical analysis of rectangular rafts on layered foundations. *Géotechnique* 28(2), 211-212. <https://doi.org/10.1680/geot.1978.28.2.211>

# NUMERICAL INVESTIGATION OF THE INFLUENCE OF SPATIAL EFFECTS AND SUPPORTING STRUCTURES DURING PIT EXCAVATION

# NUMERIČNA RAZISKAVA UČINKOV PROSTORSKIH VPLIVOV IN PODPORNIH KONSTRUKCIJ MED IZKOPAVANJEM GRADBENE JAME

## Ping Li

Hohai University,  
Department of Civil Engineering  
Nanjing 210098, China  
E-mail: lipings0110@163.com

## Junjun Chen (corresponding author)

Hohai University,  
Department of Civil Engineering  
Nanjing 210098, China  
E-mail: 806597145@qq.com

## Yaru Lv (corresponding author)

Hohai University,  
Department of Mechanics and Materials  
Nanjing 210098, China  
E-mail: yaru419828@163.com

## Zhiyuan Wang

Hohai University,  
Department of Civil Engineering  
Nanjing 210098, China  
E-mail: 1191981382@qq.com

## Xiaojing Chen

Nanjing Water Planning and Designing  
Institute. Corp. Ltd  
Nanjing 210098, China  
E-mail: 22354891@qq.com

DOI <https://doi.org/10.18690/actageotechslov.17.1.87-96.2020>

## Keywords

pit excavation; spatial effect; supporting structure combination; field test; pipeline displacement monitoring

## Ključne besede

izkop gradbene jame, prostorski vpliv, sestavljena podporna konstrukcija, terenski preizkus, spremljanje premikov cevovodov

## Abstract

*This paper reports on a field test in Nanjing, China, performed to investigate the effects of excavation on shallow-buried pipelines by monitoring and analyzing the displacements of these pipelines. A parametric study is also carried out using the finite-element program ABAQUS to investigate the influence of the spatial effects of the pit excavation and the supporting-structure combination forms. The numerical simulations are verified by the field test. The results show that the first excavating area, which is farther from the existing buried pipeline, causes smaller displacements of the pipeline. When the slope angle of the existing bored piles increases from 0° to 15°, the maximum horizontal and vertical displacements decrease by 4.92 mm and 2.49 mm, respectively. Both the maximum horizontal and vertical displacements decrease by over 20% when the front row pile length is increased by 50%. An increase in the slope angle or the front row*

## Izvilleček

*V članku je podano poročilo o terenskem preizkusu v Nanjingu na Kitajskem, ki je bil opravljen z namenom raziskovanja učinkov izkopavanja na plitveje vkopane plinovodih s spremljanjem in analiziranjem premikov teh cevovodov. Izvedena je bila tudi parametrična študija z uporabo programa na osnovi končnih elementov ABAQUS. Raziskovani so vplivi prostorskih učinkov izkopa gradbene jame in modelov sestavljenih podpornih konstrukcij. Numerične simulacije so bile preverjene s terenskimi preizkusi. Rezultati kažejo, da območje izkopavanja, ki je dlje od obstoječega zakopanega cevovoda, povzroči manjše premike cevovoda. Ko se naklon obstoječih vkopanih pilotov poveča z 0° na 15°, se največji vodoravni in navpični premiki zmanjšajo za 4,92 mm oziroma 2,49 mm. Največji vodoravni in navpični premiki se zmanjšajo za več kot 20 %, če se dolžina sprednje vrste pilotov poveča za 50 %. Povečanje naklona brežine ali*

*pile length helps to reduce the pipeline displacements due to the increase in the effective weight and bottom width of the trapezoidal gravity retaining wall that is equivalent to the double row of piles. This research has important theoretical significance and practical value for the design and construction of foundation pit engineering.*

*dolžine srednje vrste pilotov pomaga zmanjšati premike cevovoda zaradi povečanja efektivne teže in širine dna trapeznega gravitacijskega podporne stene, ki je enakovredna dvema vrstama pilotov. Ta raziskava ima pomemben teoretični pomen in praktično vrednost pri načrtovanju in izvedbi inženirskih problemov gradbenih jam.*

## 1 INTRODUCTION

---

Currently, underground space has been widely developed worldwide for all kinds of uses, resulting in a large number of excavations. It is well known that the significant changes in the surrounding soil stress [1] and strain field caused by deep excavation can change the static and dynamic response of existing structures [2]. Sharma and Hefny [3] found that the lining stiffness [4] of a tunnel has a significant impact on the displacement and deformation of the tunnel, caused by adjacent excavation. The stiffer lining sustains less displacement and deformation, but is likely to experience greater bending moments. Chen et al. [5] investigated the development of the bending moment and displacement of a tunnel during different construction stages of a nearby excavation. Chen also suggested that the bending moment and displacement of the tunnel are strongly related to the unloading effects [6] and displacement of the surrounding soils, which can be alleviated by means of a proper improvement of the excavation sequence.

Liyanapathirana and Nishanthan [7] simulated the excavation process of the foundation pit, and a finite-element method was used to analyze the stress behavior of a single pile [8] under the action of surface movement [9] caused by the excavation. The stiffness and spacing of the wall-support system significantly influence the pile behavior adjacent to the excavation. Therefore, considerable effort has been invested to study the various factors that can influence the stress behavior and displacements in a pit excavation. The method of estimating the water and earth pressures [10] on supporting structures separately and together, which has become a focus of attention and discussion in the field of geotechnical engineering, is analyzed. It is indicated that the method of estimating water and earth pressures together is inconsistent with the principal of effective stress. However, the protection of shallow-buried pipelines and constructions has gradually become the dominant control factor for design and construction in foundation-pit engineering. Despite many studies on foundation-pit engineering, at present there are some subjects that still lack consideration: (1) an improper form of support can cause pit-excavation accidents, resulting in the destruction

of the pipes; (2) for foundation-pit engineering in soft soil in the riverside of the Yangtze River, the influence of excavation on the surrounding existing structures is less-well studied; and (3) the influence of spatial effects during excavation and different combination forms of supporting structures of foundation-pit excavation are seldom considered.

This paper reports on a field test to study the deformation of existing pipelines during excavation at the riverside of the Yangtze River. According to the on-site engineering background, the numerical simulation is carried out using the three-dimensional finite-element software ABAQUS [11]. The numerical results are verified by the on-site monitoring data. Then, a parametric study is undertaken to investigate the influence of the spatial effects and the forms of supporting structures during foundation-pit engineering. This investigation is undertaken by comparing the displacements of the shallow-buried pipeline beside the pit. Finally, construction measures that can effectively reduce the influence of the foundation-pit excavation are put forward to provide a reference for similar projects in the future.

## 2 FIELD TEST

---

### 2.1 Background of the field test

The pit project is located in the Yangtze River diffuse beach landform unit in Nanjing, and there is a DN600 rainwater pipeline 5 m away from the boundary of the pit, which is buried 2 m below the surface. The DN600 pipeline is of the pre-stressed concrete cylinder pipe. The external diameter of the rainwater pipelines is 630 mm. The elastic and bending moduli of the material are 960MPa and 24MPa, respectively. The pit site profile and the pipeline distribution are shown in Figure 1. The total length of the foundation pit is approximately 628 m, the total area is approximately 27049 m<sup>2</sup>, and the soil-excavation depth is approximately 5.85 m. According to the exploration data of the stratum structure, the soil profile of the site is mainly composed of clay and silt, and the soil's physical-property parameters are shown in Table 1.

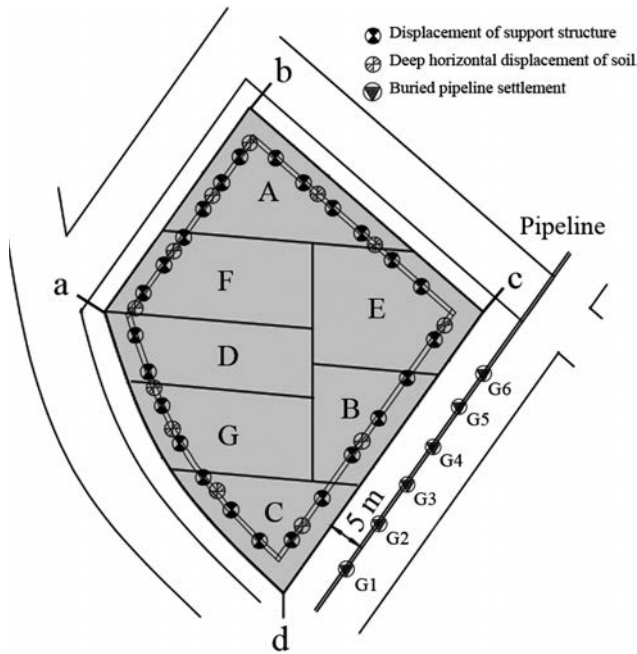


Figure 1. Location and monitoring station of the foundation-pit site and pipeline.

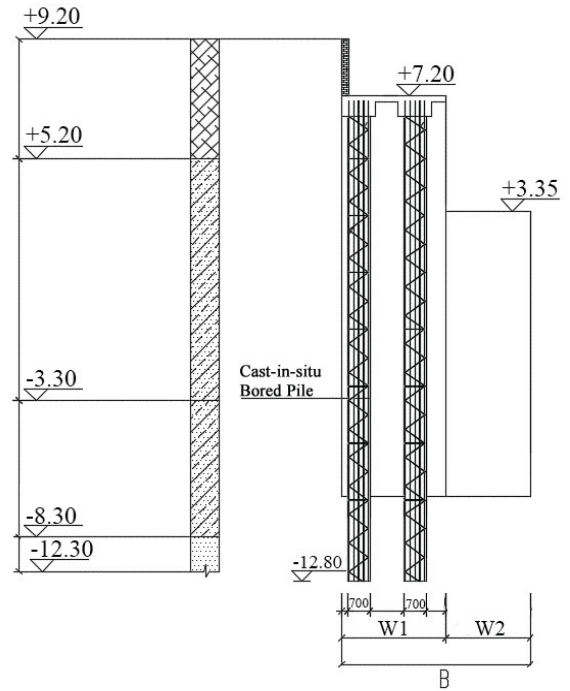


Figure 2. Schematic diagram of support-pile design.

Table 1. Physical and mechanical parameters of soil parameters.

Serial Number	Soil	Thickness (m)	$\gamma$ (kN/m <sup>3</sup> )	$E_s$ (MPa)	$\epsilon$	$c$ (kPa)	$\varphi$ (deg)
①	Plain fill	4.00	18.00	4.10	0.33	12.00	11.00
② <sub>1</sub>	Silty clay	8.50	18.10	11.40	0.33	12.90	11.00
② <sub>2</sub>	Clayey silt	5.00	19.30	10.09	0.33	3.60	32.90
② <sub>3</sub>	Silt	4.00	19.40	11.20	0.30	5.00	30.20
③ <sub>2</sub>	Fine sand	8.50	19.60	11.15	0.30	4.70	31.10

NOTES: All the data were obtained from the laboratory tests.

$\gamma$  = the unit weight     $E_s$  = the compression modulus     $\epsilon$  = the Poisson's ratio     $c$  = the cohesion of the soil     $\varphi$  = the friction angle of the soil

Soil layer ① is mainly distributed in the north and west of the study area, while soil layers ②<sub>1</sub>, ②<sub>2</sub> and ②<sub>3</sub> are unevenly distributed across the whole field and are saturated. The low density of soil layer ① leads to the existence of large pores between the soil particles, providing space for the storage of groundwater. This type of soil structure has a better connectivity and permeability than those of soil layers ②<sub>1</sub>, ②<sub>2</sub> and ②<sub>3</sub>, which have poor water permeability and supply capacities. The initial position of the shallow phreatic water is 0.1–1.5 m from the ground.

## 2.2. Construction technology and procedure

The zoning situation of the foundation pit is shown in Figure 1. The order of excavation in the construction of

the pit in this project is as follows: first, divide the pit into two layers of excavation and then dig A → B → C → D → E → F → G. The supporting structures in the pit engineering are divided into three segments, as shown in Figure 2.

- (1) From part a to part b and part b to part c, B=5.2 m (W1=3.7 m, W2=1.5 m).
- (2) From part c to part d, B=6.7 m (W1=3.7 m, W2=3.0 m).
- (3) From part d to part a, B=6.2 m (W1=3.7 m, W2=2.5 m).

B is the width of the cement retaining wall. W1 and W2 are the widths of the slabs of the cement retaining wall. A wide cement retaining wall and the double row of  $\Phi 800$  cast-in-place bored piles are used as the supporting structures.

**Table 2.** Monitoring projects.

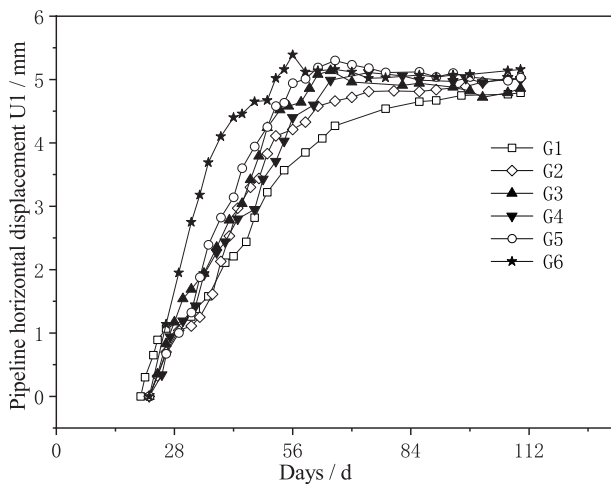
Monitoring projects		Design value		Warning value		Alarm value
		Ultimate displacements value (mm)	Rate of change (mm/d)	Cumulative change value (mm)	Rate of change (mm/d)	Cumulative change value (mm)
Horizontal and vertical displacements of the supporting structures	A~G	35.00	2.00	21.00	2.50	28.00
	Others	30.00	2.00	18.00	2.50	24.00
Deep horizontal displacements	A~G	35.00	2.00	21.00	2.50	28.00
	Others	30.00	2.00	18.00	2.50	24.00
Pipeline displacements	Rigidity	/	/	/	2.00	20.00
	Flexibility	/	/	/	3.00	30.00

### 2.3 On-Site Monitoring Design

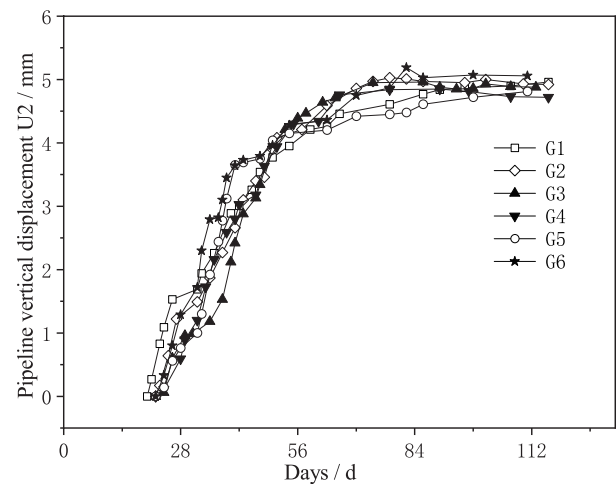
Considering the engineering monitoring projects and geological conditions, the monitoring settings are shown in Table 2.

The support structures of this foundation engineering and the shallow-buried pipeline monitoring point plane layout

are shown in Figure 1. Twenty-five monitoring points are arranged on the support structures, 12 monitoring points are arranged along the enclosure structure and 6 monitoring points are arranged along the shallow-buried pipeline to monitor the horizontal and vertical displacements so that we can evaluate the impact of the pit excavation on the surrounding existing structures. The layout principles and the numbers of test points are shown in Table 3.



(a) On-site monitoring horizontal displacements.



(b) On-site monitoring vertical displacements.

**Figure 3.** On-site monitoring displacements of the pipeline.

**Table 3.** Monitoring station layout numbers and principles.

Numbering	Monitoring projects	Quantity	Layout principle	Monitoring point number
1	Horizontal and vertical displacements of the supporting structures	25	Set one monitoring point along the top of the pile at 20-25m	QL1~QL25
2	Deep horizontal displacements	12	Set one monitoring point along the perimeter of the enclosure structures at 25-30m	CX1~CX12
3	Pipeline displacements	6	Set one monitoring point along the buried pipeline at 20-25m	G1~G6

The results of the on-site monitoring are shown in Figure 3. Both the horizontal and vertical displacements of the pipeline are compatible with the construction conditions of the foundation pit and show a synchronous trend. With the excavation of the pit, the horizontal and vertical displacements of the pipeline monitoring points gradually increase with the excavation depth. Then, the horizontal and vertical displacements of each monitoring point gradually decrease and eventually stabilize. The maximum value of the cumulative amount of horizontal displacement reaches 5.43 mm; the maximum value of the vertical displacement reaches 5.19 mm; both of which are far below the alarm value of the cumulative displacement of 20 mm. In addition, a displacement singularity occurs for the horizontal displacement of the monitoring point G6. This singularity can be caused by temporary loading on the ground and measurement errors when monitoring at this point.

### 3 NUMERICAL ANALYSIS OF THE PIT EXCAVATION

#### 3.1 Geometric models

A three-dimensional numerical analysis using ABAQUS is performed. Because of the asymmetry of the foundation pit model and pipeline position and the asymmetry of the pit excavation, it is necessary to carry out a comprehensive three-dimensional modeling of the project. According to the engineering background, the long east edge of the pit is 170 m, the southwest length of the Stone Bridge Waterway is 150 m, and the depth of the pit excavation is 5.85 m. The back boundary of the supporting structure is five times the depth of the excavation, as is the bottom boundary. Additionally, the scope of influence is 20 m outside of the pipeline. As a result, the total length of the final model is 240 m, the total width is 225 m, and the total depth is 30 m.

#### 3.2 Soil properties and constitutive models

In the three-dimensional numerical simulation calculation, the Mohr-Coulomb model is selected as the soil model. The bored pile, cement retaining wall and pipelines are all selected as isotropic elastic models. The thickness, compressive modulus, cohesive force and internal friction angle of the different soil layers in the model are evaluated according to the geological survey data measured at the beginning of the project. The physical parameters are shown in Table 1. The physical and mechanical parameters corresponding to each structural material are shown in Table 4. In the

**Table 4.** Physical and mechanical parameters of soil parameters.

Supporting structure	$\gamma$ (kN/m <sup>3</sup> )	$E$ (GPa)	$\epsilon$
Cast-in-situ bored pile	24.50	30.00	0.20
Concrete retaining wall	18.30	0.20	0.28

NOTES: All the data were obtained from the laboratory tests.

$\gamma$  = the unit weight;  $E$  = the elastic modulus;  $\epsilon$  = the Poisson's ratio

pit-supporting structure system of this project, the water curtain of the cement mixing pile and the cement retaining wall with a variable section width are soil-cement materials, while the double row of cast-in-place bored piles are C30 concrete.

#### 3.3 Finite-element meshes and boundary-condition settings

The total number of grid divisions in the model is 84205 units, of which the number of soil units is 72377 and the number of nodes is 83776. The number of units in the pipeline is 1136, and the corresponding number of nodes is 1728. The number of support structure units is 10692, and the corresponding number of nodes is 14652. Each material in the model uses a C3D8 hexahedral solid element. The boundary conditions are set in the analysis step to limit the horizontal and vertical displacements of the bottom surface of the geometric model (horizontal displacement equals 0, vertical displacement equals 0). While limiting the horizontal displacements around the soil model (x-direction displacement equals 0 or z-direction displacement equals 0), the vertical displacements can be changed freely. The grid division and boundary-limit displacements are shown in Figure 4.

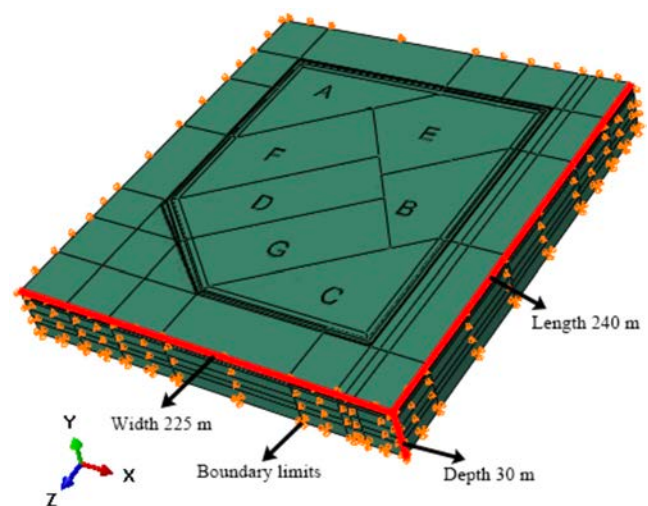
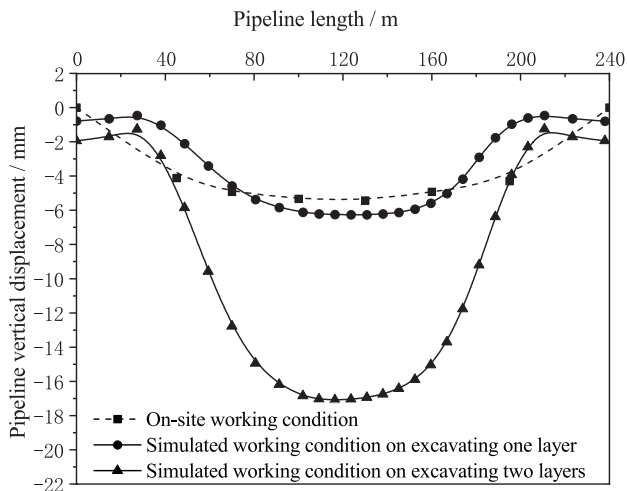
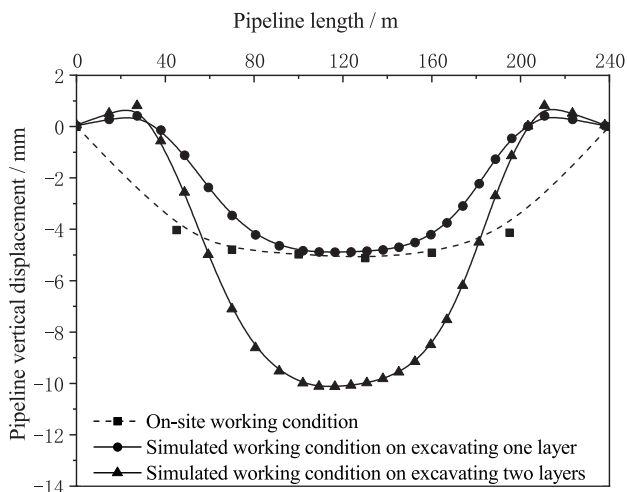


**Figure 4.** Meshing and boundary limit diagram.



(a) Horizontal displacements values comparison diagram.



(b) Vertical displacements values comparison diagram.

Figure 5. Comparison diagram of numerical simulation and measured values.

## 4 RESULTS AND COMPARISONS

### 4.1 Verification

To verify the numerical simulation, the data obtained using the simulation are compared with the on-site monitoring data. The analysis of Figure 5 shows that the simulated values of the maximum horizontal displacements appear in the middle of the pipelines and are distributed symmetrically to both sides during different excavation stages. The measured values at the middle of the pit edge, which is parallel to the pipelines, are the largest and present a symmetrical distribution state. The change law of the simulated result is consistent with the measured one. With the increase in the excavation depth of the first layer of soil, the displacements of the existing pipelines are small, but increase slowly. By analyzing

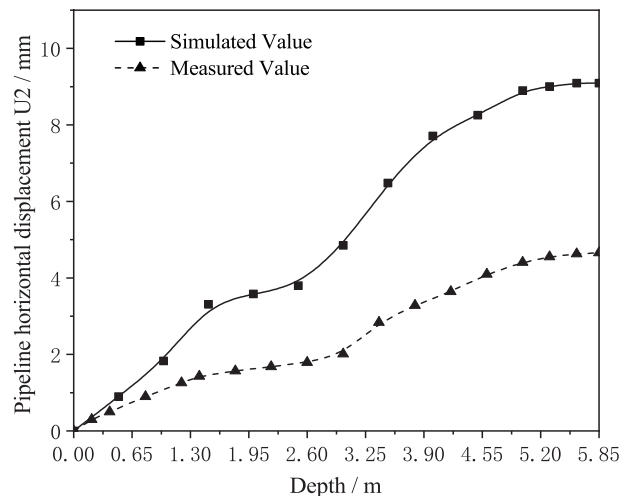


Figure 6. Vertical displacements curve with the depth of excavation.

Figure 6, as the excavation progresses, the displacements of the pipeline tend to increase gradually.

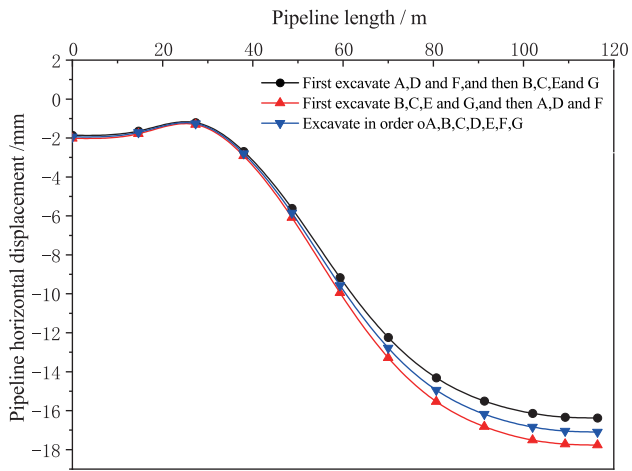
When excavating the second layer of soil, the displacements of the pipeline increase greatly with the depth of the excavation and finally tend to be stable. The measured value of the horizontal displacement of the pipeline is 5.43 mm, and the simulated value is 6.27 mm, a difference of 0.84 mm. Additionally, the measured value of the vertical displacement of the pipeline is 5.19 mm, and the simulated value is 4.87 mm, a difference of 0.32 mm. However, the measured and simulated displacement trends are slightly different in the bottom corner of the studied area because a series of idealized simplifications are carried out in the numerical simulation calculation, i.e., the bored pile, cement retaining wall and pipelines are all selected as isotropic elastic models to simplify the model and expedite the computation process. At the same time, a series of factors, such as precipitation, vehicle load and construction, which are related to the actual engineering, can also cause differences in the result.

However, as shown in Figures 6 and 7, the numerical simulated results are similar to the on-site monitoring data. Some critical points have relatively small errors, and we can clearly see that the trend of the simulated results is consistent with the on-site data. Through these points, we can determine that the numerical simulation model corresponds to the field engineering project.

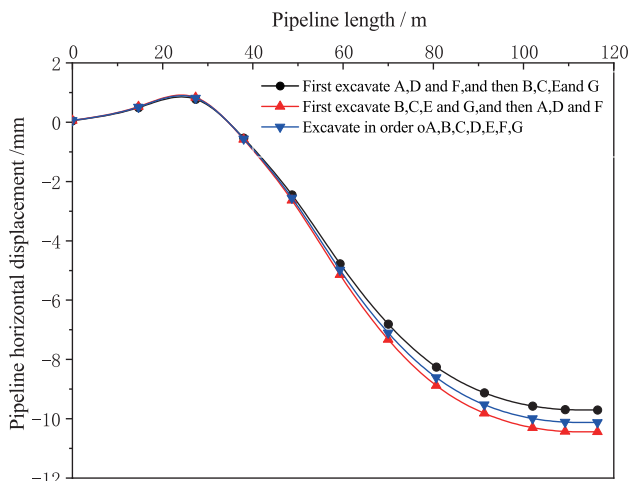
### 4.2 Influence of space effect on the pipeline displacements

#### 4.2.1 Influence of the sequence of pit excavation

Considering the distance from the excavation impact zone to the shallow-buried pipelines, along half of the



(a) Horizontal displacements comparison curve.



(b) Vertical displacements comparison curve.

Figure 7. Displacements comparison curve with excavation sequence.

pipeline length, this section sets up two simulation working conditions to compare with the on-site working condition, and the influence of the pit excavation sequence on the shallow-buried pipeline is discussed. By analyzing Figure 7, which shows the results for different excavation block ordering, it is shown that the displacements of the pipeline at the pit corner are not very different from those of the on-site working condition, yet the difference increases at the central location of the pipeline. This might be because of the stress concentration at the corner of the foundation pit, which gradually disappears along the edge of the foundation pit, causing the displacement difference in the middle part to increase.

As shown in Figure 7, first excavating the areas which are far from the existing pipeline leads to the minimum displacements. The cause of this phenomenon is that

the soil close to the pipeline is equivalent to the pressure and weight of one kind of supporting structure, which causes a reduction in the pipeline displacement when the area farther away from the pipeline is excavated first. In contrast, first excavating in the affected area near the pipeline results in larger displacements. The cause of this phenomenon is that the displacements generated by the nearer disturbance zone have a superposition effect on the displacements generated by any subsequent excavation in other areas.

#### 4.2.2 Influence of the Number of Excavation Blocks

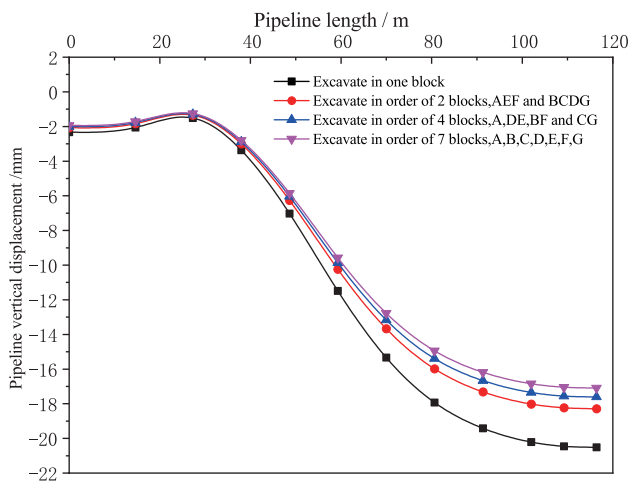
During the excavation, the block excavation can be divided into two types. One is that the block is not stratified for excavation, and the other is that the block is stratified for excavation. At present, the research on block excavation is still very vague. Some scholars mentioned that block excavation and backfilling can effectively reduce subsequent uplift displacement at the bottom of the foundation pit.

The way the case pit is used in this paper is a stratified block excavation. By keeping the number of excavation layers unchanged and changing the number of excavation blocks, this section sets up four simulation working conditions, shown in Table 5.

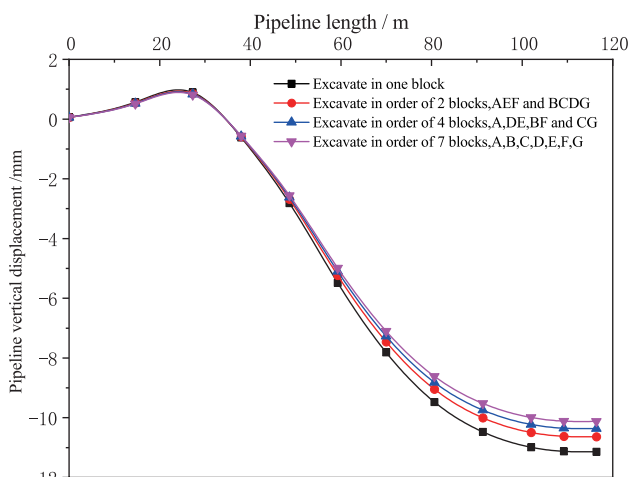
Table 5. Simulated conditions of the number of excavation blocks.

Working Condition	Forms of block excavation
On-site Condition	Each layer is excavated in order of 7 blocks, A, B, C, D, E, F, G
Simulated Condition One	Each layer is excavated in one block
Simulated Condition Two	Each layer is excavated in order of 2 blocks, AEF and BCDG
Simulated Condition Three	Each layer is excavated in order of 4 blocks, A, DE, BF and CG

With changes in the number of excavation blocks, the results shown in Figure 8 indicate that the displacement value of the pipeline increases along the long edge of the pit, from the two corners to the middle. The displacement value reaches the maximum in the middle of the pipeline. By analyzing the horizontal and vertical displacements under the four working conditions, the more blocks there are, the smaller is the displacement value of the pipeline under the same number of excavation layers. During the excavation and unloading process of the foundation pit, with the removal of the overlying soil mass, the rock and soil mass at the bottom of the foundation pit will uplift and spring back due to



(a) Horizontal displacements comparison curve.



(b) Vertical displacements comparison curve.

**Figure 8.** Displacements comparison curve with the number of excavated blocks.

the stress redistribution, and the lateral deformation will also occur due to the stress redistribution of the soil mass at the side wall of the foundation pit. Although the total amount of unloading caused by the multi-block excavation and the whole-block excavation is the same, the larger the number of blocks, the less the amount of unloading every time, the smaller the stress change rate of soil, the smaller the damage degree [12] of soil, and the smaller the displacement caused.

### 4.3 Influence of the supporting structure on the pipeline displacements

#### 4.3.1 Influence of the slope angle of the front pile

In the process of pit excavation, the supporting piles play a role in restraining the displacements, and mostly

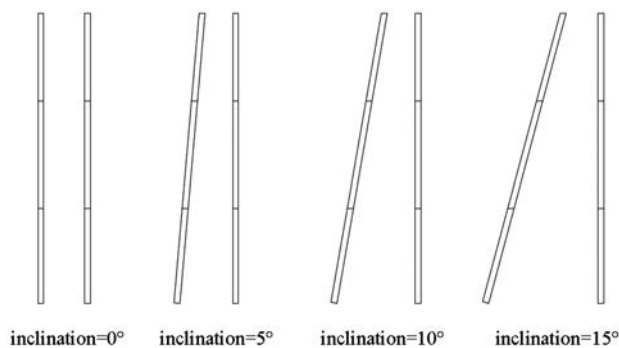


**Figure 9.** Geometric diagram of four inclined piles.

conventional engineering piles are used in the vertical direction. However, often in engineering practice, the supporting piles can effectively reduce the displacement of the soil around the pit when the piles are inclined at a certain angle, thereby reducing the influence on the displacement of the existing buried pipelines. Based on the ABAQUS model established in this pit project, this section sets up four simulation working conditions. The angle of the front pile is designed to be 0°, 5°, 10°, 15°, as shown in Figure 9. The influence of the inclined angle of the front pile on the displacements of the shallow-buried pipelines will be analyzed and discussed. The numerical simulation results of the existing pipeline displacements are shown in Table 6.

**Table 6.** Maximum displacements with the slope angle of the front pile.

Angle of slope of the front pile (°)	0	5	10	15
The maximum horizontal displacement (mm)	17.19	15.86	14.26	12.27
The maximum vertical displacement (mm)	10.28	9.91	9.03	7.79

The displacement of the pipeline decreases when the angle of the front-row pile increases. Keeping the rear-support pile vertical, the front-support pile inclined at a certain angle can effectively reduce the displacements of the existing buried pipeline. Moreover, with the increase in the slope angle, the effects of controlling the pipeline displacement become more obvious. When the current row pile is inclined, it is equivalent to forming a trapezoidal gravity retaining wall combined with the back-row pile, thus increasing its effective weight and bottom width. In the numerical simulation, the ability to reduce the deformation of the pit of the equivalent retaining wall is clearly shown.

However, the range of angles discussed in this paper is only  $0^\circ$  to  $15^\circ$ , and for larger angles, considering the increase in the difficulty in pit-supporting construction and the cost, the practical significance of the research is not considerable.

#### 4.3.2 Influence of the length of the front pile

In the design of the foundation-pit support, for the convenience of the design and construction, when designing a double row of pile support, the lengths of the front piles are usually equal. However, for the support schemes of unequal length piles, there are few studies on the influence of the pit displacements. This section sets up five simulation working conditions, as shown in Table 7. The simulation results of the buried pipeline displacements under the different lengths of the front-support piles are shown in Table 8.

**Table 7.** Simulated conditions of the length of the front piles.

Working Condition	A	B	C	D	E
Length of the front piles (m)	16	18	20	22	24
Length of the back piles (m)	20	20	20	20	20

**Table 8.** Maximum displacements with the length of the front pile.

Length of the front pile ( $^\circ$ )	16	18	20	22	24
Maximum horizontal displacement (mm)	20.20	18.26	17.19	16.78	16.70
Maximum vertical displacement (mm)	12.50	11.13	10.28	9.82	9.74

We can see that the maximum horizontal and vertical displacements decrease with the increasing pile length in the front row. The laws of the variation in the curves for the maximum horizontal and vertical displacements are the same. The cause of this phenomenon is the same as that for the equivalent retaining wall mentioned above. And it is easy to understand that the higher and heavier the retaining wall is, the less the displacements will be. This method reduces the displacement of the foundation pit by increasing its effective weight. Nevertheless, the sensitivity to the displacements of the pipelines decreases with the increasing length of the front-row pile. This is because the effective weight of the retaining wall formed by the rear pile does not increase after the front pile increases to a certain extent because the length of the rear pile does not lengthen.

## 5 CONCLUSIONS AND DISCUSSIONS

Based on previous research, this paper combines the on-site monitoring data of existing pipelines in the context of a soft soil foundation-pit project in Nanjing with an ABAQUS three-dimensional numerical simulation. By comparing the results of the simulation with the field test data, the displacements of the pipeline are studied by analyzing the spatial effects of the pit's excavation and the combination of piles in the supporting structure.

The main conclusions are as follows:

- (1) In the foundation-pit engineering of the Yangtze River plain, the horizontal and vertical displacements of the shallow-buried pipeline increase with the depth of the excavation. The displacements increase from the two external corners to the middle, which is a symmetrically distribution.
- (2) The space effect of the pit's excavation is significantly present. The soil in the area far from the pipeline should be excavated first, which can effectively restrain the displacements of the buried pipeline. In addition, it is more helpful to restrain the displacements of the pipeline by using as many layers and blocks as possible in the excavation design.
- (3) When a double-row pile support is used, the front pile is inclined at a certain angle within a certain range, which can effectively suppress the displacements of the existing buried pipeline. At the same time, the longer the front pile is, the smaller are the displacements of the pipeline.

### Funding

This work was supported by the National Natural Science Foundation of China (Grant No. 41977240 and No. 51779264); the Fundamental Research Funds for the Central Universities (No. B200202090) and the Natural Science Foundation of Jiangsu Province (No. BK20171399).

### Disclosure statement

No potential conflict of interest was reported by the authors.

## REFERENCES

---

- [1] Stille, H., Palmström, A. 2008. Ground behaviour and rock mass composition in underground excavations. *Tunnelling and Underground Space Technology* 23(1), 46-64. DOI:10.1016/j.tust.2006.11.005
- [2] Castaldo, P., Iulii, M.De. 2014. Effects of deep excavation on seismic vulnerability of existing reinforced concrete framed structures. *Soil Dynamics and Earthquake Engineering* 64, 102-112. DOI: 10.1016/j.soildyn.2014.05.005
- [3] Sharma, J.S., Hefny, A.M. 2001. Effect of large excavation on deformation of adjacent MRT tunnels. *Tunnelling and Underground Space Technology* 16(2), 93-98. DOI: 10.1016/S0886-7798(01)00033-5
- [4] Mezger, F., Ramoni, M. 2017. Evaluation of higher capacity segmental lining systems when tunnelling in squeezing rock. *Tunnelling and Underground Space Technology* 65, 200-214. DOI:10.1016/j.tust.2017.02.012
- [5] Chen, R.P., Meng, F.Y. 2016. Investigation of response of metro tunnels due to adjacent large excavation and protective measures in soft soils. *Tunnelling and Underground Space Technology* 58, 224-235. DOI:10.1016/j.tust.2016.06.002
- [6] Zhang, Z.G., Huang, M.S. 2013. Evaluation of deformation response for adjacent tunnels due to soil unloading in excavation engineering. *Tunnelling and Underground Space Technology* 38, 244-253. DOI:10.1016/j.tust.2013.07.002
- [7] Liyanapathirana, D.S., Nishanthan, R. 2016. Influence of deep excavation induced ground movements on adjacent piles. *Tunnelling and Underground Space Technology* 52, 168-181. DOI:10.1016/j.tust.2015.11.019
- [8] Sheil, B.B., McCabe, B.A. 2016. An analytical approach for the prediction of single pile and pile group behaviour in clay. *Computers and Geotechnics* 75, 145-158. DOI:10.1016/j.compgeo.2016.02.001
- [9] Yoo, C., Lee, D. 2008. Deep excavation-induced ground surface movement characteristics- A numerical investigation. *Computers and Geotechnics* 335(2), 231-252. DOI:10.1016/j.compgeo.2016.02.001
- [10] Li, G.X. 2000 Estimating the water and earth pressures on the supporting structure around a foundation pit separately and together. *Chinese Journal of Geotechnical Engineering*. DOI: 10.3321/j.issn:1000-4548.2000.03.018
- [11] Michael, K., Dimitris, L. 2017. Development of a 3D finite element model for shield EPB tunneling. *Tunnelling and Underground Space Technology* 65, 22-34. DOI:10.1016/j.tust.2017.02.001
- [12] Zhao, X.H. Sun, H. 2000. *Damage Soil Mechanics*. Tongji University Press. China.

# NAVODILA AVTORJEM

---

## Vsebina članka

Članek naj bo napisan v naslednji obliki:

- Naslov, ki primerno opisuje vsebino članka in ne presega 80 znakov.
- Izvleček, ki naj bo skrajšana oblika članka in naj ne presega 250 besed. Izvleček mora vsebovati osnove, jedro in cilje raziskave, uporabljeno metodologijo dela, povzetek izidov in osnovne sklepe.
- Največ 6 ključnih besed, ki bi morale biti napisane takoj po izvlečku.
- Uvod, v katerem naj bo pregled novejšega stanja in zadostne informacije za razumevanje ter pregled izidov dela, predstavljenih v članku.
- Teorija.
- Eksperimentalni del, ki naj vsebuje podatke o postavitvi preiskusa in metode, uporabljene pri pridobitvi izidov.
- Izidi, ki naj bodo jasno prikazani, po potrebi v obliki slik in preglednic.
- Razprava, v kateri naj bodo prikazane povezave in posplošitve, uporabljene za pridobitev izidov. Prikazana naj bo tudi pomembnost izidov in primerjava s poprej objavljenimi deli.
- Sklepi, v katerih naj bo prikazan en ali več sklepov, ki izhajajo iz izidov in razprave.
- Vse navedbe v besedilu morajo biti na koncu zbrane v seznamu literature, in obratno.

## Dodatne zahteve

- Vrstice morajo biti zaporedno oštevilčene.
- Predložen članek ne sme imeti več kot 18 strani (brez tabel, legend in literature); velikost črk 12, dvojni razmik med vrsticami. V članek je lahko vključenih največ 10 slik. Isti rezultati so lahko prikazani v tabelah ali na slikah, ne pa na oba načina.
- Potrebno je priložiti imena, naslove in elektronske naslove štirih potencialnih recenzentov članka. Urednik ima izključno pravico do odločitve, ali bo te predloge upošteval.

## Enote in okrajšave

V besedilu, preglednicah in slikah uporabljajte le standardne označbe in okrajšave SI. Simbole fizikalnih veličin v besedilu pišite poševno (npr.  $v$ ,  $T$  itn.). Simbole enot, ki so sestavljene iz črk, pa pokončno (npr. Pa, m itn.). Vse okrajšave naj bodo, ko se prvič pojavijo, izpisane v celoti.

## Slike

Slike morajo biti zaporedno oštevilčene in označene, v besedilu in podnaslovu, kot sl. 1, sl. 2 itn. Posnete naj bodo v katerem koli od razširjenih formatov, npr. BMP, JPG, GIF. Za pripravo diagramov in risb priporočamo CDR format (CorelDraw), saj so slike v njem vektorske in jih lahko pri končni obdelavi preprosto povečujemo ali pomanjšujemo.

Pri označevanju osi v diagramih, kadar je le mogoče, uporabite označbe veličin (npr.  $v$ ,  $T$  itn.). V diagramih z več krivuljami mora biti vsaka krivulja označena. Pomen oznake mora biti razložen v podnapisu slike.

Za vse slike po fotografskih posnetkih je treba priložiti izvirne fotografije ali kakovostno narejen posnetek.

## Preglednice

Preglednice morajo biti zaporedno oštevilčene in označene, v besedilu in podnaslovu, kot preglednica 1, preglednica 2 itn. V preglednicah ne uporabljajte izpisanih imen veličin, ampak samo ustrezne simbole. K fizikalnim količinam, npr.  $t$  (pisano poševno), pripišite enote (pisano pokončno) v novo vrsto brez oklepajev. Vse opombe naj bodo označene z uporabo dvignjene številke<sup>1</sup>.

## Seznam literature

### Navedba v besedilu

Vsaka navedba, na katero se sklicujete v besedilu, mora biti v seznamu literature (in obratno). Neobjavljeni rezultati in osebne komunikacije se ne priporočajo v seznamu literature, navedejo pa se lahko v besedilu, če je nujno potrebno.

### Oblika navajanja literature

**V besedilu:** Navedite reference zaporedno po številkah v oglatih oklepajih v skladu z besedilom. Dejanski avtorji so lahko navedeni, vendar mora obvezno biti podana referenčna številka.

Primer: ».... kot je razvidno [1,2]. Brandl and Blovsky [4], sta pridobila drugačen rezultat...«

**V seznamu:** Literaturni viri so oštevilčeni po vrstnem redu, kakor se pojavijo v članku. Označimo jih s številkami v oglatih oklepajih.

### Sklicevanje na objave v revijah:

- [1] Jelušič, P., Žlender, B. 2013. Soil-nail wall stability analysis using ANFIS. Acta Geotechnica Slovenica 10(1), 61-73.

*Sklicevanje na knjigo:*

- [2] Šuklje, L. 1969. Rheological aspects of soil mechanics. Wiley-Interscience, London

*Sklicevanje na poglavje v monografiji:*

- [3] Mitchel, J.K. 1992. Characteristics and mechanisms of clay creep and creep rupture, in N. Guven, R.M. Pollastro (eds.), Clay-Water Interface and Its Rheological Implications, CMS Workshop Lectures, Vol. 4, The clay minerals Society, USA, pp. 212-244..

*Sklicevanje na objave v zbornikih konferenc:*

- [4] Brandl, H., Blovsky, S. 2005. Slope stabilization with socket walls using the observational method. Proc. Int. conf. on Soil Mechanics and Geotechnical Engineering, Bratislava, pp. 2485-2488.

*Sklicevanje na spletne objave:*

- [5] Kot najmanj, je potrebno podati celoten URL. Če so poznani drugi podatki (DOI, imena avtorjev, datumi, sklicevanje na izvorno literaturo), se naj prav tako dodajo.

## INSTRUCTIONS FOR AUTHORS

---

### Format of the paper

The paper should have the following structure:

- A Title, which adequately describes the content of the paper and should not exceed 80 characters;
- An Abstract, which should be viewed as a mini version of the paper and should not exceed 250 words. The Abstract should state the principal objectives and the scope of the investigation and the methodology employed; it should also summarise the results and state the principal conclusions;
- Immediately after the abstract, provide a maximum of 6 keywords;
- An Introduction, which should provide a review of recent literature and sufficient background information to allow the results of the paper to be understood and evaluated;
- A Theoretical section;
- An Experimental section, which should provide details of the experimental set-up and the methods used to obtain the results;
- A Results section, which should clearly and concisely present the data, using figures and tables where appropriate;
- A Discussion section, which should describe the relationships shown and the generalisations made possible by the results and discuss the significance

### Podatki o avtorjih

Članku priložite tudi podatke o avtorjih: imena, nazive, popolne poštne naslove, številke telefona in faksa, naslove elektronske pošte. Navedite kontaktno osebo.

### Sprejem člankov in avtorske pravice

Uredništvo si pridržuje pravico do odločanja o sprejemu članka za objavo, strokovno oceno mednarodnih recenzentov in morebitnem predlogu za krajšanje ali izpopolnitev ter terminološke in jezikovne korekture. Z objavo preidejo avtorske pravice na revijo ACTA GEOTECHNICA SLOVENICA. Pri morebitnih kasnejših objavah mora biti AGS navedena kot vir.

---

Vsa nadaljnja pojasnila daje:

Uredništvo  
ACTA GEOTECHNICA SLOVENICA  
Univerza v Mariboru,  
Fakulteta za gradbeništvo, prometno inženirstvo in arhitekturo  
Smetanova ulica 17, 2000 Maribor, Slovenija  
E-pošta: ags@um.si

of the results, making comparisons with previously published work;

- Conclusions, which should present one or more conclusions that have been drawn from the results and subsequent discussion;
- A list of References, which comprises all the references cited in the text, and vice versa.

### Additional Requirements for Manuscripts

- Use double line-spacing.
- Insert continuous line numbering.
- The submitted text of Research Papers should cover no more than 18 pages (without Tables, Legends, and References, style: font size 12, double line spacing). The number of illustrations should not exceed 10. Results may be shown in tables or figures, but not in both of them.
- Please submit, with the manuscript, the names, addresses and e-mail addresses of four potential referees. Note that the editor retains the sole right to decide whether or not the suggested reviewers are used.

### Units and abbreviations

Only standard SI symbols and abbreviations should be used in the text, tables and figures. Symbols for physical quantities in the text should be written in Italics (e.g.  $v$ ,  $T$ , etc.). Symbols for units that consist of letters should

be in plain text (e.g. Pa, m, etc.).

All abbreviations should be spelt out in full on first appearance.

## Figures

Figures must be cited in consecutive numerical order in the text and referred to in both the text and the caption as Fig. 1, Fig. 2, etc. Figures may be saved in any common format, e.g. BMP, JPG, GIF. However, the use of CDR format (CorelDraw) is recommended for graphs and line drawings, since vector images can be easily reduced or enlarged during final processing of the paper.

When labelling axes, physical quantities (e.g.  $v$ ,  $T$ , etc.) should be used whenever possible. Multi-curve graphs should have individual curves marked with a symbol; the meaning of the symbol should be explained in the figure caption. Good quality black-and-white photographs or scanned images should be supplied for the illustrations.

## Tables

Tables must be cited in consecutive numerical order in the text and referred to in both the text and the caption as Table 1, Table 2, etc. The use of names for quantities in tables should be avoided if possible: corresponding symbols are preferred. In addition to the physical quantity, e.g.  $t$  (in Italics), units (normal text), should be added on a new line without brackets.

Any footnotes should be indicated by the use of the superscript<sup>1</sup>.

## LIST OF references

### Citation in text

Please ensure that every reference cited in the text is also present in the reference list (and vice versa). Any references cited in the abstract must be given in full. Unpublished results and personal communications are not recommended in the reference list, but may be mentioned in the text, if necessary.

### Reference style

**Text:** Indicate references by number(s) in square brackets consecutively in line with the text. The actual authors can be referred to, but the reference number(s) must always be given:

Example: "... as demonstrated [1,2]. Brandl and Blovsky [4] obtained a different result ..."

**List:** Number the references (numbers in square brackets) in the list in the order in which they appear in the text.

### Reference to a journal publication:

- [1] Jelušič, P., Žlender, B. 2013. Soil-nail wall stability analysis using ANFIS. *Acta Geotechnica Slovenica* 10(1), 61-73.

### Reference to a book:

- [2] Šuklje, L. 1969. Rheological aspects of soil mechanics. Wiley-Interscience, London

### Reference to a chapter in an edited book:

- [3] Mitchel, J.K. 1992. Characteristics and mechanisms of clay creep and creep rupture, in N. Guven, R.M. Pollastro (eds.), *Clay-Water Interface and Its Rheological Implications*, CMS Workshop Lectures, Vol. 4, The clay minerals Society, USA, pp. 212-244.

### Conference proceedings:

- [4] Brandl, H., Blovsky, S. 2005. Slope stabilization with socket walls using the observational method. *Proc. Int. conf. on Soil Mechanics and Geotechnical Engineering*, Bratislava, pp. 2485-2488.

### Web references:

- [5] As a minimum, the full URL should be given and the date when the reference was last accessed. Any further information, if known (DOI, author names, dates, reference to a source publication, etc.), should also be given.

## Author information

The following information about the authors should be enclosed with the paper: names, complete postal addresses, telephone and fax numbers and E-mail addresses. Indicate the name of the corresponding author.

## Acceptance of papers and copyright

The Editorial Committee of the Slovenian Geotechnical Review reserves the right to decide whether a paper is acceptable for publication, to obtain peer reviews for the submitted papers, and if necessary, to require changes in the content, length or language.

On publication, copyright for the paper shall pass to the ACTA GEOTECHNICA SLOVENICA. The AGS must be stated as a source in all later publication.

---

For further information contact:

Editorial Board  
ACTA GEOTECHNICA SLOVENICA  
University of Maribor,  
Faculty of Civil Engineering, Transportation Engineering and Architecture  
Smetanova ulica 17, 2000 Maribor, Slovenia  
E-mail: ags@um.si



## NAMEN REVIJE

Namen revije ACTA GEOTECHNICA SLOVENICA je objavljane kakovostnih teoretičnih člankov z novih pomembnih področij geomehanike in geotehnike, ki bodo dolgoročno vplivali na temeljne in praktične vidike teh področij.

ACTA GEOTECHNICA SLOVENICA objavlja članke s področij: mehanika zemljin in kamnin, inženirska geologija, okoljska geotehnika, geosintetika, geotehnične konstrukcije, numerične in analitične metode, računalniško modeliranje, optimizacija geotehničnih konstrukcij, terenske in laboratorijske preiskave.

Revija redno izhaja dvakrat letno.

## AVTORSKE PRAVICE

Ko uredništvo prejme članek v objavo, prosi avtorja(je), da prenese(jo) avtorske pravice za članek na izdajatelja, da bi zagotovili kar se da obsežno razširjanje informacij. Naša revija in posamezni prispevki so zaščiteni z avtorskimi pravicami izdajatelja in zanje veljajo naslednji pogoji:

### Fotokopiranje

V skladu z našimi zakoni o zaščiti avtorskih pravic je dovoljeno narediti eno kopijo posameznega članka za osebno uporabo. Za naslednje fotokopije, vključno z večkratnim fotokopiranjem, sistematičnim fotokopiranjem, kopiranjem za reklamne ali predstavitvene namene, nadaljnjo prodajo in vsemi oblikami nedobičkonosne uporabe je treba pridobiti dovoljenje izdajatelja in plačati določen znesek.

Naročniki revije smejo kopirati kazalo z vsebino revije ali pripraviti seznam člankov z izvlečki za rabo v svojih ustanovah.

### Elektronsko shranjevanje

Za elektronsko shranjevanje vsakršnega gradiva iz revije, vključno z vsemi članki ali deli članka, je potrebno dovoljenje izdajatelja.

## ODGOVORNOST

Revija ne prevzame nobene odgovornosti za poškodbe in/ali škodo na osebah in na lastnini na podlagi odgovornosti za izdelke, zaradi malomarnosti ali drugače, ali zaradi uporabe kakršnekoli metode, izdelka, navodil ali zamisli, ki so opisani v njej.

## AIMS AND SCOPE

ACTA GEOTECHNICA SLOVENICA aims to play an important role in publishing high-quality, theoretical papers from important and emerging areas that will have a lasting impact on fundamental and practical aspects of geomechanics and geotechnical engineering.

ACTA GEOTECHNICA SLOVENICA publishes papers from the following areas: soil and rock mechanics, engineering geology, environmental geotechnics, geosynthetic, geotechnical structures, numerical and analytical methods, computer modelling, optimization of geotechnical structures, field and laboratory testing.

The journal is published twice a year.

## COPYRIGHT

Upon acceptance of an article by the Editorial Board, the author(s) will be asked to transfer copyright for the article to the publisher. This transfer will ensure the widest possible dissemination of information. This review and the individual contributions contained in it are protected by publisher's copyright, and the following terms and conditions apply to their use:

### Photocopying

Single photocopies of single articles may be made for personal use, as allowed by national copyright laws. Permission of the publisher and payment of a fee are required for all other photocopying, including multiple or systematic copying, copying for advertising or promotional purposes, resale, and all forms of document delivery.

Subscribers may reproduce tables of contents or prepare lists of papers, including abstracts for internal circulation, within their institutions.

### Electronic Storage

Permission of the publisher is required to store electronically any material contained in this review, including any paper or part of the paper.

## RESPONSIBILITY

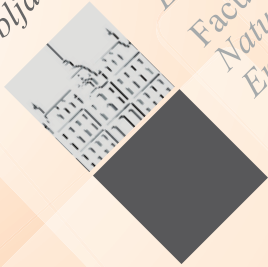
No responsibility is assumed by the publisher for any injury and/or damage to persons or property as a matter of product liability, negligence or otherwise, or from any use or operation of any methods, products, instructions or ideas contained in the material herein.



University of Maribor  
Faculty of Civil Engineering,  
Transportation Engineering  
and Architecture

[www.fgpa.um.si](http://www.fgpa.um.si)

University  
of Ljubljana



Faculty of  
Civil and Geodetic  
Engineering  
Faculty of  
Natural Sciences and  
Engineering

[www.fgg.uni-lj.si](http://www.fgg.uni-lj.si)  
[www.ntf.uni-lj.si](http://www.ntf.uni-lj.si)



[www.sloged.si](http://www.sloged.si)



SLOVENSKO DRUŠTVO ZA  
PODZEMNE GRADNJE  
SLOVENIAN SOCIETY FOR  
UNDERGROUND STRUCTURES

[www.ita-slovenia.si](http://www.ita-slovenia.si)